CNWRA 95-008

FINITE ELEMENT MODELING OF LISTRIC NORMAL FAULTING

Prepared for

Nuclear Regulatory Commission
Contract NRC-02-93-005

Prepared by

Center for Nuclear Waste Regulatory Analyses
San Antonio, Texas

April 1995

FINITE ELEMENT MODELING
OF
LISTRIC NORMAL FAULTING

Prepared for

Nuclear Regulatory Commission
Contract NRC-02-93-005

Prepared by

Goodluck I. Ofoegbu

and

David A. Ferrill

Center for Nuclear Waste Regulatory Analyses
San Antonio, Texas

APRIL 1995

THIS PAGE INTENTIONALLY LEFT BLANK

ABSTRACT

The results of finite element analyses of hangingwall deformation associated with listric faulting are presented in this report. It is demonstrated that hangingwall deformation is strongly sensitive to the values of the *in situ* stress, and that the magnitudes of ground acceleration induced in the hangingwall by slip on the listric faults is sensitive to the amount of material damping in the fault zones. On the other hand, the sensitivity of the hangingwall deformation to material parameters such as friction and dilation angles, damping factor, and elastic stiffness is overshadowed by the *in-situ*-stress effects.

The results also indicate a strong effect of fault geometry on hangingwall deformation. Faults that change in attitude gradually from steeply dipping to shallow-dipping cause more severe effects on the hangingwall than straight steeply dipping faults that terminate abruptly at the low-angle detachment. It was also observed that slip on the low-angle segment of a listric fault system occurs at a rate several orders of magnitude smaller than the slip rate in the steeply dipping segments; this difference in slip rate may explain the lack of seismicity associated with low-angle detachment faults. The strong effect of fault-zone rheology on low-angle-detachment fault slip is also demonstrated. Modeling fault zones as thin-layer isotropic solids led to the prediction of fault slip under conditions for which it would not occur if the assumed rheology restricted the development of inelastic response to planes parallel to the fault.

Based on these results, it is recommended that additional deep *in situ* stress measurements be made as part of the site characterization of the Yucca Mountain site for the proposed nuclear waste repository. Also, additional analyses are recommended, to examine the effects of fault geometry and three-dimensional *in situ* stress states on hangingwall deformation.

THIS PAGE INTENTIONALLY LEFT BLANK

CONTENTS

Section Page

FIGURES vii
TABLES xi
ACKNOWLEDGMENTS xiii
QUALITY OF DATA xiii
SOFTWARE QUALITY ASSURANCE xiii

1 INTRODUCTION 1-1
1.1 HANGINGWALL DEFORMATION ASSOCIATED WITH EXTENSIONAL FAULTING 1-1
1.2 SEISMICITY ASSOCIATED WITH EXTENSIONAL FAULTING 1-4
1.3 SCOPE OF WORK 1-4

2 DESCRIPTION OF MODEL 2-1
2.1 GEOMETRICAL MODEL 2-1
2.2 MATERIAL MODEL 2-4
2.2.1 Linear-Elastic Material Zones 2-4
2.2.2 The Elastoplastic Material Zones 2-4
2.2.3 Material Damping 2-5
2.3 INITIAL CONDITIONS 2-6
2.4 FINITE ELEMENT MODEL 2-8
2.4.1 Boundary Conditions 2-8
2.4.2 Simulation Procedure 2-9
2.4.2.1 The Initial Equilibrium State 2-9
2.4.2.2 Perturbation of Selected Fault Zone 2-10
2.4.3 Experiment Design 2-10

3 TYPICAL CALCULATED RESPONSES 3-1
3.1 STRESS DISTRIBUTIONS 3-1
3.2 DISTRIBUTIONS OF INELASTIC STRAIN 3-5
3.3 DISTRIBUTION OF DISPLACEMENTS 3-7

4 ANALYSES OF CALCULATED RESPONSES 4-1
4.1 FAULT DISPLACEMENT 4-1
4.2 SLIP LENGTH 4-3
4.3 LIMIT-EQUILIBRIUM FRICTION ANGLE 4-7
4.4 SLIP RATE 4-12
4.5 ACCELERATIONS 4-19
4.6 STRESS DISTRIBUTIONS IN THE STUDY ZONE 4-23

CONTENTS

Section Page

5 CONCLUSIONS 5-1

6 REFERENCES 6-1

APPENDIX A – TABLES OF VALUES FOR THE INPUT AND RESPONSE VARIABLES
APPENDIX B – SENSITIVITY PLOTS OF RESPONSE VERSUS INPUT VARIABLES

FIGURES

Figure		Page
1-1	Cross section C-C' from Young et al., 1992	1-2
2-1	Geometrical model, showing boundaries of the modeled domain and fault zones	2-2
2-2	Enlarged view of the geometrical model, showing the slip-rate monitoring stations and boundaries of the study zone	2-3
2-3	Enlarged view of the study zone, showing the acceleration monitoring stations	2-3
2-4	Finite element discretization of the modeled domain	2-8
2-5	Enlarged view of the finite element mesh, showing the study zone and fault zones	2-9
2-6	Illustration of the analysis domain, showing the four perturbed faults	2-11
3-1	Distribution of vertical stress: initial state with no fault slip	3-1
3-2	Distribution of horizontal stress: initial state with no fault slip	3-2
3-3	Distribution of vertical stress: initial state with previous fault slip (Case c61)	3-3
3-4	Distribution of horizontal stress: initial state with previous fault slip (Case c61)	3-3
3-5	Distribution of vertical stress: end of simulation (Case c61)	3-4
3-6	Distribution of horizontal stress: end of simulation (Case c61)	3-4
3-7	Distribution of inelastic strain for Case c51: end of simulation	3-5
3-8	Distribution of inelastic strain for Case c63: end of simulation	3-6
3-9	Distribution of horizontal displacements associated with slip on the Fmw fault zone	3-7
3-10	Distribution of vertical displacements associated with slip on the Fmw fault zone	3-8
3-11	Distribution of displacement vectors associated with slip on the Fmw fault zone	3-9
3-12	Distribution of horizontal displacements associated with slip on the FrPc fault zone	3-9
3-13	Distribution of vertical displacement associated with slip on the FrPc fault zone	3-10
3-14	Distribution of displacement vectors associated with slip on the FrPc fault zone	3-10
3-15	Distribution of horizontal displacements associated with slip on the Br fault zone	3-11
3-16	Distribution of vertical displacements associated with slip on the Br fault zone	3-11
3-17	Distribution of displacement vectors associated with slip on the Br fault zone	3-12
3-18	Hangingwall ground-surface profiles associated with slip on the Fmw, FrPc, and Br fault zones	3-13
4-1	Layout of finite elements within the fault zones: the value of fault displacement in each zone was based on the plastic shear strain in the middle layer, colored dark	4-2
4-2	Distributions of fault slip along the Fmw zone	4-2
4-3	Distributions of fault slip along the FrPc and Br zones	4-3
4-4	Sensitivity of total fault displacement in the Fmw zone to changes in the value of the principal stress ratio k_3	4-4

FIGURES (Cont'd)

Figure		Page
4-5	Sensitivity of total fault displacement in the Fmw zone to changes in the value of the friction angle	4-5
4-6	Sensitivity of total fault displacement in the Fmw zone to changes in the value of the dilation angle	4-6
4-7	Sensitivity of total fault displacement in the Fmw zone to changes in the value of the damping factor	4-7
4-8	Sensitivity of Fmw-zone slip length to changes in the value of principal stress ratio k_3	4-8
4-9	Sensitivity of Fmw-zone slip length to changes in the value of the friction angle	4-9
4-10	Sensitivity of Fmw-zone slip length to changes in the value of the dilation angle	4-10
4-11	Sensitivity of Fmw-zone slip length to changes in the value of the damping factor	4-11
4-12	Sensitivity of the limit-equilibrium friction angle for the Fmw zone to changes in the value of the principal stress ratio k_3	4-12
4-13	Sensitivity of the limit-equilibrium friction angle for the Fmw zone to changes in the value of the applied friction angle	4-13
4-14	Sensitivity of the limit-equilibrium friction angle for the Fmw zone to changes in the value of the dilation angle	4-14
4-15	Sensitivity of the limit-equilibrium friction angle for the Fmw zone to changes in the value of the damping factor	4-15
4-16	History of slip at Station Fm168 (Perturbed fault: Entire Fmw zone; Case c52)	4-16
4-17	History of slip rate at Station Fm168 (Perturbed fault: Entire Fmw zone; Case c52)	4-16
4-18	Sensitivity of the slip rates at Station Gd3194 to changes in the value of the principal stress ratio k_3	4-17
4-19	Sensitivity of the slip rates at Station Gd3194 to changes in the value of the friction angle	4-18
4-20	Sensitivity of the slip rates at Station Gd3194 to changes in the value of the dilation ratio	4-19
4-21	Sensitivity of the slip rates at Station Gd3194 to changes in the value of the damping factor	4-20
4-22	Acceleration history at Station 2537, in response to the perturbation of the entire Fmw zone (Case c64)	4-21
4-23	Acceleration history at Station 5661, in response to the perturbation of the entire Fmw zone (Case c64)	4-22
4-24	Sensitivity of the vertical acceleration at Station 2537 to changes in the value of the principal stress ratio k_3	4-24
4-25	Sensitivity of the vertical acceleration at Station 2537 to changes in the value of the friction angle	4-25
4-26	Sensitivity of the vertical acceleration at Station 2537 to changes in the value of the dilation ratio	4-26
4-27	Sensitivity of the vertical acceleration at Station 2537 to changes in the value of the damping factor	4-27
4-28	Distribution of potential instability within the study zone, based on the slip tendency on 65° W-dipping planar discontinuities (Case c61)	4-28

FIGURES (Cont'd)

Figure		Page
4-29	Distribution of potential instability within the study zone, based on the slip tendency on 75° W-dipping planar discontinuities (Case c61)	4-28
4-30	Distribution of potential instability within the study zone, based on the slip tendency on 80° W-dipping planar discontinuities (Case c61)	4-29
4-31	Distribution of vertical stress within the study zone: end of simulation (Case c61)	4-29
4-32	Distribution of horizontal stress within the study zone: end of simulation (Case c61)	4-30
4-33	Sensitivity of the area of potential instability to changes in the value of the principal stress ratio k_3, based on slip on 65° W-dipping planes with 30x-friction angle	4-31
4-34	Sensitivity of the area of potential instability to changes in the value of the rock-mass friction angle, based on slip on 65° W-dipping planes with 30°-friction angle	4-32
4-35	Sensitivity of the area of potential instability to changes in the value of the dilation angle, based on slip on 65° W-dipping planes with 30°-friction angle	4-33
4-36	Sensitivity of the area of potential instability to changes in the value of the damping factor, based on slip on 65° W-dipping planes with 30°-friction angle	4-34
5-1	Distribution of displacement vectors and inelastic strain associated with a shear perturbation of the entire Fmw listric fault zone (Case CG4). Strain rates on low angle portions of the listric fault are orders of magnitude lower than maximum values on high angle fault segments. This difference in strain rate may explain the lack of seismicity on low angle normal faults	5-4

THIS PAGE INTENTIONALLY LEFT BLANK

TABLES

Table		Page
2-1	List of input variables and their range of values	2-11
2-2	Names and description of the response variables	2-12
4-1	Range of values of fault displacement (m)	4-3
4-2	Range of values of slip length (km)	4-4
4-3	Range of values of the limit-equilibrium friction angle	4-10
4-4	Range of values of slip rate ($m.s^{-1}$)	4-15
4-5	Range of values of maximum vertical acceleration ($m{\cdot}s^{-2}$)	4-23
4-6	Range of values of maximum horizontal acceleration ($m{\cdot}s^{-2}$)	4-23
4-7	Range of values of the area of potential instability (m^2), based on the slip tendency for selected planar discontinuities that have friction angles of 30° or 40°	4-30
5-1	Summary of the sensitivity of the response variables to changes in the values of the input parameters	5-2

THIS PAGE INTENTIONALLY LEFT BLANK

ACKNOWLEDGMENTS

This report was prepared to document work performed by the Center for Nuclear Waste Regulatory Analyses (CNWRA) for the Nuclear Regulatory Commission (NRC) under Contract NRC-02-93-005. The activities reported here were performed on behalf of the NRC Office of Nuclear Material Safety and Safeguards (NMSS), Division of Waste Management (DWM). The report is an independent product of the CNWRA and does not necessarily reflect the views or regulatory position of the NRC.

S. Young and R. Hofmann made important contributions during the early stages of the work presented in this report. K. Polk and B. Henderson assisted with handling quantitative model results, plotting graphs, and generating figures for the report. Clerical and editorial assistance were provided by E. Cantu, R. Sanchez, J. Pryor, and C. Cudd.

QUALITY OF DATA

There is no CNWRA-generated original data contained in this report. Sources for other data should be consulted for determining the level of quality for those data.

SOFTWARE QUALITY ASSURANCE

The finite element code ABAQUS, the mesh-generation code PATRAN-3, and the statistical analysis code S-PLUS were used for some of the analyses contained in this report. These codes are commercially available, and the CNWRA does not have access to their source codes; therefore, they are not controlled under the CNWRA Software Configuration Procedure (TOP-018: Development and Control of Scientific and Engineering Software).

THIS PAGE INTENTIONALLY LEFT BLANK

1 INTRODUCTION

The Nuclear Regulator Commission (NRC) is required to review a license application from the U.S. Department of Energy (DOE) to construct and operate a proposed repository for high-level radioactive waste (HLW) at Yucca Mountain (YM), Nevada. YM is located in a tectonically active area, and contains numerous normal faults. Key issues for compliance evaluation include whether a mined geologic repository at that location will provide effective long-term waste isolation from the accessible environment and whether short-term safety and retrievability objectives will be met as specified in 10 CFR Part 60. Because of risks to long-term performance associated with structural deformation and seismicity, potentially adverse conditions related to structural deformation and seismicity have been included in 10 CFR Part 60: (i) structural deformation, such as uplift, subsidence, folding, or faulting, that may adversely affect the regional groundwater flow system [60.122(c)(4)]; (ii) structural deformation, such as uplift, subsidence, folding, and faulting that may have occurred during the Quaternary Period (i.e., within the last approximately 2 million yr) [60.122(c)(11)]; (iii) earthquakes that have occurred historically that if they were to be repeated could affect the site significantly [60.122(c)(12)]; (iv) indications, based on correlations of earthquakes with tectonic processes and features, that may increase either the frequency of occurrence or the magnitude of earthquakes [60.122(c)(13)]; (v) more frequent occurrence of earthquakes or earthquakes of higher magnitude than are typical of the area in which the geologic setting is located [60.122(c)(14)]. Additionally, design criteria must be met to provide protection against natural phenomena as specified in 10 CFR Part 60: the structures, systems, and components important to safety shall be designed so that natural phenomena and environmental conditions anticipated at the geologic repository operations area will not interfere with necessary safety functions [60.131(b)(1)]. Because of these regulatory concerns regarding structural deformation and seismicity, it is critical that the geologic structure of YM is well understood as well as the potential for displacement and seismicity on faults in the YM area.

There is considerable uncertainty regarding the subsurface fault geometry beneath YM and Crater Flat Valley as summarized by Young et al. 1992. One subsurface interpretation for the faults beneath YM is that the YM normal faults flatten with depth into a subhorizontal detachment (Scott and Bonk 1984, Scott 1990). Young et al. (1992) used geometrical balancing techniques to test the listric faulting interpretation for YM and found that a listric fault model can explain the displacement magnitudes, fault block rotations, and differences in fault block rotation observed at the surface and in boreholes at YM. Listric normal fault models have been questioned based on arguments that normal stresses resolved on subhorizontal faults in normal faulting regions are too large to allow slip (Sibson 1985). Additionally, seismicity in regions of normal faulting is predominantly associated with slip on high angle normal faults (Jackson, 1987). In the present study, the listric fault model is approached on a mechanical basis using finite element modeling in order to evaluate the stress and seismicity arguments against listric normal faulting and to study ground accelerations associated with slip on listric normal faults.

1.1 HANGINGWALL DEFORMATION ASSOCIATED WITH EXTENSIONAL FAULTING

Normal faults that have listric shapes or are concave-upward in profile are a common feature in extensional tectonic regions. Listric geometries have been interpreted for the normal faults in YM, Nevada (Figure 1-1) (Scott and Bonk, 1984; Scott, 1990; Young et al., 1992). Because of the fault shape, extension parallel to the low-angle part of a listric normal fault necessitates deformation of the hangingwall, footwall,

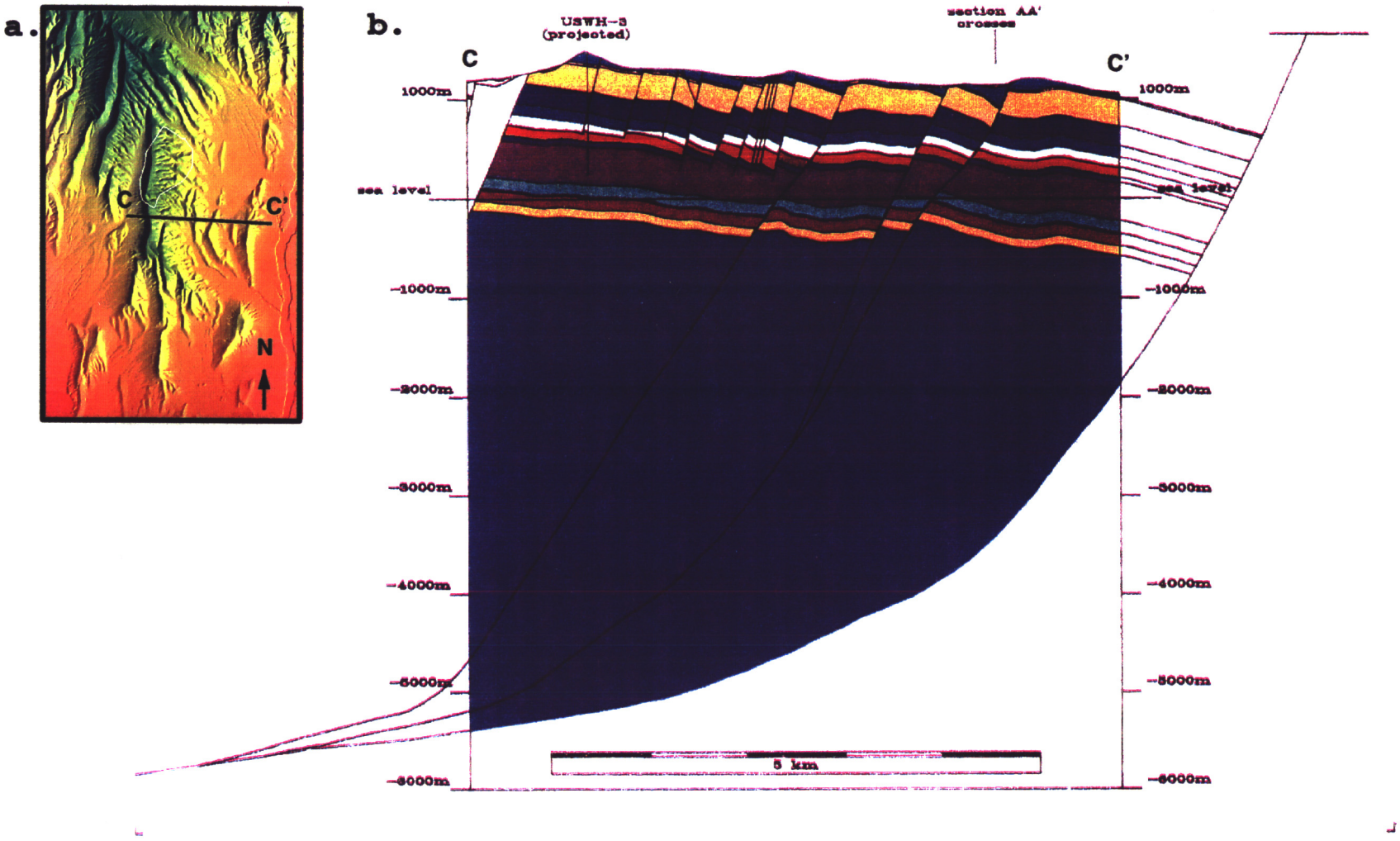

Figure 1-1. Cross section C-C´ from Young et al., 1992

or both in order to maintain constant volume. Hamblin (1965) interpreted listric fault geometry to explain the rollover that is commonly observed in the hangingwalls of normal faults. Models that involve only planar normal faults cannot easily explain the antithetic rotation of fault blocks. The origin of listric normal faults and the deformation mechanisms in hangingwalls have been the subject of much debate in the geological literature. The mechanical argument against listric normal faulting is that in regions of extensional faulting, in which the maximum principal compressive stress (σ_1) is vertical, new faults would be expected to form with steep dips. In a normal-faulting stress regime, the resolved normal stress on a subhorizontal fault would be nearly equal to the σ_1. Therefore, slip on the subhorizontal fault is, based on the assumption of stress state, mechanically difficult or impossible (e.g. Sibson, 1985; Ferrill et al., 1995). Listric faults in the crust have been explained as follows:

(i) High-angle faults merging at depth with weak (e.g., salt) or overpressured (e.g., shale) sedimentary horizons (e.g., Vendeville, 1991);

(ii) Synsedimentary extension and fault propagation that causes rotation of early-formed fault segments to lower dips and upward propagation of faults at a high angle through newly deposited sediments (Vendeville and Cobbold, 1988);

(iii) Differential compaction increasing with depth, causing flattening of originally planar faults with depth (Xiao and Suppe, 1989);

(iv) High-angle faults rotating to low-angle orientations by footwall uplift (Wernicke and Axen, 1988);

(v) Continuation of high-angle faults downward to the brittle/ductile transition, and horizontal detachment below the transition zone in the realm of ductile deformation (Wernicke and Burchfiel, 1982; Miller et al., 1983; Allmendinger et al., 1987); and

(vi) Rotation of principal stress directions at mid-crustal depths, due to rheology change or stress changes associated with igneous intrusion, which causes a 45° change in optimal fault dip, from steep (e.g. 60°) to very shallow (e.g. 15°) dip (Melosh, 1990; Parsons and Thompson, 1993).

Low-angle origination of extensional faults has been interpreted in numerous extensional fault systems in the Basin and Range province (e.g. Wernicke, 1981; McGrew, 1993; Scott and Lister, 1992); and continues as a topic of debate (e.g. Scott and Lister, 1995; Brun et al., 1995). Analysis of listric-fault hangingwall deformation has most commonly been approached using either geometric and kinematic models that are based on assumptions of conservation of cross-section area and various deformation mechanisms (Suppe, 1983; Williams and Vann, 1987; Groshong, 1989, 1990), or using physical analog modeling (Cloos, 1968; McClay and Ellis, 1987; Dula, 1991; Brun et al., 1994; Withjack et al., 1995). The mechanics of listric normal faulting and hangingwall deformation are relatively poorly understood, yet are critical to the assessment of earthquake and fault-slip-related hazards for YM.

1.2 SEISMICITY ASSOCIATED WITH EXTENSIONAL FAULTING

The vast majority of earthquakes related to normal faulting (worldwide) occur in the depth range of 6 to 15 km on faults that dip between 30° and 60° (Jackson, 1987). Evidence for seismic slip on low-angle normal faults is extremely rare (Abers, 1991; Johnson and Loy, 1992). On the basis of resolved stress alone, the slip tendency for low-angle normal faults in a normal faulting stress state is extremely low when compared with high-angle faults that dip in the direction of least principal compressive stress (Ferrill et al., 1995). The occurrence of earthquakes is largely dependent on the rate of slip or the rate of rupture propagation on the fault. Beroza and Jordan (1990) illustrate that rupture propagation rates are typically in the range of kilometers per second for earthquakes, 10 to 1,000 m/s for slow and silent earthquakes, and less than 10 m/s for aseismic slip events. It has been suggested that the lack of seismicity on low-angle faults does not reflect lack of slip on the faults but instead that slip is at aseismic rates and may either precede or postdate seismic slip on high-angle portions of the fault (Melosh, 1990).

1.3 SCOPE OF WORK

In the present work, we perform finite element modeling to evaluate hangingwall deformation associated with listric faulting. The two-dimensional finite-element models presented here focus on testing the sensitivity of deformation in the hangingwall to material properties and *in situ* stress. The effects of fault geometry on hangingwall deformation will be included in future three-dimensional (3D) finite element modeling. Measurements from the 1992 Little Skull Mountain earthquake sequence can be used to test the results of the 3D finite element models. Young et al. (1992) balanced a set of cross sections through YM that were originally constructed by Scott and Bonk (1984) using data from surface geologic mapping and from boreholes. The listric fault geometry in these cross sections was interpreted based on the rotation of fault blocks and the fact that the amount of rotation of fault blocks varies through YM (Scott, 1990). Cross-section balancing was performed assuming constant area and oblique simple shear deformation antithetic to the normal faults. The balancing effort supports the original interpretation of a listric fault system for YM. However, other interpretations are possible, especially if addition of volume at depth, for example through magma intrusion, occurred to fill voids. Of the balanced cross sections in Young et al. (1992), C-C' was chosen as the basis for the finite element modeling because it is most nearly perpendicular to the strike of the majority of the faults and is near the interpreted displacement direction on the faults. The geometry of the fault system is that of classic listric fan with high-angle faults near the surface that continue downward and flatten with depth to merge with a subhorizontal detachment as shown in Figure 1-1.

2 DESCRIPTION OF MODEL

2.1 GEOMETRICAL MODEL

The geometrical model is shown in Figure 2-1; the modeled domain is approximately rectangular, extending 43.5 km horizontally and 17.25 km vertically. The vertical axis corresponds with axis-2 in the figure, and the horizontal axis with axis-1; axis-3 is normal to the plane of the figure. These coordinate axes will hereafter also be referred to as the x-, y-, and z-axes, corresponding to axis-1, axis-2, and axis-3, respectively. The positive direction of the x-axis corresponds to east, and that of the y-axis is vertically up. The ground surface was assumed to be horizontal at elevation 1.25 km above sea level; its y-coordinate is 7,250 m. All dimensions in the model are in meters.

As the figure shows, the faults were modeled as thin zones of rock, which were assigned mechanical properties and behavior that differ from those of the surrounding rock mass. This fault model was chosen from the following list of three possible models:

- The block-on-block model, in which a fault is modeled as a contact between two rock blocks, and the mechanical behavior of the fault is modeled using contact elements (cf. Curran and Ofoegbu, 1993). This model was not selected, because field observations (Scott, 1990) suggest that the faults that are of interest in this study consist of variably thick zones of breccia and densely fractured rock. Furthermore, the finite element code ABAQUS (Hibbit, Karlsson and Sorensen, Inc., 1994), which was used for the analyses, does not permit the contact elements to intersect, as would be required for the fault system being studied.

- Thin-solid model with anisotropic properties, in which a fault is modeled as a thin-solid zone, as was done in this study, but the fault is assigned smaller shear strength in the tangential direction than in all other directions. This model was not selected because it is possible that the initiation of slip at a point within a fault zone follows a direction different from the general tangential direction of the fault. The stress state at a point may initially not permit slip to occur in the tangential direction, but the occurrence of slip in other directions may subsequently cause the development of tangential slip. This deformation mechanism is likely to be all the more important for low-angle detachment faults.

- The thin-solid model with isotropic properties was chosen for this study.

Each fault was assigned a thickness of about 500 m, based mainly on finite-element meshing considerations. It was considered necessary to represent each fault zone in the finite element model by at least three layers of elements (in the direction normal to the fault), such that there is at least one layer of fault elements that do not interact directly with the stronger unfractured rock. As a result the 500-m thickness for each fault zone implies fault elements that are about 167 m thick, which is close to the minimum that can be accommodated in the finite element mesh. Although the choice of fault-zone thickness was influenced primarily by meshing considerations, the 500-m thickness chosen is within the range of values suggested by Scott (1990) for the YM fault zones. The faults modeled are: (i) a fault similar in geometry to the interpreted Fortymile Wash Fault (Figure 1-1), which is represented by the curved fault in Figure 2-1; it will hereafter be referred to as the Fmw zone; (ii) a fault similar in attitude to the Fran Ridge and Paintbrush Canyon fault system; this fault zone will hereafter be referred to as the FrPc

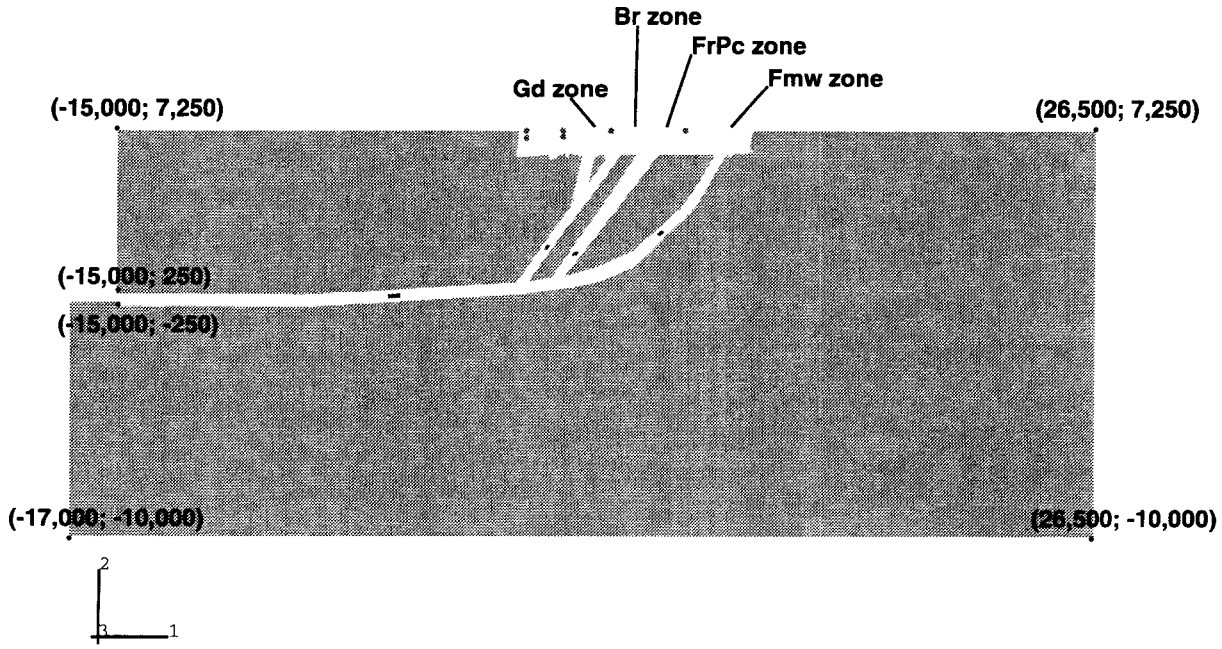

Figure 2-1. Geometrical model, showing boundaries of the modeled domain and fault zones

zone; (iii) a fault similar in attitude to the Bow Ridge fault, hereafter referred to as the Br zone; and (iv) a fault having an attitude similar to that of the Ghost Dance fault; it will hereafter be referred to as the Gd zone.

An enlarged view of the geometrical model is shown in Figure 2-2, which shows stations selected for monitoring fault slip rate. Each of the stations (St. Fm58, Fm168, Fr635, Br833, and Gd3194) is a finite element, and slip rate was monitored at the centroid of such elements. The elements were chosen to lie within zones in which the largest values of slip were observed in a series of preliminary analyses conducted by the authors. The region labeled ABCD in the figure was selected to monitor changes in stress induced by slip on the faults. This region, which covers a horizontal distance of about 10 km and extends vertically to a depth of about 1 km from the ground surface, includes most of the volcanic deposits shown in the geologic cross section (Figure 1-1). This region will hereafter be referred to as the study zone.

An enlarged view of the study zone is shown in Figure 2-3, which also shows the stations selected for monitoring ground accelerations. The acceleration-monitoring stations were selected to lie within the epicentral zones of slip events originating near the base of the steeply dipping faults, that is, the Br, FrPc, and steep part of the Fmw fault zones.

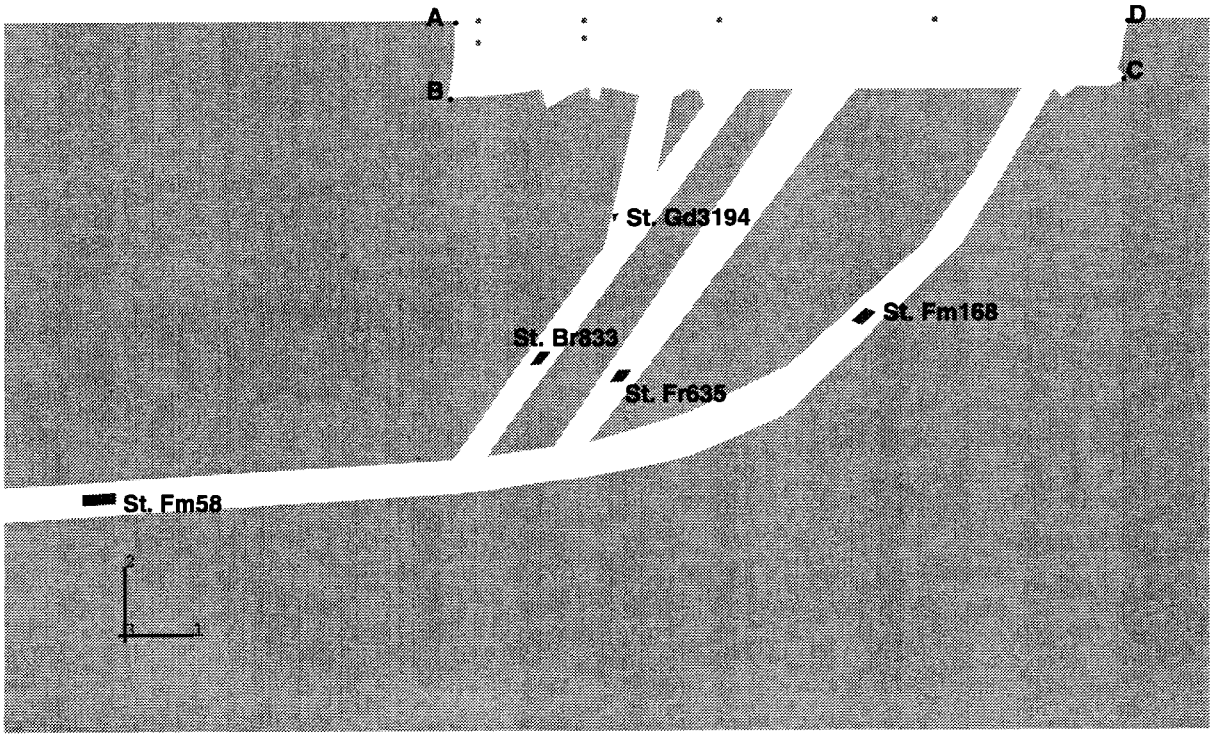

Figure 2-2. Enlarged view of the geometrical model, showing the slip-rate monitoring stations and boundaries of the study zone

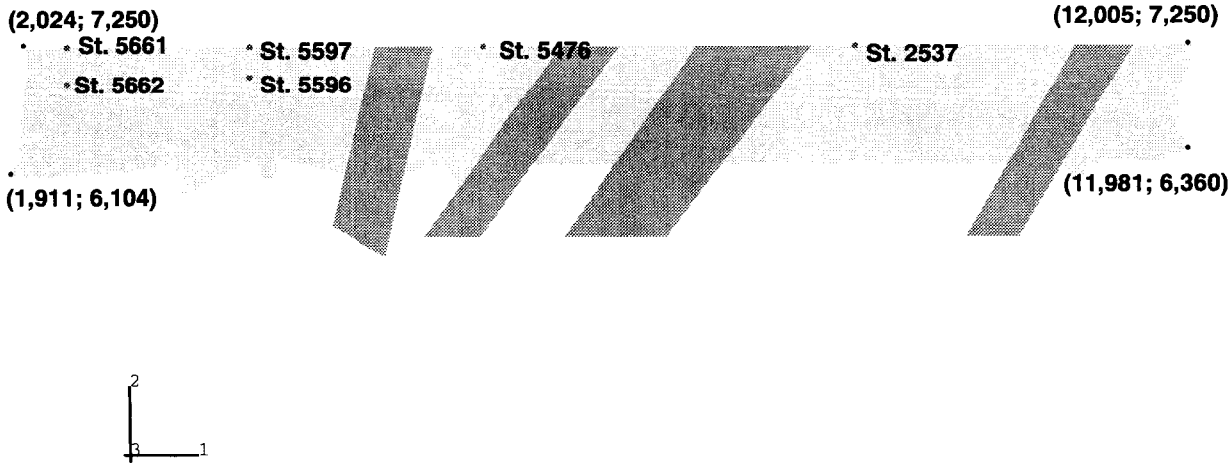

Figure 2-3. Enlarged view of the study zone, showing the acceleration monitoring stations

2.2 MATERIAL MODEL

The fault-zone materials were modeled as elastoplastic, with a yield strength defined in terms of the Drucker-Prager failure criterion (Drucker and Prager, 1952). The rest of the rock mass was modeled as linear-elastic, homogeneous, and isotropic. The stress distributions computed within the study zone were interpreted using a set of anisotropic failure criteria based on the Mohr-Coulomb failure law; the failure criteria and the interpretations will be presented in a subsequent section.

2.2.1 Linear-Elastic Material Zones

The linear-elastic material zones are the footwall of the Fmw zone and the part of the hangingwall outside the fault zones. The material parameters required for the isotropic linear-elastic model are the Young's modulus, E, and the Poisson's ratio, ν. The model relates the stress and strain changes at a point, $\Delta\sigma$ and Δe, respectively, through the equation

$$\begin{bmatrix} \Delta\sigma_{11} \\ \Delta\sigma_{22} \\ \Delta\sigma_{33} \\ \Delta\sigma_{12} \end{bmatrix} = \begin{bmatrix} \lambda+2G & \lambda & \lambda & 0 \\ \lambda & \lambda+2G & \lambda & 0 \\ \lambda & \lambda & \lambda+2G & 0 \\ 0 & 0 & 0 & 2G \end{bmatrix} \begin{bmatrix} \Delta e_{11} \\ \Delta e_{22} \\ \Delta e_{33} \\ \Delta e_{12} \end{bmatrix} \tag{2-1}$$

where $\lambda = \nu E/[(1+\nu)(1-2\nu)]$ and $G = E/[2(1+\nu)]$; subscripts 11, 22, and 33 denote the direct stress (or strain) components in the x, y, and z directions, respectively; and subscript 12 denotes the xy-plane shear stress (or strain) component.

Eq. (2-1) shows that the magnitudes of stress change components depend on the magnitudes of strain change components through the corresponding elastic stiffness components. Therefore, the effects of E and ν on the results of the simulations depend on the magnitudes and distributions of deformation. On the other hand, the deformations in this problem are localized, being limited to areas close to the fault zones. Therefore, it was decided that uncertainties in the values of E and ν are not likely to be critical in a large-scale problem such as this. As a result, constant values were assigned to E and ν for all the simulations. The value of E was set to 3.25×10^4 MPa, based on an examination of values reported for carbonate rocks in Goodman (1980). The value of ν was set to 1/3 based on considerations of the initial stress state, as is discussed subsequently.

2.2.2 The Elastoplastic Material Zones

The elastoplastic material zones consist of all the fault zones. The same values of E and ν were applied to the linear-elastic and elastoplastic material zones. The additional parameters required for the elastoplastic zones are the unconfined compressive strength, q_u, the Drucker-Prager friction angle β, and the dilation angle φ. For the conditions of plane strain, the Drucker-Prager friction angle is related to the Mohr-Coulomb friction angle through the following equations (cf. Hibbit, Karlsson and Sorensen, Inc., 1994):

$$\tan\beta = \frac{\sqrt{3}\sin\phi}{\sqrt{1+\frac{1}{3}\sin^2\phi}} \tag{2-2}$$

$$\tan\beta = \sqrt{3}\sin\phi \tag{2-3}$$

where ϕ is the Mohr-Coulomb friction angle, Eq. (2-2) applies to associative flow (i.e., when the friction and dilation angles are equal), and Eq. (2-3) applies to nondilatant flow (i.e., case of zero dilation angle).

The fault zones are expected to be essentially cohesionless; therefore, q_u was assigned a low constant value of 1.0 MPa. The friction and dilation angles were considered among the list of parameters to be included in the program of parametric investigation. The values of ϕ were varied in the range $30^\circ \leq \phi \leq 40^\circ$ (cf. Byerlee, 1978) and those of the ratio φ/ϕ were varied in the range $0 \leq \varphi/\phi \leq 1$.

2.2.3 Material Damping

An additional material parameter is required in dynamic analysis to describe the capacity of the material to absorb dynamic energy. If an isolated mass of a material, for example, a rod, is set into free vibration, the amplitude of vibration decreases with time and will eventually disappear. This reduction in the amplitude of vibration is referred to as material damping, which is related to energy loss caused by inelastic deformations of the material. Wave propagation in infinite medium is also affected by another kind of damping referred to as geometrical damping, which is caused by the fact that the dynamic energy is distributed within an increasing volume of material as the distance from the source of dynamic excitation increases. Numerical models such as the finite element method automatically account for geometrical damping. On the other hand, the amount of material damping required in a model has to be specified through an input parameter referred to as the damping factor.

The damping factor, D_α, can be defined loosely through the following equation (cf. Richart et al., 1970):

$$\ln\left(\frac{z_1}{z_2}\right) = \frac{2\pi D_\alpha}{\sqrt{1-D_\alpha^2}} \tag{2-4}$$

where z_1 and z_2 are two successive amplitudes of vibration.

Very little measured data exist on the damping property of rocks. Most of the data available for geologic materials, which were obtained for cohesionless soils, indicate values of damping factor of 0.01 to 0.1; for example, see Table 10-12 of Richart et al. (1970). In addition, analytical investigations by Hardin (1965) suggest that the value of damping factor for geologic materials varies inversely with the value of shear modulus, $E/2(1+\nu)$. Therefore, because the shear modulus of rocks is several orders of magnitude larger than that of soils, it is likely that the value of damping factor for rocks is very small. As a result, the value of material damping for high-stiffness rocks, such as are considered to constitute the

linear-elastic zones in this study, is considered negligible. But the elastoplastic zones are considered to consist essentially of cohesionless material, for which the value of damping factor may lie within the range of $0.01 \leq D_\alpha \leq 0.1$, following the data referred to earlier in Richart et al. (1970). The value of damping factor for the elastoplastic material zones was varied within this range, whereas the linear-elastic material zones were assigned zero damping.

2.3 INITIAL CONDITIONS

The medium was assumed to be under zero strain at the initial state, the justification for the assumption being that the focus of the investigation is the mechanical changes induced by a perturbation of the current state. The strains associated with previous deformations of the medium are not relevant to the investigation, except to the extent that they may assist in defining the initial stress state, as is discussed later.

In defining the initial stress state, it is assumed that the ground surface is horizontal, which implies that one of the principal compressive stress components is vertical, and that the other two are horizontal. The directions of the principal stress components deviate from vertical and horizontal as the ground surface relief increases, as is demonstrated in Goodman (1980), for example. This assumption was made only to remove the ground-surface relief from the list of unknown variables, because it can be measured accurately and incorporated in the anticipated 3D analyses.

Having assumed a horizontal ground surface, the magnitude, σ_v, of the initial vertical principal compressive stress component depends only on the density of the overlying rock, and can be calculated using the equation

$$\sigma_v = \gamma d \tag{2-5}$$

where γ is the unit weight of the rock, and d is the depth at which σ_v is calculated. In assigning a value to γ, the stratigraphic contrasts in the top 1 km (or so) of the domain was ignored, and γ was assigned a constant value of 0.025 MN/m^3 (cf. Hoek and Brown, 1980), which corresponds to a vertical compressive stress gradient of 25 MPa/km.

The magnitude of each of the two horizontal principal compressive stress components can be computed using the equation

$$\sigma_h = k\sigma_v \tag{2-6}$$

where σ_h denotes horizontal stress; generally, the value of k is different for each horizontal stress component. If the ground surface is horizontal and the rock mass has not undergone any previous horizontal deformation, the value of k would be calculated using the theory of elasticity, which gives the equation

$$k_o = \frac{\nu}{1-\nu} \tag{2-7}$$

where k_o is the value of k for the zero-horizontal-deformation state, at times referred to as the at-rest or uniaxial-strain state (cf. Jaeger and Cook, 1979).

The value of k is usually smaller or larger than k_o, depending on whether the rock mass underwent net horizontal extension or compression previously. Under horizontal extension, k attains a minimum value, denoted k_a, at incipient failure, given by the equation (cf. Goodman, 1980)

$$k_a = \cot^2\left(45 + \frac{\phi}{2}\right) - \left[\left(\frac{q_u}{\gamma}\right)\cot^2\left(45 + \frac{\phi}{2}\right)\right]\left(\frac{1}{d}\right) \tag{2-8}$$

Rock failure under this condition occurs in the form of normal faulting. The minimum principal compressive stress component is horizontal, normal to the strike of the resulting fault planes, and has a magnitude equal to $k_a\sigma_v$. The maximum principal compressive stress component is vertical, and the intermediate principal stress coincides with the strike of the fault planes.

Under horizontal compression, the value of k reaches a maximum, denoted k_p, at incipient failure, given by the equation (cf. Goodman, 1980)

$$k_p = \tan^2\left(45 + \frac{\phi}{2}\right) + \frac{q_u}{\gamma d} \tag{2-9}$$

This condition corresponds to reverse faulting. The maximum principal compressive stress component is horizontal, normal to the strike of the fault planes, and has a magnitude equal to $k_p\sigma_v$; the minimum principal compressive stress is vertical; and the intermediate principal stress coincides with the strike of the fault planes.

The relationship between the magnitude and directions of the principal stress components can deviate from that described in the foregoing paragraphs, because of changes caused by erosion, deposition on irregular surfaces, igneous intrusion, and volcanism. As a result, the value of k is often different from k_o, k_a, or k_p, and the principal stress directions may not be vertical and horizontal, and may be oblique to the fault planes.

This notwithstanding, the direction of the minimum principal compressive stress in extensional tectonic regions, such as the Basin and Range (Ferrill et al., 1995), is likely to be closely normal to the strike of the fault planes, and that of the maximum is likely to be near vertical. The magnitude of the minimum principal compressive stress under this condition is expressed as $k_3\sigma_v$, where $k_a \le k_3 \le k_o$. Eq. (2-8) gives a value of k_a of about 0.2 for a friction angle of about 40° (neglecting the second part of the equation); also, Eq. (2-7) gives $k_o = 0.5$ for $\nu = 1/3$. Therefore, the value of k_3 for the current program of parametric investigation was varied in the range $0.2 \le k_3 \le 0.5$; the direction of the minimum principal compressive stress was assumed to be normal to the strike of the faults, whereas the maximum was assumed to be vertical.

The intermediate principal stress was assumed to coincide in direction with the fault strike, and as a result, has little effect on the two-dimensional simulations. Therefore, the magnitude of the intermediate principal stress was assigned a fixed value of $0.9\sigma_v$.

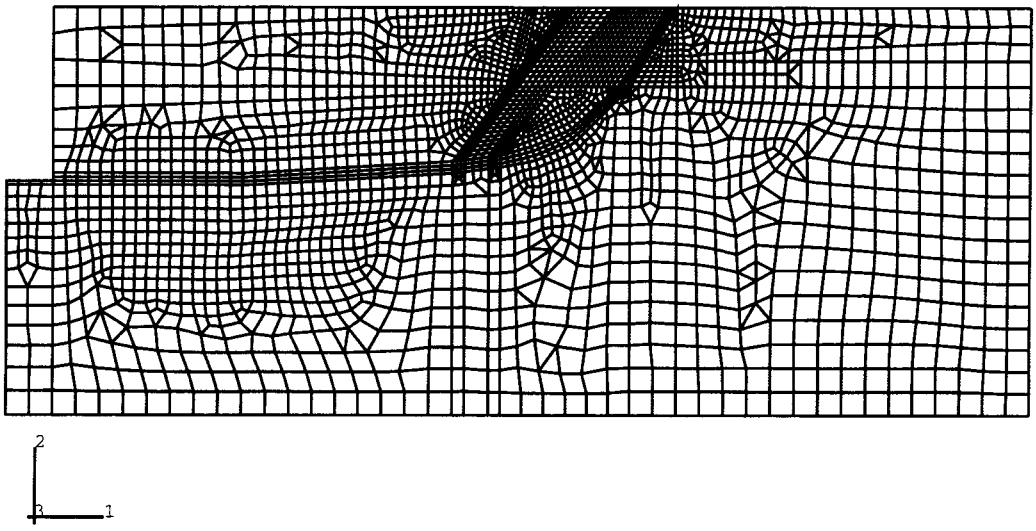

Figure 2-4. Finite element discretization of the modeled domain

2.4 FINITE ELEMENT MODEL

The finite element mesh is shown in Figure 2-4 and Figure 2-5. Both the linear-elastic and elastoplastic zones were modeled using four-noded quadrilateral elements, with a few three-noded triangles added to smooth the mesh. The mesh was generated using PATRAN (PDA Engineering, 1994), and the finite element analyses were conducted using ABAQUS (Hibbit, Karlsson, and Sorensen, Inc., 1994).

2.4.1 Boundary Conditions

The top of the model (see Figure 2-1) coincides with the ground surface and was therefore treated as a free surface. The base of the model and the right boundary of the Fmw-zone footwall were held to zero displacement in the direction normal to the boundary. The left boundary of the Fmw-zone footwall was also held at zero normal displacement. A vertical downward pressure of 183.33 MPa was applied on the horizontal bench at the left end of the model. The left boundary of the model above this bench was subjected to a horizontal eastward pressure equal to $0.025k_3d$ MPa, where d is the depth in meters.

The primary consideration in selecting the minimum distance of the base and vertical boundaries of the model from the fault zones was the requirement that the calculated response should not be influenced by energy reflected from the boundaries (except the ground surface). This requirement could have been met by modeling the base and vertical boundaries with infinite elements, which have the built-in capacity to reduce the reflection of dynamic energy. Although such elements may be satisfactory for modeling the base, they are not designed for semi-infinite boundaries, such as occur at the intersection of the vertical boundaries with the ground surface. Secondly, because the infinite elements are based on the analytic behavior of a linear-elastic space, they are not satisfactory for modeling the left boundary of the

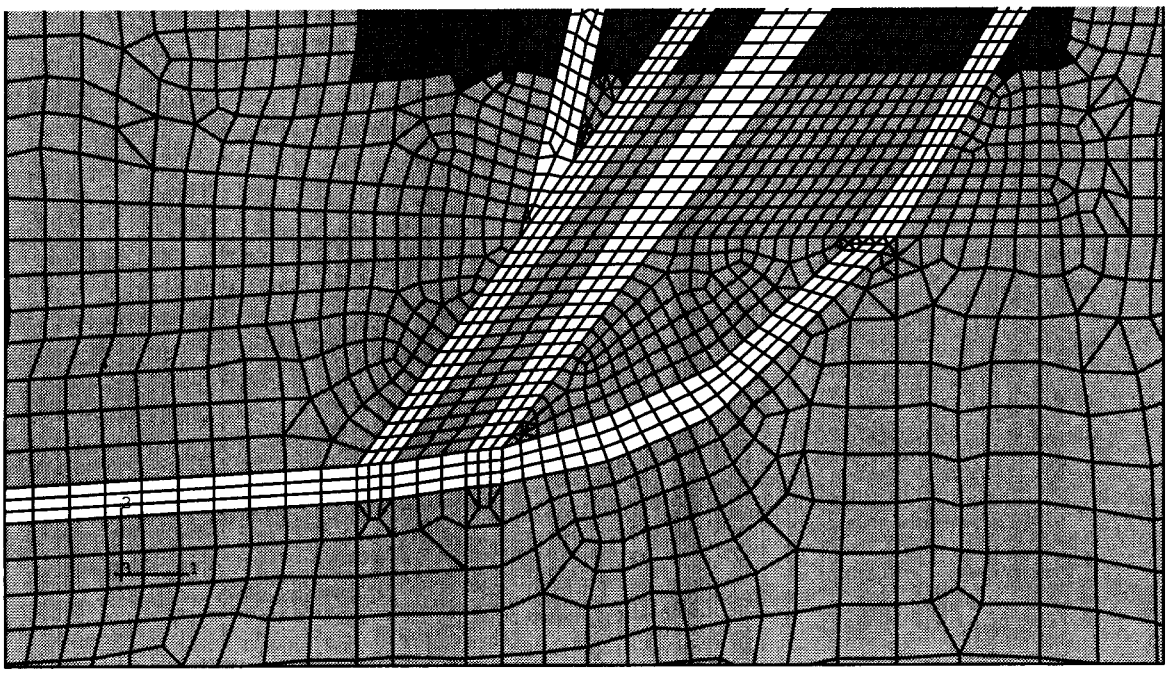

Figure 2-5. Enlarged view of the finite element mesh, showing the study zone and fault zones

Fmw fault zone. Therefore, the size of the model was increased to preclude boundary reflections, instead of using infinite elements at the boundaries.

2.4.2 Simulation Procedure

Each simulation was conducted in two steps: (i) establish the initial equilibrium state, and (ii) induce slip on a selected fault zone and monitor the selected response measures for a period of time.

2.4.2.1 The Initial Equilibrium State

The participants in the initial equilibrium state are the initial stress, the gravitational force, and the boundary pressures. The initial stress was applied using the ABAQUS command

```
*INITIAL CONDITIONS,TYPE=STRESS,GEOSTATIC
FOOTWALL,0.0,7250.0,-181.25,0.0,0.30,0.9
etc
```

which applies a vertical stress at each element, the magnitude of which is determined by the y-coordinate at the element centroid. The vertical stress gradient is calculated from the specified values of 0.0 at $y = 7{,}250.0$ and -181.25 at $y = 0.0$ (ABAQUS uses the compression-negative sign convention). The horizontal-to-vertical stress ratio is 0.3 in the x-direction and 0.9 in the z-direction, for the case illustrated. The values of stress so specified are applied uniformly over each element. The boundary pressure and gravitational force that are required to establish equilibrium with the initial stress state were applied using the "DLOAD" command, in a static-analysis step.

There were situations for which equilibrium could not be established under the specified initial stress and material properties. Equilibrium under such situations required slip to occur on sections of the fault zones, leading to localized changes in stress (within the slip zones and their immediate surrounding). The initial equilibrium state for such a case was established in two static-analysis steps: First, equilibrium was established with the fault zones assigned a very large value of unconfined compressive strength, q_u. Then the value of q_u was reduced incrementally to the required value of 1.0 MPa. The amount of fault displacement calculated at the end of this step was subtracted from the total fault displacement calculated subsequently, in order to obtain the fault displacement induced by the perturbation of a selected fault, as is described next.

2.4.2.2 Perturbation of Selected Fault Zone

Having established the initial state, slip was forced to occur on a selected fault zone by reducing the value of friction angle on the fault, in a dynamic-analysis step. The state of incipient slip on a fault can be described in terms of the Mohr-Coulomb failure law, using the equation

$$\tau - \sigma_n \tan \phi = 0 \tag{2-10}$$

where τ and σ_n are the shear and normal stress components on the fault plane. The magnitude of τ for the faults at the end of the static step(s) was usually insufficient to cause slip; that is, the relationship between τ and σ_n at the end of the static-analysis step(s) was represented by the inequality

$$\tau - \sigma_n \tan \phi < 0 \tag{2-11}$$

Therefore, to force the occurrence of slip on a fault, the value of ϕ was reduced enough to satisfy Eq. (2-10) on a section of the selected fault. This process of reducing ϕ to induce slip is equivalent to applying a distribution of forces on the fault surface, thereby changing the relationship between τ and σ_n enough to satisfy Eq. (2-10).

2.4.3 Experiment Design

The perturbed faults, shown in Figure 2-6, are Upper Fmw zone (Fault 1), FrPc zone (Fault 2), Br zone (Fault 3), and the entire Fmw zone (Fault 4). Only one fault was perturbed at a time; the response of the medium to the fault perturbation was expected to vary, depending on the values assigned to the parameters k_3, ϕ, φ/ϕ, and D_α. Therefore, the analyses consisted of generating combinations of values of the five input parameters listed in Table 2-1 and monitoring the response of the medium under each combination, in terms of the 35 response variables listed in Table 2-2. The combinations were chosen in terms of the normalized values of k_3, ϕ, φ/ϕ, and D_α.

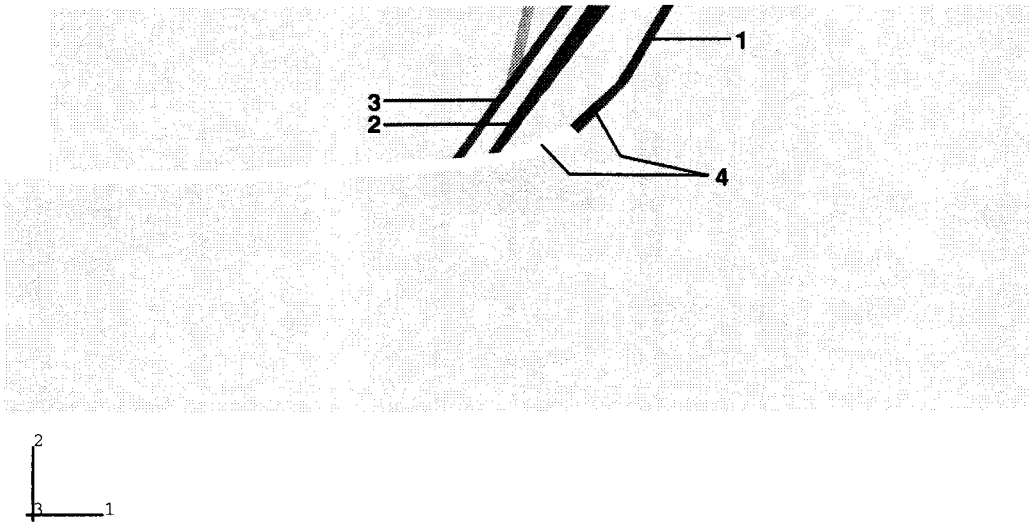

Figure 2-6. Illustration of the analysis domain, showing the four perturbed faults

Table 2-1. List of input variables and their range of values

Variable Name	Description	Value	
		Minimum	Maximum
Fault	Perturbed fault	1	4
k_3	Minimum-to-maximum principal stress ratio	0.2	0.5
ϕ	Friction angle	30°	40°
φ/ϕ	Ratio: Dilation angle to friction angle	0.0	1.0
D_α	Damping factor	0.0	0.1

The normalized value, θ_r, for a variable θ, was defined as follows:

$$\theta_r = \frac{\theta - \theta_{min}}{\theta_{max} - \theta_{min}} \tag{2-12}$$

where θ_{max} and θ_{min} are the maximum and minimum values of θ, respectively; this equation gives values of θ_r in the range $0 \le \theta_r \le 1$. Therefore, a set of four random numbers converted to this range were generated, and were in turn converted to values of k_3, ϕ, φ/ϕ, and D_α, using the inversion of Eq. (2-12), as follows:

$$\theta = \theta_{min} + \theta_r(\theta_{max} - \theta_{min}) \quad (2\text{-}13)$$

Each such combination of four parameter values was applied to the perturbation of each of the four faults shown in Figure 2-6, giving four simulations for each combination. A total of 68 simulations (using 17 parameter-value combinations) were conducted.

Table 2-2. Names and description of the response variables

Variable Name	Explanation
fmdisp	Fault displacement: Fmw zone
frdisp	Fault displacement: FrPc zone
brdisp	Fault displacement: Br zone
gddisp	Fault displacement: Gd zone
fmsl	Slip length: Fmw zone
frsl	Slip length: FrPc zone
brsl	Slip length: Br zone
gdsl	Slip length: Gd zone
fmlf	Limit-equilibrium friction angle: Fmw zone
frlf	Limit-equilibrium friction angle: FrPc zone
brlf	Limit-equilibrium friction angle: Br zone
gdlf	Limit-equilibrium friction angle: Gd zone
sr3194	Slip rate: Station 3194 (Gd zone)
sr833	Slip rate: Station 833 (Br zone)
sr635	Slip rate: Station 635 (FrPc zone)
sr168	Slip rate: Station 168 (Upper Fmw zone)
sr58	Slip rate: Station 58 (Lower Fmw zone)
av2537	Maximum vertical acceleration: Station 2537
av5476	Maximum vertical acceleration: Station 5476
av5596	Maximum vertical acceleration: Station 5596
av5597	Maximum vertical acceleration: Station 5597
av5661	Maximum vertical acceleration: Station 5661
av5662	Maximum vertical acceleration: Station 5662
ah2537	Maximum horizontal acceleration: Station 2537
ah5476	Maximum horizontal acceleration: Station 5476
ah5596	Maximum horizontal acceleration: Station 5596
ah5597	Maximum horizontal acceleration: Station 5597
ah5661	Maximum horizontal acceleration: Station 5661
ah5662	Maximum horizontal acceleration: Station 5662
ap3065	Unstable area: 30° friction angle, 65° plane

Table 2-2. Names and description of the response variables (cont'd)

Variable Name	Explanation
ap3075	Unstable area: 30° friction angle, 75° plane
ap3080	Unstable area: 30° friction angle, 80° plane
ap4065	Unstable area: 40° friction angle, 65° plane
ap4075	Unstable area: 40° friction angle, 75° plane
ap4080	Unstable area: 40° friction angle, 80° plane

3 TYPICAL CALCULATED RESPONSES

The calculated responses of the model are described in this chapter, in terms of the distributions of stresses and deformations. The effects of varying the values of the input parameters (Table 2-1) on the calculated response are discussed in Chapter 4, in terms of the response measures listed in Table 2-2.

3.1 STRESS DISTRIBUTIONS

The distributions of the vertical and horizontal stress components at the initial state are shown in Figure 3-1 and Figure 3-2, respectively, for the situations in which the initial equilibrium state did not require prior fault slip. In the figures S22 and S11 stand for σ_{22} (vertical stress) and σ_{11} (horizontal stress), respectively; the stresses are negative because ABAQUS uses the tension-positive sign convention. All stresses are in MPa units. Under the condition of no previous fault slip, the magnitude of each stress component varies only with the depth below the ground surface; therefore, the stress contours are horizontal, as the figures show. The magnitudes of vertical compressive stress at the base of the model (i.e., at a depth of 17,250 m) should be 431.25 MPa, which is larger than the maximum value (419 MPa) given by the model. The types of finite elements used in the study, that is, 4-noded quadrilaterals and 3-noded triangles, are based on linear variation of displacements along the element boundaries, which gives a constant value of stress within each element. The value of stress within such an element is equal to the value calculated at the element centroid. The finite elements at the base of the model consist of rectangles approximately 1,000 m long in the vertical direction, with centroids at a depth of about

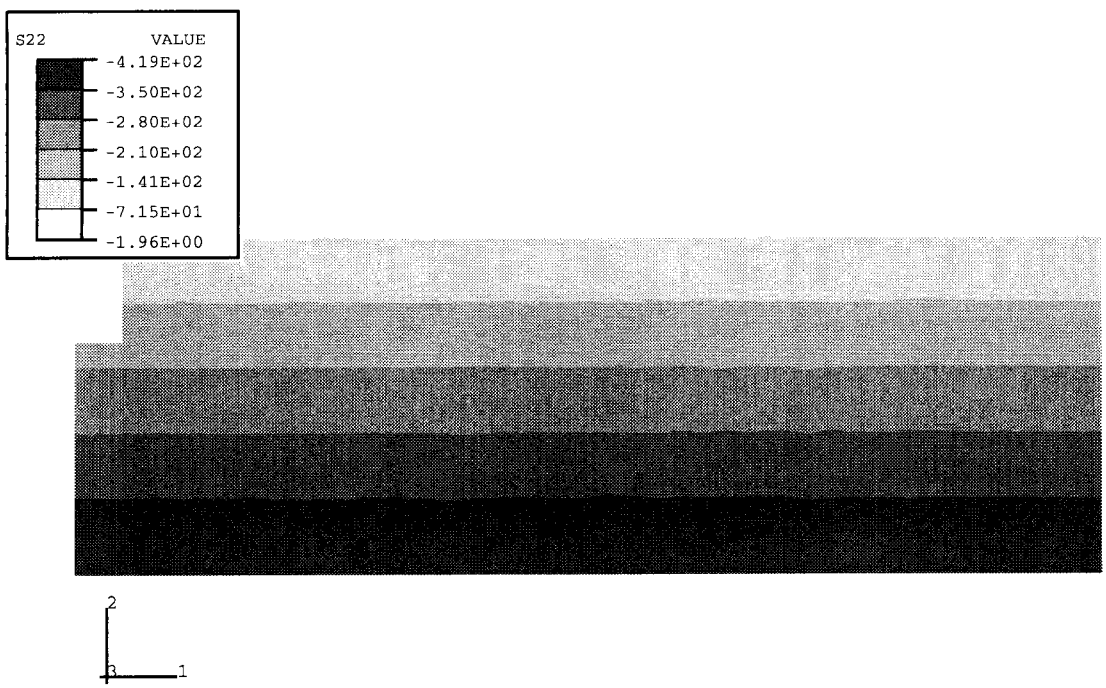

Figure 3-1. Distribution of vertical stress: initial state with no fault slip

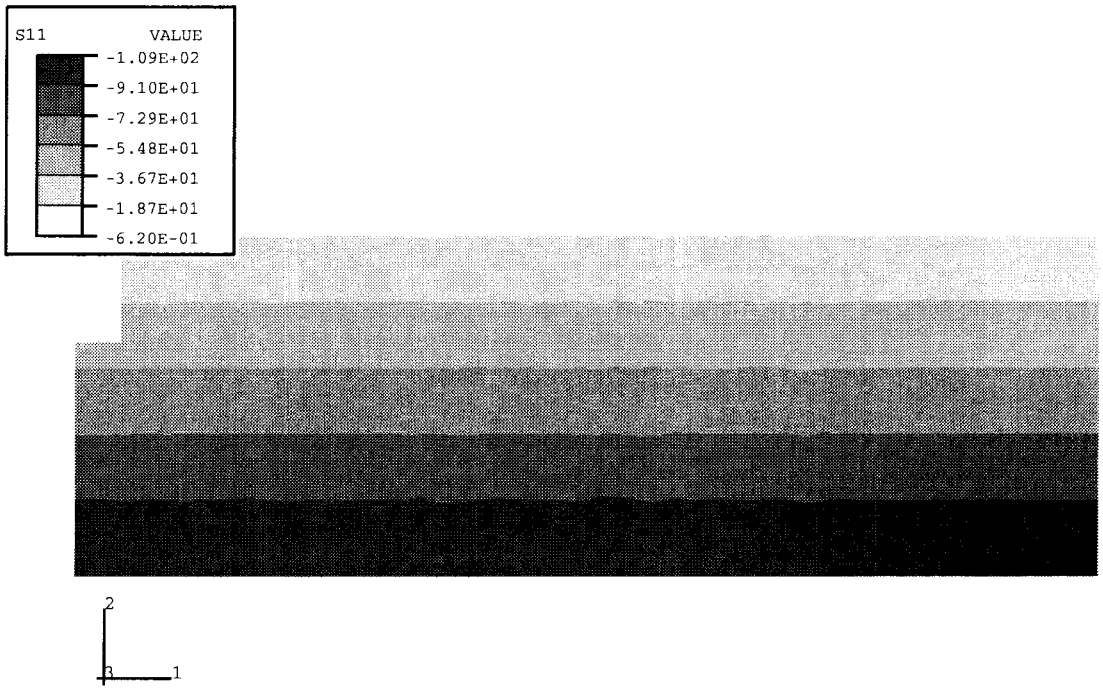

Figure 3-2. Distribution of horizontal stress: initial state with no fault slip

16,750 m (Figure 2-4). The vertical compressive stress at this depth is 418.75 MPa, which is close to the maximum value given in Figure 3-1.

The stress distributions shown in Figure 3-3 and Figure 3-4 are typical initial-state distributions for those situations in which the initial equilibrium state would include previous fault slip. The distributions in the figures were calculated for the initial state of Case c61, with parameters $k_3 = 0.26$, $\phi = 32°$, and $q_u = 1.0$ MPa. For the regional stress state represented by this value of k_3, inelastic deformation, such as fault slip, would occur on geologic structures having the geometrical and strength properties specified in the c61 model. As a result of the inelastic deformation, the local stress conditions near such geologic structures would be modified relative to the regional stress state. Such local modifications of regional stress states might account for the wide variations often observed in stress-measurement data (cf. Martin, 1990; Hoek and Brown, 1980), and may be a cause for concern regarding the use of regional stress states for the stability analyses of pre-existing geologic structures (cf. Harmsen, 1994). As the figures show, the stress change in this example consists of decrease in vertical stress within the fault zones, increase in vertical stress immediately outside of the fault zones, and increase in horizontal stress within and near to the fault zones; the increase in horizontal stress is most pronounced in the low-angle part of the Fmw zone.

Having established the initial state for Case c61 as described in the foregoing paragraphs, the value of ϕ in the Fmw zone was reduced instantaneously to 24°, thereby causing additional inelastic deformation. The stress distributions after 5 s, following this reduction of friction angle, are given in Figure 3-5 and Figure 3-6. The stress change associated with the additional inelastic deformation follows the pattern described in the foregoing paragraph. The effects of such stress changes on conditions in the hangingwall will be examined in a subsequent chapter, using the stability of selected planar discontinuities within the study zone.

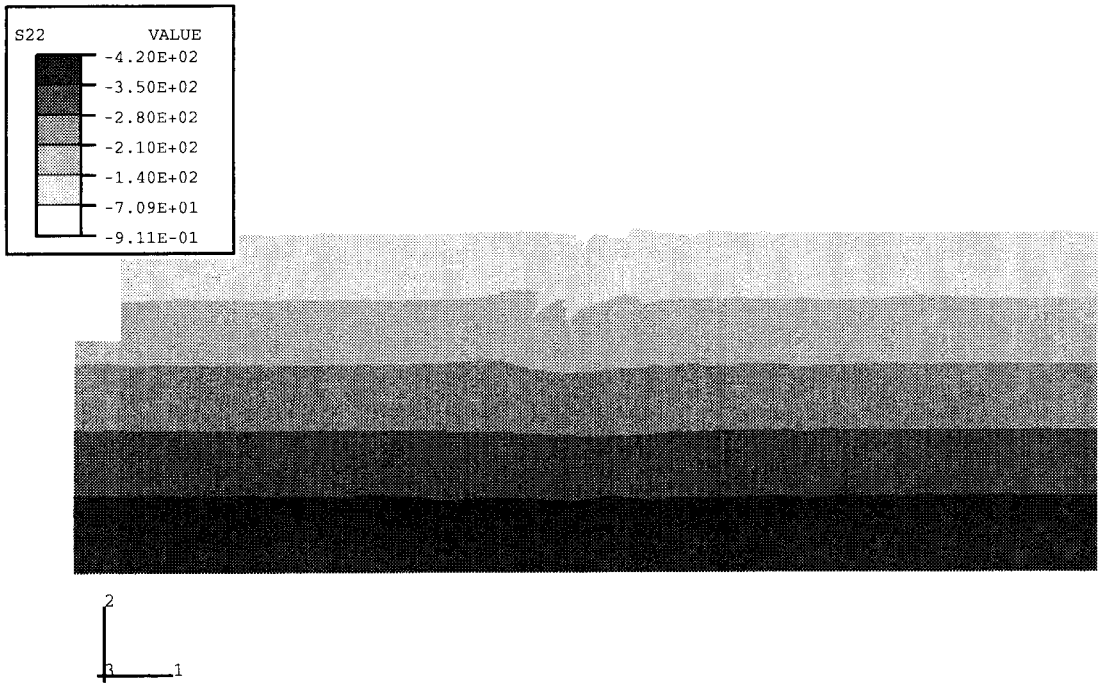

Figure 3-3. Distribution of vertical stress: initial state with previous fault slip (Case c61)

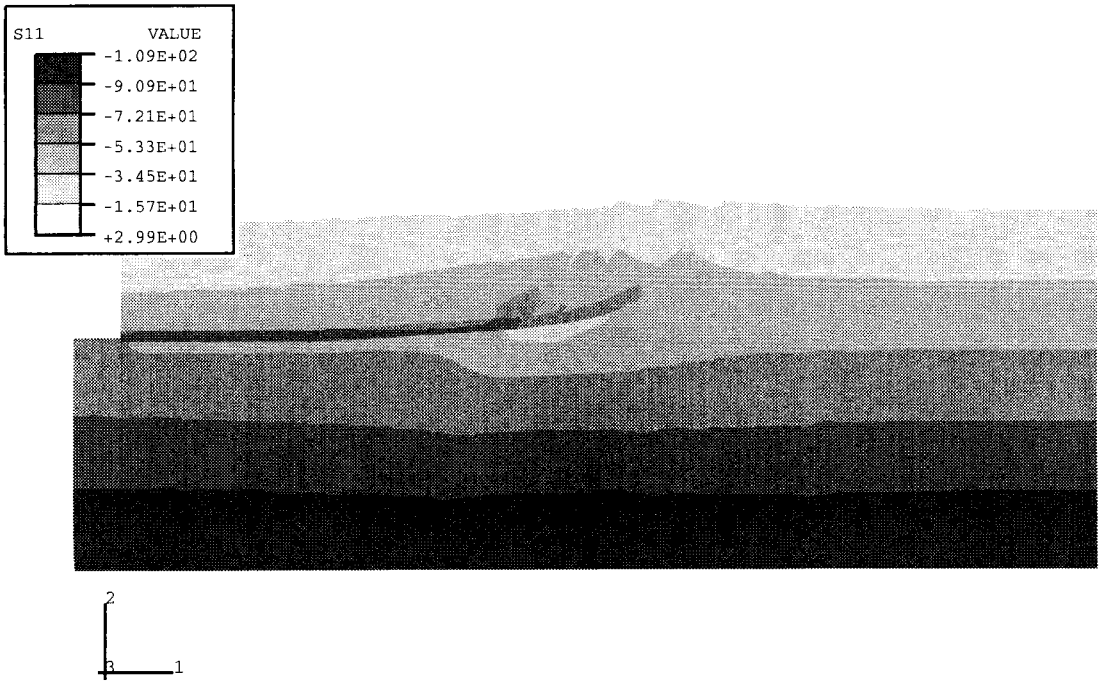

Figure 3-4. Distribution of horizontal stress: initial state with previous fault slip (Case c61)

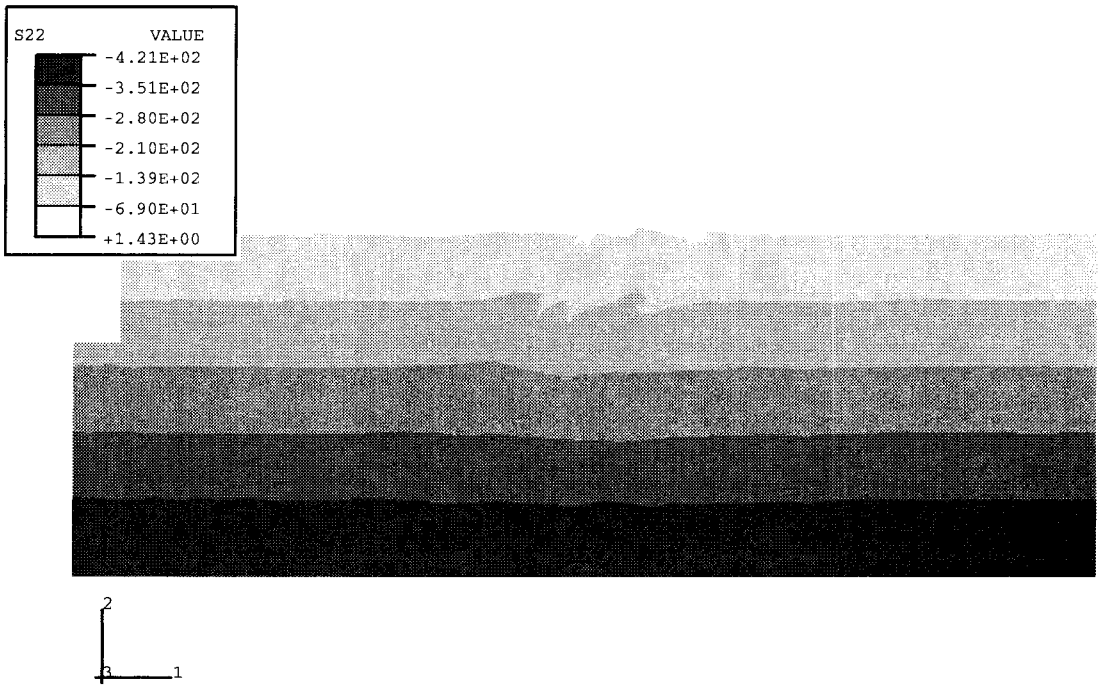

Figure 3-5. Distribution of vertical stress: end of simulation (Case c61)

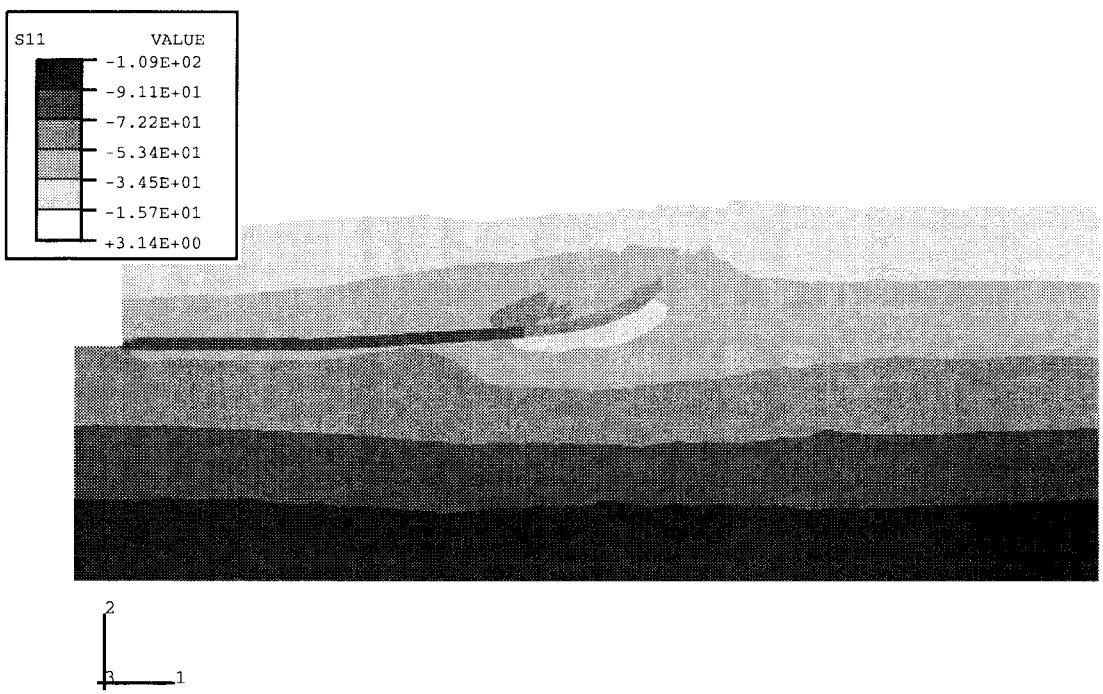

Figure 3-6. Distribution of horizontal stress: end of simulation (Case c61)

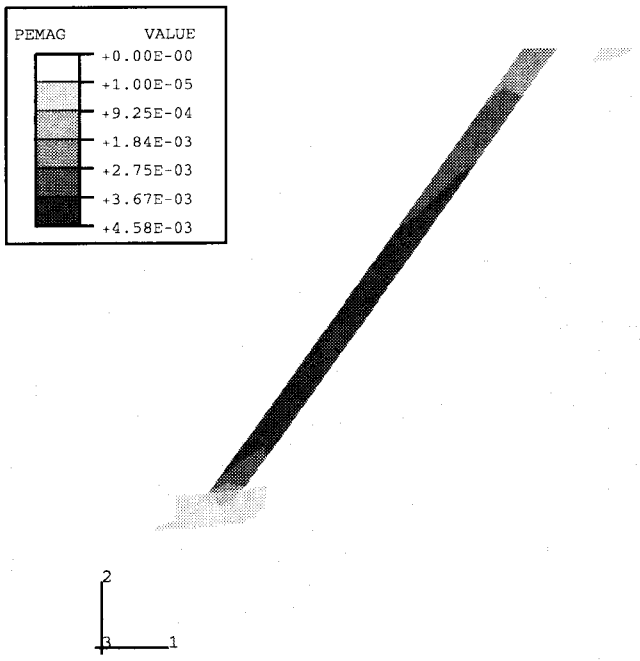

Figure 3-7. Distribution of inelastic strain for Case c51: end of simulation

3.2 DISTRIBUTIONS OF INELASTIC STRAIN

The distributions of inelastic strain for the end-of-simulation state of Cases c51 and c63 are plotted in Figure 3-7 and Figure 3-8. The values of the input parameters (see Table 2-1) for the two cases are: $k_3 = 0.4$, ϕ=30°, $\varphi/\phi = 0.1$, and $D_\alpha = 0.05$, for c51; $k_3 = 0.26$, $\phi = 32°$, $\varphi/\phi = 0.3$, and $D_\alpha = 0.02$, for c63. The Br zone was the perturbed fault for both cases; that is, having established the initial state, additional inelastic deformation was induced in the domain by reducing the value of ϕ for the Br zone. The parameter PEMAG used in the figures as the measure of inelastic strain is the magnitude of plastic strain, denoted Γ^p, and defined as:

$$\Gamma^p = \sqrt{\frac{2}{3}\left[(e^p_{11})^2 + (e^p_{22})^2 + (e^p_{33})^2 + 2(e^p_{12})^2\right]} \qquad (3\text{-}1)$$

where $e^p{}_{11}$, $e^p{}_{22}$, and $e^p{}_{33}$, are the x-, y-, and z-components of plastic direct strain, and $e^p{}_{12}$ is the plastic shear strain component in the x-y plane.

In the case of c63, inelastic deformation occurred at the initial state; hence, the distribution of inelastic strain given in Figure 3-8 includes pre-existing inelastic strain. On the other hand, the initial state for Case c51 did not include prior inelastic deformation. Therefore, all the inelastic strain shown in

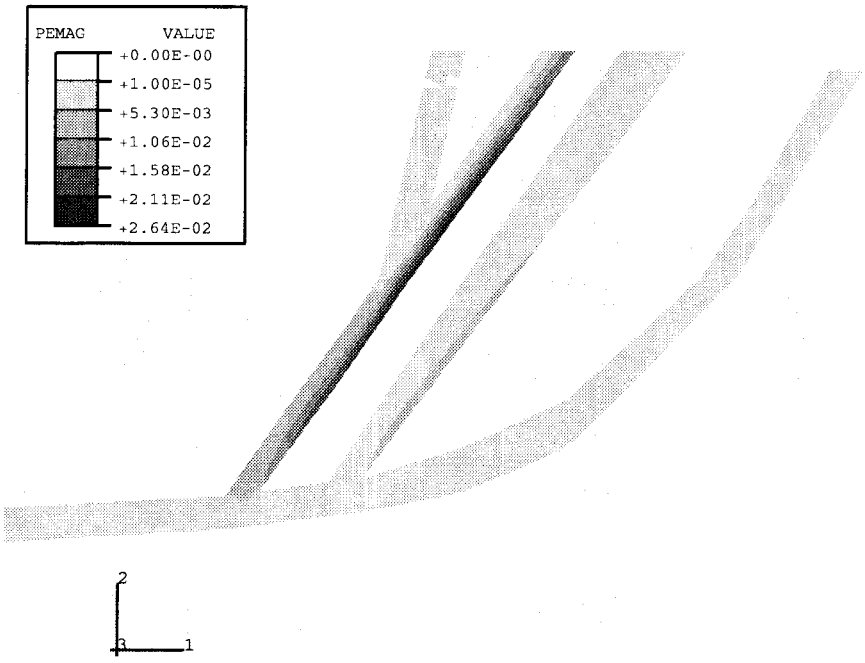

Figure 3-8. Distribution of inelastic strain for Case c63: end of simulation

Figure 3-7 was induced by the perturbation of the Br zone. As the figure shows, the perturbation of the Br zone in Case c51 caused inelastic deformation in the low-angle detachment fault, near the base of the Br zone. An examination of the stress data for this area shows that the normal and shear stresses on the low-angle fault are 154 and 2.5 MPa, respectively. Under this stress state, the condition of incipient slip on the fault requires a friction angle of 0.93°; slip would not occur if the value of friction angle for the fault is larger. Therefore, the fact that slip occurred on the low-angle fault would be inconsistent with the fact that the value of friction angle for the fault zone is 30°.

The explanation for this paradox lies in the fact that the fault zones were assigned isotropic strength properties, as was explained in Section 2.1. The isotropic strength properties allow the development of inelastic response on any plane for which the failure condition is satisfied. The observed inelastic response would not have occurred if the applied material model had restricted slip to a plane parallel to the fault, by modeling the fault either as a contact between two blocks or as a zone with anisotropic strength, both of which models were described briefly in Section 2.1.

This observation regarding the occurrence of slip on the low-angle fault raises an important question regarding the choice of models for the mechanical simulation of faults, especially those faults that are approximately normal to the general direction of the maximum principal compressive stress. It is frequently observed that the stress conditions on such faults would not permit fault slip, considering a resistance to slip described in terms of the Mohr-Coulomb failure law. For example, Byerlee (1990), in an examination of a similar paradox for the San Andreas fault, noted that the condition for sliding under the existing stress state would require a friction angle smaller than 6°, which is much smaller than would

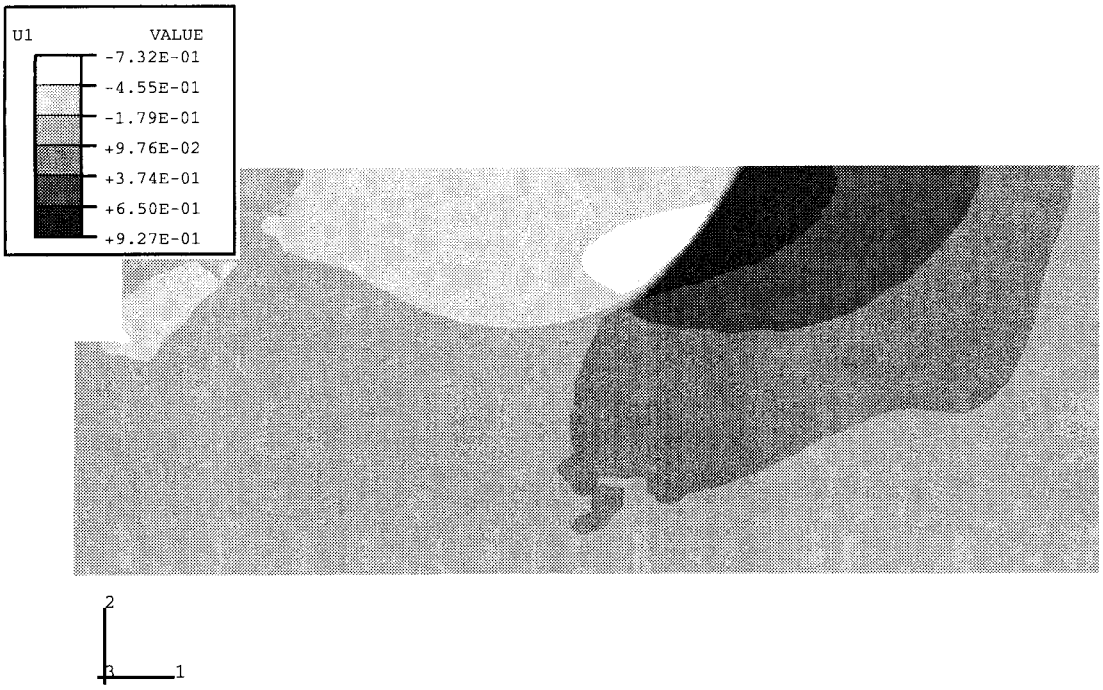

Figure 3-9. Distribution of horizontal displacements (m) associated with slip on the Fmw fault zone

reasonably be expected for most geologic materials (cf. Kenney, 1967). The fact that slip occurs on such faults suggests a re-examination of the methods of modeling their mechanical response. It has been observed in this study that the use of isotropic strength properties for the fault zone led to the prediction of fault slip under conditions for which it would not occur if the material model restricted the development of inelastic response to planes parallel to the fault.

3.3 DISTRIBUTION OF DISPLACEMENTS

Contours of vertical and horizontal displacements and plots of the resultant displacement vectors are given in Figure 3-9 through Figure 3-17, illustrating the distributions of displacements associated with slip on each of the Fmw, FrPc, and Br fault zones. The hangingwall profiles resulting from the fault slips are also given in Figure 3-18. All displacements are in m. As Figures 3-11, 3-14, and 3-17 show, the displacement pattern associated with each fault consists of upward-eastward displacements on the footwall, and downward-westward displacements on the hangingwall. This displacement pattern is consistent with normal faulting on the perturbed fault. The results presented in the figures were obtained for Cases c52 (perturbed fault: Fmw zone), c50 (perturbed fault: FrPc zone), and c51 (perturbed fault: Br zone), for which the input parameters (see Table 2-1) were assigned the following values: $k_3 = 0.4$, $\phi = 30^\circ$, $\varphi/\phi = 0.1$, and $D_\alpha = 0.05$. The initial equilibrium state was established in each case without any deformation occurring; therefore, each of the displacement distributions shown in the figures was induced entirely by the associated fault slip.

The perturbed fault is shown in white in each of the vector plots (Figure 3-11, Figure 3-14, and Figure 3-17); the low-angle part of the Fmw zone is also shown in white, to draw attention to its

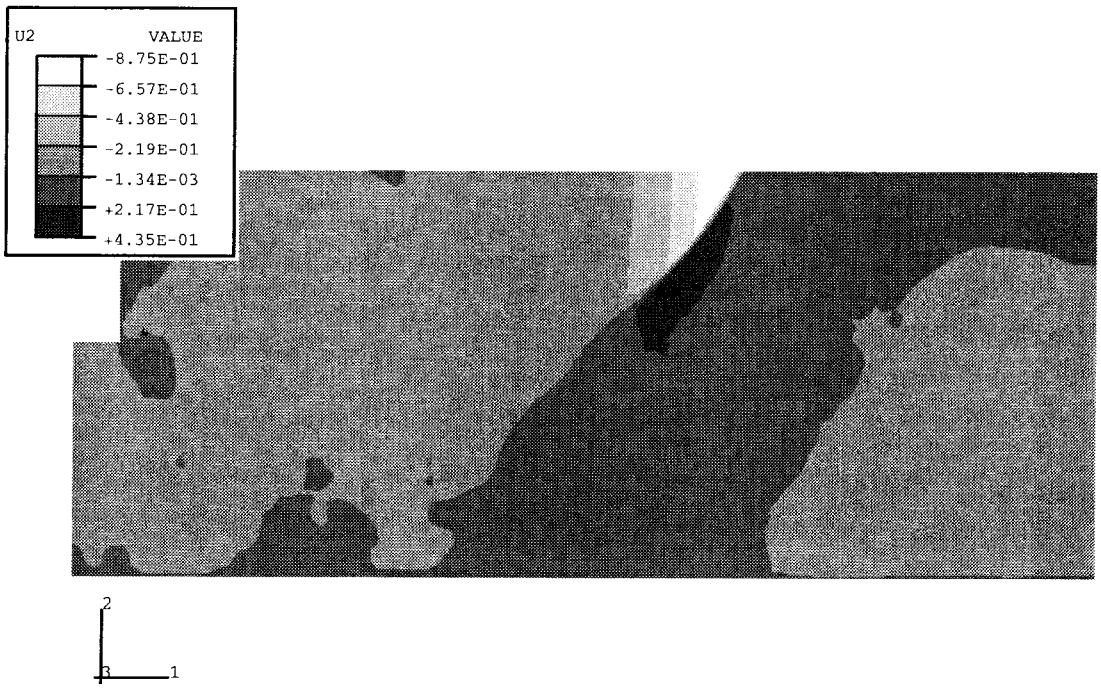

Figure 3-10. Distribution of vertical displacements associated with slip on the Fmw fault zone

relationship with the directions of the displacement vectors. The hangingwall displacement vectors associated with slip on the Fmw zone (Figure 3-11) generally follow the orientation of the fault in the high-angle region and in the high-to-low angle transition region. On the other hand, the hangingwall displacement vectors associated with slip on the FrPc zone (Figure 3-14) and those associated with the Br zone (Figure 3-17) follow the orientation of the faults in the steeply dipping regions only. The vectors are curved in the zone of intersection of the faults with the low-angle detachment, suggesting that the transition from the steep to low-angle faults is more gradual for these two faults than is represented in the current model. The transitions are indeed shown as gradual in (Figure 1-1), but were modeled as abrupt in this study, in order to simplify the finite element mesh.

It should also be noted that the displacement vectors in the low-angle detachment are all oblique to the fault in all three vector plots. This direction of displacement is consistent with the fact that the slip planes within the low-angle fault zone are inclined to the general direction of the fault, which may suggest that the dip of the low-angle fault may be much larger than was used in this model. One way to investigate this possibility would be to conduct a mechanical analysis of a rock mass with no predetermined fault orientations, assign to the rock mass a material model similar to the one assigned to the fault zones in this study, and use the resulting pattern of displacement vectors to determine the most likely location and orientation of faults.

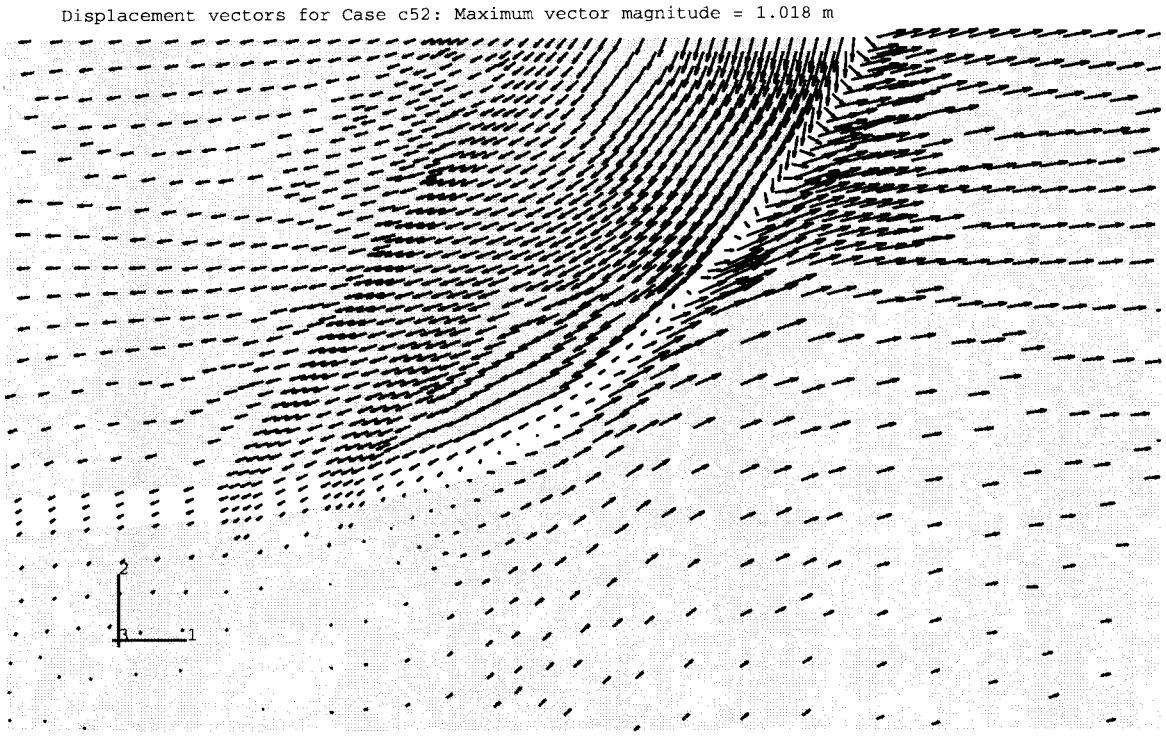

Figure 3-11. Distribution of displacement vectors associated with slip on the Fmw fault zone

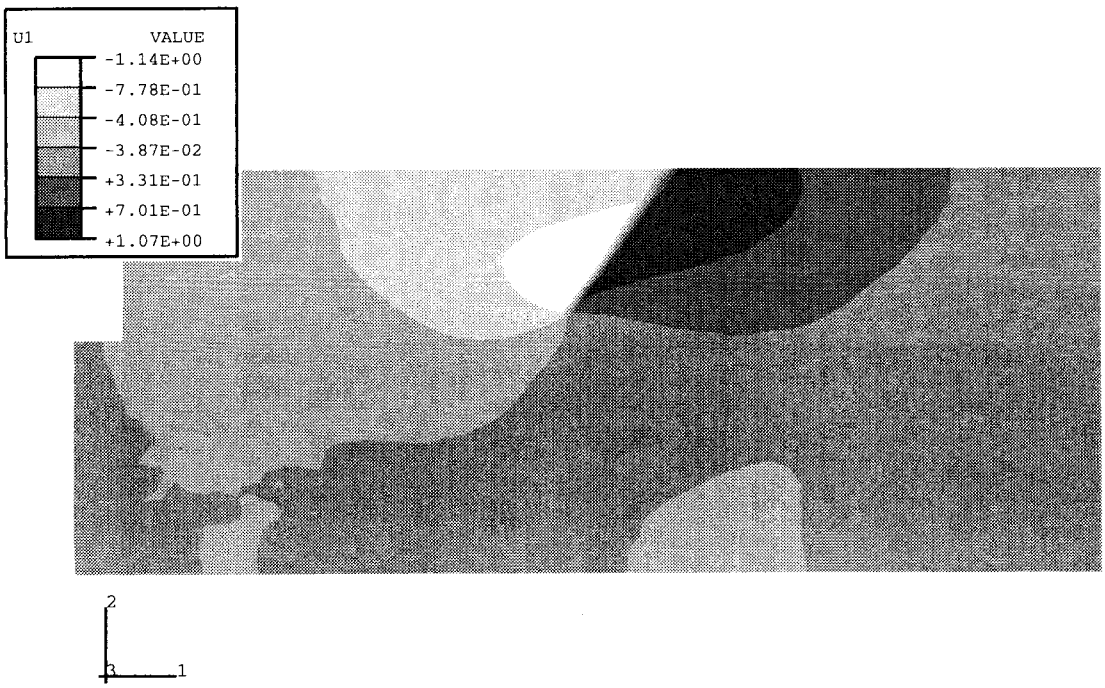

Figure 3-12. Distribution of horizontal displacements associated with slip on the FrPc fault zone

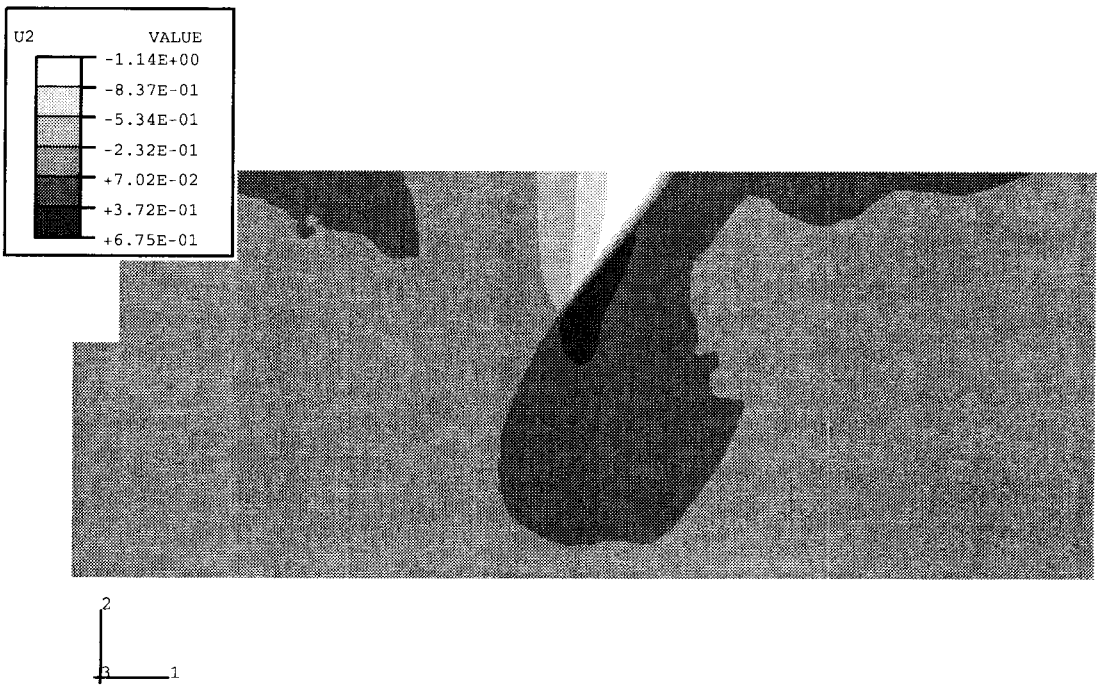

Figure 3-13. Distribution of vertical displacement associated with slip on the FrPc fault zone

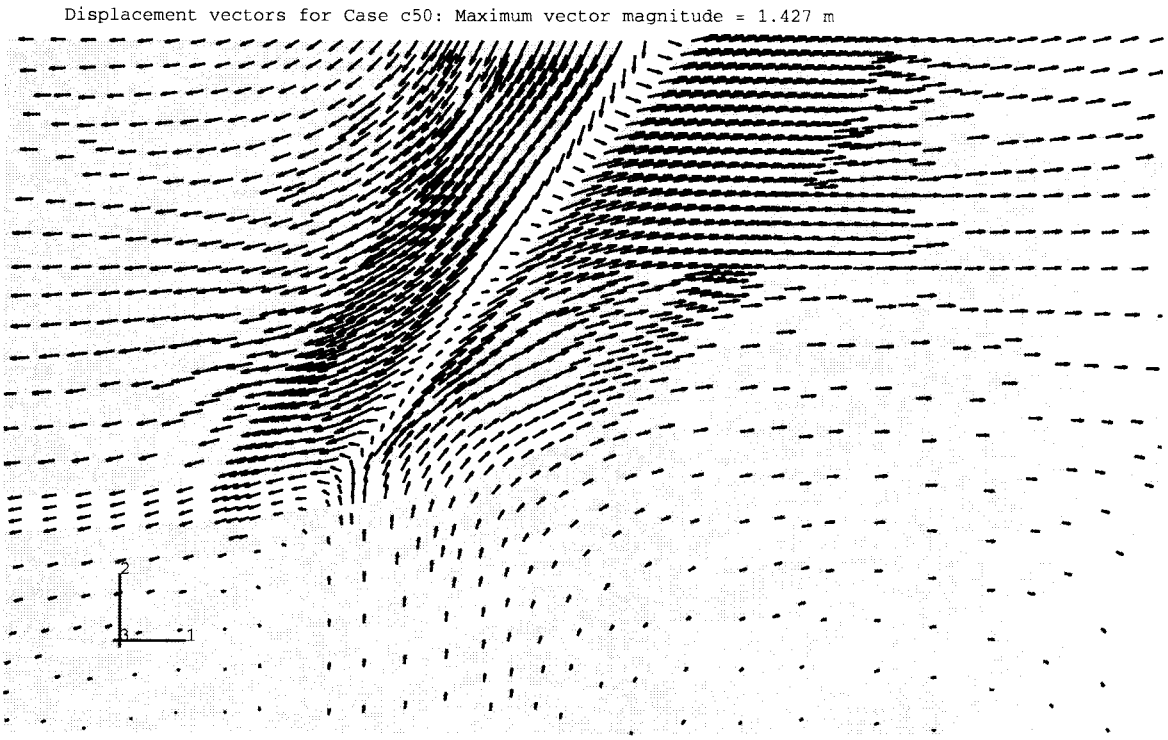

Figure 3-14. Distribution of displacement vectors associated with slip on the FrPc fault zone

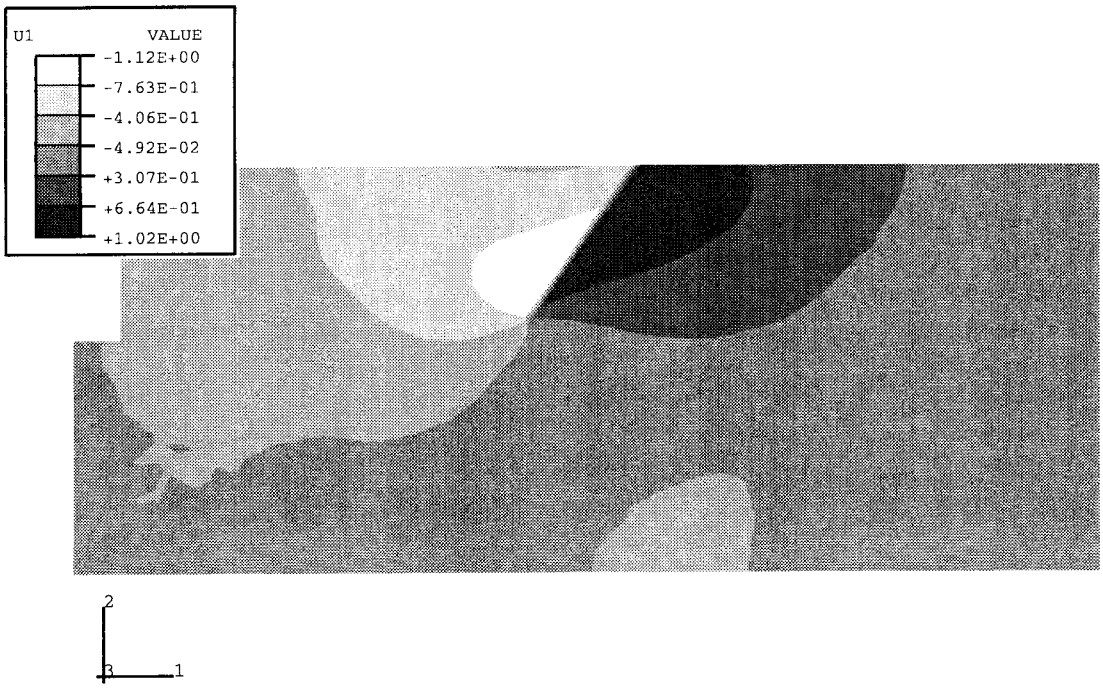

Figure 3-15. Distribution of horizontal displacements associated with slip on the Br fault zone

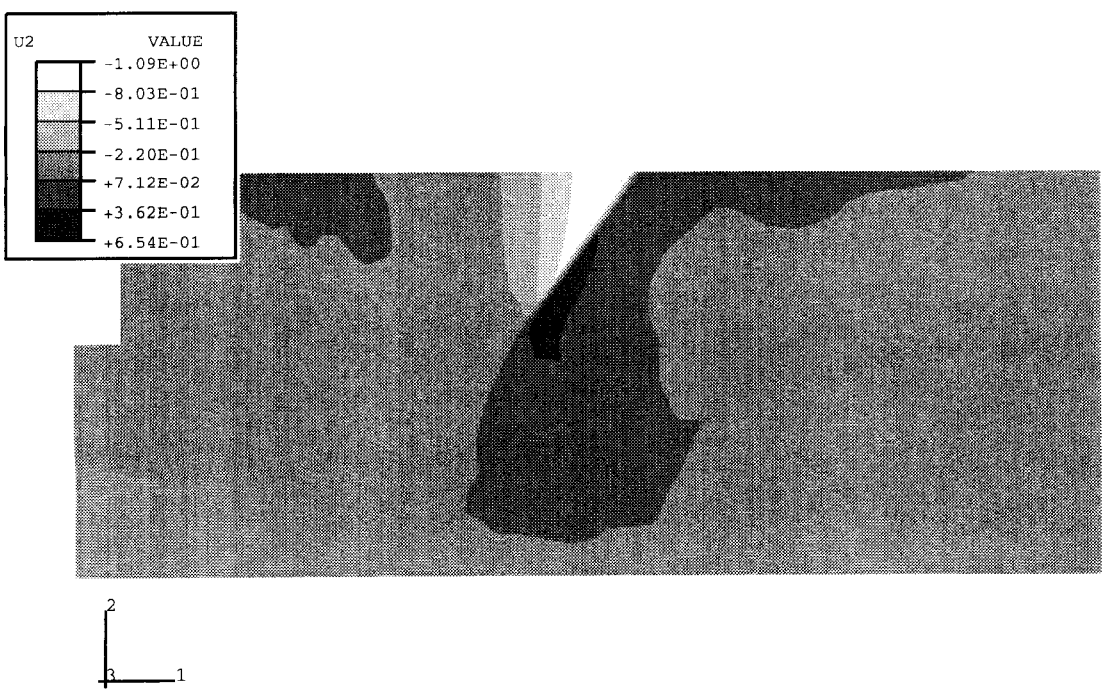

Figure 3-16. Distribution of vertical displacements associated with slip on the Br fault zone

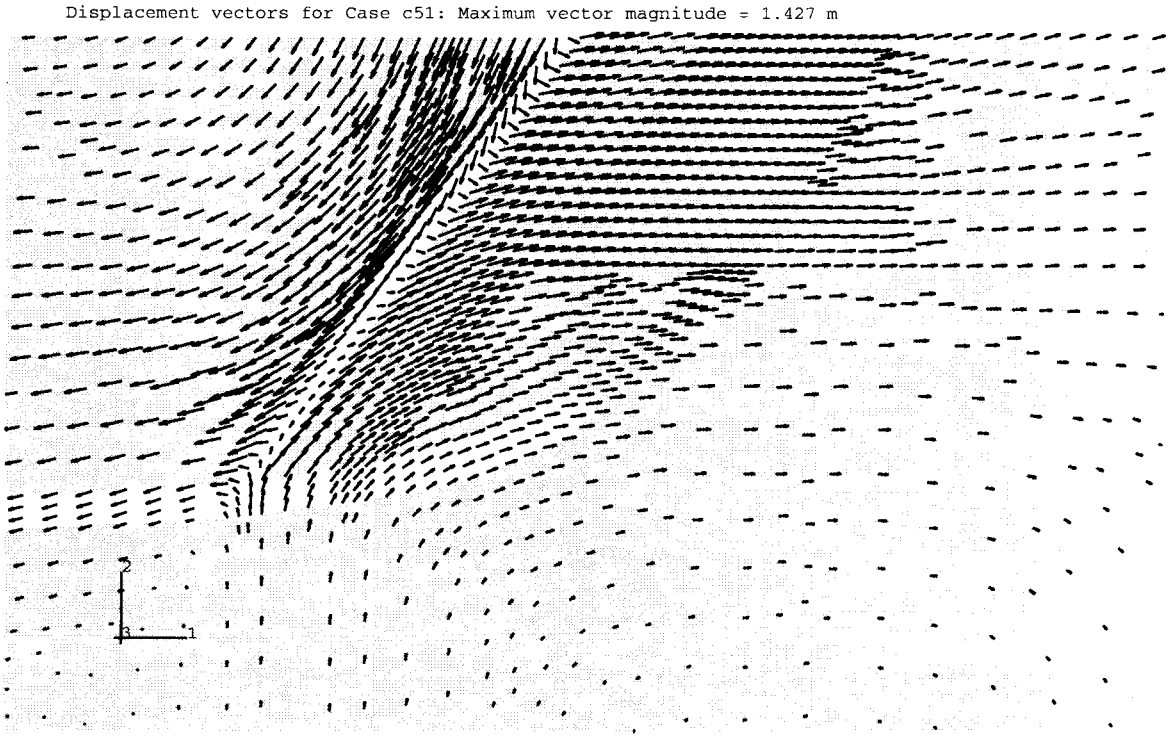

Figure 3-17. Distribution of displacement vectors associated with slip on the Br fault zone

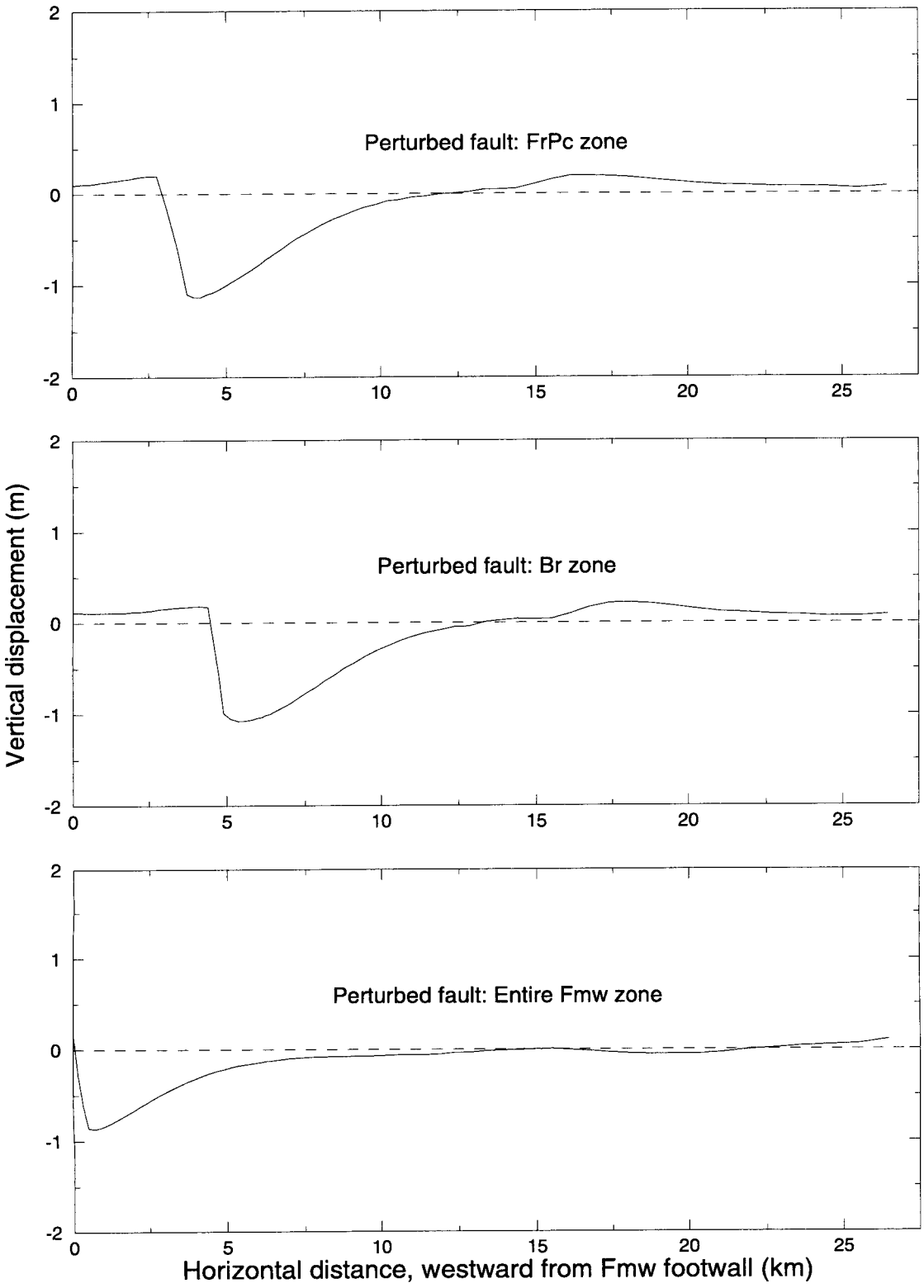

Figure 3-18. Hangingwall ground-surface profiles associated with slip on the Fmw, FrPc, and Br fault zones

4 ANALYSES OF CALCULATED RESPONSES

The values of the input and response variables for the 68 fault-slip simulations (described in Section 2.4.2.3) are summarized in Appendix A (Tables A-1 through A-10). The relationships between the response and input variables are examined in this chapter, to determine which of the input variables have the dominant effects on the response variables. Scatter plots of values of the variables, normalized according to Eq. (2-12), are presented. The plots are also used to determine if there is significant correlation between pairs of response and input variables, based on visual examination only.

A strong correlation between a pair of input and response variables implies that the variability of the particular input parameter has a dominant effect on the predicted values of the response variable. On the other hand, the absence of significant correlation between a pair of input and response variables implies that any effect of the input parameter on the response variable is overshadowed by the effects of other input parameters. This distinction between input parameters that have a dominant effect and those that do not leads to recommendations regarding the input parameters that can be assigned a single value and those whose values need to be varied within a range, in an analysis to predict values of a selected response variable.

4.1 FAULT DISPLACEMENT

The total fault displacement, U_f, is the cumulative slip along the entire length of a fault; it was calculated using the following summation

$$U_f = \sum_{n=1}^{N} (l_t \varepsilon_t)_n \tag{4-1}$$

where l_t is the length of a finite element in the tangential direction of the fault, ε_t (referred to as the tangential plastic strain) is the plastic shear strain component parallel to the fault at the centroid of the element, and N is the total number of elements along the fault. Each fault zone was modeled using three fault-parallel layers of finite elements, and Eq. (4-1) was applied to the middle layer, colored dark in Figure 4-1. The average fault displacement for a fault is U_f/N.

The tangential plastic strain, ε_t, was calculated through a transformation of the plastic strain tensor, using the following equation (cf. Jaeger and Cook, 1979):

$$\varepsilon_t = \frac{1}{2} (e_{22}^{\ p} - e_{11}^{\ p}) \sin(2\alpha) + e_{12}^{\ p} \cos(2\alpha) \tag{4-2}$$

where $\alpha = \theta + \pi/2$, and θ is the dip of the fault.

As Table 4-1 shows, the calculated maximum values of total fault displacement are about 78, 36, and 57 m, for the Fmw, FrPc, and Br zones, respectively, which correspond to average fault displacements of about 0.9, 1.1, and 1.7 m. Typical profiles of tangential plastic strain for the faults are given in Figure 4-2

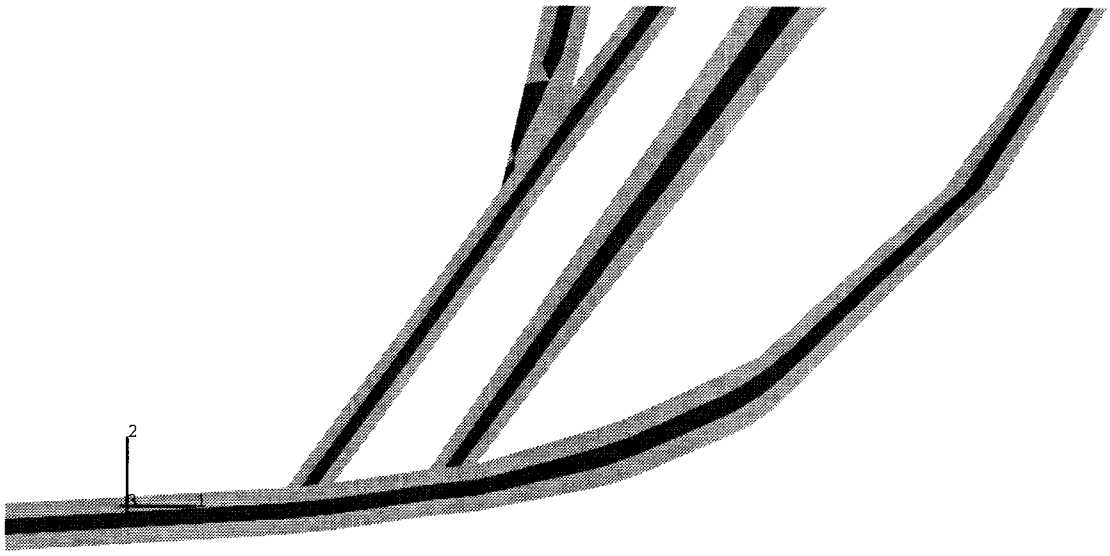

Figure 4-1. Layout of finite elements within the fault zones: the value of fault displacement in each zone was based on the plastic shear strain in the middle layer, colored dark

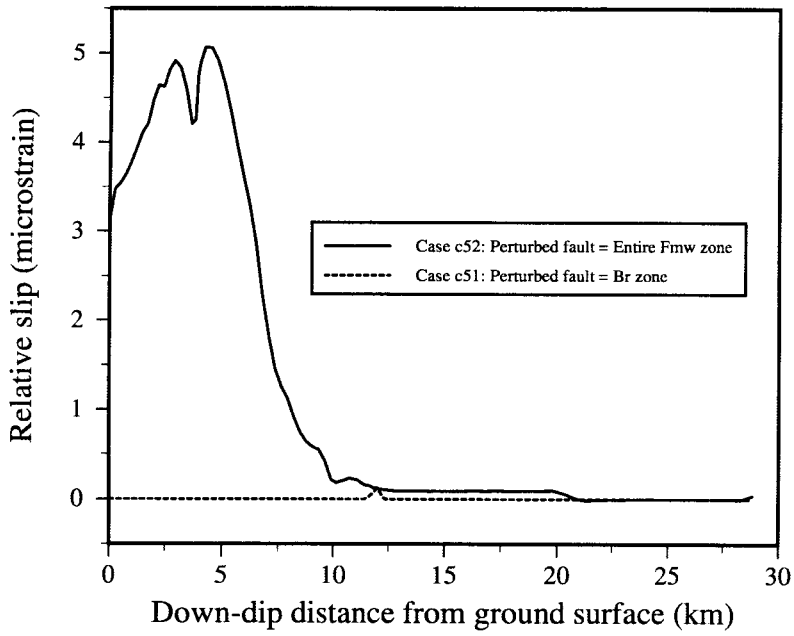

Figure 4-2. Distributions of fault slip along the Fmw zone

and Figure 4-3; these figures show that a large fraction of the displacement on each fault is concentrated in a small fraction of the total fault length. For the FrPc and Br faults, the displacement occurred mainly close to the base; for the Fmw fault, it occurred near the base of the high-angle region. This pattern of displacement distribution implies that a significant proportion of the fault displacement is taken up through the deformation of the hangingwall and footwall.

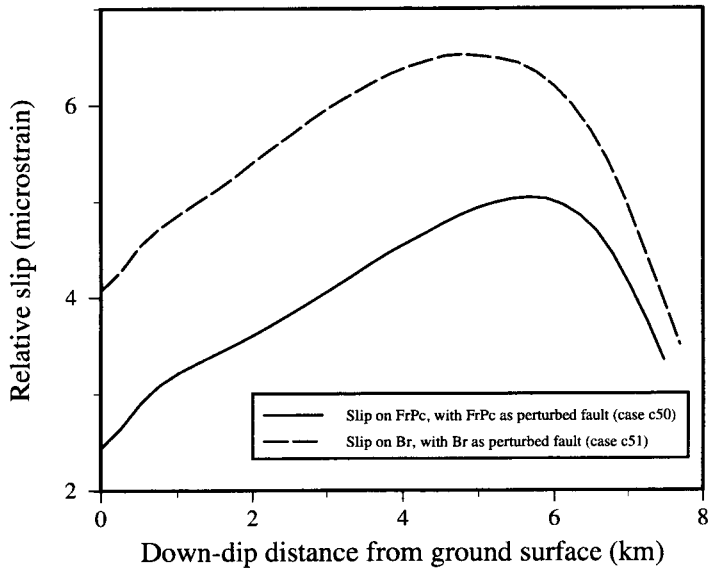

Figure 4-3. Distributions of fault slip along the FrPc and Br zones

Table 4-1. Range of values of fault displacement (m)

Monitored Fault	Perturbed Fault			
	Upper Fmw	FrPc	Br	Entire Fmw
Fmw	13.9–61.9	0–0.52	0–0.57	19.7–77.5
FrPC	0– 0.08	20–36	0–0.02	0– 0.08
Br	0– 0.54	0–0.11	22.2–57.4	0– 0.51
Gd	0– 0.07	0–0.01	0–0.01	0– 0.06

The sensitivity of the total fault displacement in the Fmw zone to changes in the values of the input variables, k_3, ϕ, φ/ϕ, and D_α, is illustrated in Figure 4-4 through Figure 4-7. Similar figures are given in Appendix B for the sensitivity of total fault displacement in the FrPc, Br, and Gd zones to changes in the values of the input variables. Generally, the plots show a strong correlation between total fault displacement and k_3, and no significant correlation between it and the other input variables. This observation implies that the effects of the variability of ϕ, φ/ϕ, and D_α on fault-displacement predictions are likely to be overshadowed by the effects of k_3 variability. Therefore, in an analysis in which the prediction of fault displacement is important, each of the parameters ϕ, φ/ϕ, and D_α may be assigned a single value, but the effect of k_3 variability on the predictions should be considered carefully.

4.2 SLIP LENGTH

The slip length was defined as the total length of a fault over which a tangential plastic strain, ε_t, of at least 1.0×10^{-5} occurred. The calculated range of values of slip length is presented in Table 4-2, based on which the following observations are made:

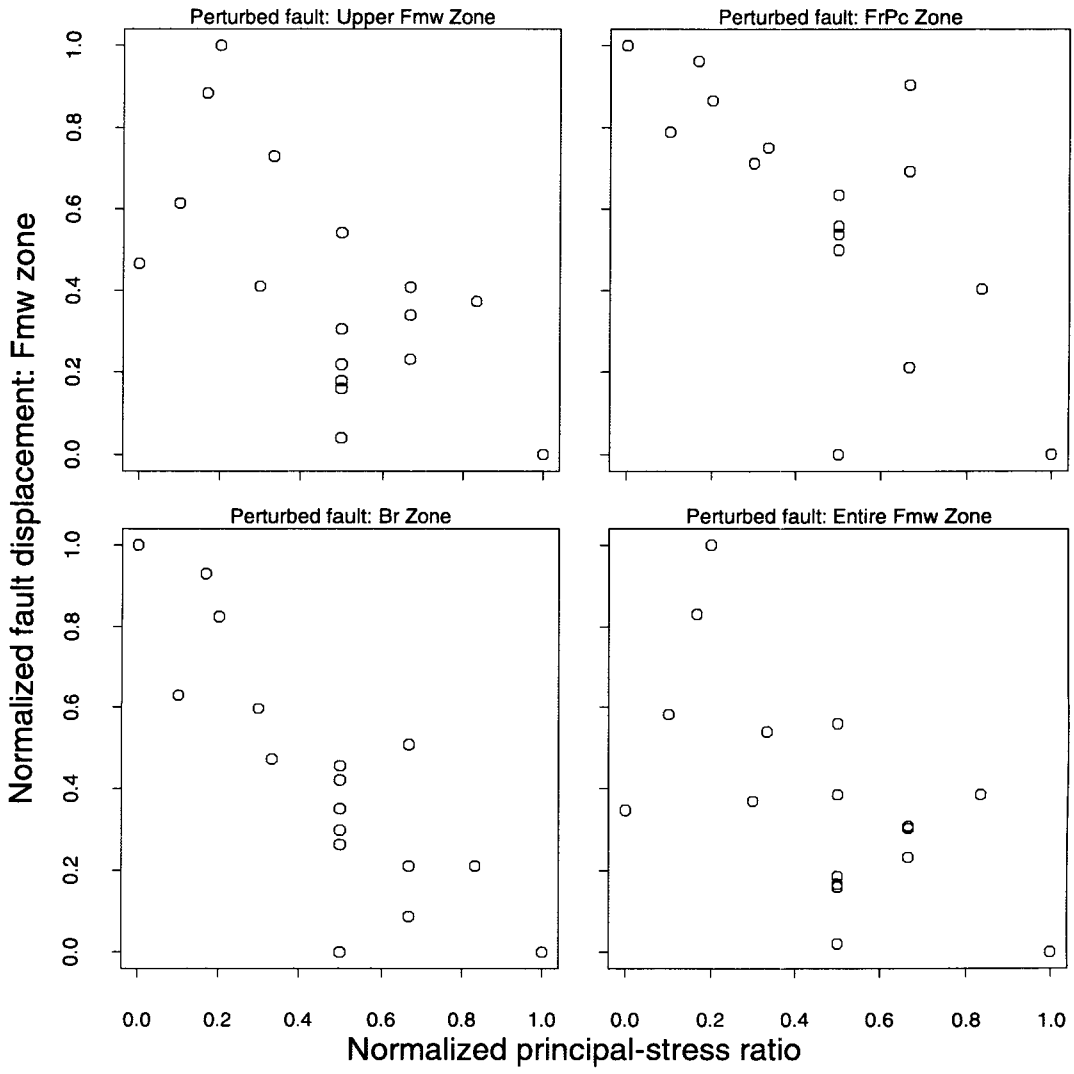

Figure 4-4. Sensitivity of total fault displacement in the Fmw zone to changes in the value of the principal stress ratio k_3

Table 4-2. Range of values of slip length (km)

Monitored Fault	Perturbed Fault			
	Upper Fmw	FrPc	Br	Entire Fmw
Fmw	6.75–9.88	0–4.76	0–5.6	21.19–29.2
FrPC	0–2.28	7.72–7.72	0–0.76	0–2.53
Br	0–3.26	0–2.49	7.94–7.94	0–3.71
Gd	0–1.74	0–0.48	0–0.1	0–1.96

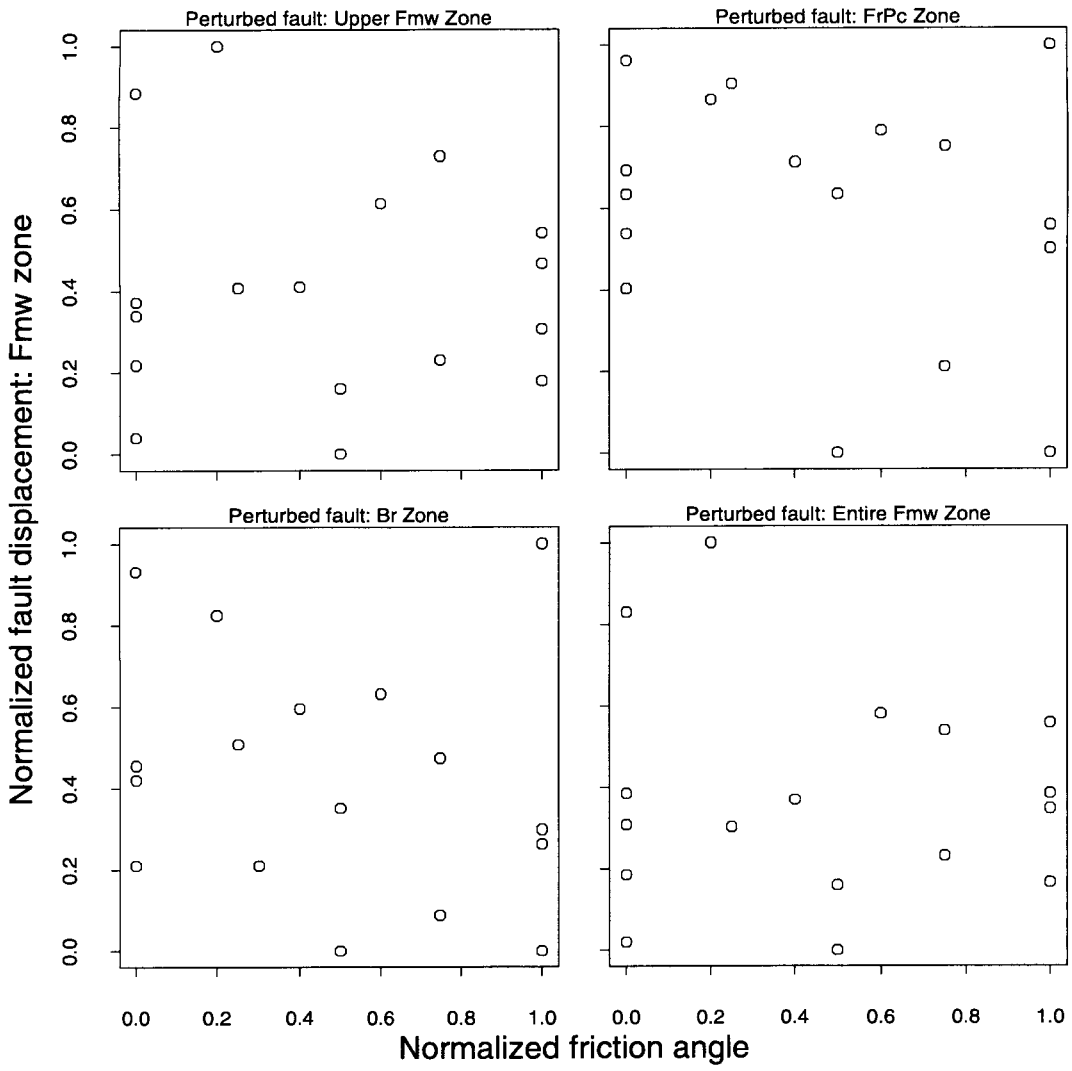

Figure 4-5. Sensitivity of total fault displacement in the Fmw zone to changes in the value of the friction angle

(i) Self-induced slips, that is, slip induced on a fault by a perturbation of the same fault, tend to occur over the entire length of the fault. As a result, the self-induced slip lengths on the FrPc and Br zones have constant values of 7.72 and 7.94 km, respectively.

(ii) The perturbation of the Fmw zone has stronger effects than the perturbation of either the FrPc or Br zones. For example, whereas slip lengths on the Gd zone induced by the perturbation of the Fmw zone attained a maximum of about 2 km, the maximum slip length caused on the Gd zone by a perturbation of either the FrPc or Br zones is about 0.5 km.

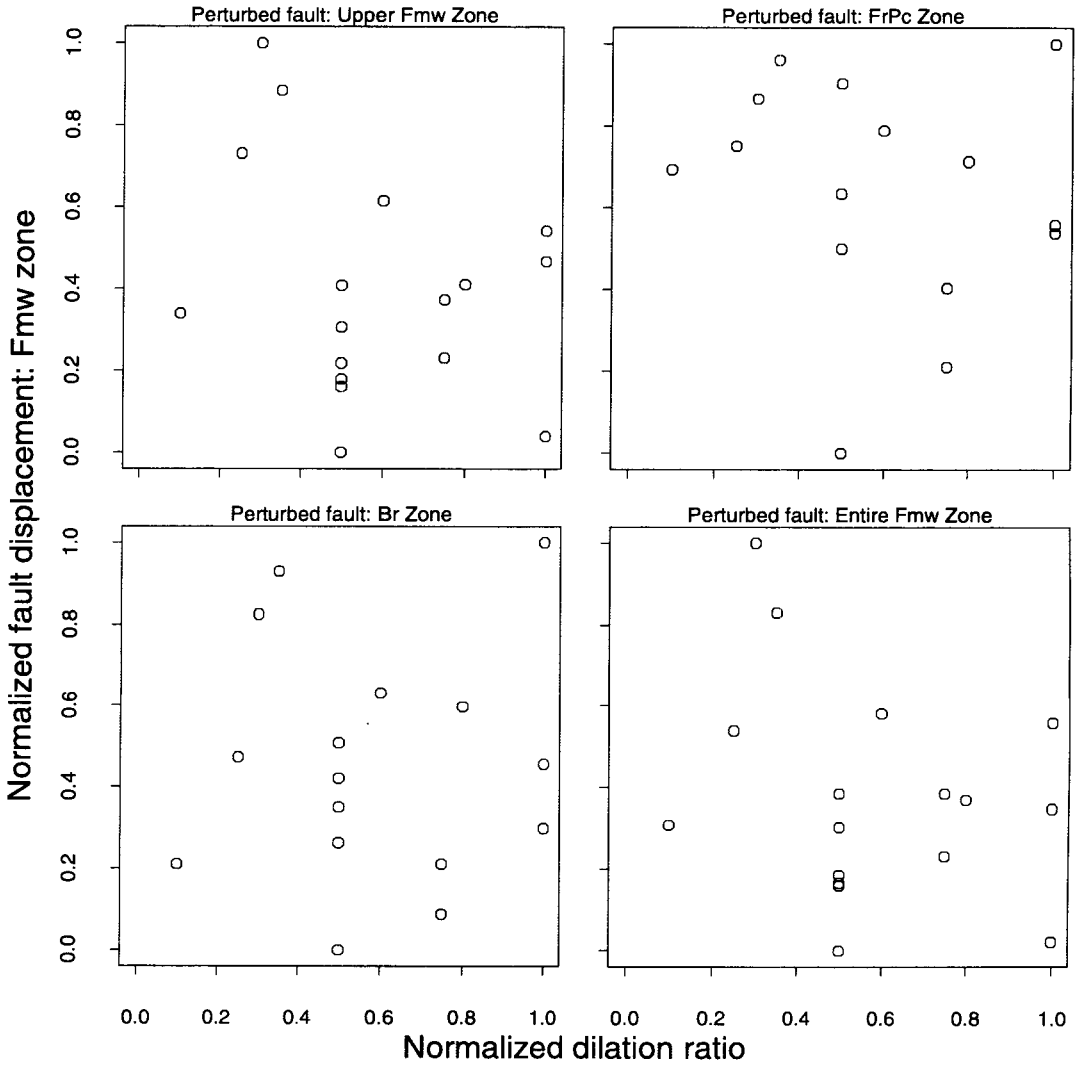

Figure 4-6. Sensitivity of total fault displacement in the Fmw zone to changes in the value of the dilation angle

(iii) Slips induced on a fault due to the perturbation of another fault were observed to initiate either at the ground surface, or at depth near the base of the fault. All the induced slip on the Gd zone initiated at the ground surface, and, as Table 4-2 shows, extended to depths of between 0.5 and 2.0 km. The initiation of induced slip at the ground surface is consistent with the distribution of stress change within the study zone, which will be presented in a subsequent section.

The sensitivity of slip length to changes in the values of the input parameters is illustrated in Figure 4-8 through Figure 4-11 for the Fmw zone. Similar figures are given in Appendix B for the FrPc, Br, and Gd zones. The plots show a strong correlation between slip length and k_3, but no significant correlation between it and the other input variables, which leads to the conclusion that the effects of the

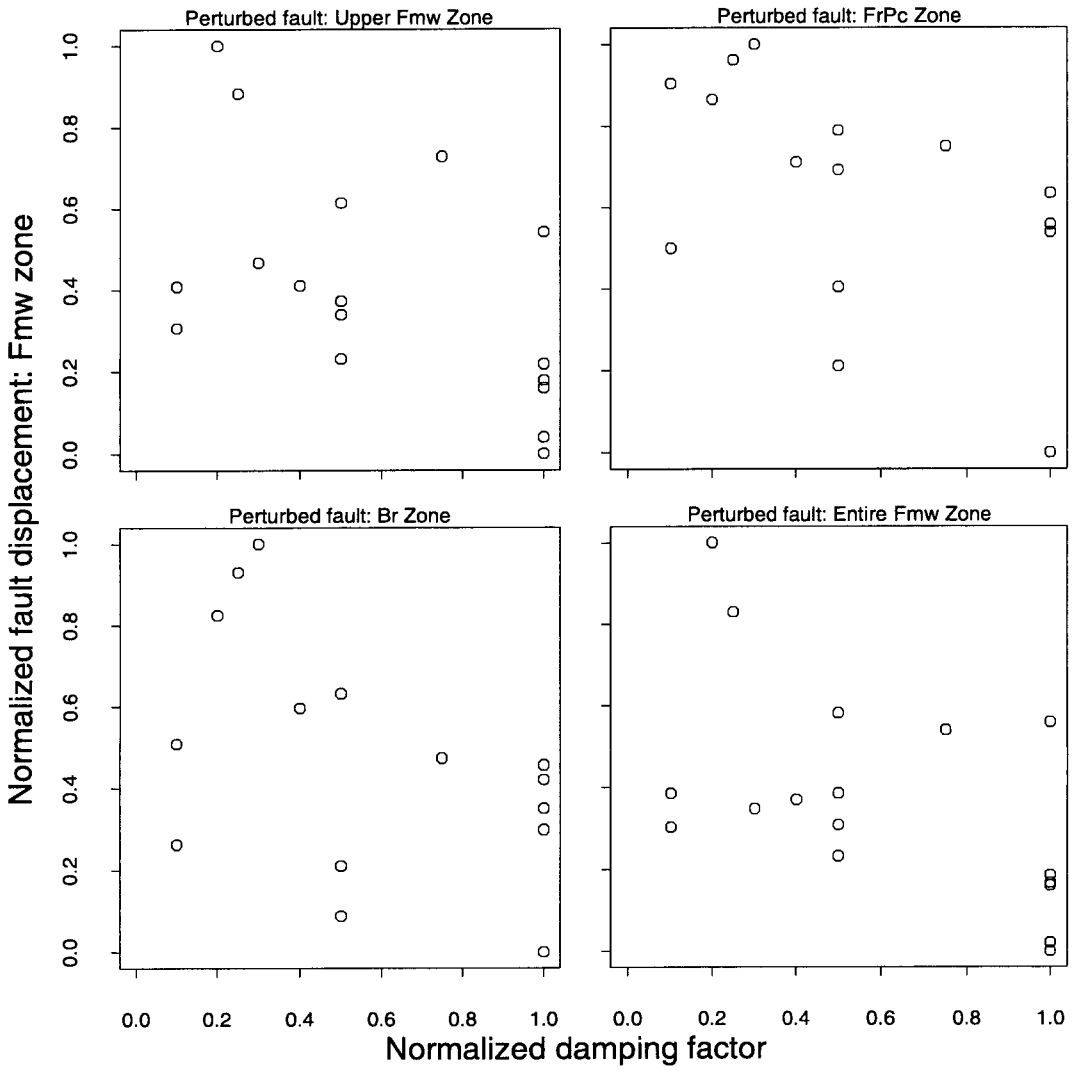

Figure 4-7. Sensitivity of total fault displacement in the Fmw zone to changes in the value of the damping factor

variability of ϕ, φ/ϕ, and D_α on slip-length predictions are likely to be overshadowed by the effect of k_3. Therefore, in an analysis for which the prediction of slip length is important, each of the parameters ϕ, φ/ϕ, and D_α may be assigned a single value, but the effect of k_3 variability on the predictions need be considered carefully.

4.3 LIMIT-EQUILIBRIUM FRICTION ANGLE

The limit-equilibrium friction angle, ϕ_{lim}, for a rock interface is the value of friction angle that would satisfy the condition for incipient slip [Eq. (2-10)] under the existing stress state. If the value of ϕ_{lim} is smaller than the actual value of friction angle for the interface, then slip will not occur; on the other hand, unstable conditions are predicted if the calculated ϕ_{lim} is equal to or larger than the actual friction angle for the interface. The values of ϕ_{lim} were calculated using the inverse of Eq. (2-10), that is.,

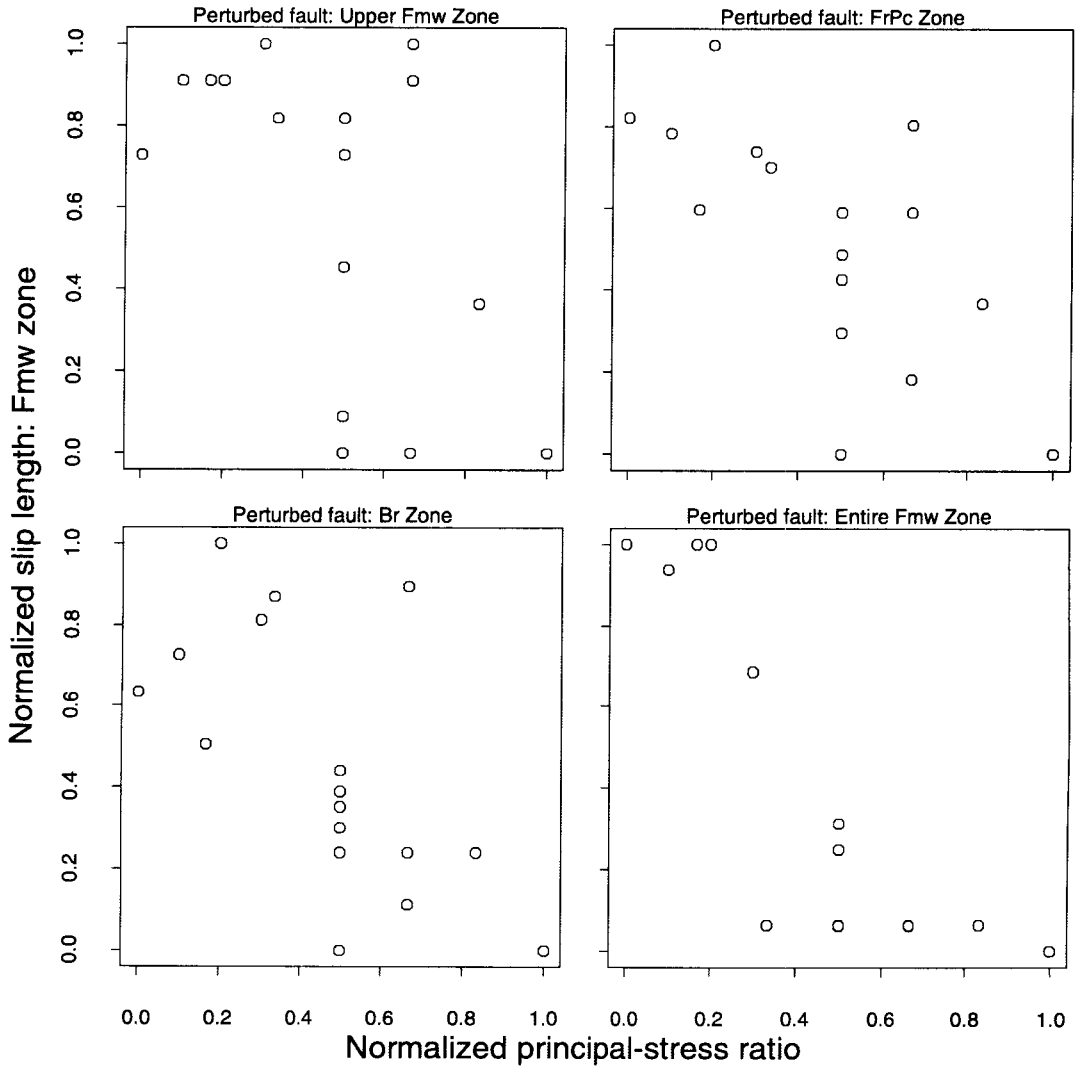

Figure 4-8. Sensitivity of Fmw-zone slip length to changes in the value of principal stress ratio k_3

$$\phi_{lim} = \arctan\ (\tau/\sigma_n) \tag{4-3}$$

where τ and σ_n for a fault were calculated using a transformation of the stress tensor, as follows:

$$\sigma_n = \sigma_{11} \cos^2\alpha + 2\sigma_{12} \sin\alpha \cos\alpha + \sigma_{22} \sin^2\alpha \tag{4-4}$$

$$\tau = \frac{1}{2}(\sigma_{22} - \sigma_{11}) \sin\ (2\alpha) + \sigma_{12}\cos\ (2\alpha) \tag{4-5}$$

and α is related to the dip of the fault as was explained for Eq. (4-2).

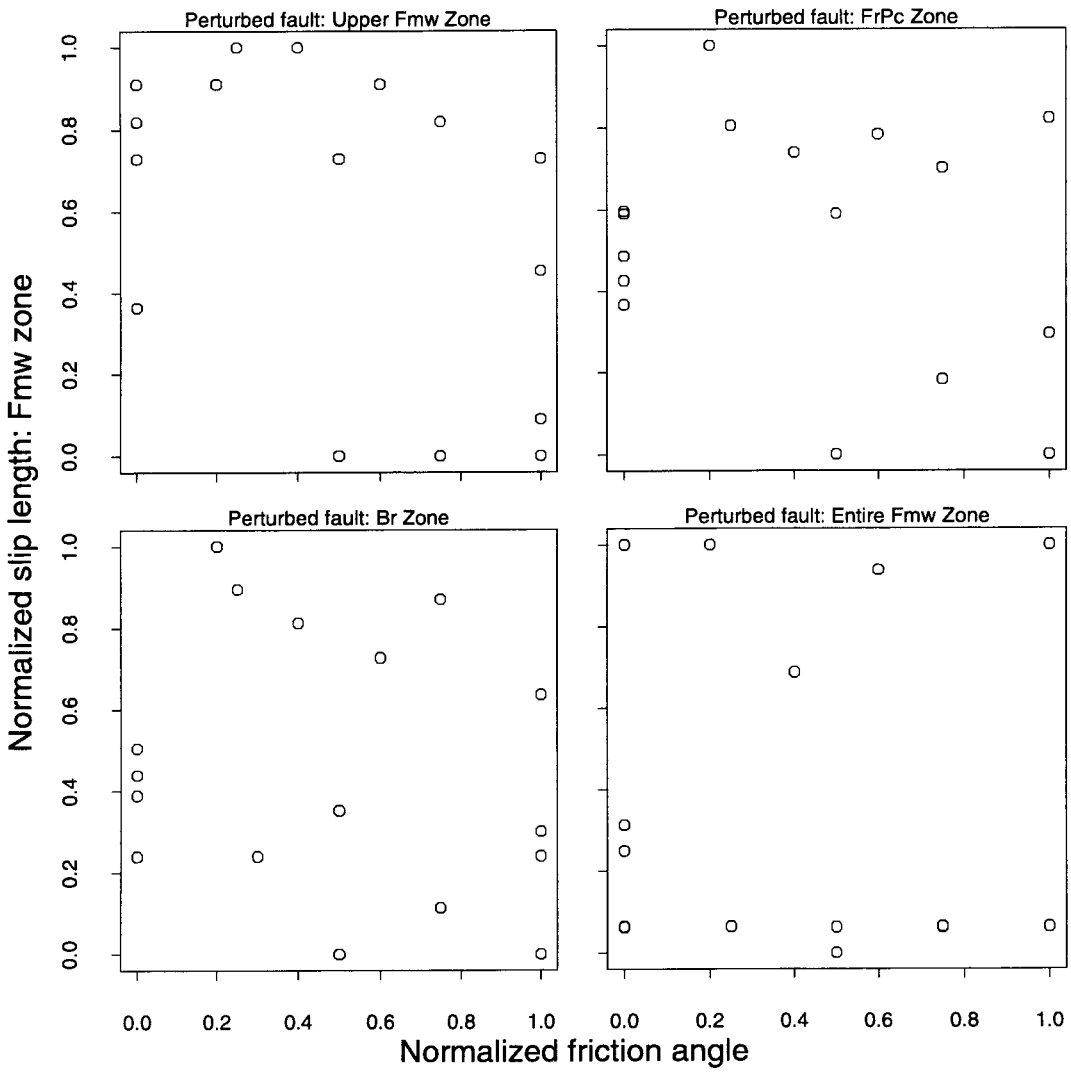

Figure 4-9. Sensitivity of Fmw-zone slip length to changes in the value of the friction angle

The value of ϕ_{lim} was not calculated for the perturbed fault, but only for the other faults, its purpose being to monitor how the perturbation of a given fault would affect the slip tendency of other faults. The calculated ranges of ϕ_{lim} values are given in Table 4-3, based on which of the following observations can be made:

(i) The largest value of ϕ_{lim} occurred on the Fmw zone;

(ii) For the other faults, the largest values of ϕ_{lim} were associated with the perturbation of the Fmw zone, which strengthens an observation made earlier that the perturbation of the Fmw zone produced more severe effects than the perturbation of any of the other faults.

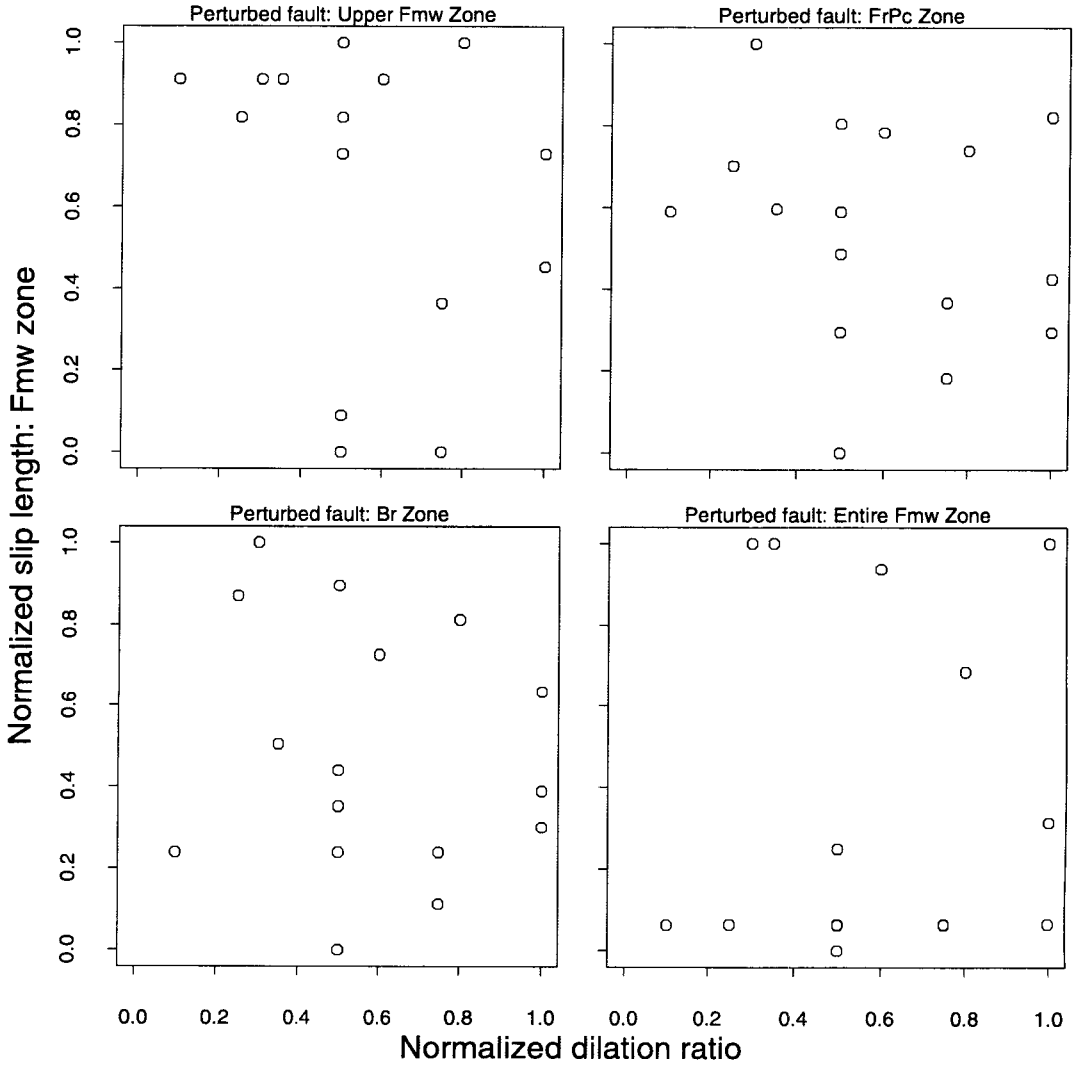

Figure 4-10. Sensitivity of Fmw-zone slip length to changes in the value of the dilation angle

Table 4-3. Range of values of the limit-equilibrium friction angle

Monitored Fault	Perturbed Fault			
	Upper Fmw	FrPc	Br	Entire Fmw
Fmw	NA–NA	18.4–39	18.8–28.3	NA–NA
FrPC	20.2–34.4	NA–NA	20.7–29.2	20–33.8
Br	23.1–35.8	19.6–30.2	NA–NA	22–36.4
Gd	13.9–29.4	7.6–19.4	8.7–24.2	14–30.3

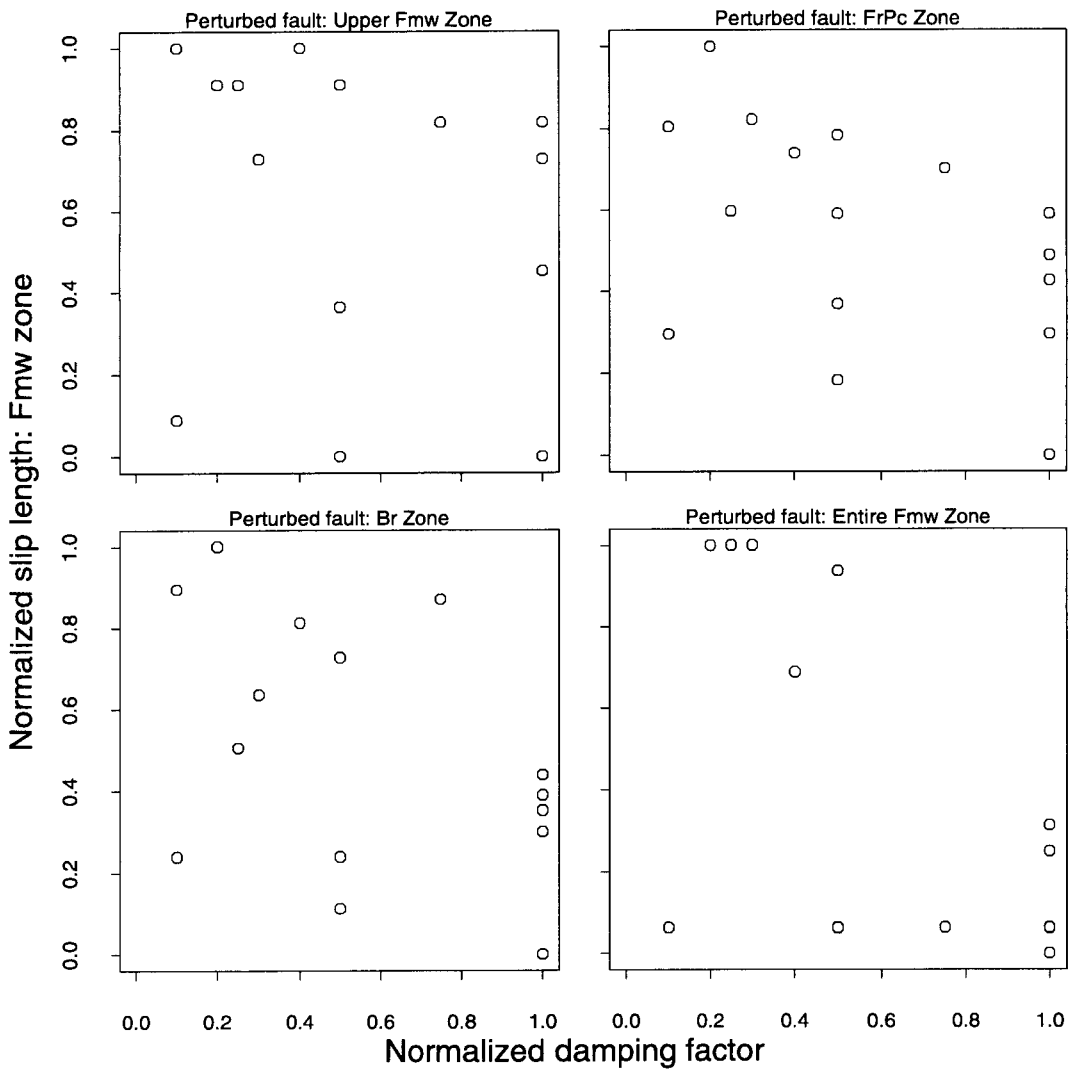

Figure 4-11. Sensitivity of Fmw-zone slip length to changes in the value of the damping factor

The sensitivity of the limit-equilibrium friction angle to changes in the values of the input parameters is illustrated in Figure 4-12 through Figure 4-15 for the Fmw zone. Similar figures are given in Appendix B for the FrPc, Br, and Gd zones. The plots show strong ϕ_{lim}-versus-k_3 and ϕ_{lim}-versus-ϕ correlations, but no significant correlation between ϕ_{lim} and any of the other input variables. Therefore, the effects of the variability of φ/ϕ, and D_α on the predictions of slip tendency are likely to be overshadowed by the effects of k_3 and ϕ. Therefore, in an analysis for which the prediction of slip tendency is important, each of the parameters φ/ϕ, and D_α may be assigned a single value, but the effects of variations in the values of k_3 and ϕ need to be considered carefully.

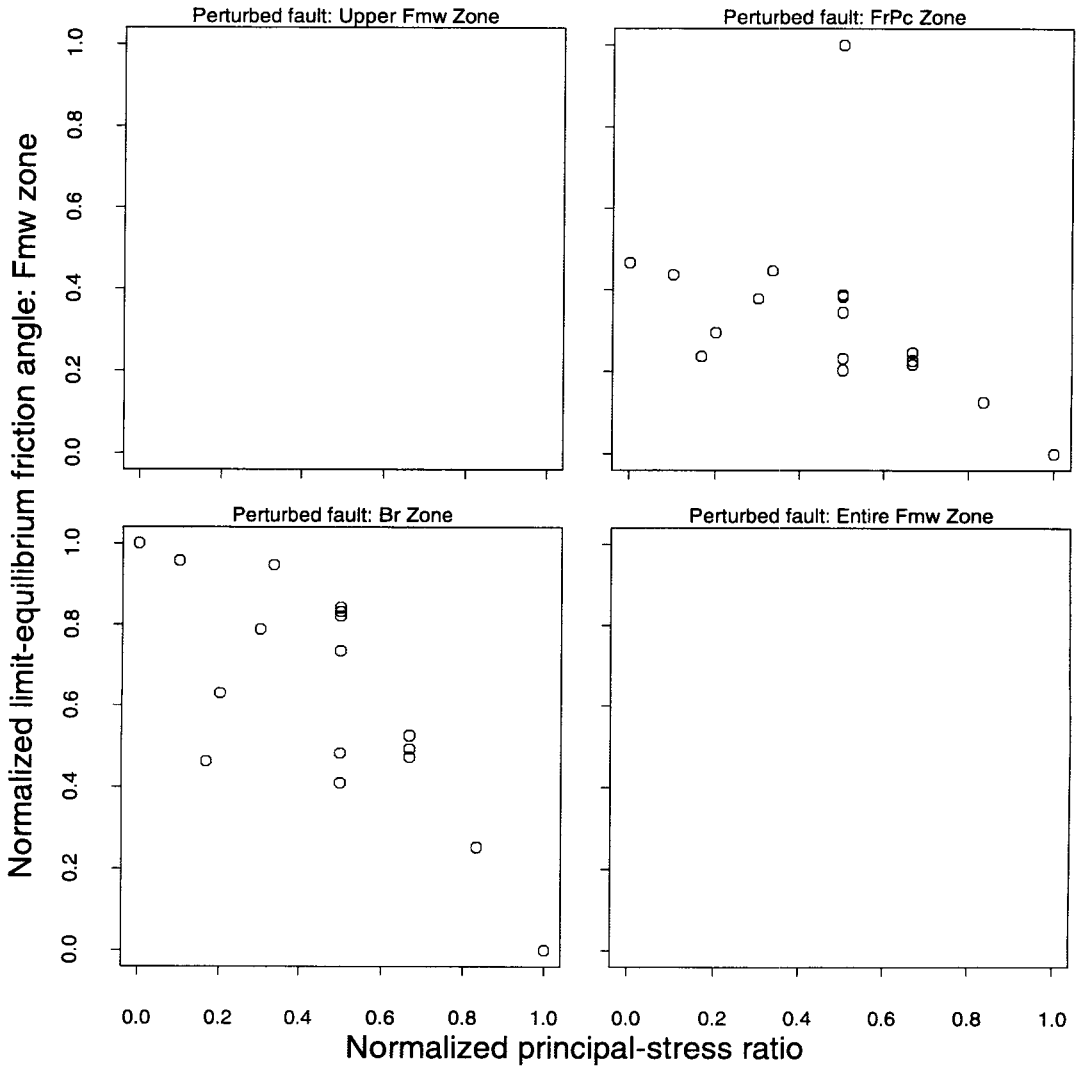

Figure 4-12. Sensitivity of the limit-equilibrium friction angle for the Fmw zone to changes in the value of the principal stress ratio k_3

4.4 SLIP RATE

The history of slip was monitored at the five stations identified in Figure 2-2. Each of the stations is the centroid of a finite element, and their locations were chosen to monitor the rate of slip near the base of the steep part of the Fmw zone (Station Fm168), the base of the FrPc, Br, and Gd zones (Stations Fr635, Br833, and Gd3194, respectively), and the low-angle section of the Fmw zone (Station Fm58). In each case, the slip at the element centroid was calculated as the product $l_t\varepsilon_t$, where l_t and ε_t retain the meanings assigned in Eq. (4-1). The slip rate was calculated through a numerical differentiation of the slip history, using an ABAQUS utility.

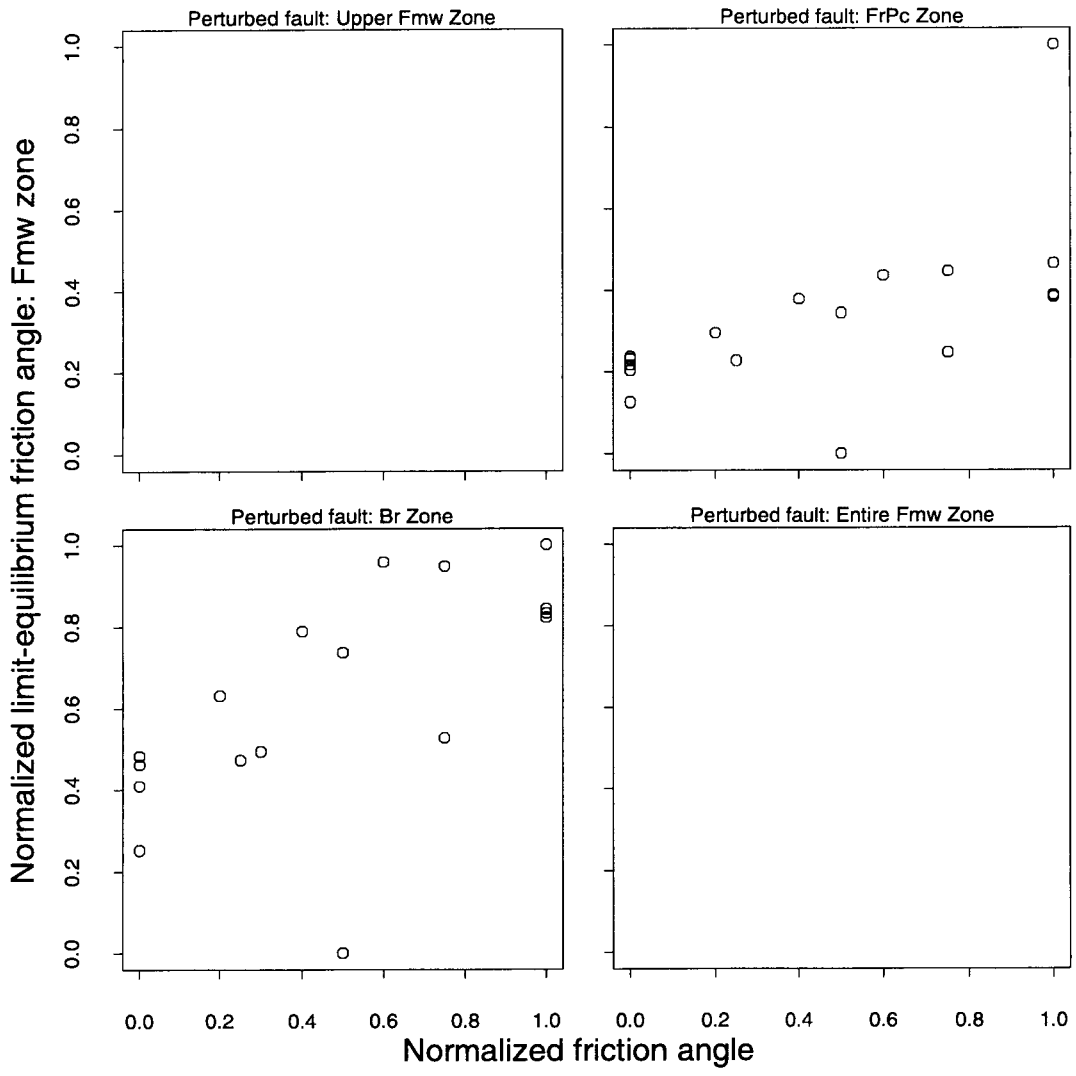

Figure 4-13. Sensitivity of the limit-equilibrium friction angle for the Fmw zone to changes in the value of the applied friction angle

The slip and slip-rate histories for Station Fm168 under simulation Case c52 (with the entire Fmw zone as the perturbed fault) are shown in Figure 4-16 and Figure 4-17. The response shown in the figures is typical of the slip response observed for all cases of slip on a fault induced by a perturbation of the same fault. In all such cases, the slip response consists of an instantaneous rupture at a rate of about 15–35 $m \cdot s^{-1}$, followed by several seconds of movement at relatively slow and progressively decreasing rates. The range of values of slip rate observed for the monitored stations are given in Table 4-4, based on which the following observations are made:

(i) Slip rates in the perturbed fault are generally about three orders of magnitude larger than the induced slip rates. For example, whereas the maximum slip rate at Station Fm168 is 31 $m \cdot s^{-1}$ for cases of Fmw-zone perturbation, it is only 1.1 $cm \cdot s^{-1}$ for cases of slip induced by the perturbation of other faults;

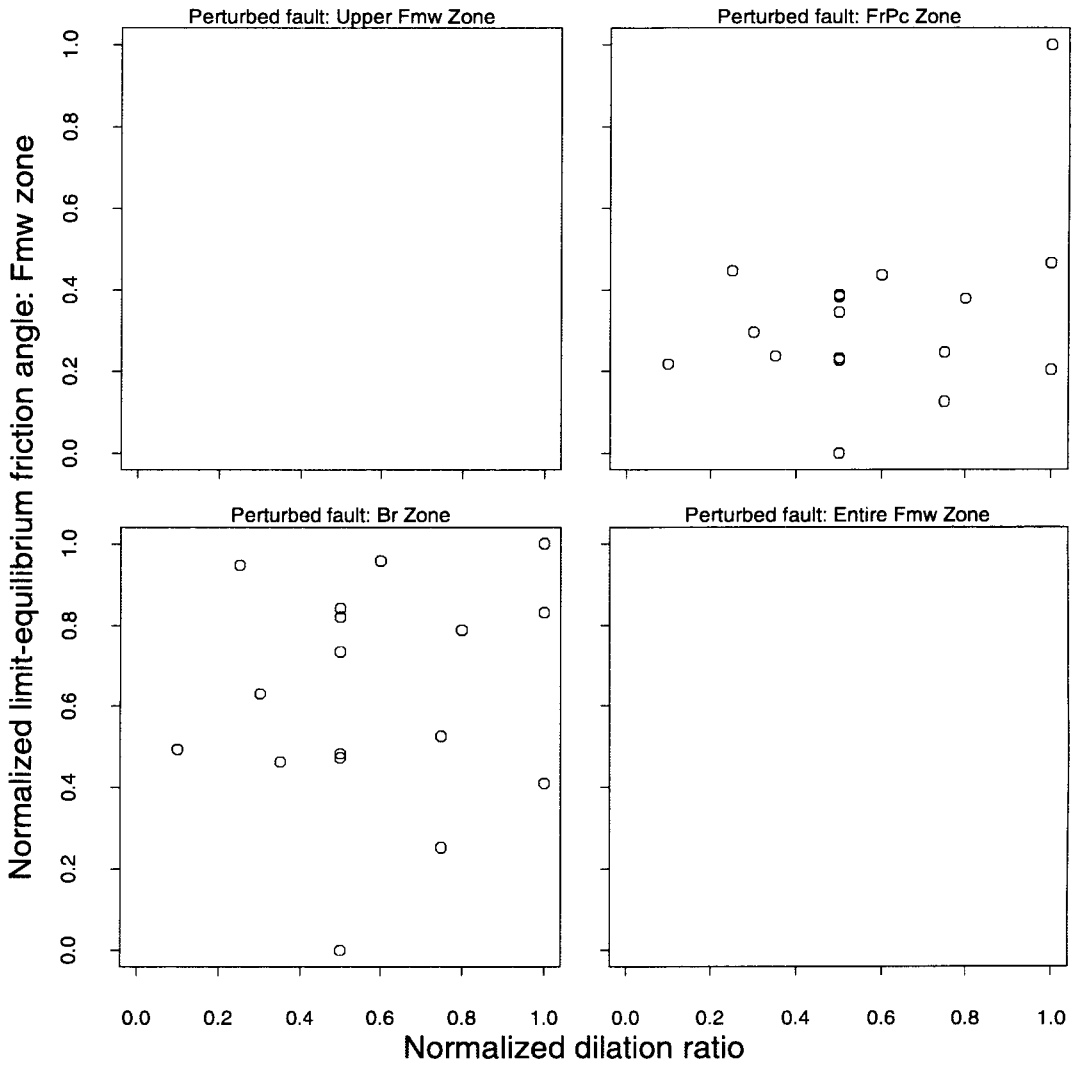

Figure 4-14. Sensitivity of the limit-equilibrium friction angle for the Fmw zone to changes in the value of the dilation angle

(ii) Slip rates induced in the low-angle detachment by the perturbation of the entire Fmw zone are of the same order of magnitude as slip rates in the steep part of the Fmw zone;

(iii) Slip rates induced in the low-angle detachment by the perturbation of any of the steeply dipping faults (i.e., the Br, FrPc, or Upper Fmw zone) is about six orders of magnitude smaller than the slip rates in the perturbed fault.

One possible significance of these observations relates to the classification of lithospheric deformations suggested by Beroza and Jordan (1990), according to which deformational events are classified as seismic or aseismic, depending on the associated rupture velocity. Based on this classification, silent earthquakes are associated with slip rates of 10–100 $m \cdot s^{-1}$, slow earthquakes with 100–1,000 $m \cdot s^{-1}$,

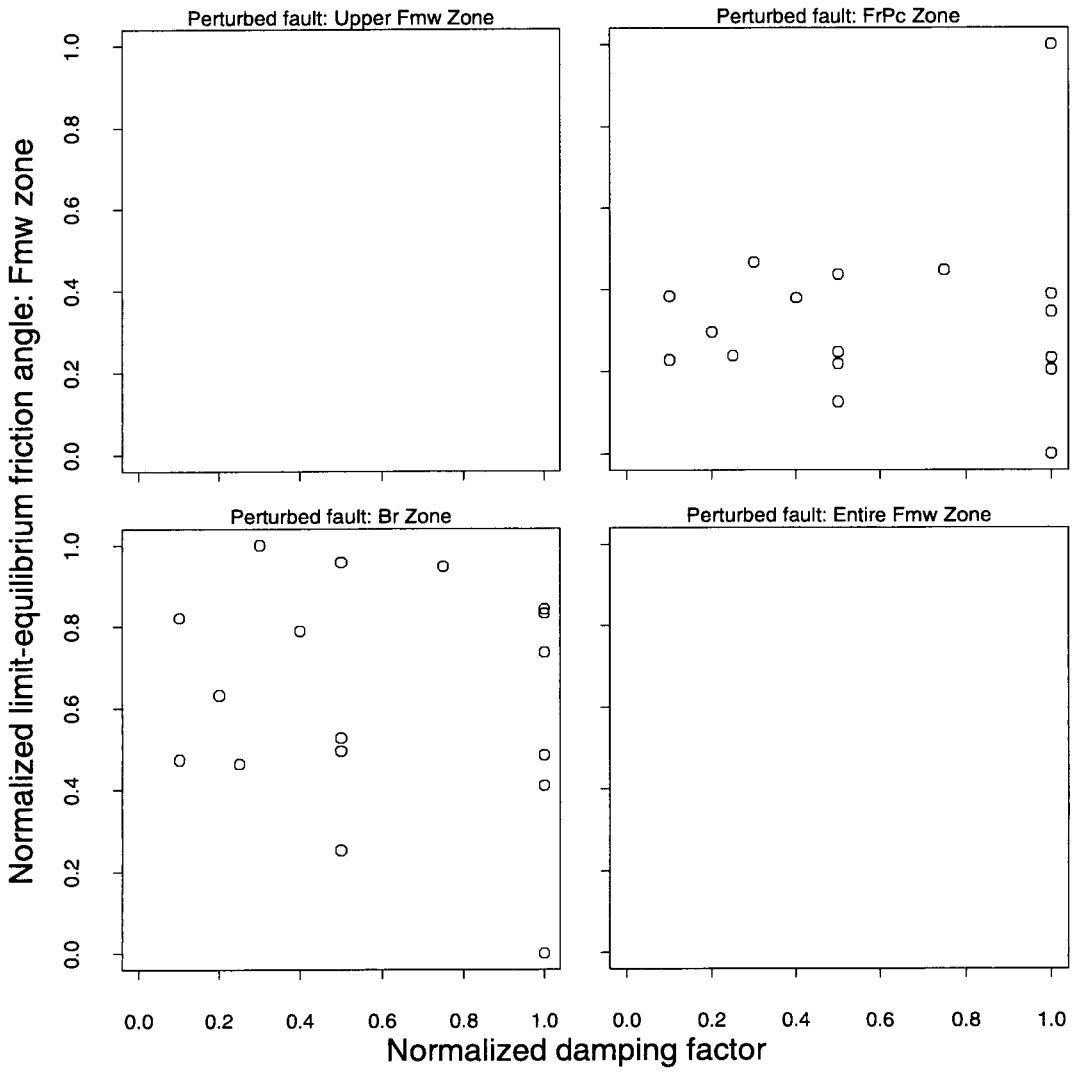

Figure 4-15. Sensitivity of the limit-equilibrium friction angle for the Fmw zone to changes in the value of the damping factor

Table 4-4. Range of values of slip rate ($m.s^{-1}$)

Monitored Station	Perturbed Fault			
	Upper Fmw	FrPc	Br	Entire Fmw
Gd 3194	$0–1.1\times10^{-4}$	$0–3.8\times10^{-4}$	$0–7.1\times10^{-4}$	$0–8.5\times10^{-4}$
Br 833	$0–2.\times10^{-4}$	$0–1.1\times10^{-3}$	$5.22\times10^{-1}–2.06\times10^{1}$	$0–1.6\times10^{-2}$
Fr635	$0–2.\times10^{-4}$	$5.24\times10^{-1}–1.95\times10^{1}$	$0–5.1\times10^{-4}$	$0–1.\times10^{-2}$
Fm168	$5.01\times10^{-1}–3.1\times10^{1}$	$0–5.1\times10^{-4}$	$0–1.1\times10^{-2}$	$4.98\times10^{-1}–3.1\times10^{1}$
Fm58	$0–3.6\times10^{-5}$	$0–5.3\times10^{-5}$	$0–3.\times10^{-4}$	$1.47\times10^{-3}–1.23\times10^{1}$

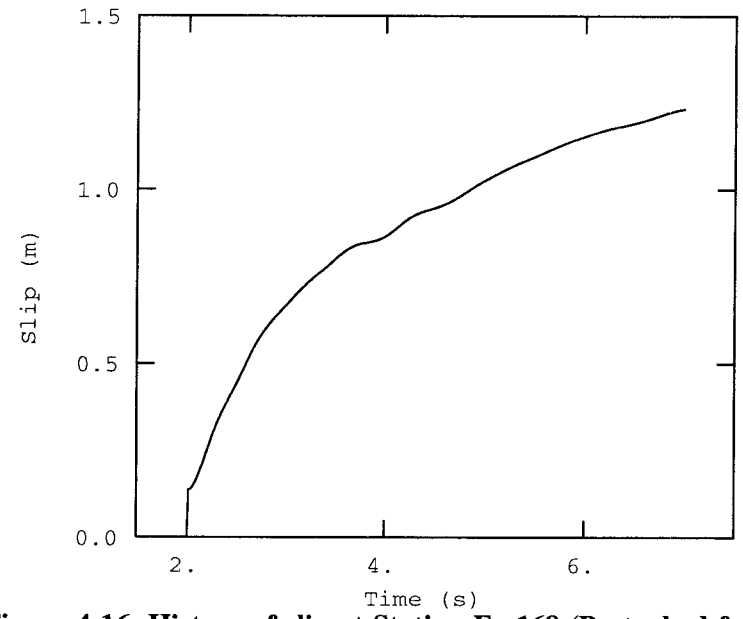

Figure 4-16. History of slip at Station Fm168 (Perturbed fault: Entire Fmw zone; Case c52)

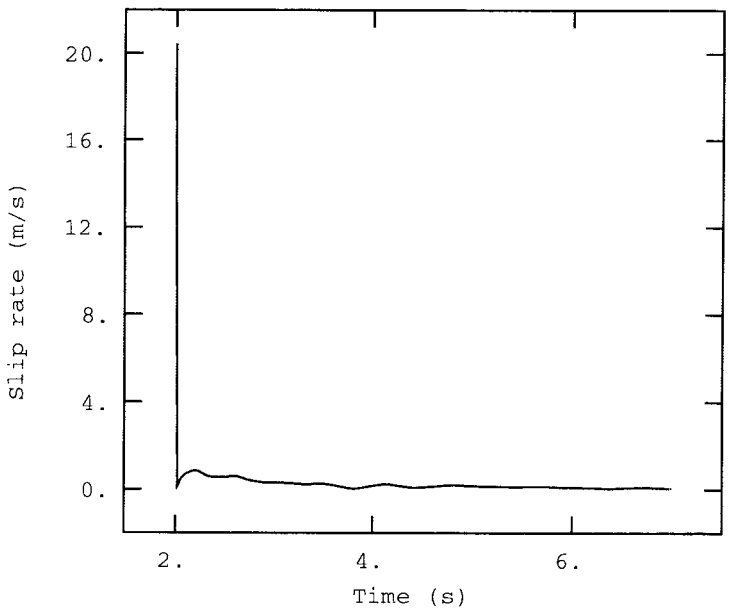

Figure 4-17. History of slip rate at Station Fm168 (Perturbed fault: Entire Fmw zone; Case c52)

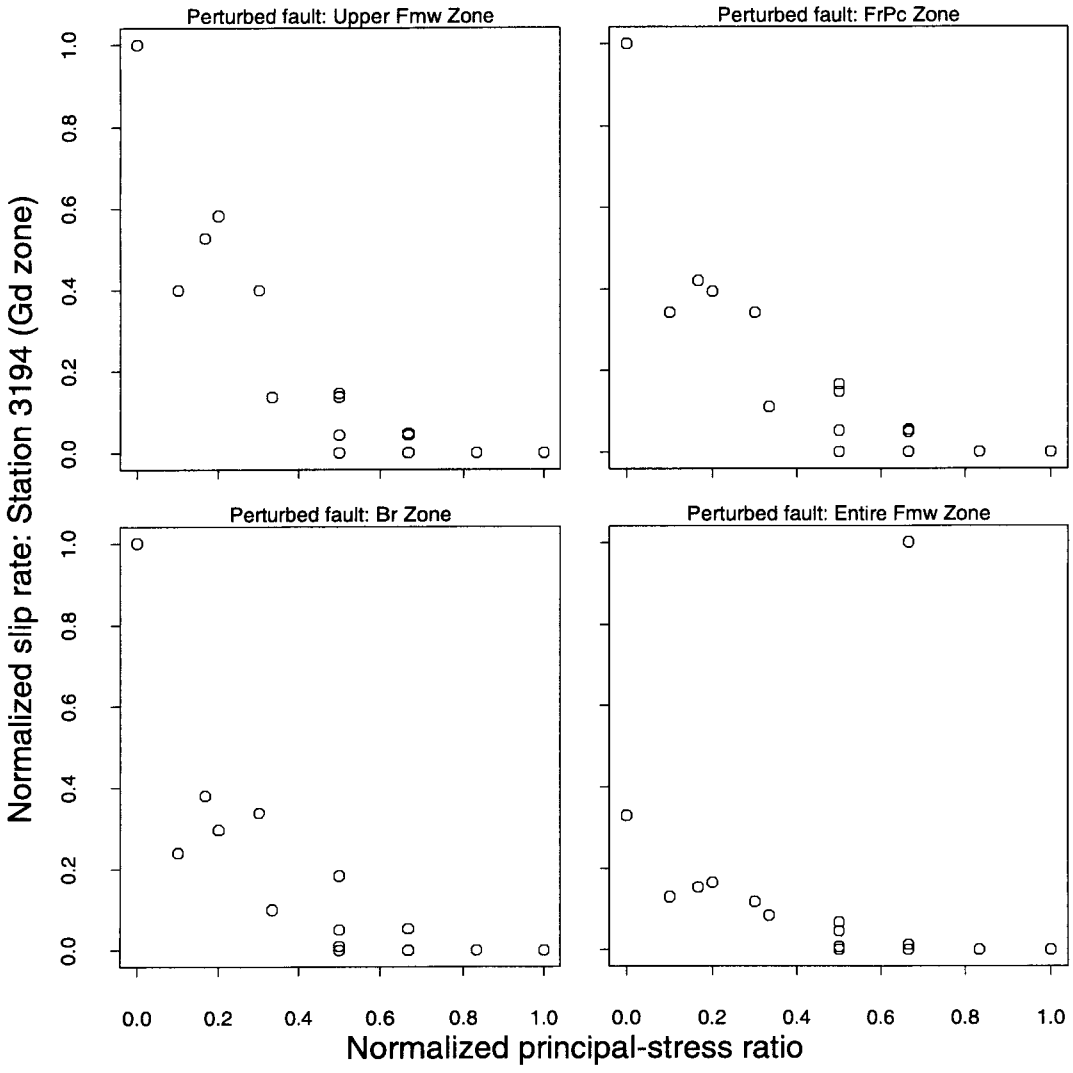

Figure 4-18. Sensitivity of the slip rates at Station Gd3194 to changes in the value of the principal stress ratio k_3

whereas ordinary earthquakes occur at slip rates larger than 1 $km \cdot s^{-1}$. Deformational events associated with smaller slip rates are classified as creep events (slip rates of 1 $cm \cdot s^{-1}$ through 1 $m \cdot s^{-1}$) or strain migration (slip rates less than 1 $cm \cdot s^{-1}$). These values suggest a 1–4 order-of-magnitude difference between the slip rates associated with the slowest seismic events (silent earthquakes) and the fastest aseismic events (creep).

Therefore, the six orders-of-magnitude difference between the slip rates in the low-angle detachment fault and the corresponding rates in the perturbed steeply dipping faults suggests that the low-angle detachment fault is likely to slip aseismically in response to slip events that may occur at seismic rates in the associated steeply dipping faults. The specific values of slip rate calculated in this study were found to vary, depending on the values assigned to the input parameters.

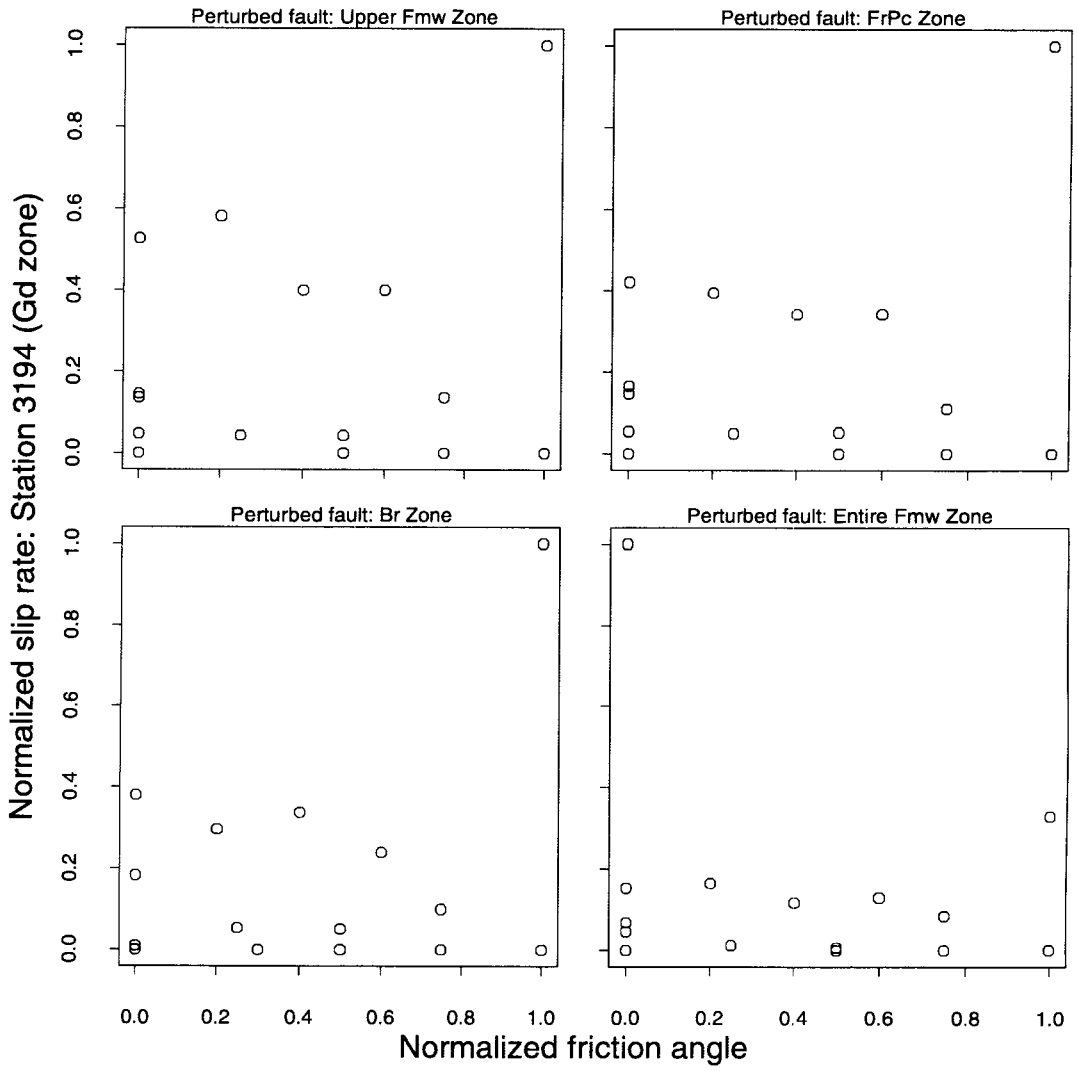

Figure 4-19. Sensitivity of the slip rates at Station Gd3194 to changes in the value of the friction angle

The sensitivity of the slip rates to changes in the values of the input parameters is illustrated in Figure 4-18 through Figure 4-21 for Station Gd3194 (located in the Gd zone). Similar figures are given in Appendix B for the other stations monitored for slip rates. The plots show strong correlation between the induced slip rates (i.e., slip rate on a fault due to the perturbation of another fault) and the principal stress ratio, k_3, but no significant correlation between slip rate and the other input variables. Therefore, the effects of the variability of ϕ, φ/ϕ, and D_α on the predictions of slip rate are likely to be overshadowed by the effects of k_3. Therefore, in an analysis for which the prediction of slip rate is important, each of the parameters ϕ, φ/ϕ, and D_α may be assigned a single value, but the effects of variations in the values of k_3 need to be considered carefully.

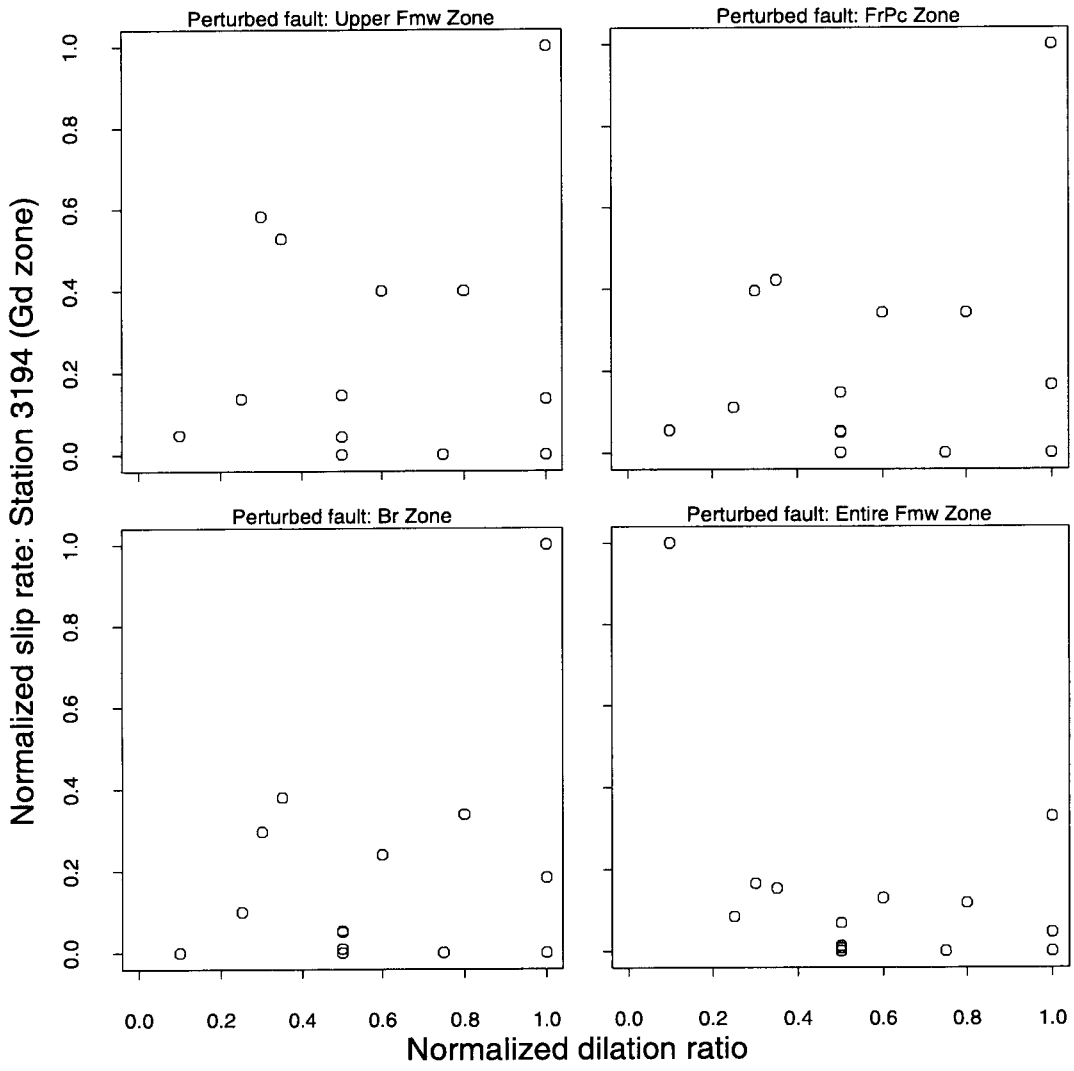

Figure 4-20. Sensitivity of the slip rates at Station Gd3194 to changes in the value of the dilation ratio

4.5 ACCELERATIONS

The values of induced ground acceleration may be calculated using a numerical model, either to predict the magnitudes of acceleration that may be associated with a predetermined slip on a predetermined fault, or to verify the fault geometries obtained from fault-plane solutions of known earthquakes.

In this study, the history of vertical and horizontal accelerations was monitored at the six locations identified in Figure 2-3. Four of the monitoring stations (Stations 2537, 5476, 5597, and 5661) are located on the ground surface, whereas the other two (Stations 5596 and 5662) are located at depths of about 300 m below the ground surface. As Figure 2-2 shows, all the stations are located approximately within the epicentral area of slip events originating from the base of the Br, FrPc, or Upper Fmw zone.

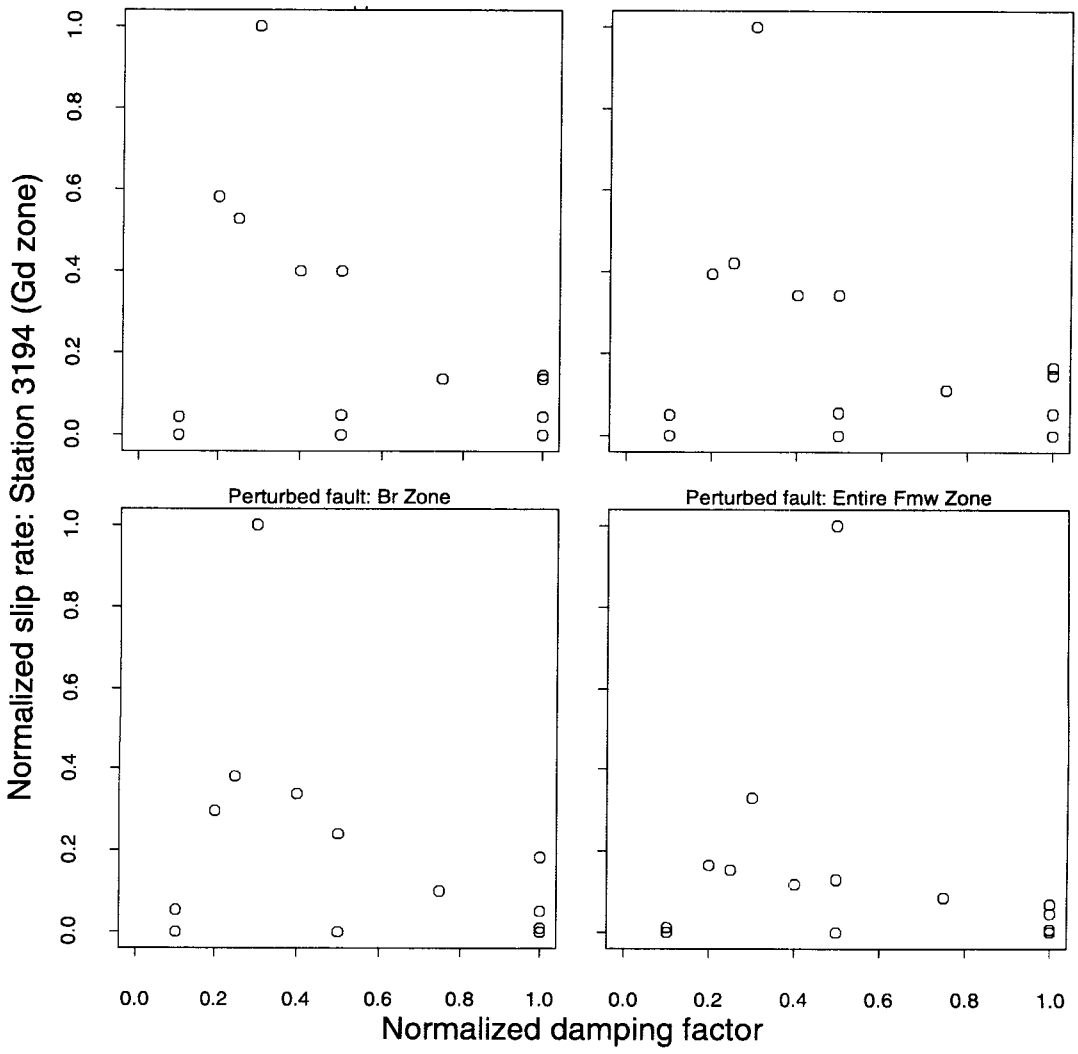

Figure 4-21. Sensitivity of the slip rates at Station Gd3194 to changes in the value of the damping factor

The acceleration history for Stations 2537 and 5661, associated with the perturbation of the entire Fmw zone in Simulation Case c64, are given in Figure 4-22 and Figure 4-23, respectively. The figures show differences in the arrival time, maximum acceleration, and frequency content of the seismic event as recorded at the two stations. The strongest vibrations associated with the event originated from the Upper Fmw zone; as a result, Station 2537 is considered to be closer to the epicentral area than the other station, which would explain the differences in the arrival times and frequency content observed at the two stations. Events originating from the low-angle detachment fault would cause stronger ground motions at Station 5661 than at Station 2537. Therefore, the relatively large magnitude of horizontal acceleration observed at Station 5661 is believed to be caused by the superposition of ground motions originating from the low-angle detachment fault and those originating from the Upper Fmw zone.

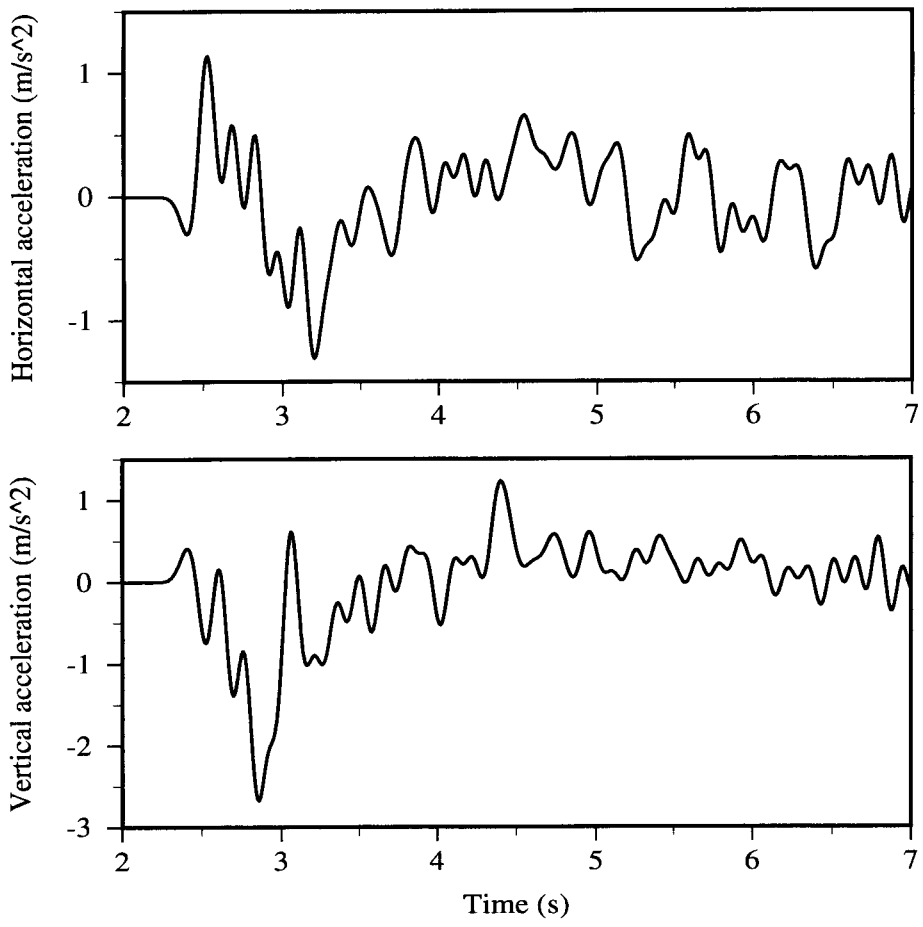

Figure 4-22. Acceleration history at Station 2537, in response to the perturbation of the entire Fmw zone (Case c64)

No attempt was made to determine the earthquake magnitudes implied by the modeled slip events [using Wells and Coppersmith, (1994), for example], which would lead to a comparison of the calculated accelerations with those implied by empirical equations such as Campbell (1987). The slip events were not converted to earthquake magnitudes for the following reasons:

(i) The distribution of forces that corresponds to the applied friction-angle reduction is not known;

(ii) As Figure 4-2 and Figure 4-3 show, the distribution of slip on the faults is nonuniform; furthermore, as Figure 4-16 and Figure 4-17 show, each slip event consisted of a short period of high slip rate followed by a much longer period of low-rate (probably aseismic) slip. Therefore, it is not yet clear how much of the calculated slip length should be used for earthquake-magnitude calculation;

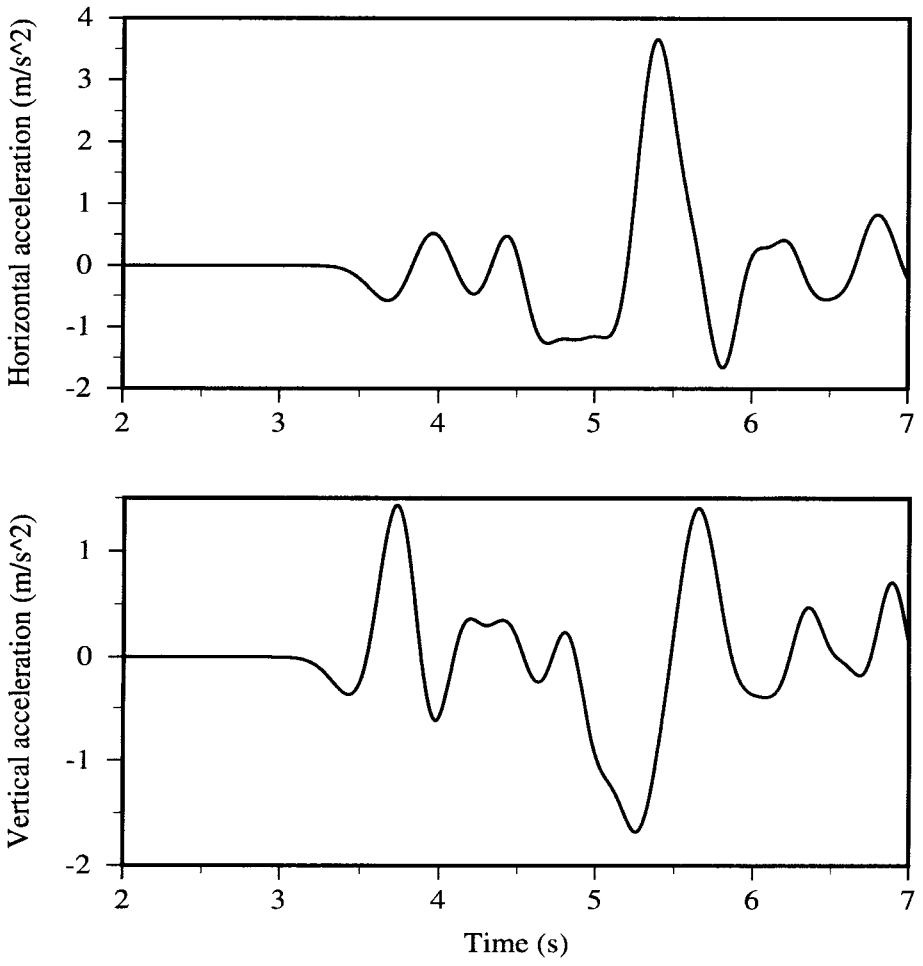

Figure 4-23. Acceleration history at Station 5661, in response to the perturbation of the entire Fmw zone (Case c64)

(iii) The absolute magnitude of calculated ground accelerations is really not a concern for the current study, which is focused on determining how the input parameters affect the prediction of ground acceleration.

The calculated range of values of maximum vertical and horizontal accelerations are given in Table 4-5 and Table 4-6, respectively, based on which the following observations are made:

(i) The perturbation of the entire Fmw zone or the Upper Fmw zone caused larger ground motions at the monitoring stations than the perturbation of the Br or FrPc zone;

(ii) A difference of up to 1 $m \cdot s^{-2}$ was observed between the magnitudes of acceleration at a location on the ground surface and at a depth of about 300 m below the same location.

Table 4-5. Range of values of maximum vertical acceleration ($m \cdot s^{-2}$)

Monitored Station	Perturbed Fault			
	Upper Fmw	FrPc	Br	Entire Fmw
2537	0.85–2.7	0.45–1.3	0.15–0.55	0.85–2.8
5476	0.55–3.4	0.71–2.2	0.4–1.4	0.61–3.5
5596	0.46–3.2	0.68–2.7	0.72–2.2	0.53–3.7
5597	0.44–2.3	0.66–2.2	0.64–1.8	0.44–2.8
5661	0.45–1.9	0.67–2.6	0.7–2.1	0.45–2.3
5662	0.38–1.5	0.58–2	0.49–1.7	0.34–1.3

Table 4-6. Range of values of maximum horizontal acceleration ($m \cdot s^{-2}$)

Monitored Station	Perturbed Fault			
	Upper Fmw	FrPc	Br	Entire Fmw
2537	0.38–1.7	0.52–1.4	0.096–0.51	0.38–1.6
5476	0.38–2.1	0.3–1.4	0.31–1	0.38–2.3
5596	0.2–1.5	0.39–1.6	0.32–1.3	0.41–3.1
5597	0.24–2.2	0.24–1.2	0.21–0.83	0.42–3.9
5661	0.21–1.6	0.42–1.9	0.45–1.4	0.47–3.8
5662	0.21–1.5	0.26–1.4	0.34–1.1	0.63–3.5

The sensitivity of the predicted magnitudes of ground acceleration to changes in the values of the input parameters is illustrated in Figure 4-24 through Figure 4-27 for the vertical acceleration at Station 2537. Similar figures are given in Appendix B for the other monitored accelerations. The plots show a strong correlation between the ground acceleration and damping factor D_α, but no significant correlation between it and the other input variables. Therefore, the effects of the variability of k_3, ϕ, and φ/ϕ, on the predictions of ground acceleration are likely to be overshadowed by the effects of D_α. Thus, in an analysis for which the prediction of ground acceleration is important, each of the parameters k_3, ϕ, and φ/ϕ, may be assigned a single value, but the effects of variations in the values of D_α need to be considered carefully.

4.6 STRESS DISTRIBUTIONS IN THE STUDY ZONE

The area identified as the study zone in Figure 2-1 through Figure 2-3 contains several steeply dipping planar discontinuities (cf. Figure 1-1) that were not explicitly included in the model. Therefore, the stress conditions within the study zone were processed to determine if such stresses would cause slip to occur on such planar discontinuities. Three sets of discontinuities, dipping at 65°, 75°, and 80°, west, were selected. The values of limit-equilibrium friction angle, ϕ_{lim}, for the discontinuities were calculated using the procedure described in Eq. (4-3) through Eq. (4-5). Their calculation was implemented in ABAQUS through its user-variable-subroutine interface, which ensured that the calculated distributions of ϕ_{lim} can be contoured using ABAQUS, like any of the other variables calculated by the code.

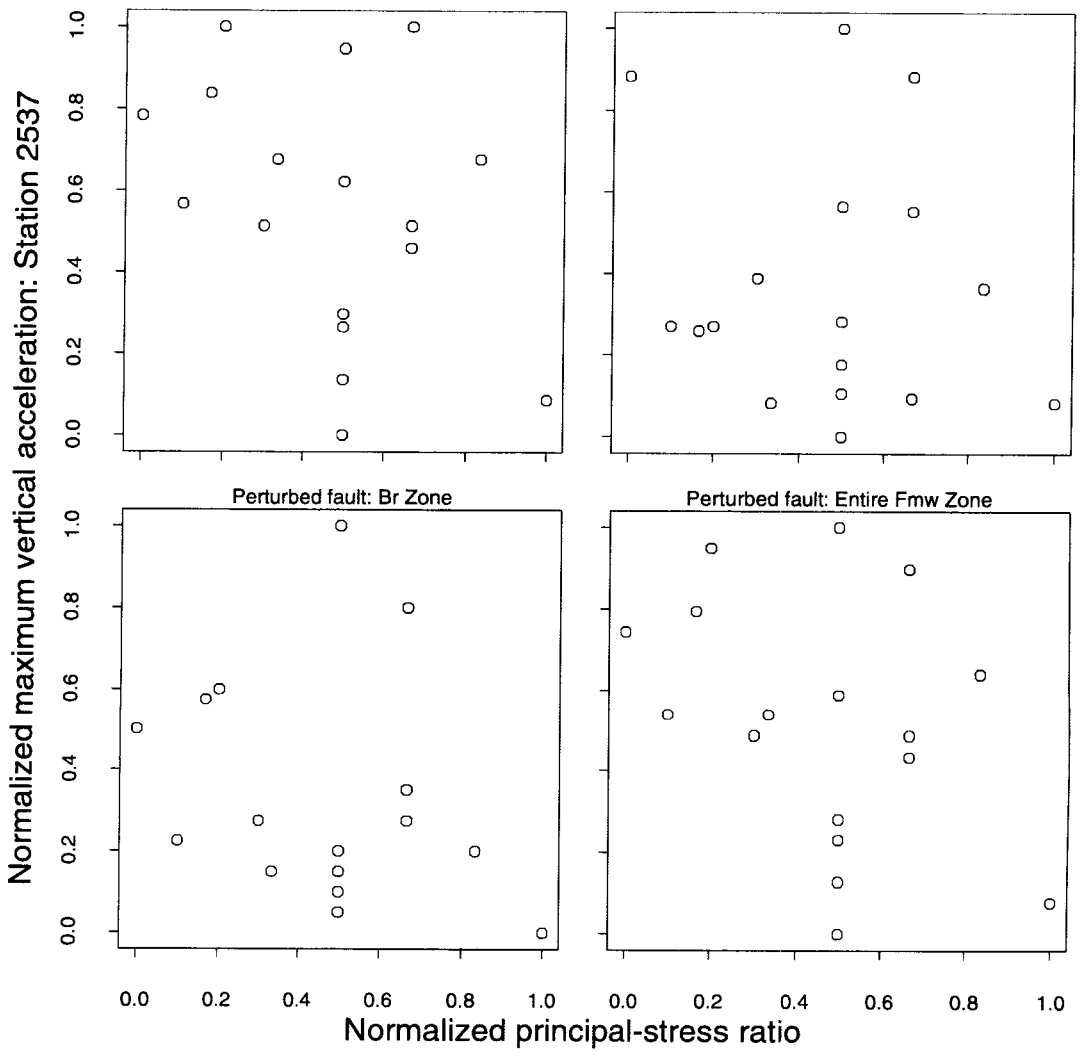

Figure 4-24. Sensitivity of the vertical acceleration at Station 2537 to changes in the value of the principal stress ratio k_3

The distributions of ϕ_{lim} are given in Figure 4-28 through Figure 4-30, which show the sections of the study zone within which the value of ϕ_{lim} is smaller than 30°, between 30° and 40°, or larger than 40°. The names UVARM1, UVARM2, and UVARM3 in the figures refer to ϕ_{lim} for the 65°-, 75°-, and 80°-dipping planes, respectively. The zone within which $\phi_{lim} \geq 40°$ represents the potentially unstable zone, based on the consideration of the slip tendency for planar features having a friction angle of 40°. Similarly, the $\phi_{lim} \geq 30°$ zone represents the potentially unstable zone, considering planar structures with values of friction angle of 30°. The distributions of vertical and horizontal stresses corresponding to the ϕ_{lim}-distributions in these figures are given in Figure 4-31 and Figure 4-32, respectively.

The nature and amount of departure of the stress contours from horizontal (compare with Figure 3-1 and Figure 3-2) is related to the nature and magnitude of the stress change (relative to the initial state) represented by the stress distributions. As Figure 4-31 and Figure 4-32 show, the magnitude of vertical compressive stress increased, whereas the horizontal one decreased, in the area of the study zone

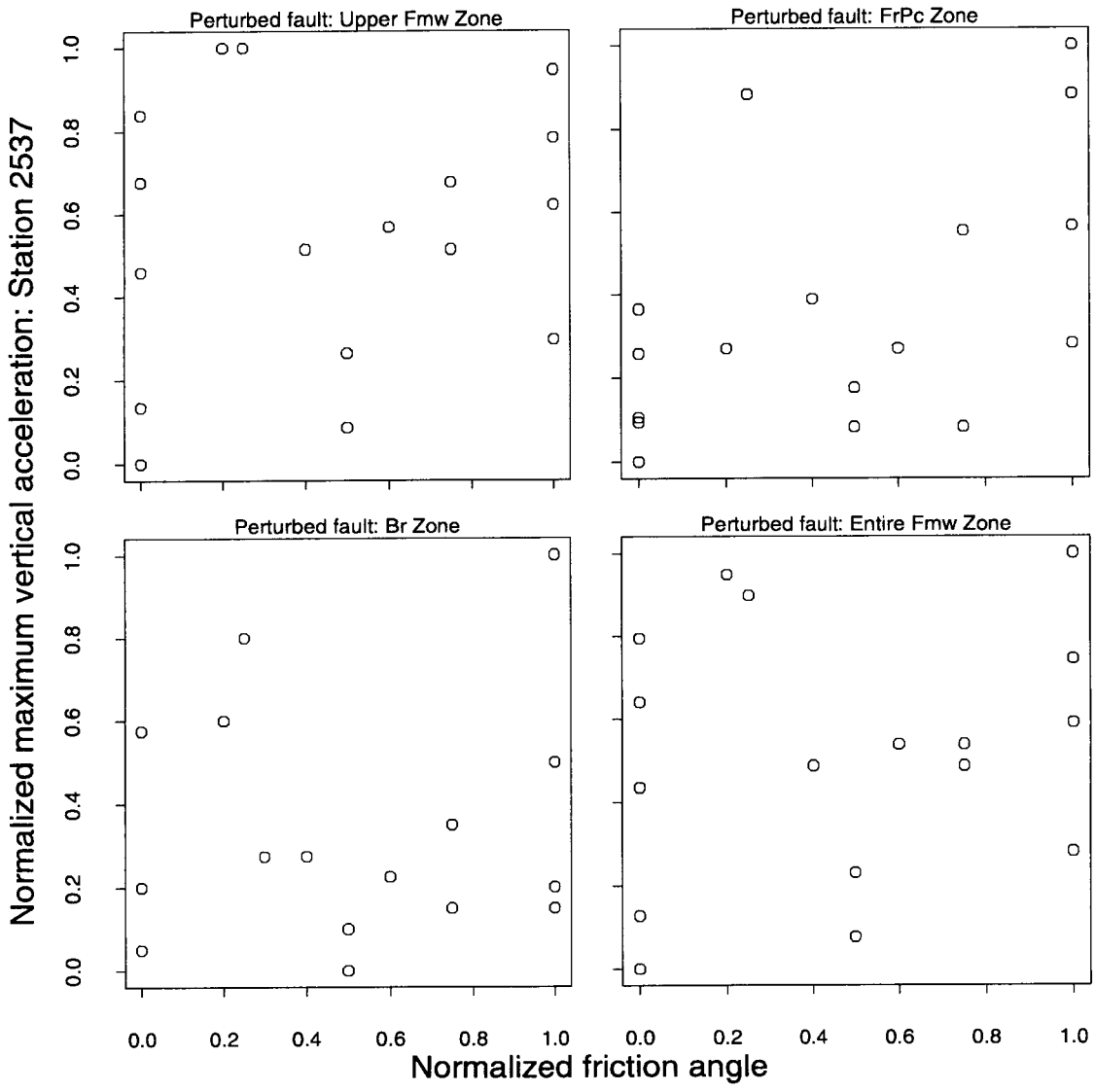

Figure 4-25. Sensitivity of the vertical acceleration at Station 2537 to changes in the value of the friction angle

west of the Gd fault zone, which corresponds with the zone of potential instability identified in Figure 4-28 through Figure 4-30.

The spread of potential instability in the study zone was measured in terms of the area of the $\phi_{lim} \geq 30^{\circ}$ zone (representing the case of planar discontinuities that have friction angle of 30°), and the area of the $\phi_{lim} \geq 40^{\circ}$ zone, which represents the case of 40° friction angle for the discontinuities. The range of values of these areas is given in Table 4-7, based on which the following observations are made:

(i) The spread of potential instability caused by the perturbation of the Fmw zone is much larger than that caused by the perturbation of the Br or FrPc zones.

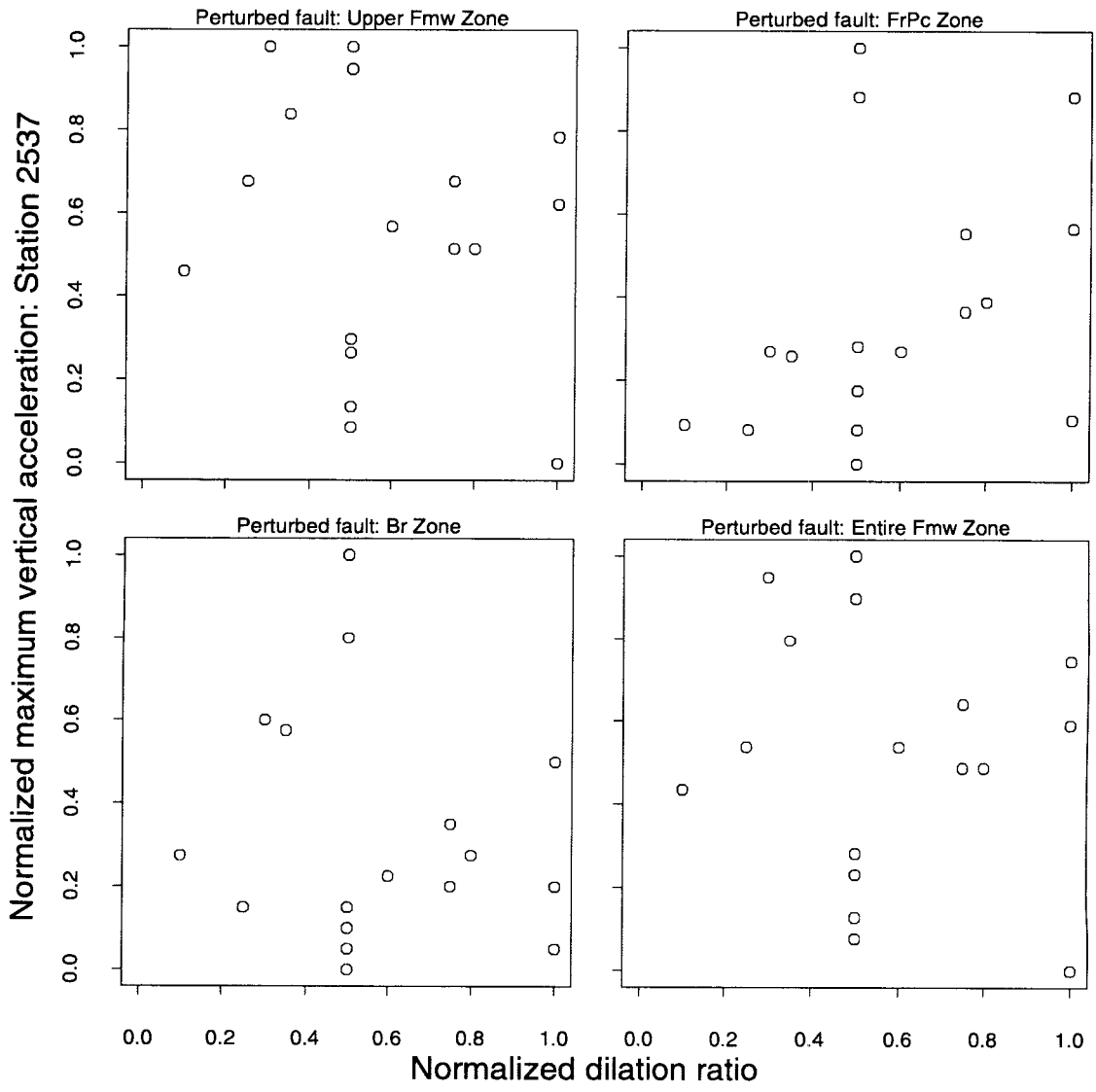

Figure 4-26. Sensitivity of the vertical acceleration at Station 2537 to changes in the value of the dilation ratio

(ii) For planar discontinuities dipping more than 60°, the area of potential instability due to slip on the planes decreases as the magnitude of dip increases. This case only occurs when the principal stresses are vertical and horizontal, and instability is related to slip alone. The magnitude of shear stress on the planes approaches zero as the dip approaches 90° [cf. Eq. (4-3) and Eq. (4-5)]; near-vertical planes under such stress state are more likely to open than they are to slip.

The sensitivity of the area of potential instability to changes in the values of the input parameters is illustrated in Figure 4-33 through Figure 4-36, based on the consideration of the slip

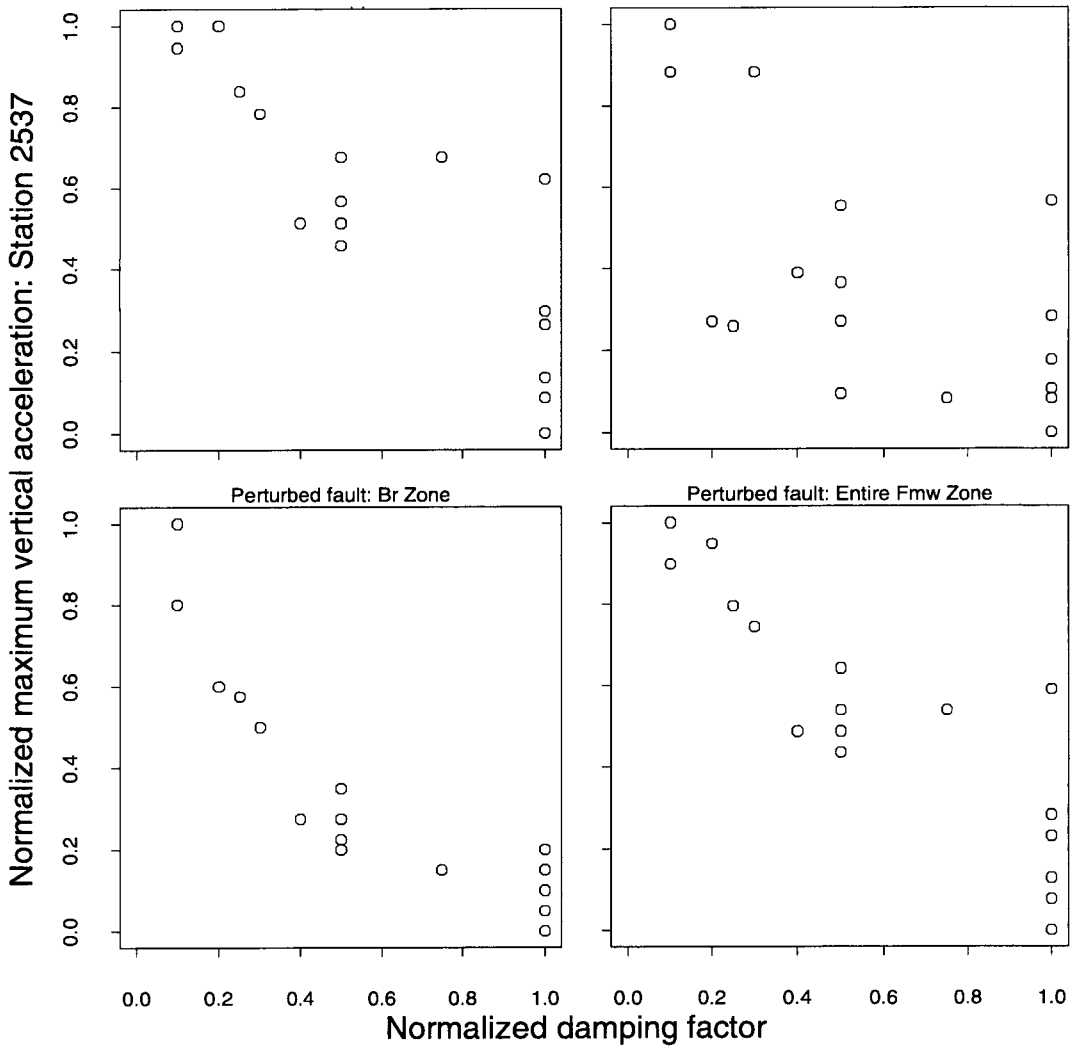

Figure 4-27. Sensitivity of the vertical acceleration at Station 2537 to changes in the value of the damping factor

tendency on 65° W-dipping planes that have a value of friction angle of 30°. Similar figures are given in Appendix B for the results based on the consideration of other values of dip angle, Ψ, and friction angle, ϕ, for the planar discontinuities. The plots show strong correlation between the area of instability and the principal stress ratio; on the other hand, there is no significant correlation between the area and any of the other input variables. Therefore, the effects of the variability of the values of friction angle, dilation angle and damping factor (for the rock mass) on the predictions of the spread of instability due to slip on specific planar features, are likely to be overshadowed by the effects of the principal stress ratio. Therefore, in an analysis for which the prediction of slip tendency of specific planar features is important, the friction angle, dilation angle, and damping factor for the rock mass may each be assigned a single value. On the other hand, a range of values of slip tendency should be calculated for the accepted range of values of the principal stress ratio.

Figure 4-28. Distribution of potential instability within the study zone, based on the slip tendency on 65° W-dipping planar discontinuities (Case c61)

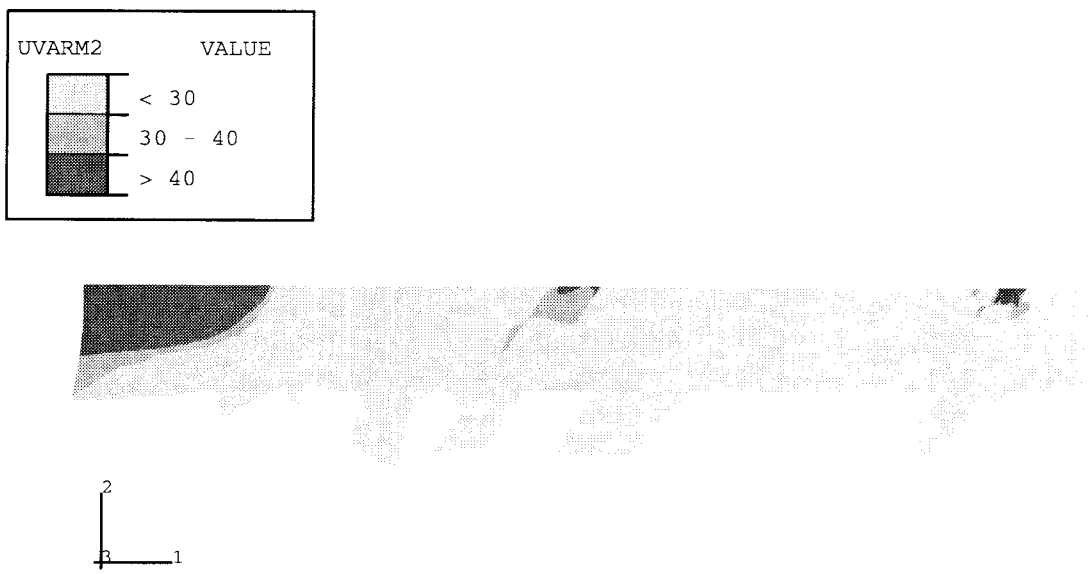

Figure 4-29. Distribution of potential instability within the study zone, based on the slip tendency on 75° W-dipping planar discontinuities (Case c61)

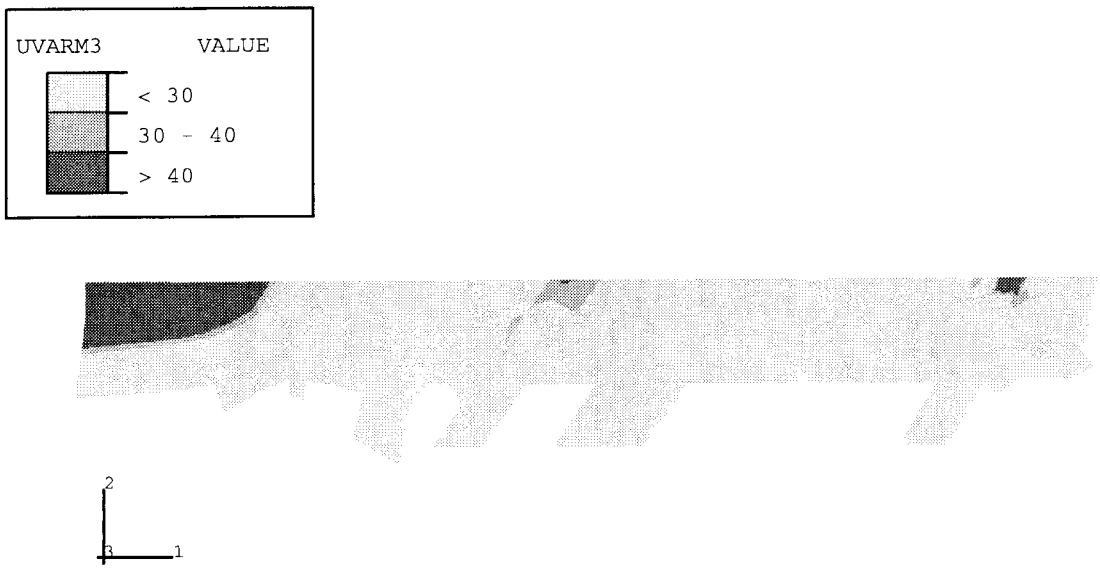

Figure 4-30. Distribution of potential instability within the study zone, based on the slip tendency on 80° W-dipping planar discontinuities (Case c61)

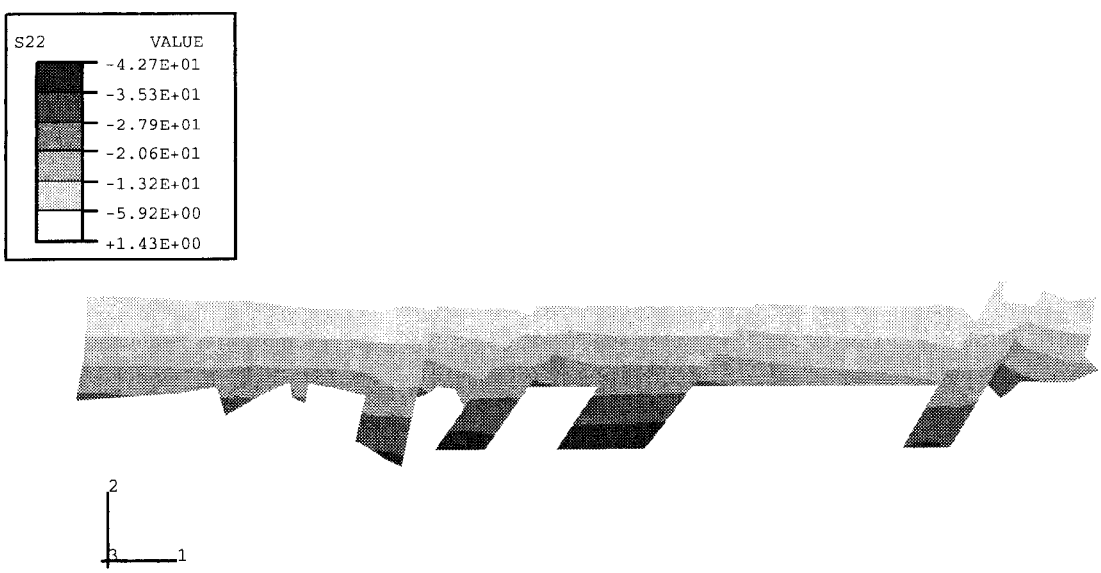

Figure 4-31. Distribution of vertical stress within the study zone: end of simulation (Case c61)

Figure 4-32. Distribution of horizontal stress within the study zone: end of simulation (Case c61)

Table 4-7. Range of values of the area of potential instability (m^2), based on the slip tendency for selected planar discontinuities that have friction angles of 30° or 40°

Monitored Fault		Perturbed Fault			
Friction	**Dip**	**Upper Fmw**	**FrPc**	**Br**	**Entire Fmw**
30	65	7.13×10^5–7.1×10^6	4.43×10^5–4.3×10^6	2.23×10^5–3.22×10^6	1.01×10^6–7.49×10^6
30	75	4.15×10^5–3.99×10^6	2.14×10^5–2.65×10^6	1.81×10^5–1.84×10^6	3.55×10^5–3.19×10^6
30	80	1.28×10^5–2.33×10^6	3.89×10^4–1.84×10^6	1.61×10^5–1.4×10^6	1.28×10^5–1.69×10^6
40	65	7.56×10^4–2.04×10^6	3.89×10^4–1.78×10^6	4.48×10^4–1.36×10	1.43×10^5–1.78×10^6
40	75	6.01×10^4–1.52×10^6	0–1.74×10^6	3.42×10^4–1.07×10	6.01×10^4–1.57×10^6
40	80	6.01×10^4–1.25×10^6	0–9.55×10^5	0–8.07×10^5	6.01×10^4–1.36×10^6

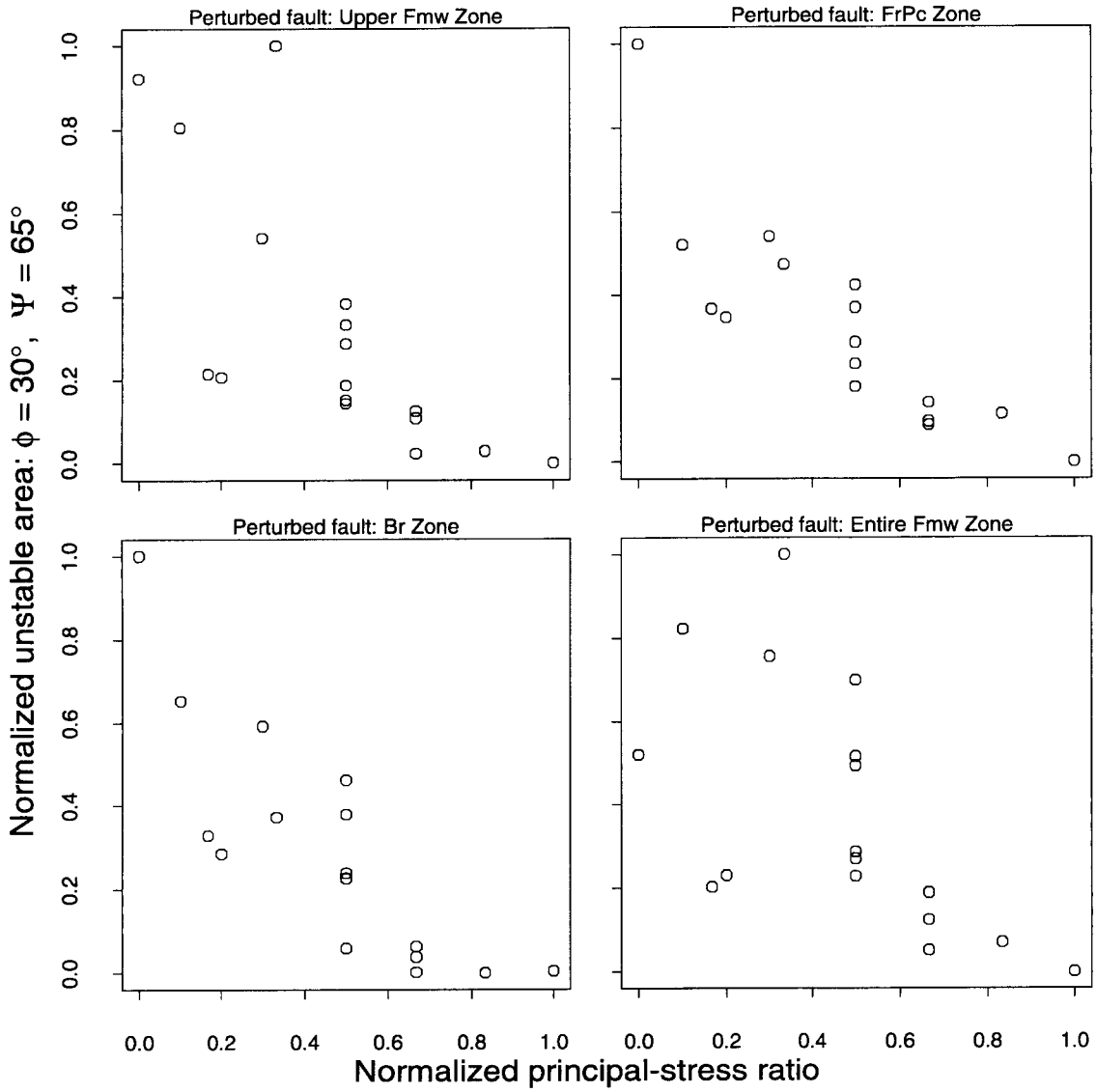

Figure 4-33. Sensitivity of the area of potential instability to changes in the value of the principal stress ratio k_3, based on slip on 65° W-dipping planes with 30°-friction angle

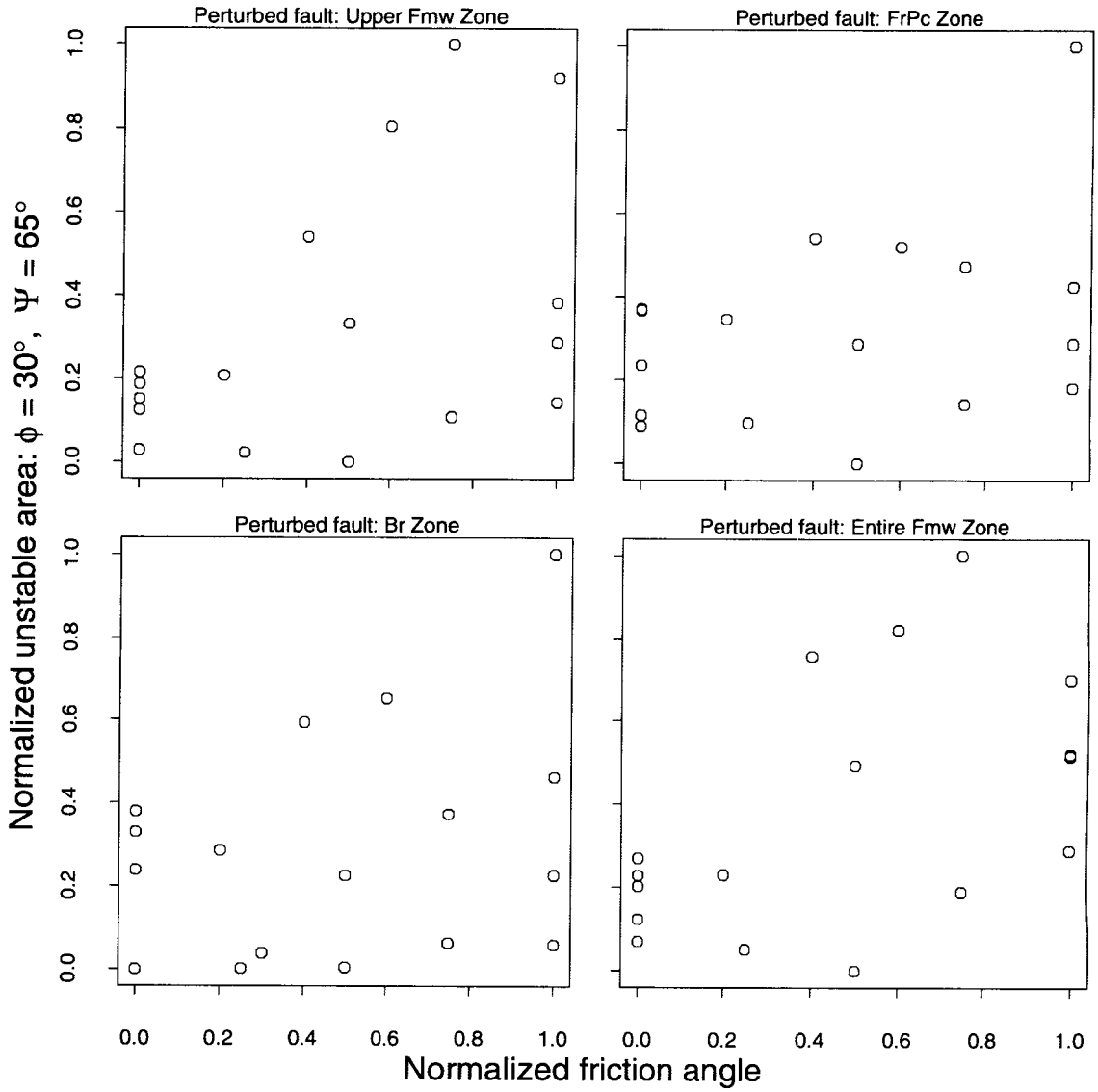

Figure 4-34. Sensitivity of the area of potential instability to changes in the value of the rock-mass friction angle, based on slip on 65° W-dipping planes with 30°-friction angle

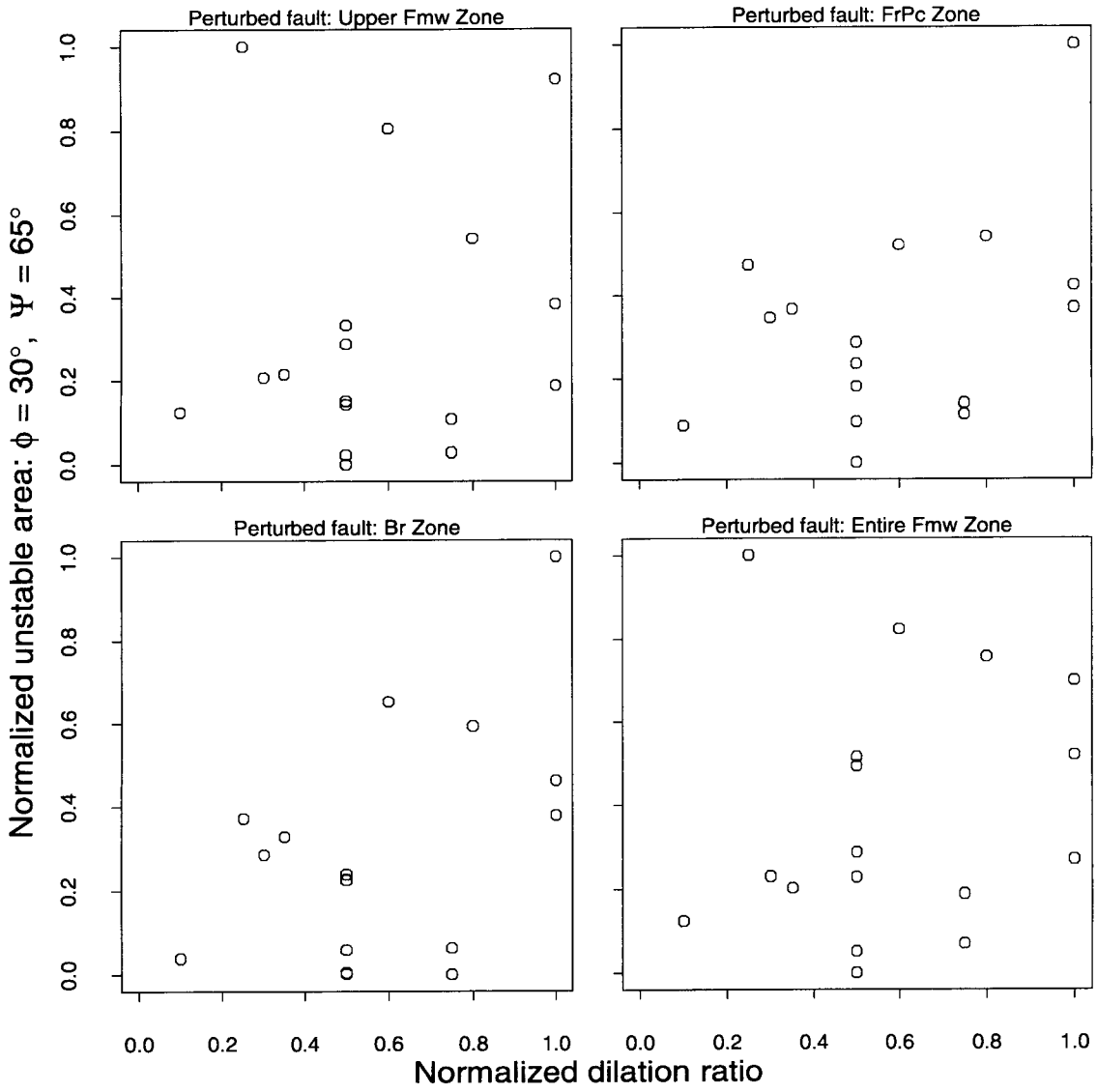

Figure 4-35. Sensitivity of the area of potential instability to changes in the value of the dilation angle, based on slip on 65° W-dipping planes with 30°-friction angle

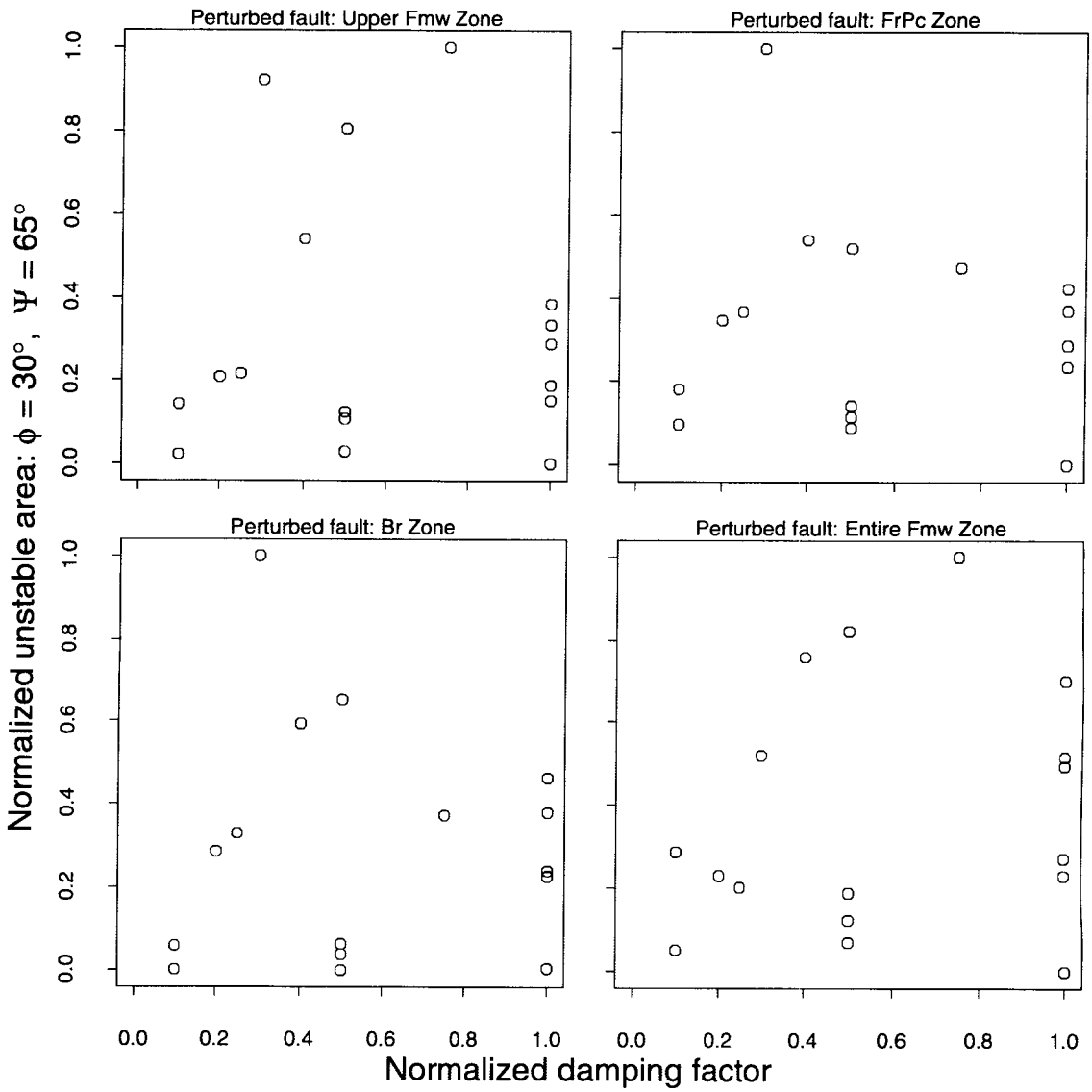

Figure 4-36. Sensitivity of the area of potential instability to changes in the value of the damping factor, based on slip on 65° W-dipping planes with 30°-friction angle

5 CONCLUSIONS

The nature of hangingwall deformations associated with listric faulting was investigated through a series of two-dimensional finite element analyses. The investigations focused on the effects of *in situ* stress and material parameters (such as friction angle, dilation angle, and damping factor) on the predicted hangingwall deformation. The hangingwall response was measured in terms of variables such as fault displacement, slip length, slip rate, ground acceleration, and the area of the zone of potential instability based on the slip tendency for selected planar features. The results, summarized in Table 5-1, show a strong correlation between the response variables (except ground acceleration) and the *in situ* stress ratio k_3 ($= \sigma_3/\sigma_1$); also, a strong correlation was found between ground acceleration and material damping. No significant correlation was found between the response variables and either the friction angle or dilation angle. The following conclusions were drawn based on an examination of these results:

- The values of *in situ* stress used in the analyses of hangingwall deformations deserve particular attention. For the case of Yucca Mountain, Nevada, these results indicate a strong need for additional *in situ* stress measurements, preferably at depths below the zone of influence of ground-surface topography.

- For analyses in which values of ground acceleration are important, it is necessary to constrain damping as much as possible, and then to evaluate the range of accelerations for the range of accepted values of the material damping factor.

- Slip on the interpreted Fortymile Wash Fault has greater impact on deformation than does slip on other faults. This difference in associated deformation is likely to be due to the more broadly curved shape of the Fortymile Wash Fault when compared to the abrupt dip change of the other faults where they intersect with the low-angle detachment.

- Low-angle segments of the modeled listric fault system slipped in the models. However, they slipped at slower rates than the high-angle fault segments (e.g., Figure 5-1). Differences between strain rates for high-angle and low-angle fault segments may explain the lack of seismicity associated with low angle faults. Slip on low angle faults may occur at aseismic rates and either precede or postdate seismic slip on high-angle fault segments.

- The best approach to modeling listric faults contained entirely in brittle crust is to represent each fault zone as a thin deformable solid. When modeling a listric fault in brittle material over ductile material, another approach such as the block-on-block model (with contact elements) may be more appropriate; for such a situation long-term viscous flow in the ductile zone may cause sufficient frictional drag at the base of the brittle layer to initiate fault slip.

- In future 3D models of faulting, critical modeling parameters will be the *in situ* stress, 3D fault geometry, and the material damping factor. Results from varying the material damping factor can be tested against measurements of ground accelerations associated with the Little Skull Mountain earthquake sequence.

Table 5-1. Summary of the sensitivity of the response variables to changes in the values of the input parameters

Response Variables	Sensitivity to Input-Parameter Variability, Under Perturbed Fault Upper Fmw (1), FrPc (2), Br (3), or Entire Fmw (4): • Indicates Strong Correlation															
	k_3				ϕ				φ/ϕ				D_α			
	1	2	3	4	1	2	3	4	1	2	3	4	1	2	3	4
fmdisp	•	•	•	•												
frdisp		•														
brdisp	•		•	•												
gddisp	•			•					•			•	•			•
fmsl	•	•	•	•												
frsl																
brsl	•			•								•				
gdsl	•			•					•			•	•			•
fmlf		•	•			•	•									
frlf	•		•	•	•		•	•								
brlf	•	•		•	•	•		•								
gdlf	•	•	•	•												
sr3194	•	•	•	•												
sr833	•	•	•													
sr635	•	•	•													
sr168			•													
sr58	•	•	•	•												
av2537													•	•	•	•
av5476													•	•	•	•
av5596													•	•	•	•
av5597													•	•	•	•
av5661													•	•	•	•

Table 5-1. Summary of the sensitivity of the response variables to changes in the values of the input parameters (cont'd)

Response Variables	Sensitivity to Input-Parameter Variability, Under Perturbed Fault Upper Fmw (1), FrPc (2), Br (3), or Entire Fmw (4): • Indicates Strong Correlation															
	k_3				ϕ				φ/ϕ				D_α			
	1	2	3	4	1	2	3	4	1	2	3	4	1	2	3	4
av5662													•	•	•	•
ah2537													•	•	•	•
ah5476													•	•	•	•
ah5596													•	•	•	•
ah5597													•	•	•	•
ah5661													•	•	•	•
ah5662													•	•	•	•
ap3065	•	•	•	•												
ap3075	•	•	•	•												
ap3080	•	•	•	•												
ap4065	•	•	•	•												
ap4075	•	•	•	•												
ap4080	•	•	•	•												

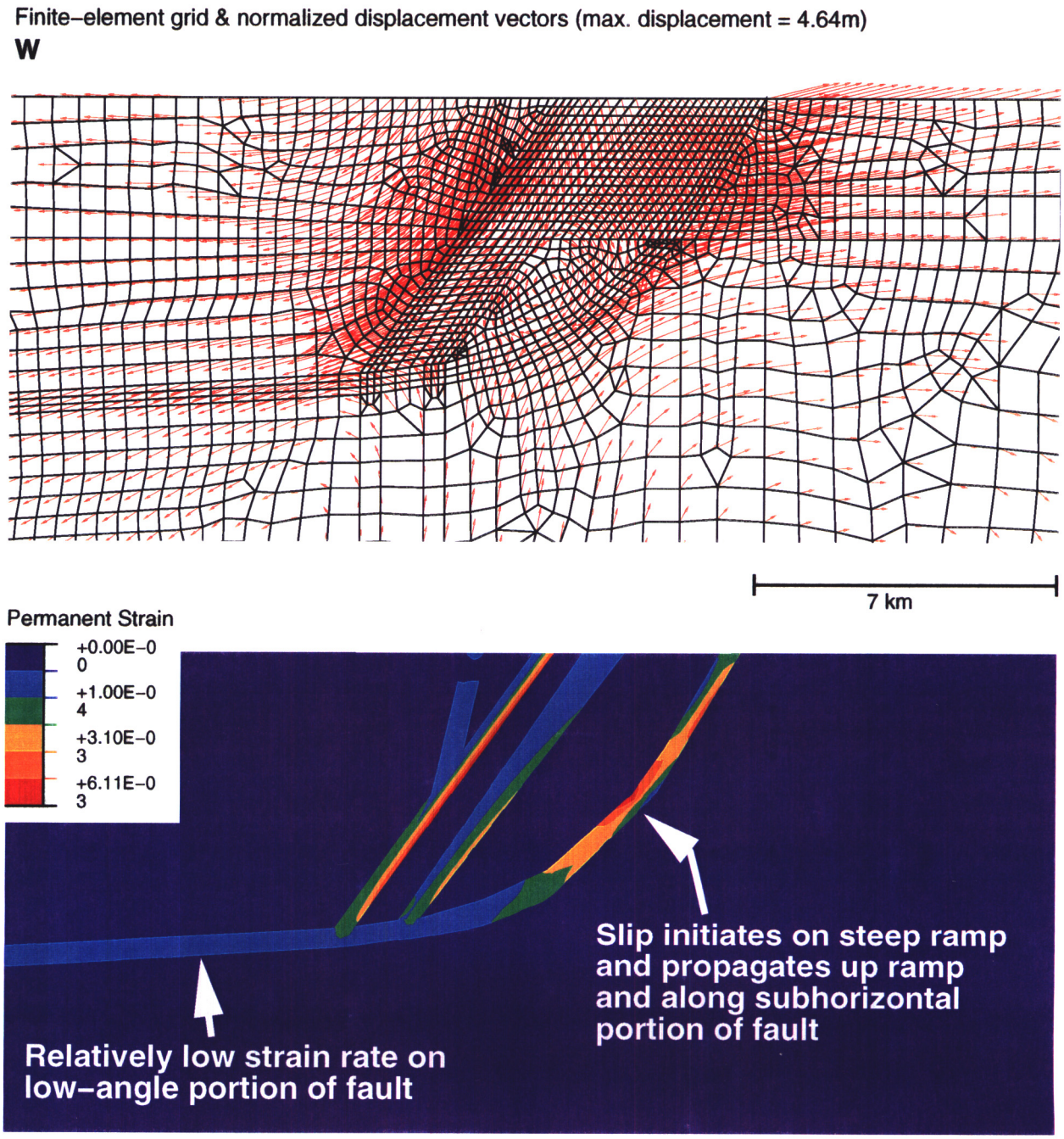

Figure 5-1. Distribution of displacement vectors and inelastic strain associated with a shear perturbation of the entire Fmw listric fault zone (Case CG4). Strain rates on low angle portions of the listric fault are orders of magnitude lower than maximum values on high angle fault segments. This difference in strain rate may explain the lack of seismicity on low angle normal faults.

6 REFERENCES

Abers, G.A. 1991. Possible seismogenic shallow-dipping normal faults in the Woodlark-D'Entrecasteaux extensional province, Papua New Guinea. *Geology* 19: 1,205–1,208.

Allmendinger, R.W., T.A. Hauge, E.C. Hauser, C.J. Potter, S.L. Klemperer, K.D. Nelson, P. Knuepfer, and J. Oliver. 1987. Overview of the COCORP 40°N Transect, western United States: The fabric of an orogeninc belt. *Geological Society of America Bulletin* 98: 308–319.

Beroza, G.C. and T.H. Jordan. 1990. Searching for slow and silent earthquakes using free oscillations. *Journal of Geophysical Research* 95(B3): 2,485–2,510.

Brun, J.P., D. Sokoutis, and J. Van Den Driessche, 1994. Analogue modeling of detachment fault systems and core complexes. *Geology* 22: 319–322.

Brun, J.-P., D. Sokoutis, and J. Van Den Driessche, 1995. Analogue modeling of detachment fault systems and core complexes: Reply *Geology* 23: 288.

Byerlee, J. 1978. Friction of rocks. *Pure and Applied Geophysics* 116: 615–626.

Byerlee, J. 1990. Friction, overpressure and fault normal compression. *Geophysical Research Letters* 17(12): 2,109–2,112.

Campbell, K.W. 1987. Predicting strong ground motion in Utah. Evaluation of Regional and Urban Earthquakes and Risk in Utah, W.W. Hays and P.L. Gori, eds. USGS Professional Paper 87-585II, L1-L90. Washington DC: Department of the Interior.

Cloos, E. 1968. Experimental analysis of Gulf Coast fracture patterns. American *Association of Petroleum Geologists Bulletin* 52: 420–444.

Curran, J.H., and G.I. Ofoegbu. 1993. Modeling discontinuities in numerical analysis. *Comprehensive Rock Engineering, 1.* J.A. Hudson, ed. New York, NY: Pergamon Press: 1: 443–468.

Davis, G.H. 1983. Shear-zone model for the origin of metamorphic core complexes. *Geology* 11: 342–347.

Drucker, D.C., and W. Prager. 1952. Soil mechanics and plastic analysis of limit design. *Quarterly of Applied Mathematics* 10(2): 157–172.

Dula, W.F., Jr. 1991. Geometric models of listric normal faults and rollover folds. *American Association of Petroleum Geologists Bulletin* 75: 1,609–1,625.

Ferrill, D.A., A.P. Morris, D.B. Henderson, and R.H. Martin. 1995. Tectonic processes in the central Basin and Range region. *NRC High-Level Radioactive Waste Research at CNWRA, July-December 1994.* CNWRA 94-02S. B.Sagar, ed. San Antonio, TX: Center for Nuclear Waste Regulatory Analyses: 121–139.

Goodman, R.E. 1980. *Introduction to Rock Mechanics*. New York, NY: John Wiley and Sons.

Groshong, R.H., Jr. 1989. Half-graben structures: Balanced models of extensional fault-bend folds. *Geological Society of America Bulletin* 101: 96–105.

Groshong, R.H., Jr. 1990. Unique determination of normal fault shape from hanging-wall bed geometry in detached half grabens. *Eclogae geol. Helv.* 83: 455–471.

Hamblin, W.K. 1965. Origin of "reverse drag" on the downthrown side of normal faults. *Geological Society of America Bulletin* 76: 1,145–1,164.

Hardin, B.O. 1965. The nature of damping in sands. *American Society of Civil Engineers Journal of Soil Mechanics and Foundations Division* 91(SM1): 63–97.

Harmsen, S.C. 1994. The Little Skull Mountain, Nevada, earthquake of 29 June 1992: Aftershock focal mechanisms and tectonic stress field implications. *Bulletin of the Seismological Society of America* 84(5): 1,484–1,505.

Hoek, E., and E.T. Brown. 1980. *Underground Excavations in Rock*. London: Institution of Mining and Metallurgy.

Hibbitt, Karlsson and Sorensen, Inc. 1994. *ABAQUS Users' Manual, Version 5.4*. Pawtucket, RI: Hibbit, Karlsson and Sorensen, Inc.

Jackson, J.A. 1987. Active normal faulting and crusta extension. in Coward, M.P., et al. eds. Continental extensonal tectonics. *Geological Society of London Special Publication* 28: 3–17.

Jaeger, J.C., and N.G.W. Cook. 1979. *Fundamentals of Rock Mechanics*. London: Chapman and Hall.

Johnson, R.A., and K.L. Loy, 1992. Seismic reflection evidence for seismogenic low-angle faulting in southeastern Arizona. *Geology* 20: 597–600.

Kenney, T.C. 1967. The influence of mineralogical composition on the residual strength of natural soils. *Proceedings of the Oslo Geotechnical Conference on the Shear Strength Properties of Natural Soils and Rocks*. I: 123–129. Oslo, Norway.

Martin, C.D. 1990. Characterizing in situ stress domains at the AECL Underground Research Laboratory. *Canadian Geotechnical Journal*. 27(5): 631–646.

McClay, K.R., and Ellis, P.G. 1987. Geometries of extensional faults systems developed in model experiments. *Geology* 15: 341–344.

McGrew, A.J. 1993. The origin and evolution of the southern Snake Range devollement, east central Nevada. *Tectonics* 12: 21–34.

Melosh, H.J. 1990. Mechanical basis for low-angle normal faulting in the Basin and Range Province. *Nature* 343: 331–335.

Miller, E.L., Gans, P.B., and Garing, J. 1983. The Snake Range décollement: An exhumed mid-Teritary ductile-brittle transition. *Tectonics* 2: 239–263.

Parsons, T. and Thompson, G.A. 1993. Does magmatism influence low-angle normal faulting? *Geology* 21: 247–250.

PDA Engineering. 1994. *PAT3/ABAQUS Interface Guide*. Costa Mesa, CA: PDA Engineering, PATRAN Division.

Richart, F.E., R.D. Woods, and J.R. Hall. 1970. *Vibrations of Soils and Foundations*. Englewood Cliffs, NJ: Prentice-Hall.

Scott, R.B. 1990. Tectonic setting of Yucca Mountain, southwestern Nevada. B.P. Wernicke, ed. *Basin and Range Extensional Tectonics Near the Latitude of Las Vegas, Nevada*. Geological Society of America Memeoir 176: 251–282.

Scott, R.B., and J. Bonk 1984. Preliminary geologic map of Yucca Mountain, Nye County, Nevada, with geologic sections. 1:12,000. U.S. Geological Survey Open-File Report 84-494.

Scott, R.J., and G.S. Lister 1992. Detachment faults: Evidence for a low-angle origin. *Geology* 20: 833–836.

Scott, R.J., and G.S. Lister 1995. Analogue modeling of detachment fault systems and core complexes: Comment. *Geology* 23: 287–288.

Sibson, R.H. 1985. A note on fault reactivation. *Journal of Structural Geology* 7: 751–754.

Suppe, J. 1983. Geometry and kinematics of fault-bend folding. *American Journal of Science* 283: 684–721.

Vendeville, B. 1991. Mechanisms generating normal fault curvature: a review illustrated by physical models. In Roberts, A.M., G. Yielding, and B. Freeman (eds.), *The Geometry of Normal Faults*. Geological Society of London Special Publication 56: 241–249.

Vendeville, B., and P.R. Cobbold, 1988. How normal faulting and sedimentation interact to produce listric fault profiles and stratigraphic wedges. *Journal of Structural Geology* 10: 649–659.

Wells, D.L., and K.J. Coppersmith. 1994. New empirical relationships among magnitude, rupture length, rupture width, rupture area, and surface displacement. *Bulletin of the Seismological Society of America* 84: 974–1,002.

Wernicke, B., 1981. Low-angle normal faults in the Basin and Range Province: Nappe tectonics in an extending orogen. *Nature* 291: 645–648.

Wernicke, B., and Axen, G.J. 1988. On the role of isostacy in the evolution of normal fault systems. *Geology* 16: 848–851.

Wernicke, B., and Burchfiel, B.C. 1982. Modes of extensional tectonics. *Journal of Structural Geology* 4: 105–115.

Williams, G., and Vann, I. 1987. The geometry of listric normal faults and deformation in their hangingwalls. *Journal of Structural Geology* 9: 789-795.

Withjack, M.O., Islam, Q.T., and La Pointe, P.R. 1995. Normal faults and their hanging-wall deformation: an experimental study. *Machine Association of Petroleum Geologists Bulletin* 79: 1–18.

Xiao, H.B., and J. Suppe. Role of compaction in listric shape of growth normal faults. *American Association of Petroleum Geologists Bulletin* 73: 777–786.

Young, S.R., Stirewalt, G.L. and Morris, A.P. 1992. *Geometric Models of Faulting at Yucca Mountain.* CNWRA 92-008. Center for Nuclear Waste Regulatory Analyses, San Antonio, TX.

APPENDIX A

TABLES OF VALUES FOR THE INPUT AND RESPONSE VARIABLES

Table A-1. Names and descriptions of the input parameters

Input Parameters	Description
Fault	Perturbed fault: Upper Fmw zone (1), FrPc zone (2), Br zone (3), Entire Fmw zone (4)
k_3	Minimum-to-maximum principal stress ratio
ϕ	Friction angle
φ/ϕ	Ratio of dilation angle to friction angle
D_α	Damping factor

Table A-2. Names and descriptions of the response variables

Variable Name	Description
fmdisp	Fault displacement: Fmw zone
frdisp	Fault displacement: FrPc zone
brdisp	Fault displacement: Br zone
gddisp	Fault displacement: Gd zone
fmsl	Slip length: Fmw zone
frsl	Slip length: FrPc zone
brsl	Slip length: Br zone
gdsl	Slip length: Gd zone
fmlf	Limit-equilibrium friction angle: Fmw zone
frlf	Limit-equilibrium friction angle: FrPc zone
brlf	Limit-equilibrium friction angle: Br zone
gdlf	Limit-equilibrium friction angle: Gd zone
sr3194	Slip rate: Station 3194 (Gd zone)
sr833	Slip rate: Station 833 (Br zone)
sr635	Slip rate: Station 635 (FrPc zone)
sr168	Slip rate: Station 168 (Upper Fmw zone)
sr58	Slip rate: Station 58 (Lower Fmw zone)
av2537	Maximum vertical acceleration: Station 2537
av5476	Maximum vertical acceleration: Station 5476
av5596	Maximum vertical acceleration: Station 5596
av5597	Maximum vertical acceleration: Station 5597
av5661	Maximum vertical acceleration: Station 5661
av5662	Maximum vertical acceleration: Station 5662
ah2537	Maximum horizontal acceleration: Station 2537
ah5476	Maximum horizontal acceleration: Station 5476
ah5596	Maximum horizontal acceleration: Station 5596
ah5597	Maximum horizontal acceleration: Station 5597
ah5661	Maximum horizontal acceleration: Station 5661
ah5662	Maximum horizontal acceleration: Station 5662
ap3065	Unstable area: 30-degree friction angle, 65-degree plane
ap3075	Unstable area: 30-degree friction angle, 75-degree plane
ap3080	Unstable area: 30-degree friction angle, 80-degree plane
ap4065	Unstable area: 40-degree friction angle, 65-degree plane
ap4075	Unstable area: 40-degree friction angle, 75-degree plane
ap4080	Unstable area: 40-degree friction angle, 80-degree plane

Table A-3. Values of the input variables

Simulation Case ID	Fault	k_3	ϕ	φ/ϕ	D_α
c01	1	0.50	35.0	0.50	0.100
c02	2	0.50	35.0	0.50	0.100
c03	3	0.50	35.0	0.50	0.100
c04	4	0.50	35.0	0.50	0.100
c05	1	0.35	40.0	0.50	0.100
c06	2	0.35	40.0	0.50	0.100
c07	3	0.35	40.0	0.50	0.100
c08	4	0.35	40.0	0.50	0.100
c09	1	0.35	35.0	0.50	0.100
c10	2	0.35	35.0	0.50	0.100
c11	3	0.35	35.0	0.50	0.100
c12	4	0.35	35.0	0.50	0.100
c13	1	0.35	30.0	0.50	0.100
c14	2	0.35	30.0	0.50	0.100
c15	3	0.35	30.0	0.50	0.100
c16	4	0.35	30.0	0.50	0.100
c17	1	0.35	40.0	1.00	0.100
c18	2	0.35	40.0	1.00	0.100
c19	3	0.35	40.0	1.00	0.100
c20	4	0.35	40.0	1.00	0.100
c21	1	0.35	30.0	1.00	0.100
c22	2	0.35	30.0	1.00	0.100
c23	3	0.35	30.0	1.00	0.100
c24	4	0.35	30.0	1.00	0.100
c25	1	0.35	40.0	0.50	0.010

Table A-3. Values of the input variables (cont'd)

Simulation Case ID	Fault	k_3	ϕ	φ/ϕ	D_α
c26	2	0.35	40.0	0.50	0.010
c27	3	0.35	40.0	0.50	0.010
c28	4	0.35	40.0	0.50	0.010
c29	1	0.40	32.5	0.50	0.010
c30	2	0.40	32.5	0.50	0.010
c31	3	0.40	32.5	0.50	0.010
c32	4	0.40	32.5	0.50	0.010
c33	1	0.45	30.0	0.75	0.050
c34	2	0.45	30.0	0.75	0.050
c35	3	0.45	30.0	0.75	0.050
c36	4	0.45	30.0	0.75	0.050
c37	1	0.20	40.0	1.00	0.030
c38	2	0.20	40.0	1.00	0.030
c39	3	0.20	40.0	1.00	0.030
c40	4	0.20	40.0	1.00	0.030
c41	1	0.30	37.5	0.25	0.075
c42	2	0.30	37.5	0.25	0.075
c43	3	0.30	37.5	0.25	0.075
c44	4	0.30	37.5	0.25	0.075
c45	1	0.25	30.0	0.35	0.025
c46	2	0.25	30.0	0.35	0.025
c47	3	0.25	30.0	0.35	0.025
c48	4	0.25	30.0	0.35	0.025
c49	1	0.40	37.5	0.75	0.050
c50	2	0.40	37.5	0.75	0.050
c51	3	0.40	37.5	0.75	0.050

Table A-3. Values of the input variables (cont'd)

Simulation Case ID	Fault	k_3	ϕ	φ/ϕ	D_α
c52	4	0.40	37.5	0.75	0.050
c53	1	0.40	30.0	0.10	0.050
c54	2	0.40	30.0	0.10	0.050
c55	3	0.40	33.0	0.10	0.050
c56	4	0.40	30.0	0.10	0.050
c57	1	0.23	36.0	0.60	0.050
c58	2	0.23	36.0	0.60	0.050
c59	3	0.23	36.0	0.60	0.050
c60	4	0.23	36.0	0.60	0.050
c61	1	0.26	32.0	0.30	0.020
c62	2	0.26	32.0	0.30	0.020
c63	3	0.26	32.0	0.30	0.020
c64	4	0.26	32.0	0.30	0.020
c65	1	0.29	34.0	0.80	0.040
c66	2	0.29	34.0	0.80	0.040
c67	3	0.29	34.0	0.80	0.040
c68	4	0.29	34.0	0.80	0.040

Table A-4. Values of fault displacement (m)

Simulation Case ID	fmdisp	frdisp	brdisp	gddisp
c01	13.90	0.00	0.00	0.00
c02	0.00	20.00	0.00	0.00
c03	0.00	0.00	22.20	0.00
c04	19.70	0.00	0.00	0.00
c05	22.50	0.00	0.00	0.00
c06	0.00	29.70	0.00	0.00
c07	0.00	0.00	39.70	0.00
c08	29.30	0.00	0.00	0.00
c09	21.60	0.01	0.13	0.01
c10	0.33	29.70	0.00	0.00
c11	0.20	0.02	40.50	0.00
c12	28.90	0.02	0.13	0.02
c13	24.40	0.01	0.07	0.02
c14	0.33	29.60	0.00	0.00
c15	0.24	0.00	40.90	0.00
c16	30.40	0.01	0.06	0.02
c17	39.90	0.01	0.08	0.00
c18	0.29	29.80	0.00	0.00
c19	0.17	0.00	38.30	0.00
c20	52.00	0.01	0.08	0.02
c21	15.80	0.02	0.09	0.01
c22	0.28	21.40	0.00	0.00
c23	0.26	0.01	34.70	0.00
c24	20.90	0.04	0.10	0.02
c25	28.60	0.01	0.02	0.03

Table A-4. Values of fault displacement (m) (cont'd)

Simulation Case ID	fmdisp	frdisp	brdisp	gddisp
c26	0.26	35.30	0.00	0.00
c27	0.15	0.00	52.50	0.00
c28	42.00	0.01	0.03	0.02
c29	33.50	0.08	0.25	0.07
c30	0.47	32.10	0.00	0.01
c31	0.29	0.01	51.00	0.00
c32	37.20	0.08	0.24	0.06
c33	31.80	0.00	0.03	0.01
c34	0.21	25.40	0.00	0.00
c35	0.12	0.00	35.00	0.00
c36	42.00	0.00	0.03	0.01
c37	36.30	0.06	0.11	0.02
c38	0.52	36.00	0.00	0.00
c39	0.57	0.00	57.40	0.00
c40	39.80	0.04	0.07	0.02
c41	48.90	0.03	0.49	0.04
c42	0.39	35.10	0.00	0.00
c43	0.27	0.00	52.30	0.00
c44	50.90	0.04	0.37	0.04
c45	56.30	0.00	0.30	0.02
c46	0.50	30.60	0.03	0.00
c47	0.53	0.00	56.10	0.00
c48	67.70	0.00	0.30	0.02
c49	25.00	0.00	0.01	0.00
c50	0.11	31.40	0.00	0.00
c51	0.05	0.00	43.90	0.00

Table A-4. Values of fault displacement (m) (cont'd)

Simulation Case ID	fmdisp	frdisp	brdisp	gddisp
c52	33.10	0.00	0.01	0.00
c53	30.20	0.04	0.25	0.02
c54	0.36	29.70	0.00	0.00
c55	0.12	0.00	52.00	0.00
c56	37.50	0.05	0.24	0.02
c57	43.40	0.03	0.54	0.01
c58	0.41	35.10	0.00	0.00
c59	0.36	0.00	49.90	0.00
c60	53.30	0.03	0.51	0.02
c61	61.90	0.00	0.32	0.03
c62	0.45	20.10	0.11	0.00
c63	0.47	0.00	38.10	0.00
c64	77.50	0.00	0.34	0.04
c65	33.60	0.04	0.19	0.01
c66	0.37	30.00	0.00	0.00
c67	0.34	0.01	46.20	0.01
c68	41.10	0.04	0.18	0.01

Table A-5. Values of slip length (km)

Simulation Case ID	fmsl	frsl	brsl	gdsl
c01	6.75	0.00	0.00	0.00
c02	0.00	7.72	0.00	0.00
c03	0.00	0.00	7.94	0.00
c04	21.19	0.00	0.00	0.00
c05	6.75	0.00	0.00	0.00
c06	0.00	7.72	0.00	0.00
c07	0.00	0.00	7.94	0.00
c08	21.70	0.00	0.00	0.00
c09	9.03	0.25	2.02	0.72
c10	2.81	7.72	0.00	0.00
c11	1.97	0.76	7.94	0.00
c12	21.69	0.76	1.51	0.72
c13	9.31	0.25	1.01	0.72
c14	2.32	7.72	0.00	0.00
c15	2.46	0.00	7.94	0.00
c16	23.19	0.25	1.01	0.95
c17	8.17	0.51	1.01	0.00
c18	1.41	7.72	0.00	0.00
c19	1.68	0.00	7.94	0.00
c20	21.70	0.76	1.01	0.82
c21	9.03	1.01	1.51	0.42
c22	2.03	7.72	0.00	0.00
c23	2.18	0.51	7.94	0.00
c24	23.70	1.52	1.77	0.82
c25	7.03	0.25	0.50	0.82

Table A-5. Values of slip length (km) (cont'd)

Simulation Case ID	fmsl	frsl	brsl	gdsl
c26	1.41	7.72	0.00	0.00
c27	1.34	0.00	7.94	0.00
c28	21.70	0.25	0.50	0.82
c29	9.88	2.28	2.52	1.74
c30	3.83	7.72	0.00	0.48
c31	5.01	0.23	7.94	0.00
c32	21.70	2.53	2.78	1.96
c33	7.89	0.00	0.76	0.42
c34	1.75	7.72	0.00	0.00
c35	1.34	0.00	7.94	0.00
c36	21.70	0.00	0.76	0.42
c37	9.03	1.26	2.02	0.57
c38	3.91	7.72	0.00	0.00
c39	3.56	0.00	7.94	0.00
c40	29.20	0.76	1.77	0.57
c41	9.31	1.26	2.52	0.90
c42	3.34	7.72	0.00	0.00
c43	4.87	0.00	7.94	0.00
c44	21.70	1.26	2.50	1.13
c45	9.60	0.00	1.50	0.94
c46	2.84	7.72	1.25	0.00
c47	2.83	0.00	7.94	0.00
c48	29.20	0.00	2.23	1.17
c49	6.75	0.00	0.25	0.00
c50	0.87	7.72	0.00	0.00
c51	0.63	0.00	7.94	0.00

Table A-5. Values of slip length (km) (cont'd)

Simulation Case ID	fmsl	frsl	brsl	gdsl
c52	21.69	0.00	0.25	0.00
c53	9.60	1.52	2.78	0.95
c54	2.81	7.72	0.00	0.00
c55	1.34	0.00	7.94	0.00
c56	21.69	1.77	3.71	0.95
c57	9.60	1.27	3.26	0.48
c58	3.73	7.72	0.00	0.00
c59	4.07	0.00	7.94	0.00
c60	28.70	1.26	2.76	0.72
c61	9.60	0.00	2.49	1.17
c62	4.76	7.72	2.49	0.00
c63	5.60	0.00	7.94	0.00
c64	29.20	0.00	2.97	1.17
c65	9.88	1.27	2.27	0.66
c66	3.52	7.72	0.00	0.00
c67	4.55	0.10	7.94	0.10
c68	26.70	1.27	2.02	0.66

Table A-6. Values of limit-equilibrium friction angle (°)

Simulation Case ID	fmlf	frlf	brlf	gdlf
c01	NA	20.2	23.1	13.9
c02	18.4	NA	19.6	9.2
c03	18.8	20.7	NA	11.6
c04	NA	20.0	22.0	14.0
c05	NA	31.3	34.3	26.7
c06	26.4	NA	28.0	15.5
c07	26.8	28.5	NA	20.0
c08	NA	32.0	34.0	28.0
c09	NA	33.0	33.1	26.0
c10	25.5	NA	26.5	15.3
c11	25.8	28.2	NA	19.1
c12	NA	32.8	33.1	26.4
c13	NA	29.2	29.9	24.6
c14	23.2	NA	24.1	14.1
c15	23.4	25.8	NA	16.2
c16	NA	29.3	29.8	26.0
c17	NA	33.1	33.7	25.5
c18	39.0	NA	27.9	17.1
c19	26.7	27.6	NA	24.2
c20	NA	33.0	33.5	28.4
c21	NA	29.3	29.6	24.0
c22	22.6	NA	24.7	17.3
c23	22.7	25.6	NA	18.6
c24	NA	29.2	29.6	24.8
c25	NA	33.4	34.0	21.7

Table A-6. Values of limit-equilibrium friction angle (°) (cont'd)

Simulation Case ID	fmlf	frlf	brlf	gdlf
c26	26.3	NA	28.0	13.7
c27	26.6	27.9	NA	14.6
c28	NA	32.6	34.2	24.8
c29	NA	28.5	30.4	17.7
c30	23.1	NA	24.0	11.3
c31	23.3	24.2	NA	11.7
c32	NA	28.5	29.9	19.9
c33	NA	25.2	27.5	18.2
c34	21.0	NA	21.8	11.0
c35	21.2	21.8	NA	13.2
c36	NA	25.6	27.5	18.2
c37	NA	34.4	35.8	26.5
c38	28.0	NA	30.2	19.4
c39	28.3	29.2	NA	21.0
c40	NA	33.8	36.4	22.9
c41	NA	33.1	35.7	29.4
c42	27.6	NA	28.9	16.8
c43	27.8	29.0	NA	19.3
c44	NA	33.8	35.6	30.3
c45	NA	25.3	27.1	15.0
c46	23.3	NA	24.2	7.6
c47	23.2	24.8	NA	8.7
c48	NA	24.6	26.6	14.3
c49	NA	29.1	32.8	20.7
c50	23.5	NA	25.1	12.5
c51	23.8	24.8	NA	15.3

Table A-6. Values of limit-equilibrium friction angle (°) (cont'd)

Simulation Case ID	fmlf	frlf	brlf	gdlf
c52	NA	29.5	32.3	22.8
c53	NA	28.3	30.4	21.4
c54	22.9	NA	23.6	11.5
c55	23.5	24.7	NA	13.1
c56	NA	28.2	30.2	21.1
c57	NA	33.6	33.4	27.2
c58	27.4	NA	29.2	15.0
c59	27.9	28.6	NA	18.1
c60	NA	33.5	33.3	27.8
c61	NA	26.7	27.8	15.8
c62	24.5	NA	25.7	8.7
c63	24.8	26.1	NA	11.0
c64	NA	26.0	27.4	15.9
c65	NA	33.1	33.3	27.0
c66	26.2	NA	27.3	17.6
c67	26.3	27.1	NA	18.3
c68	NA	33.0	33.3	29.1

Table A-7. Values of slip rate ($m \cdot s^{-1}$)

Simulation Case ID	sr3194	sr833	sr635	sr168	sr58
c01	0.0	0.0	0.0	5.01×10^{-1}	0.0
c02	0.0	0.0	5.24×10^{-1}	0.0	0.0
c03	0.0	5.22×10^{-1}	0.0	0.0	0.0
c04	0.0	0.0	0.0	4.98×10^{-1}	1.47×10^{-3}
c05	0.0	0.0	0.0	2.14×10^{-1}	0.0
c06	0.0	0.0	1.95×10^{-1}	0.0	0.0
c07	0.0	1.97×10^{-1}	0.0	0.0	0.0
c08	0.0	0.0	0.0	2.14×10^{-1}	7.30
c09	4.8×10^{-6}	8.2×10^{-6}	4.3×10^{-6}	1.92×10^{1}	1.0×10^{-5}
c10	2.0×10^{-5}	6.4×10^{-5}	1.7×10^{1}	3.5×10^{-6}	4.2×10^{-6}
c11	3.6×10^{-5}	1.72×10^{1}	3.9×10^{-5}	1.5×10^{-6}	6.9×10^{-6}
c12	6.0×10^{-6}	2.1×10^{-3}	5.6×10^{-4}	1.92×10^{1}	6.94
c13	1.6×10^{-5}	1.4×10^{-5}	1.1×10^{-5}	1.6×10^{1}	7.6×10^{-6}
c14	5.6×10^{-5}	1.8×10^{-4}	1.37×10^{1}	5.60×10^{-6}	2.1×10^{-6}
c15	7.1×10^{-6}	1.41×10^{1}	1.0×10^{-5}	4.50×10^{-4}	5.9×10^{-6}
c16	5.8×10^{-5}	1.1×10^{-3}	4.1×10^{-4}	1.6×10^{1}	6.9
c17	0.0	0.0	0.0	3.1×10^{1}	0.0
c18	0.0	0.0	1.82×10^{1}	0.0	0.0
c19	0.0	1.84×10^{1}	0.0 .0	0.0	0.0
c20	0.0	0.0	0.0	3.1×10^{1}	1.05×10^{1}
c21	1.5×10^{-5}	1.6×10^{-5}	1.1×10^{-5}	1.26×10^{1}	4.3×10^{-6}
c22	6.3×10^{-5}	2.0×10^{-4}	1.07×10^{1}	1.2×10^{-7}	1.2×10^{-5}

Table A-7. Values of slip rate ($m \cdot s^{-1}$) (cont'd)

Simulation Case ID	sr3194	sr833	sr635	sr168	sr58
c23	1.3×10^{-4}	1.24×10^{1}	1.3×10^{-4}	4.7×10^{-4}	2.0×10^{-5}
c24	3.9×10^{-5}	6.67×10^{-5}	6.8×10^{-5}	1.26×10^{1}	5.70
c25	0.0	0.0	0.0	2.02×10^{1}	0.0
c26	0.0	0.0.0	1.95×10^{1}	0.0	0.0
c27	0.0	1.97×10^{1}	0.0	0.0	0.0
c28	0.0	0.0	0.0	2.14×10^{1}	7.30
c29	4.8×10^{-6}	7.0×10^{-6}	4.4×10^{-6}	2.0×10^{1}	2.0×10^{-6}
c30	1.9×10^{-5}	8.3×10^{-5}	1.79×10^{1}	4.1×10^{-6}	1.4×10^{-5}
c31	3.8×10^{-5}	1.81×10^{1}	5.6×10^{-5}	2.0×10^{-5}	3.0×10^{-4}
c32	1.0×10^{-5}	7.8×10^{-3}	2.3×10^{-3}	1.89×10^{1}	6.50
c33	0.0	0.0	0.0	2.35×10^{1}	0.0
c34	0.0	0.0	1.61×10^{1}	0.0	0.0
c35	0.0	1.63×10^{1}	0.0	0.0	0.0
c36	0.0	0.0	0.0	2.35×10^{1}	8.0
c37	1.1×10^{-4}	2.0×10^{-4}	2.0×10^{-4}	2.0×10^{1}	1.7×10^{-5}
c38	3.8×10^{-4}	1.1×10^{-3}	1.28×10^{1}	1.2×10^{-5}	$5.3\times\times10^{-5}$
c39	7.1×10^{-4}	1.33×10^{1}	2.4×10^{-4}	5.6×10^{-3}	6.0×10^{-5}
c40	2.8×10^{-4}	5.1×10^{-4}	3.3×10^{-4}	2.0×10^{1}	1.02×10^{1}
c41	1.5×10^{-5}	1.5×10^{-5}	1.2×10^{-5}	2.65×10^{1}	6.9×10^{-6}
c42	4.2×10^{-5}	1.4×10^{-4}	1.6×10^{1}	8.6×10^{-6}	7.4×10^{-6}
c43	7.1×10^{-5}	1.62×10^{1}	8.7×10^{-5}	1.9×10^{-3}	1.2×10^{-5}
c44	7.2×10^{-5}	1.3×10^{-2}	7.0×10^{-3}	2.34×10^{1}	9.0
c45	5.8×10^{-5}	6.9×10^{-5}	5.0×10^{-5}	2.1×10^{1}	3.6×10^{-5}

Table A-7. Values of slip rate ($m \cdot s^{-1}$) (cont'd)

Simulation Case ID	sr3194	sr833	sr635	sr168	sr58
c46	1.6×10^{-4}	8.1×10^{-4}	1.41×10^{1}	5.1×10^{-4}	4.5×10^{-5}
c47	2.7×10^{-4}	1.49×10^{1}	5.1×10^{-4}	1.1×10^{-2}	1.4×10^{-4}
c48	1.3×10^{-4}	2.7×10^{-4}	3.1×10^{-4}	2.1×10^{1}	1.22×10^{1}
c49	0.0	0.0	0.0	2.05×10^{1}	0.0
c50	0.0	0.0	1.87×10^{1}	0.0	0.0
c51	0.0	1.89×10^{1}	0.0	0.0	0.0
c52	0.0	0.0	0.0	2.05×10^{1}	7.0
c53	5.3×10^{-6}	6.3×10^{-6}	5.3×10^{-6}	1.82×10^{1}	2.9×10^{-6}
c54	2.1×10^{-5}	8.3×10^{-5}	1.62×10^{1}	6.2×10^{-6}	4.6×10^{-6}
c55	0.0	2.06×10^{1}	0.0	0.0	0.0
c56	8.5×10^{-4}	1.6×10^{-2}	1.0×10^{-2}	1.82×10^{1}	6.6
c57	4.4×10^{-5}	1.2×10^{-4}	3.7×10^{-5}	2.05×10^{1}	2.1×10^{-5}
c58	1.3×10^{-4}	1.0×10^{-3}	1.26×10^{1}	5.6×10^{-6}	2.4×10^{-5}
c59	1.7×10^{-4}	1.27×10^{1}	2.9×10^{-4}	6.1×10^{-3}	3.7×10^{-5}
c60	1.1×10^{-4}	4.0×10^{-4}	2.6×10^{-4}	2.05×10^{1}	1.03×10^{1}
c61	6.4×10^{-5}	6.7×10^{-5}	5.2×10^{-5}	2.25×10^{1}	3.1×10^{-5}
c62	1.5×10^{-4}	6.9×10^{-4}	1.32×10^{1}	4.5×10^{-4}	3.6×10^{-5}
c63	2.1×10^{-4}	1.22×10^{1}	4.1×10^{-4}	7.2×10^{-3}	7.2×10^{-5}
c64	1.4×10^{-4}	2.5×10^{-4}	3.2×10^{-4}	2.25×10^{1}	1.23×10^{1}
c65	4.4×10^{-5}	4.5×10^{-5}	2.5×10^{-5}	1.79×10^{1}	2.7×10^{-6}
c66	1.3×10^{-4}	3.8×10^{-4}	1.18×10^{1}	5.0×10^{-6}	2.0×10^{-5}
c67	2.4×10^{-4}	1.21×10^{1}	2.4×10^{-4}	4.3×10^{-3}	2.7×10^{-5}
c68	1.0×10^{-4}	1.5×10^{-4}	1.6×10^{-4}	1.79×10^{1}	7.9

Table A-8. Values of maximum vertical acceleration ($m \cdot s^{-2}$)

Simulation Case ID	av2537	av5476	av5596	av5597	av5661	av5662
c01	1.01	0.63	0.56	0.52	0.49	0.41
c02	0.52	0.81	0.78	0.76	0.77	0.67
c03	0.15	0.40	0.72	0.64	0.70	0.49
c04	1.00	0.68	0.58	0.50	0.54	0.36
c05	1.40	0.87	0.75	0.71	0.67	0.56
c06	0.69	1.10	1.00	1.00	1.00	0.91
c07	0.21	0.63	1.00	0.92	1.00	0.75
c08	1.40	0.93	0.77	0.67	0.72	0.45
c09	1.34	0.80	0.65	0.62	0.62	0.52
c10	0.60	1.00	0.93	0.92	0.91	0.82
c11	0.19	0.70	0.96	0.85	0.95	0.70
c12	1.30	0.85	0.70	0.61	0.65	0.41
c13	1.10	0.66	0.53	0.52	0.50	0.42
c14	0.45	0.85	0.76	0.76	0.73	0.69
c15	0.17	0.61	0.80	0.73	0.83	0.61
c16	1.10	0.72	0.59	0.52	0.55	0.34
c17	2.00	1.30	1.10	1.10	1.10	0.90
c18	0.93	1.00	1.10	1.10	1.10	0.91
c19	0.23	0.66	0.99	0.83	1.00	0.83
c20	2.00	1.40	1.20	1.00	1.00	0.76
c21	0.85	0.55	0.46	0.44	0.45	0.38
c22	0.54	0.71	0.68	0.66	0.67	0.58
c23	0.17	0.56	0.74	0.64	0.78	0.62
c24	0.85	0.61	0.53	0.44	0.45	0.35
c25	2.60	3.40	3.20	2.30	1.90	1.50

Table A-8. Values of maximum vertical acceleration ($m \cdot s^{-2}$) (cont'd)

Simulation Case ID	av2537	av5476	av5596	av5597	av5661	av5662
c26	1.30	2.20	2.70	2.20	2.60	2.00
c27	0.55	1.10	2.20	1.80	2.10	1.70
c28	2.80	3.50	3.50	2.80	2.30	1.30
c29	2.70	2.90	3.10	2.00	1.80	1.50
c30	1.20	2.10	2.30	2.00	2.40	1.90
c31	0.47	1.40	2.10	1.70	2.00	1.60
c32	2.60	2.80	3.70	2.40	2.10	1.20
c33	2.10	1.60	1.40	1.30	1.20	0.94
c34	0.76	1.10	1.30	1.20	1.20	1.10
c35	0.23	0.59	1.20	1.00	1.10	0.87
c36	2.10	1.70	1.60	1.40	1.20	0.72
c37	2.30	2.20	2.00	1.70	1.70	1.30
c38	1.20	1.20	1.80	1.60	1.70	1.40
c39	0.35	0.89	1.40	1.20	1.70	1.30
c40	2.30	2.30	2.10	1.90	1.50	1.20
c41	2.10	1.30	1.10	1.00	0.95	0.79
c42	0.52	1.10	0.99	0.98	0.97	0.92
c43	0.21	0.81	1.00	0.96	1.00	0.76
c44	1.90	1.20	1.10	0.94	0.95	0.63
c45	2.40	2.00	1.60	1.70	1.40	1.20
c46	0.67	1.30	1.20	1.30	1.40	1.30
c47	0.38	1.10	1.40	1.50	1.60	1.20
c48	2.40	2.20	2.20	1.90	1.40	0.91
c49	1.80	1.40	1.20	1.20	1.10	0.85
c50	0.92	1.30	1.60	1.40	1.50	1.30
c51	0.29	0.74	1.40	1.20	1.40	1.00

Table A-8. Values of maximum vertical acceleration ($m \cdot s^{-2}$) (cont'd)

Simulation Case ID	av2537	av5476	av5596	av5597	av5661	av5662
c52	1.80	1.50	1.50	1.20	1.10	0.62
c53	1.70	1.10	0.96	0.90	0.79	0.65
c54	0.53	1.20	1.10	1.10	1.10	1.10
c55	0.26	0.87	1.40	1.30	1.40	0.95
c56	1.70	1.20	1.20	0.98	1.00	0.76
c57	1.90	1.40	1.20	1.20	1.10	0.91
c58	0.68	1.00	1.10	1.10	1.10	1.00
c59	0.24	0.70	0.94	0.86	1.00	0.76
c60	1.90	1.60	1.50	1.30	1.20	0.64
c61	2.70	2.50	2.00	2.00	1.70	1.40
c62	0.68	1.30	1.20	1.30	1.40	1.30
c63	0.39	0.87	1.20	1.30	1.40	0.99
c64	2.70	2.60	2.70	2.30	1.70	1.10
c65	1.80	1.60	1.20	1.20	1.20	0.93
c66	0.78	1.00	1.20	1.20	1.20	1.00
c67	0.26	0.72	1.10	1.00	1.20	0.94
c68	1.80	1.70	1.80	1.30	1.20	0.66

Table A-9. Values of maximum horizontal acceleration ($m \cdot s^{-2}$)

Simulation Case ID	ah2537	ah5476	ah5596	ah5597	ah5661	ah5662
c01	0.380	0.38	0.20	0.30	0.21	0.26
c02	0.540	0.31	0.47	0.30	0.57	0.30
c03	0.096	0.31	0.34	0.22	0.47	0.35
c04	0.380	0.38	0.48	0.49	0.73	0.76
c05	0.580	0.52	0.33	0.40	0.32	0.34
c06	0.730	0.42	0.59	0.37	0.71	0.36
c07	0.160	0.48	0.47	0.30	0.66	0.48
c08	0.580	0.52	0.63	0.65	0.87	1.00
c09	0.580	0.47	0.30	0.34	0.30	0.29
c10	0.680	0.38	0.54	0.33	0.62	0.31
c11	0.150	0.50	0.43	0.26	0.57	0.42
c12	0.580	0.48	0.58	0.60	0.80	0.90
c13	0.420	0.41	0.24	0.30	0.24	0.24
c14	0.520	0.30	0.43	0.27	0.51	0.26
c15	0.130	0.40	0.36	0.21	0.45	0.35
c16	0.420	0.43	0.49	0.54	0.72	0.76
c17	1.100	0.84	0.74	0.62	0.66	0.48
c18	0.900	0.52	0.63	0.38	0.69	0.42
c19	0.200	0.48	0.43	0.31	0.71	0.48
c20	1.100	0.87	0.94	0.99	1.00	1.40
c21	0.460	0.38	0.34	0.24	0.31	0.21
c22	0.560	0.32	0.39	0.24	0.42	0.26
c23	0.140	0.42	0.32	0.23	0.48	0.34
c24	0.460	0.40	0.41	0.42	0.47	0.63
c25	1.500	2.10	1.50	2.10	1.60	1.50

Table A-9. Values of maximum horizontal acceleration ($m \cdot s^{-2}$) (cont'd)

Simulation Case ID	ah2537	ah5476	ah5596	ah5597	ah5661	ah5662
c26	1.400	1.40	1.60	1.20	1.90	1.40
c27	0.510	0.97	1.30	0.83	1.40	1.10
c28	1.600	2.30	3.10	3.90	3.80	3.50
c29	1.700	1.90	1.20	2.20	1.50	1.30
c30	1.300	1.30	1.50	1.00	1.80	1.20
c31	0.490	1.00	1.20	0.75	1.30	0.97
c32	1.600	1.90	2.70	3.50	3.30	3.00
c33	1.100	1.10	0.64	0.88	0.66	0.76
c34	0.770	0.57	0.72	0.54	0.88	0.46
c35	0.200	0.48	0.60	0.36	0.80	0.61
c36	1.000	1.10	1.50	1.60	1.80	2.00
c37	1.600	1.60	1.50	1.40	1.20	1.10
c38	1.200	0.92	1.10	0.76	1.10	0.80
c39	0.340	0.90	0.84	0.64	1.10	0.76
c40	1.600	1.70	1.70	2.60	2.10	1.50
c41	0.790	0.81	0.42	0.63	0.42	0.53
c42	0.610	0.43	0.54	0.38	0.70	0.35
c43	0.170	0.51	0.49	0.28	0.56	0.46
c44	0.700	0.74	0.96	1.00	1.50	1.40
c45	0.910	1.40	0.79	1.50	1.00	1.00
c46	0.640	0.71	0.75	0.53	1.20	0.67
c47	0.350	0.65	0.79	0.48	0.83	0.64
c48	0.970	1.70	1.90	2.60	3.00	2.70
c49	1.000	0.96	0.62	0.81	0.63	0.70
c50	0.940	0.69	0.87	0.64	1.00	0.56
c51	0.240	0.63	0.70	0.44	0.95	0.72

Table A-9. Values of maximum horizontal acceleration ($m \cdot s^{-2}$) (cont'd)

Simulation Case ID	ah2537	ah5476	ah5596	ah5597	ah5661	ah5662
c52	0.960	0.99	1.30	1.50	1.50	1.80
c53	0.660	0.73	0.38	0.67	0.44	0.54
c54	0.610	0.55	0.62	0.47	0.85	0.42
c55	0.190	0.61	0.73	0.43	0.79	0.68
c56	0.660	0.77	1.10	1.20	1.80	1.50
c57	0.890	1.00	0.62	0.82	0.65	0.67
c58	0.640	0.54	0.57	0.46	0.76	0.37
c59	0.220	0.50	0.49	0.31	0.50	0.40
c60	0.890	1.10	1.40	1.50	1.70	1.90
c61	1.200	1.70	0.90	1.90	1.30	1.30
c62	0.650	0.65	0.76	0.51	1.10	0.69
c63	0.320	0.54	0.71	0.43	0.76	0.60
c64	1.300	2.00	2.30	3.10	3.70	3.20
c65	1.000	1.10	0.80	0.94	0.76	0.72
c66	0.750	0.64	0.67	0.52	0.80	0.45
c67	0.260	0.61	0.60	0.41	0.73	0.55
c68	1.000	1.20	1.50	1.70	1.60	1.90

Table A-10. Values of the area of potential instability (m^2) based on the slip tendency for selected planar surfaces

Simulation Case ID	ap3065	ap3075	ap3080	ap4065	ap4075	ap4080
c01	7.13×10^5	4.15×10^5	1.28×10^5	7.56×10^4	6.01×10^4	6.01×10^4
c02	4.43×10^5	2.14×10^5	3.89×10^4	7.77×10^4	7.77×10^4	3.89×10^4
c03	2.37×10^5	2.37×10^5	1.61×10^5	1.34×10^5	8.96×10^4	8.96×10^4
c04	1.01×10^6	3.55×10^5	1.28×10^5	1.43×10^5	6.01×10^4	6.01×10^4
c05	2.55×10^6	1.32×10^6	9.69×10^5	9.29×10^5	8.44×10^5	6.57×10^5
c06	1.55×10^56	1.02×10^6	8.66×10^5	7.85×10^5	7.08×10^5	5.49×10^5
c07	9.0×10^5	7.0×10^5	4.38×10^5	3.16×10^5	3.07×10^5	2.63×10^5
c08	4.35×10^6	2.19×10^6	1.47×10^6	1.39×10^6	1.3×10^6	1.1×10^6
c09	2.84×10^6	1.16×10^6	8.46×10^6	7.38×10^5	7.73×10^5	6.1×10^5
c10	1.55×10^6	8.99×10^5	8.22×10^5	7.85×10^5	7.08×10^5	6.4×10^5
c11	8.98×10^5	$7.\times10^5$	5.53×10^5	3.85×10^5	2.63×10^5	2.63×10^5
c12	4.21×10^6	1.82×10^6	1.63×10^6	1.51×10^6	1.32×10^6	8.68×10^5
c13	1.68×10^6	1.39×10^6	1.15×10^6	1.26×10^6	8.5×10^5	4.55×10^5
c14	1.35×10^6	8.6×10^5	7.83×10^5	7.85×10^5	6.69×10^5	6.02×10^5
c15	9.38×10^5	6.15×10^5	6.25×10^5	4.55×10^5	4.84×10^5	3.78×10^5
c16	2.49×10^6	1.49×10^6	1.32×10^6	1.39×10^6	1.12×10^6	8.77×10^5
c17	3.16×10^6	1.39×10^6	1.04×10^6	9.17×10^5	8.89×10^5	6.67×10^5
c18	2.08×10^6	1.13×10^6	9.84×10^5	8.97×10^5	6.64×10^5	2.2×10^5
c19	1.61×10^6	1.09×10^6	6.79×10^5	5.12×10^5	4.06×10^5	3.54×10^5
c20	5.54×10^6	2.38×10^6	1.56×10^6	1.42×10^6	1.35×10^6	1.11×10^6
c21	1.91×10^6	1.53×10^6	1.25×10^6	1.34×10^6	1.02×10^6	3.8×10^5

Table A-10. Values of the area of potential instability (m^2) based on the slip tendency for selected planar surfaces (cont'd)

Simulation Case ID	ap3065	ap3075	ap3080	ap4065	ap4075	ap4080
c22	1.87×10^6	9.04×10^5	8.01×10^5	8.13×10^5	7.33×10^5	7.33×10^5
c23	1.36×10^6	8.92×10^5	6.1×10^5	6.34×10^5	5.8×10^5	5.35×10^5
c24	2.76×10^6	1.65×10^6	1.37×10^6	1.47×10^6	1.13×10^6	9.38×10^5
c25	1.63×10^6	7.72×10^5	4.62×10^5	5.3×10^5	4.62×10^5	3.91×10^5
c26	1.14×10^5	8.24×10^5	7.56×10^5	7.49×10^5	7.1×10^5	5.36×10^5
c27	3.99×10^5	2.96×10^5	2.51×10^5	2.28×10^5	2.14×10^5	6.47×10^4
c28	2.87×10^6	1.4×10^6	1.08×10^6	1.09×10^6	8.98×10^5	6.5×10^5
c29	8.57×10^5	6.47×10^5	5.08×10^5	4.62×10^5	3.94×10^5	2.78×10^5
c30	8.17×10^5	7.78×10^5	6.19×10^5	6.43×10^5	6.43×10^5	3.75×10^5
c31	2.28×10^5	2.14×10^5	2.14×10^5	1.15×10^5	3.42×10^4	$0.\times10^5$
c32	1.34×10^6	1.1×10^6	9.6×10^5	7.49×10^5	7.18×10^5	4.64×10^5
c33	8.95×10^5	7.05×10^5	4.62×10^5	5.56×10^5	4.54×10^5	2.92×10^5
c34	8.85×10^5	2.59×10^5	6.79×10^4	3.89×10^4	$0.\times10^5$	$0.\times10^5$
c35	2.23×10^5	1.81×10^5	1.81×10^5	4.48×10^4	4.48×10^4	4.48×10^4
c36	1.46×10^6	1.35×10^6	1.05×10^6	9.84×10^5	7.3×10^5	4.2×10^5
c37	6.6×10^6	3.99×10^6	2.33×10^6	2.04×10^6	1.52×10^6	1.25×10^6
c38	4.3×10^6	2.65×10^6	1.84×10^6	1.78×10^6	1.74×10^6	9.55×10^5
c39	3.22×10^6	1.84×10^6	1.4×10^6	1.36×10^6	1.07×10^6	8.07×10^5
c40	4.38×10^6	1.59×10^6	7.83×10^5	1.33×10^6	6.94×10^5	5.38×10^5
c41	7.1×10^6	2.12×10^6	1.65×10^6	1.57×10^6	1.4×10^6	1.16×10^6
c42	2.27×10^6	1.28×10^6	8.22×10^5	7.85×10^5	7.08×10^5	7.08×10^5
c43	1.34×10^6	8.03×10^5	6.55×10^5	3.49×10^5	3.41×10^5	3.78×10^5

Table A-10. Values of the area of potential instability (m^2) based on the slip tendency for selected planar surfaces (cont'd)

Simulation Case ID	ap3065	ap3075	ap3080	ap4065	ap4075	ap4080
c44	7.49×10^6	3.19×10^6	1.69×10^6	1.59×10^6	1.49×10^6	1.36×10^6
c45	2.09×10^6	1.35×10^6	1.11×10^6	1.17×10^6	1.0×10^6	8.02×10^5
c46	1.86×10^6	1.16×10^6	8.93×10^5	1.14×10^6	9.46×10^5	7.58×10^5
c47	1.21×10^6	7.57×10^5	5.31×10^5	7.38×10^5	5.91×10^5	4.56×10^5
c48	2.32×10^6	1.45×10^6	1.27×10^6	1.4×10^6	1.24×10^6	1.13×10^6
c49	1.4×10^6	8.07×10^6	5.64×10^5	5.9×10^5	4.96×10^5	3.37×10^5
c50	9.88×10^5	9.3×10^5	3.66×10^5	6.34×10^5	3.0×10^5	6.79×10^4
c51	4.12×10^5	3.99×10^5	2.18×10^5	8.96×10^4	1.12×10^5	1.12×10^5
c52	2.23×10^6	1.26×10^6	1.2×10^6	8.99×10^5	7.73×10^5	3.8×10^5
c53	1.51×10^6	9.13×10^5	5.37×10^5	5.29×10^5	5.03×10^5	3.61×10^5
c54	7.85×10^5	7.08×10^5	6.24×10^5	6.4×10^5	5.56×10^5	4.27×10^5
c55	3.38×10^5	2.6×10^5	2.6×10^5	1.24×10^5	1.88×10^5	1.54×10^5
c56	1.81×10^6	1.54×10^6	1.27×10^6	1.3×10^6	8.99×10^5	8.12×10^5
c57	5.85×10^6	1.93×10^6	1.09×10^6	1.28×10^6	9.0×10^5	7.98×10^5
c58	2.45×10^6	1.65×10^6	1.25×10^6	1.35×10^6	1.14×10^6	8.2×10^5
c59	2.18×10^6	1.27×10^6	7.81×10^5	8.62×10^5	6.81×10^5	6.13×10^5
c60	6.34×10^6	2.79×10^6	1.55×10^6	1.78×10^6	1.57×10^6	9.35×10^5
c61	2.04×10^6	1.16×10^6	1.04×10^6	1.06×10^6	8.6×10^5	5.97×10^5
c62	1.78×10^6	1.01×10^6	8.93×10^5	9.46×10^5	8.26×10^5	8.3×10^5
c63	1.08×10^6	6.38×10^5	5.31×10^5	6.17×10^5	4.19×10^5	4.56×10^5
c64	2.5×10^6	1.6×10^6	1.23×10^6	1.43×10^6	1.17×10^6	9.37×10^5
c65	4.17×10^6	1.52×10^6	7.41×10^5	8.57×10^5	7.08×10^5	4.19×10^5

Table A-10. Values of the area of potential instability (m^2) based on the slip tendency for selected planar surfaces (cont'd)

Simulation Case ID	ap3065	ap3075	ap3080	ap4065	ap4075	ap4080
c66	2.53×10^6	1.54×10^6	8.01×10^5	8.36×10^5	7.56×10^5	7.56×10^5
c67	$2.\times10^6$	8.08×10^5	6.34×10^5	5.55×10^5	5.03×10^5	4.69×10^5
c68	5.91×10^6	2.27×10^6	1.48×10^6	1.36×10^6	1.32×10^6	1.1×10^6

APPENDIX B

SENSITIVITY PLOTS OF RESPONSE VERSUS INPUT VARIABLES

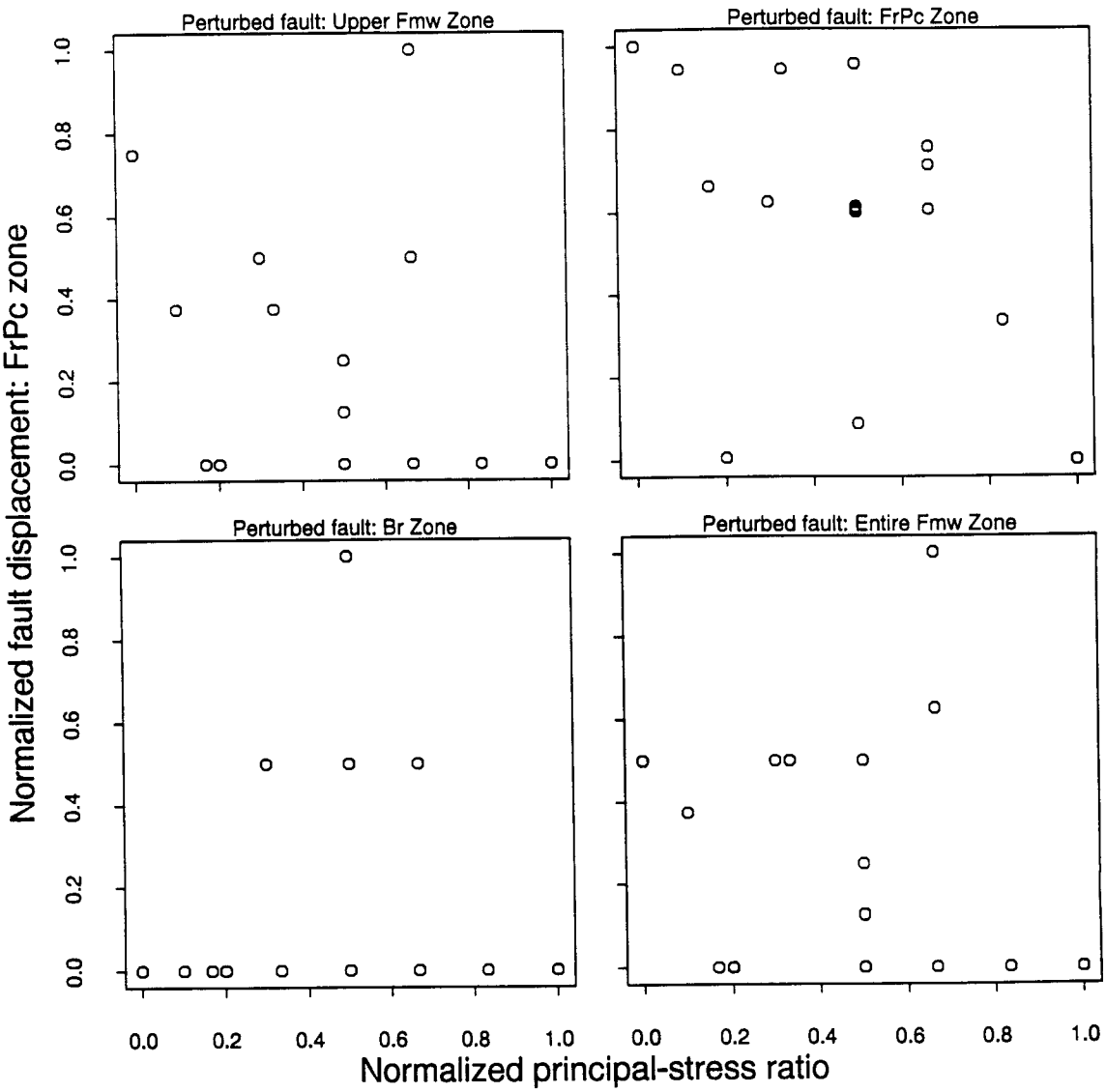

Figure B-1. Sensitivity of total fault displacement in the FrPc zone to changes in the value of the principal stress ratio k_3

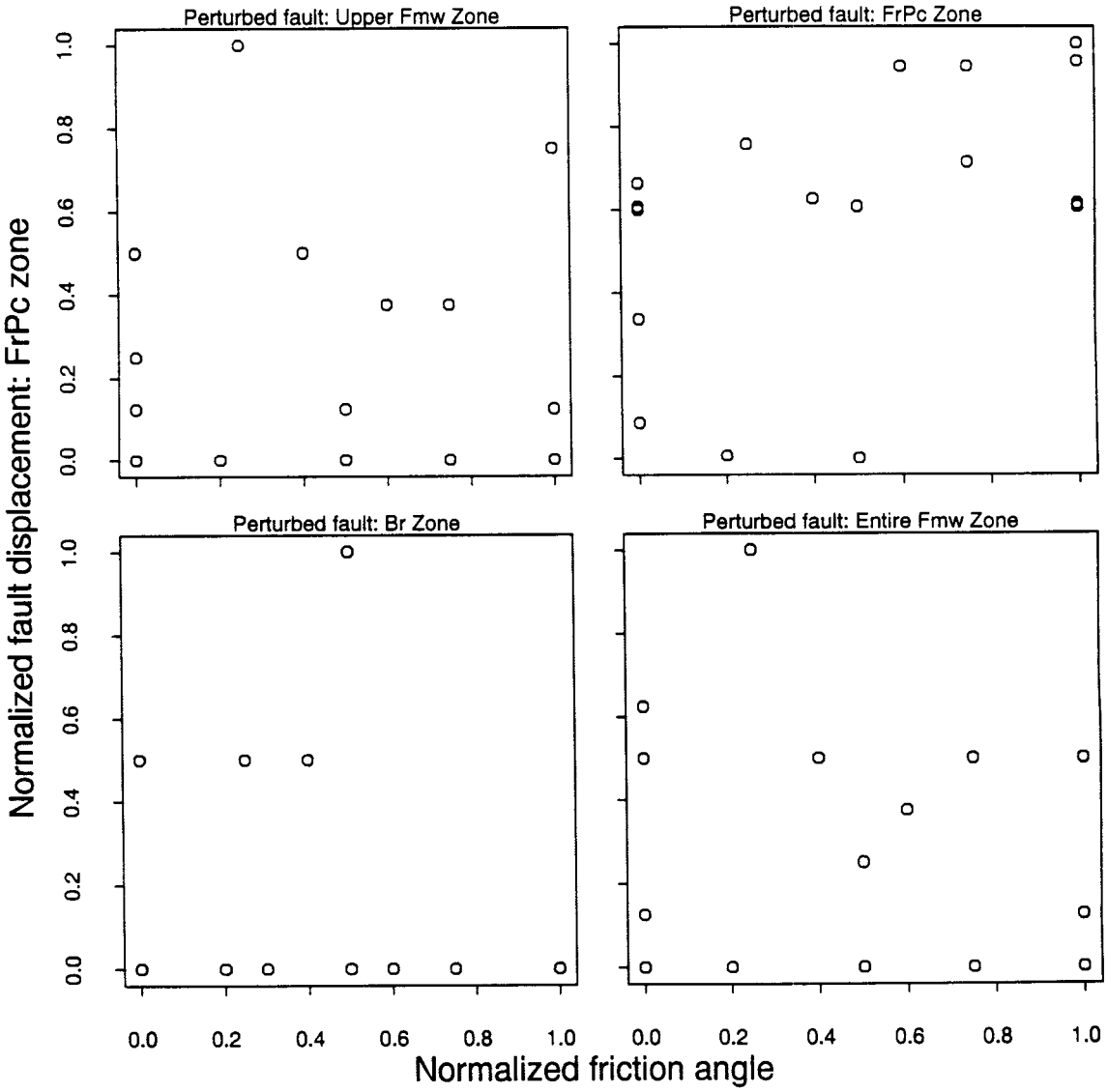

Figure B-2. Sensitivity of total fault displacement in the FrPc zone to changes in the value of the friction angle

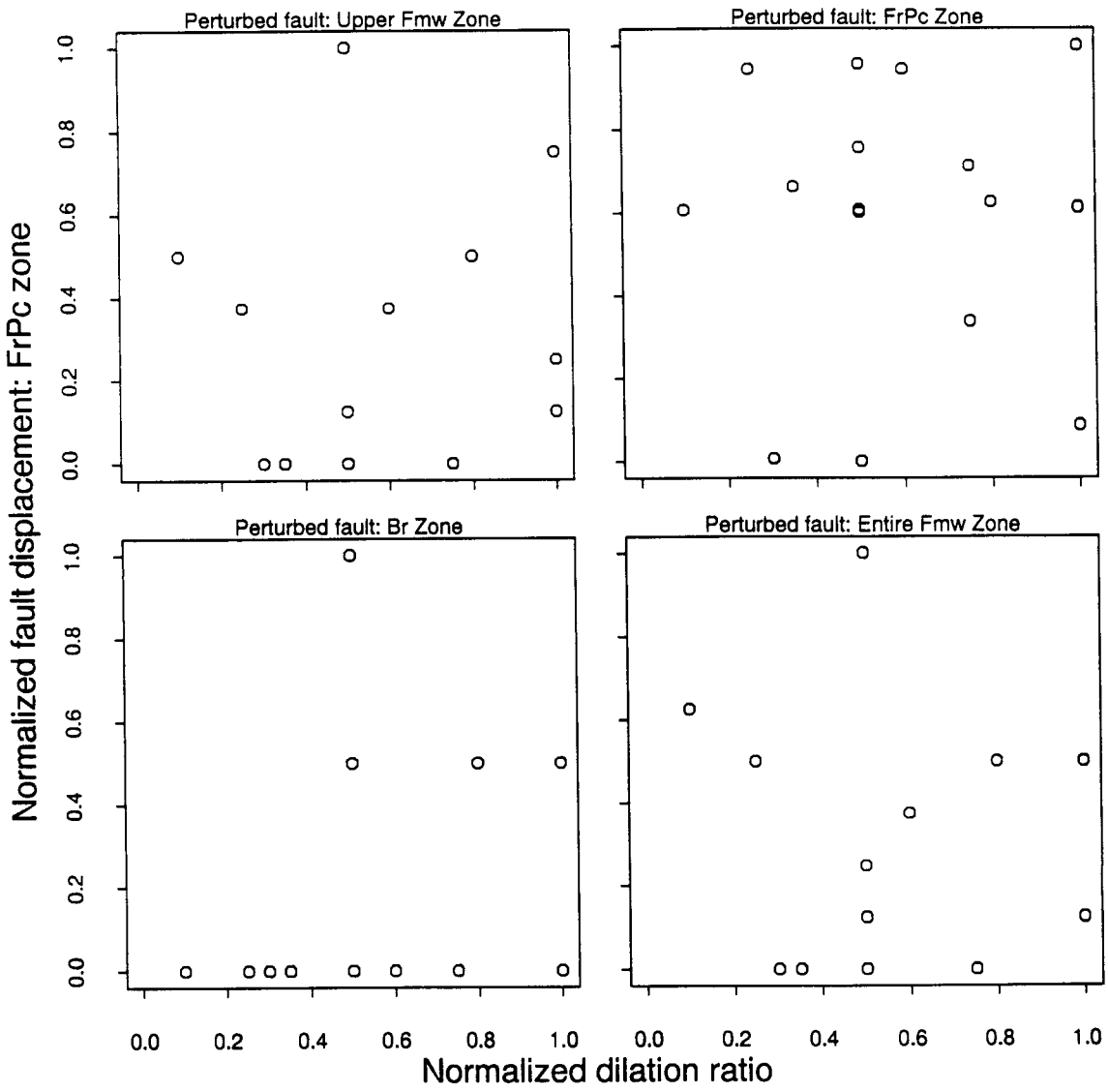

Figure B-3. Sensitivity of total fault displacement in the FrPc zone to changes in the value of the dilation angle

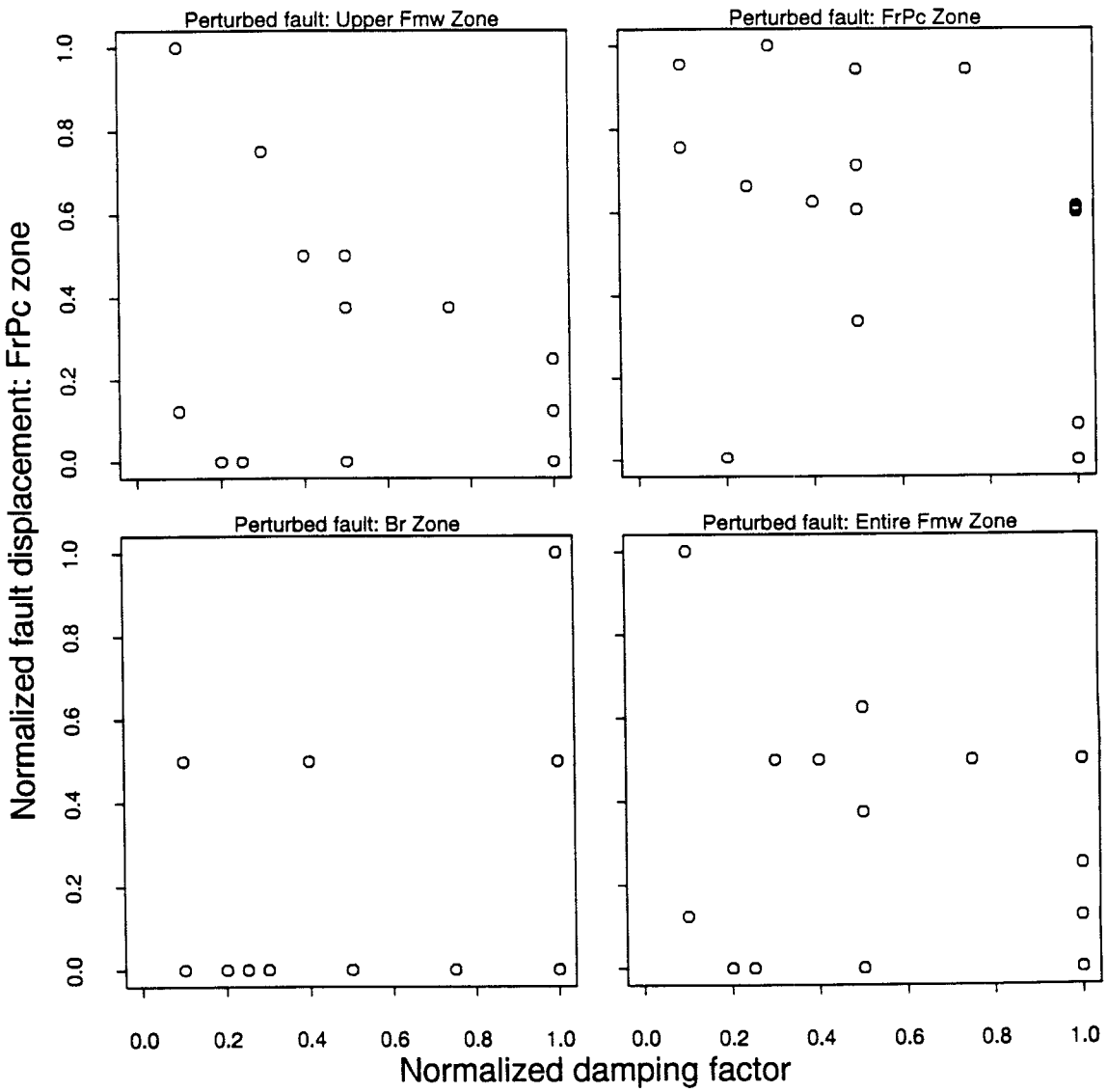

Figure B-4. Sensitivity of total fault displacement in the FrPc zone to changes in the value of the damping factor

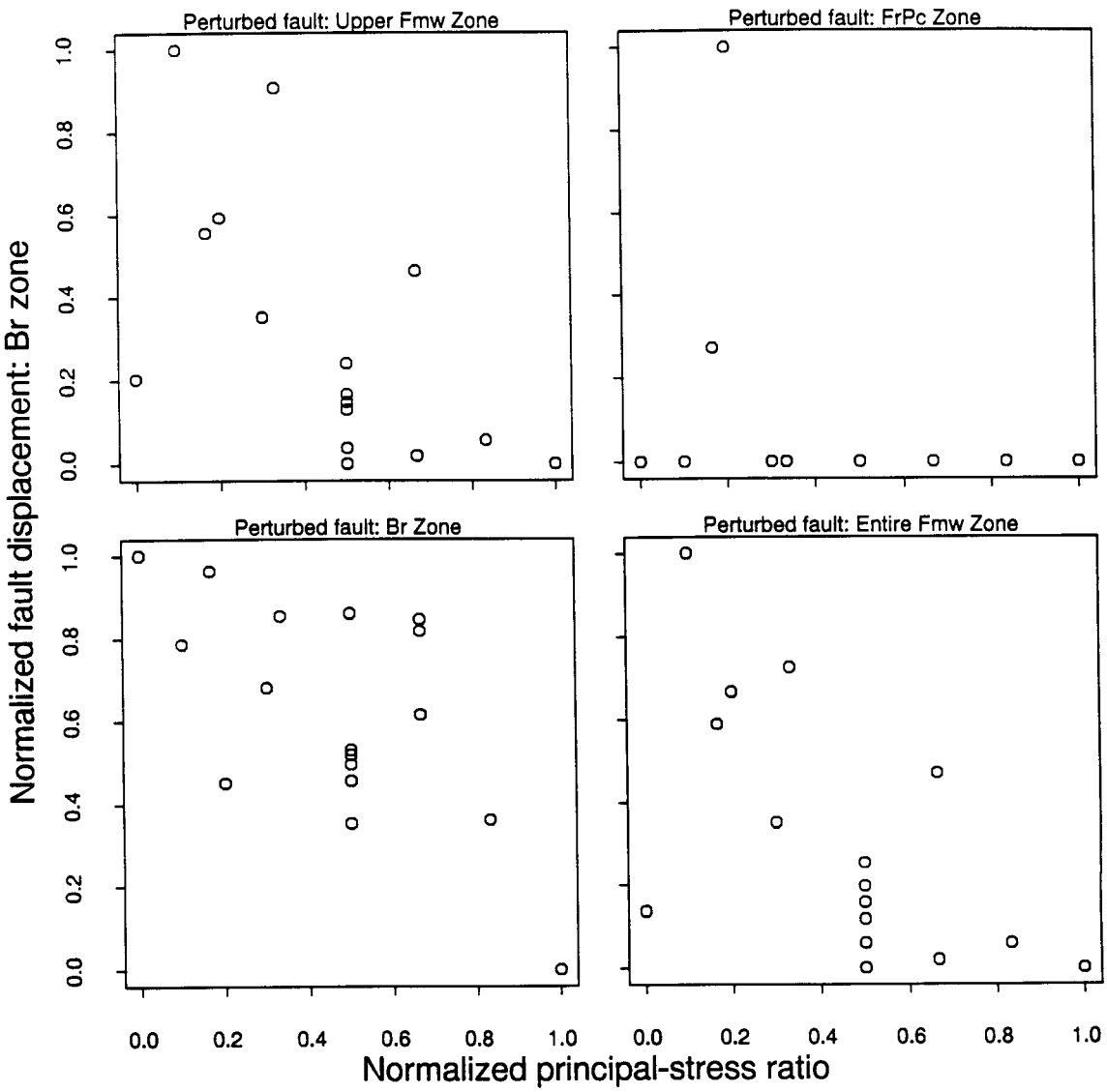

Figure B-5. Sensitivity of total fault displacement in the Br zone to changes in the value of the principal stress ratio k_3

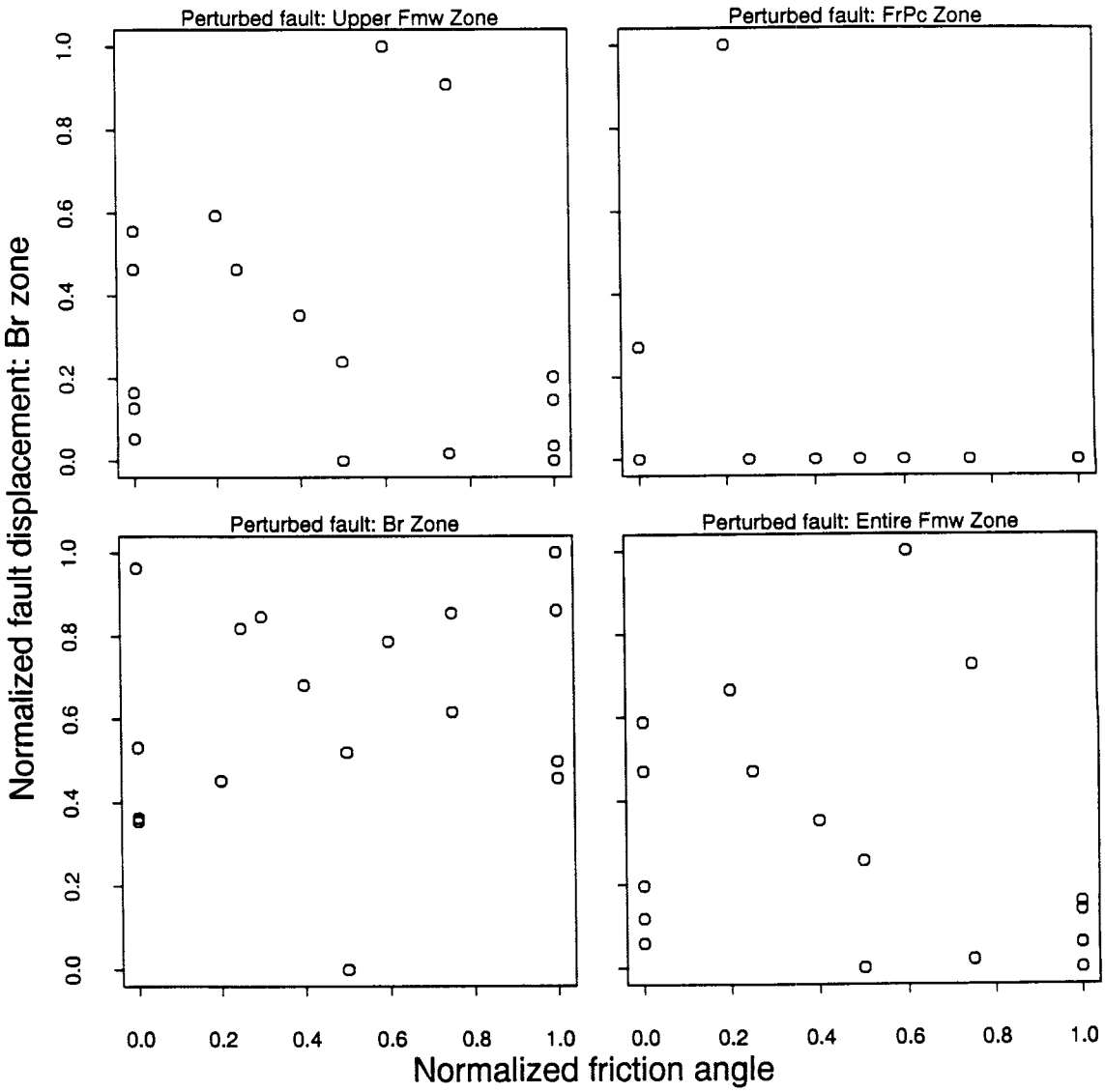

Figure B-6. Sensitivity of total fault displacement in the Br zone to changes in the value of the friction angle

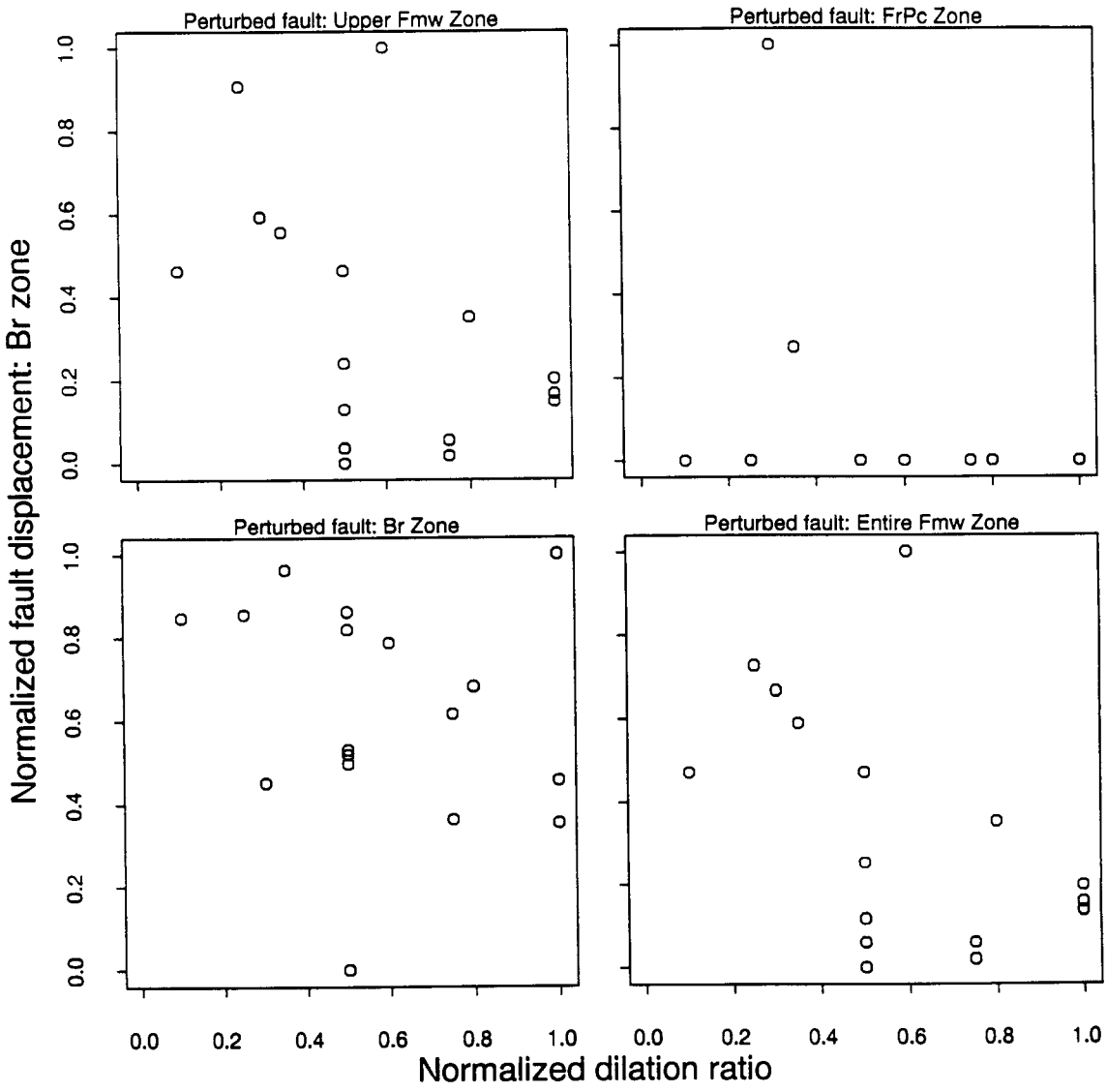

Figure B-7. Sensitivity of total fault displacement in the Br zone to changes in the value of the dilation angle

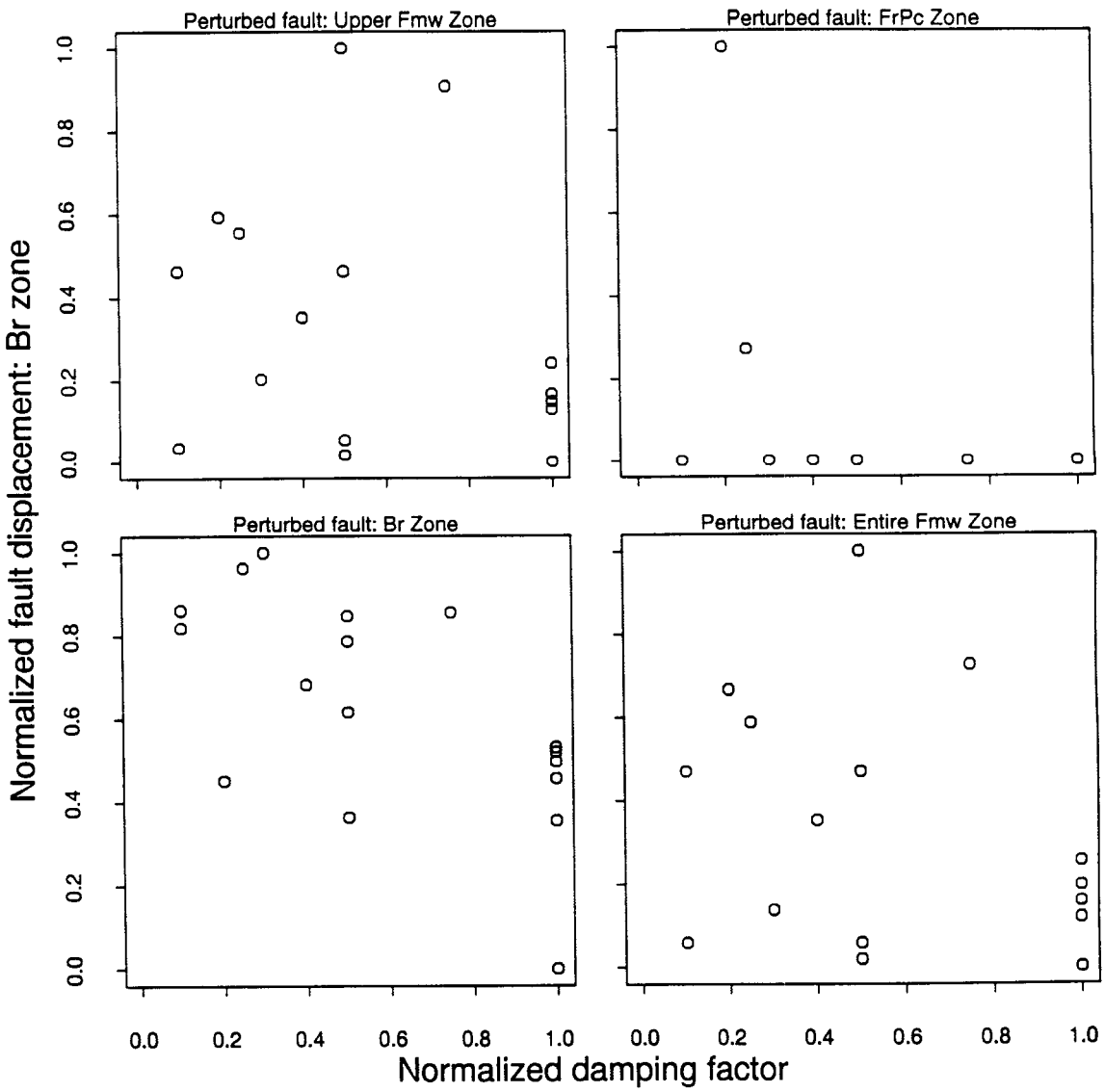

Figure B-8. Sensitivity of total fault displacement in the Br zone to changes in the value of the damping factor

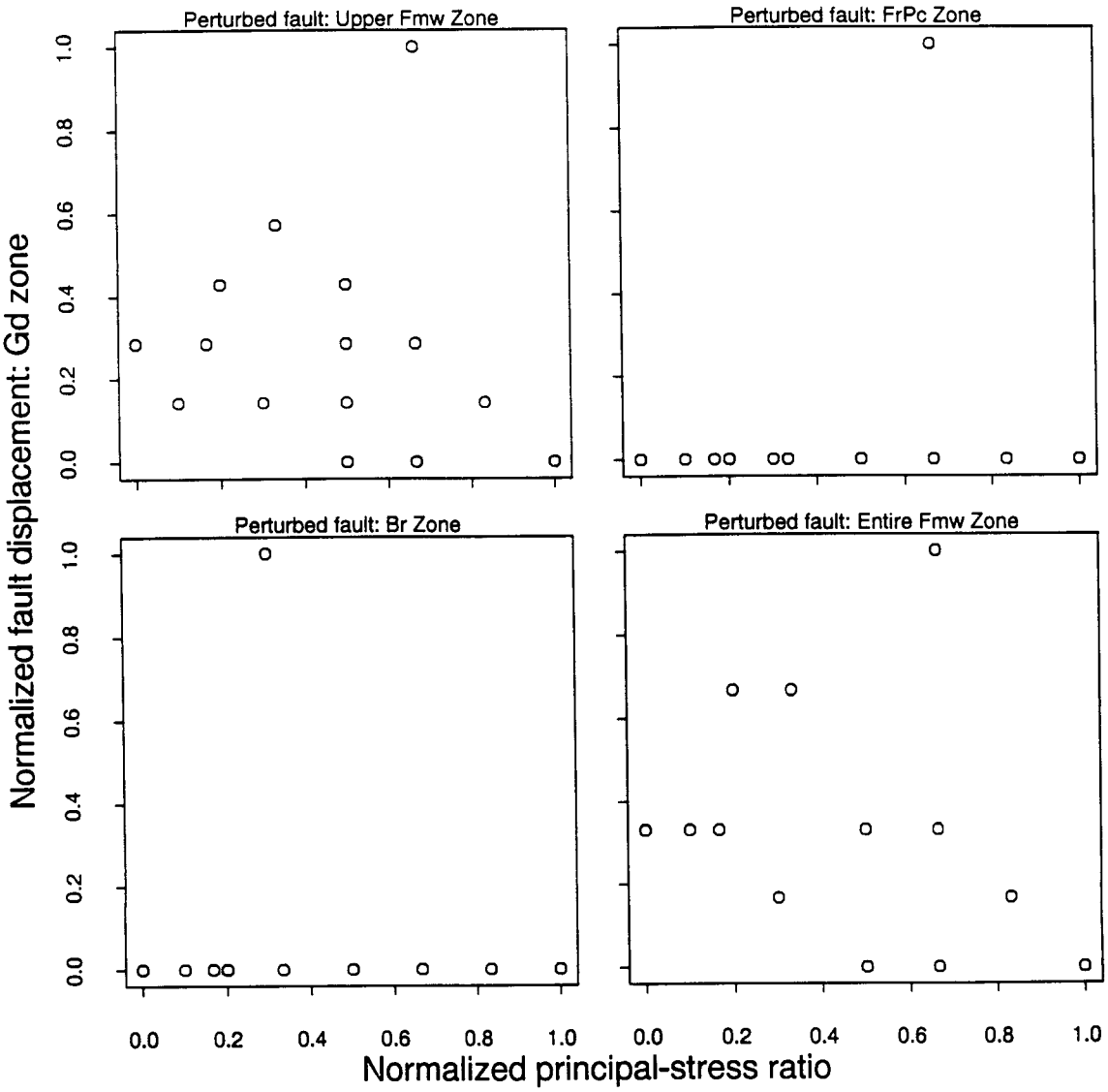

Figure B-9. Sensitivity of total fault displacement in the Gd zone to changes in the value of the principal stress ratio k_3

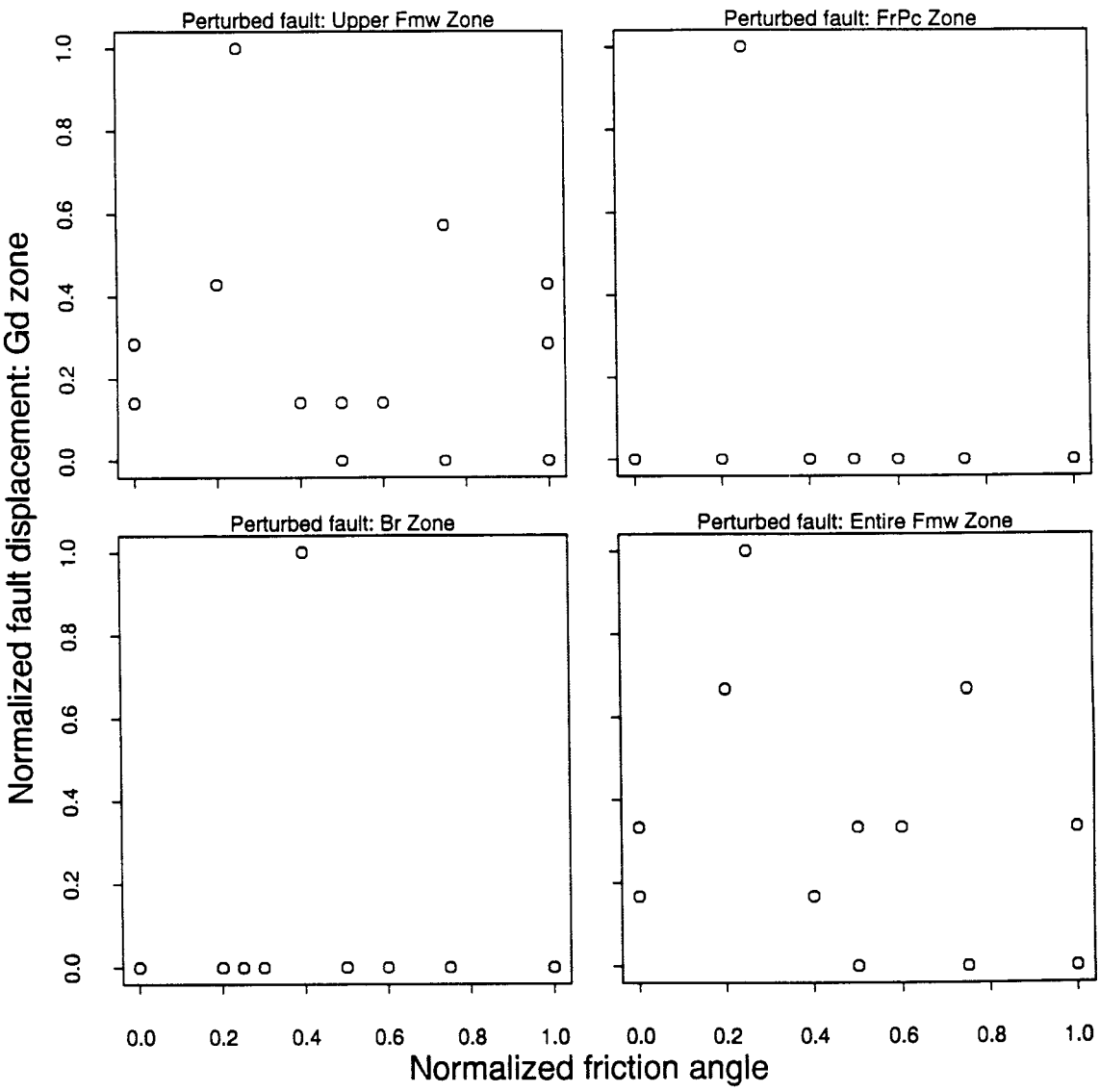

Figure B-10. Sensitivity of total fault displacement in the Gd zone to changes in the value of the friction angle

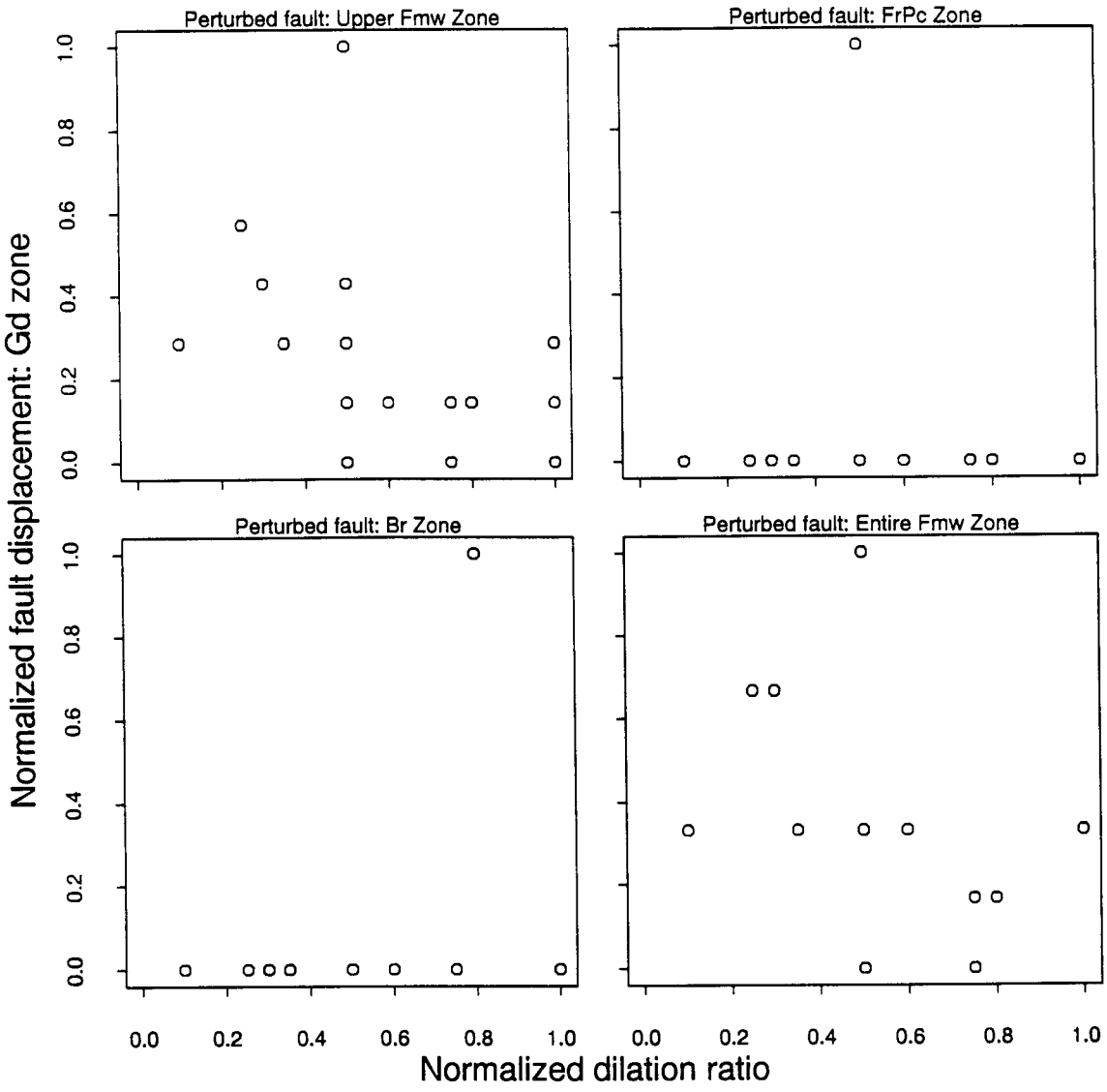

Figure B-11. Sensitivity of total fault displacement in the Gd zone to changes in the value of the dilation angle

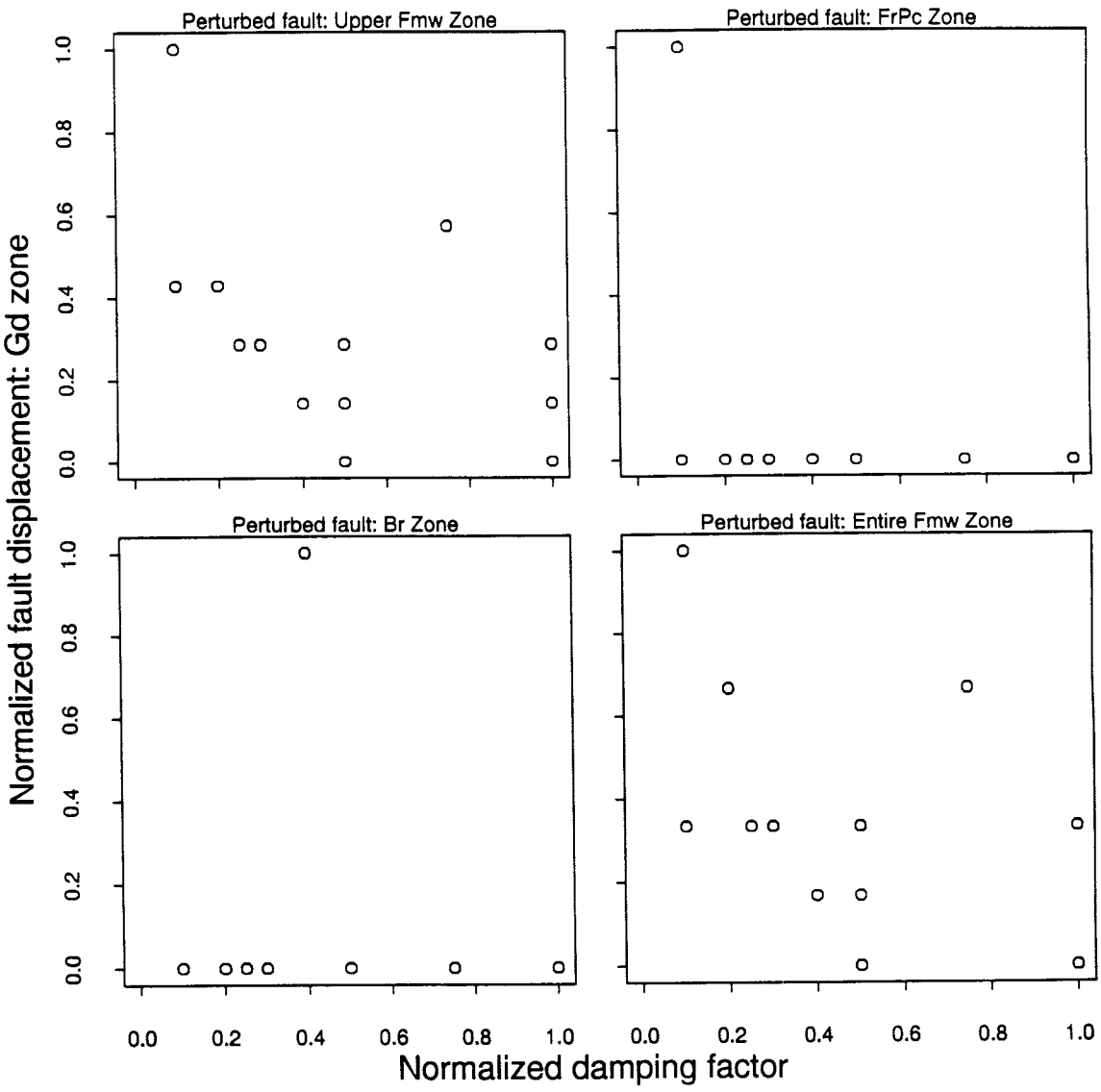

Figure B-12. Sensitivity of total fault displacement in the Gd zone to changes in the value of the damping factor

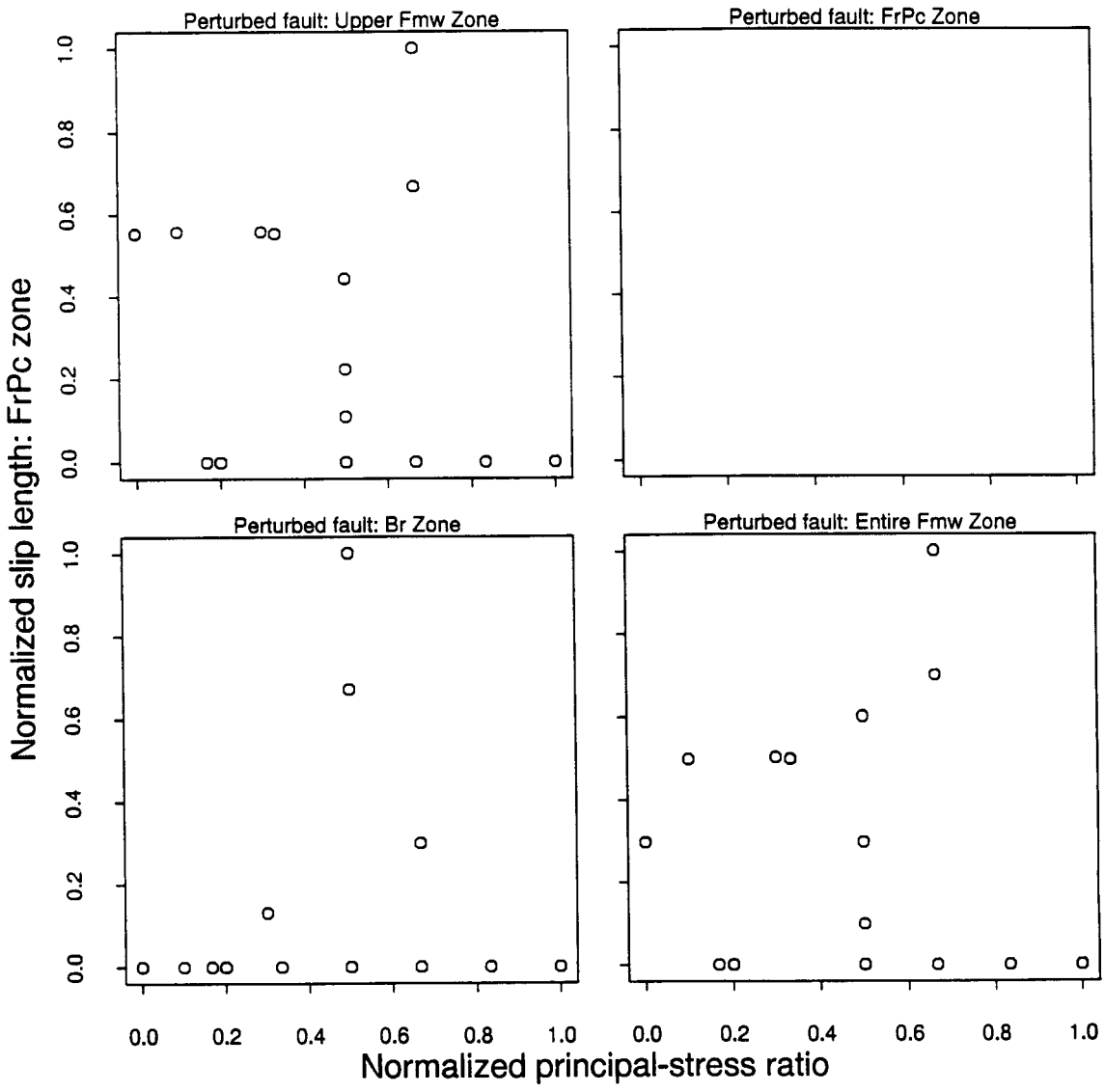

Figure B-13. Sensitivity of FrPc-zone slip length to changes in the value of the principal stress ratio k_3

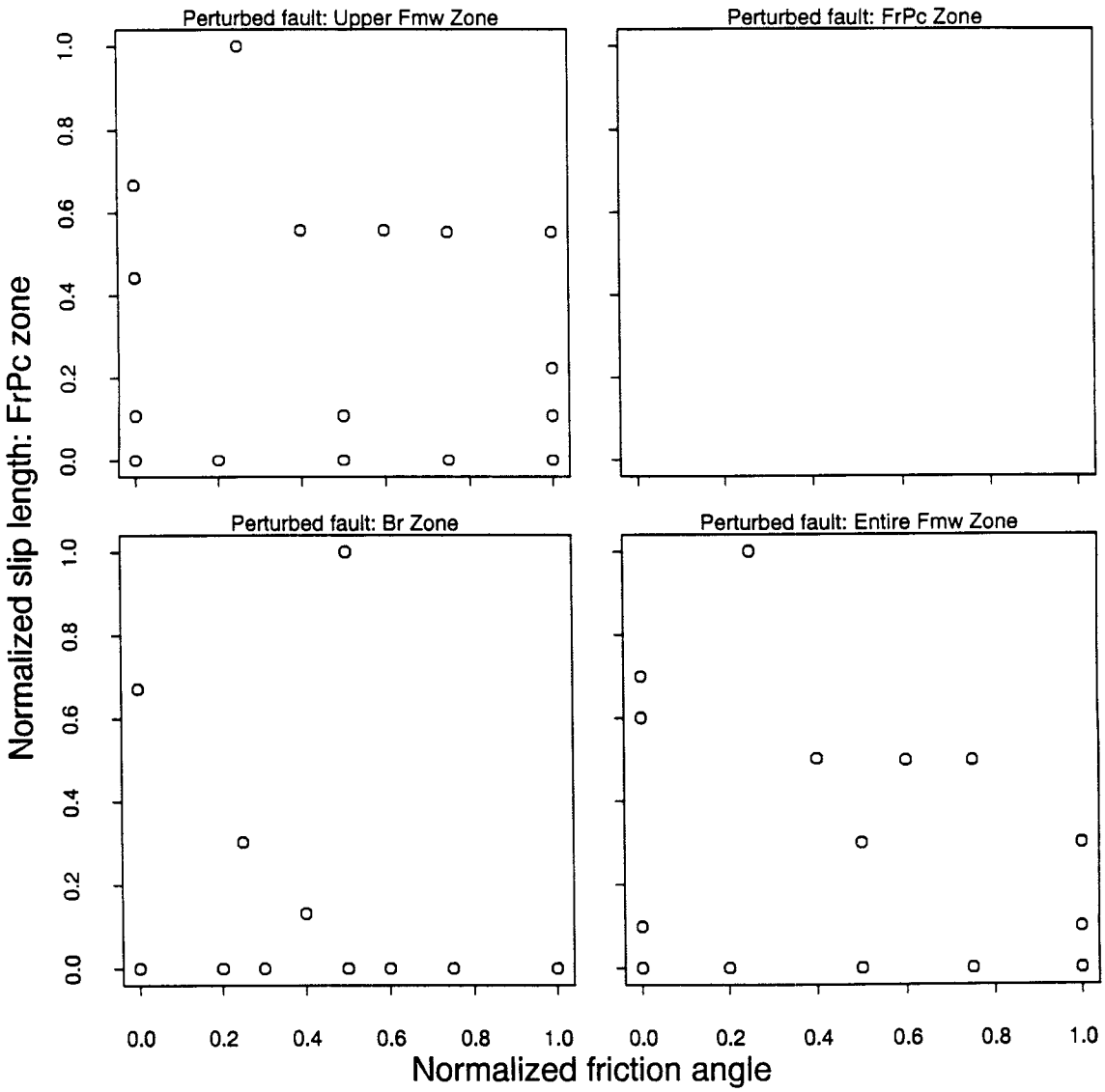

Figure B-14. Sensitivity of FrPc-zone slip length to changes in the value of the friction angle

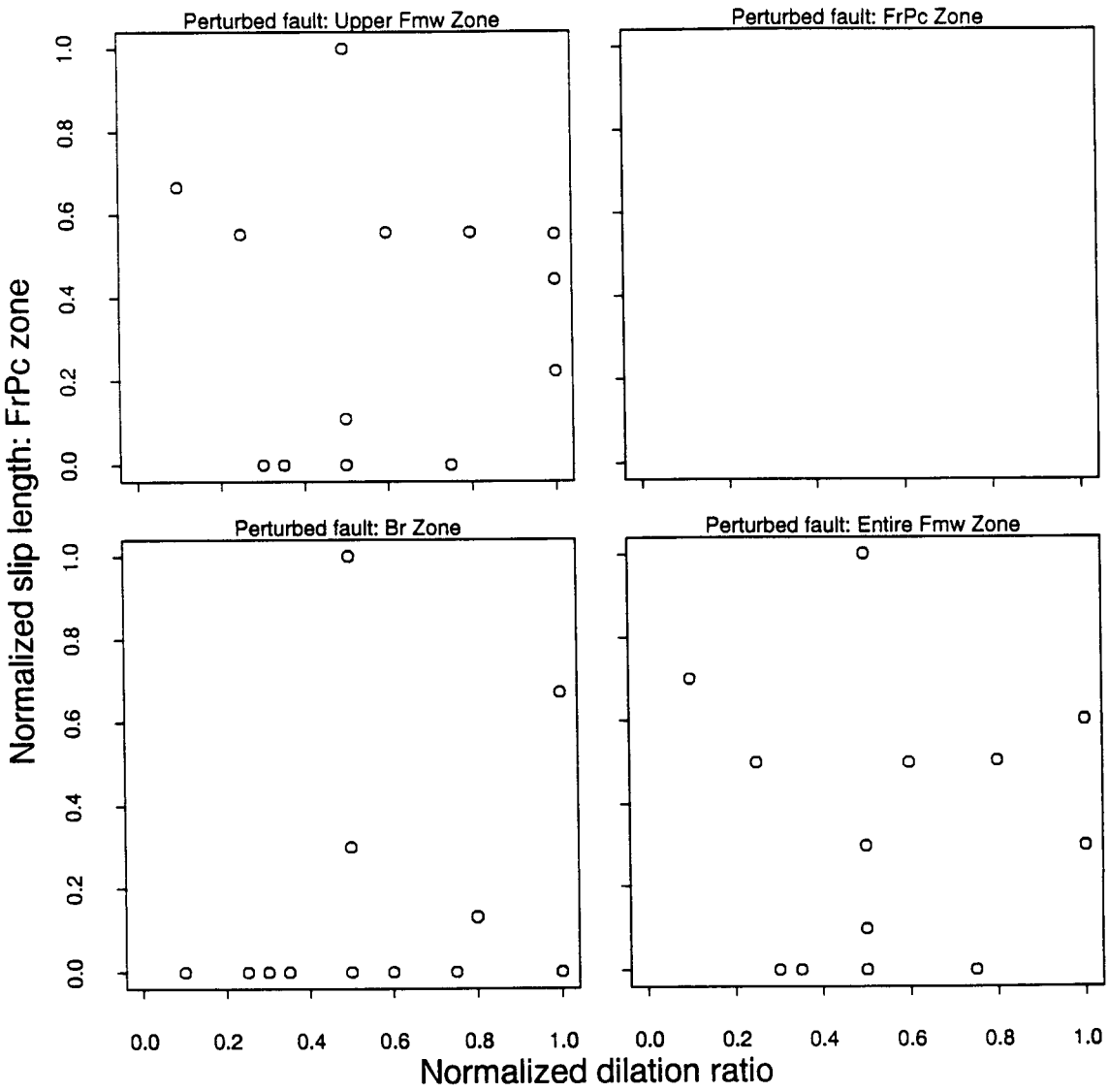

Figure B-15. Sensitivity of FrPc-zone slip length to changes in the value of the dilation angle

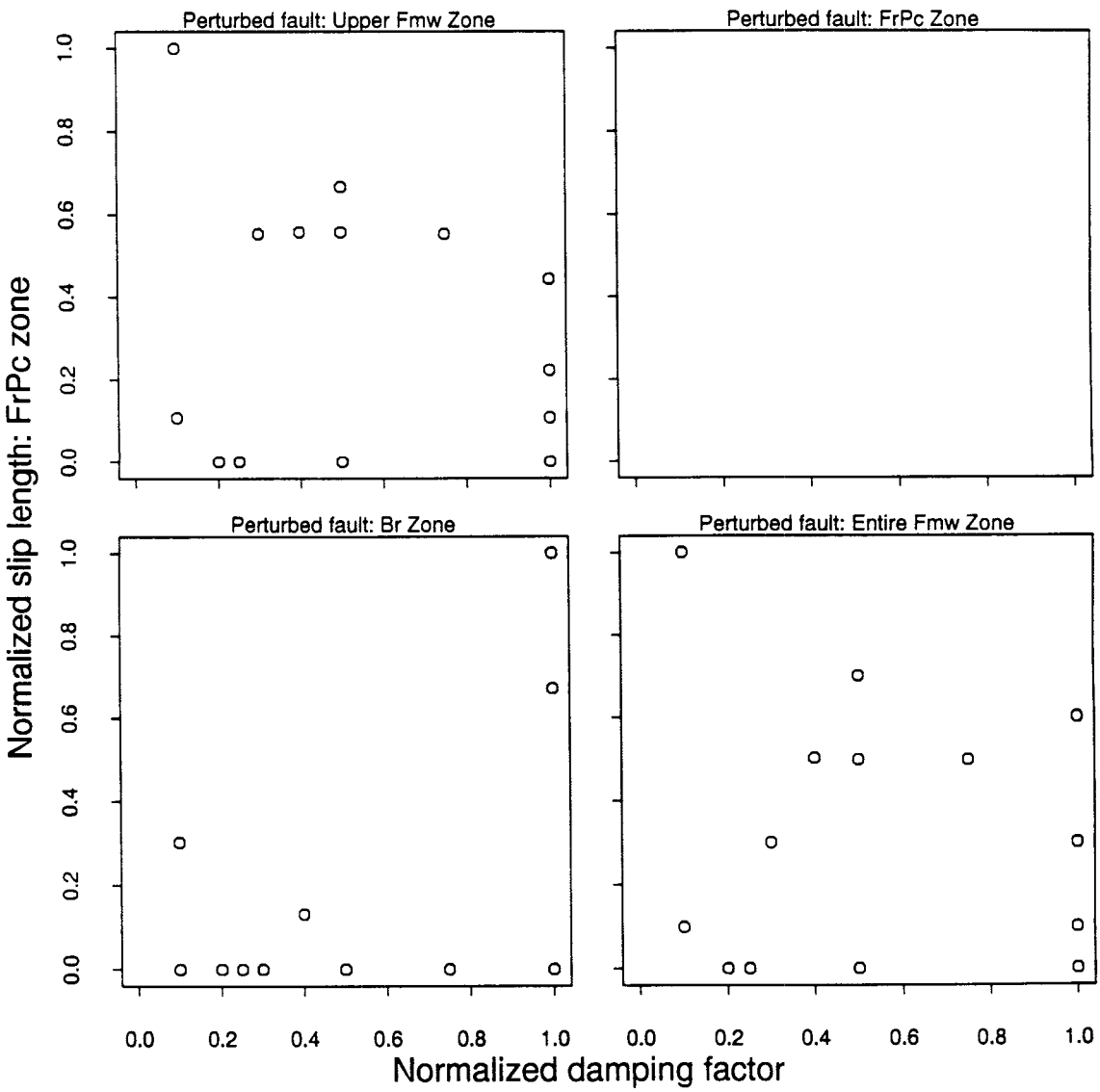

Figure B-16. Sensitivity of FrPc-zone slip length to changes in the value of the damping factor

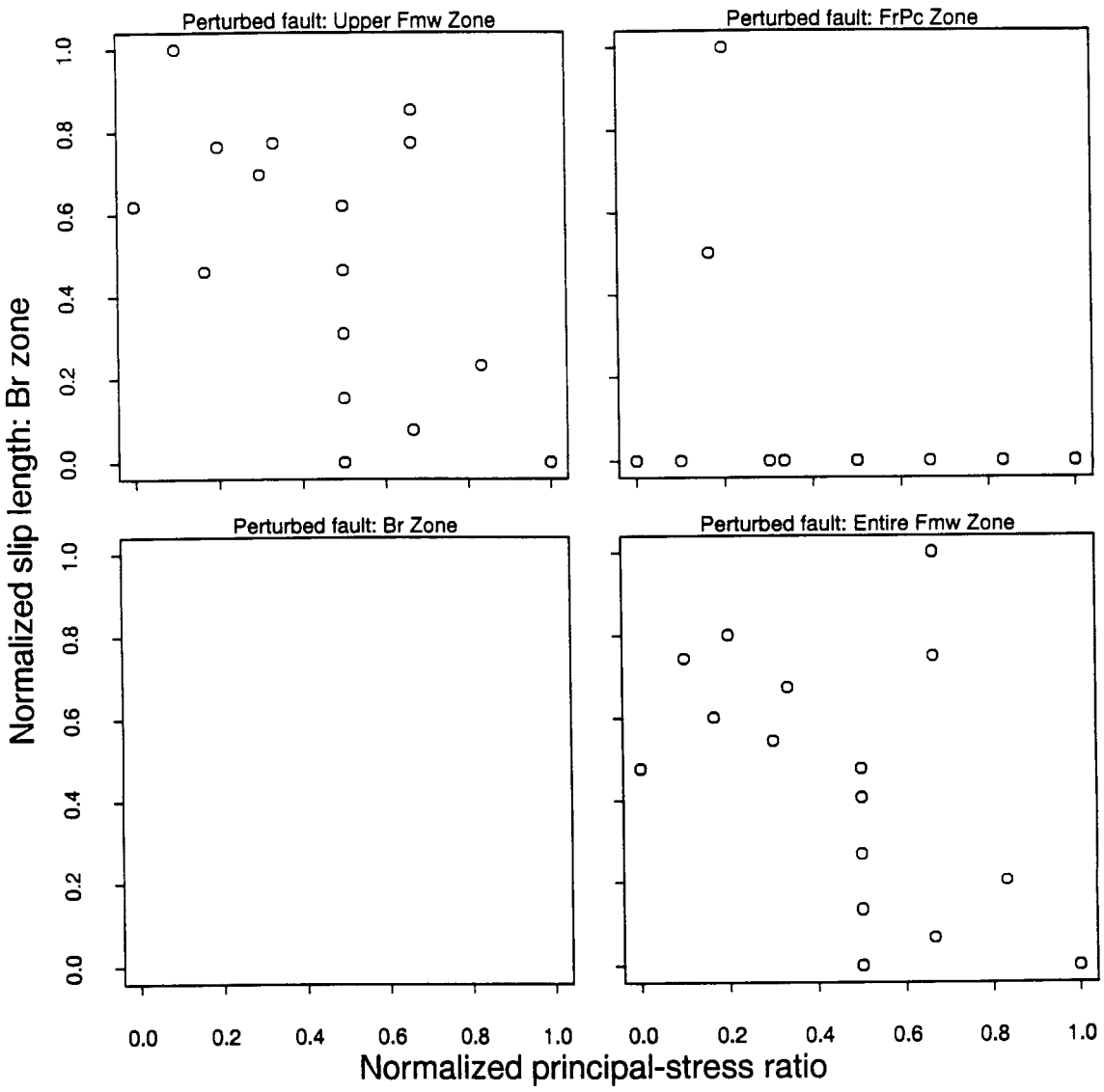

Figure B-17. Sensitivity of Br-zone slip length to changes in the value of the principal stress ratio k_3

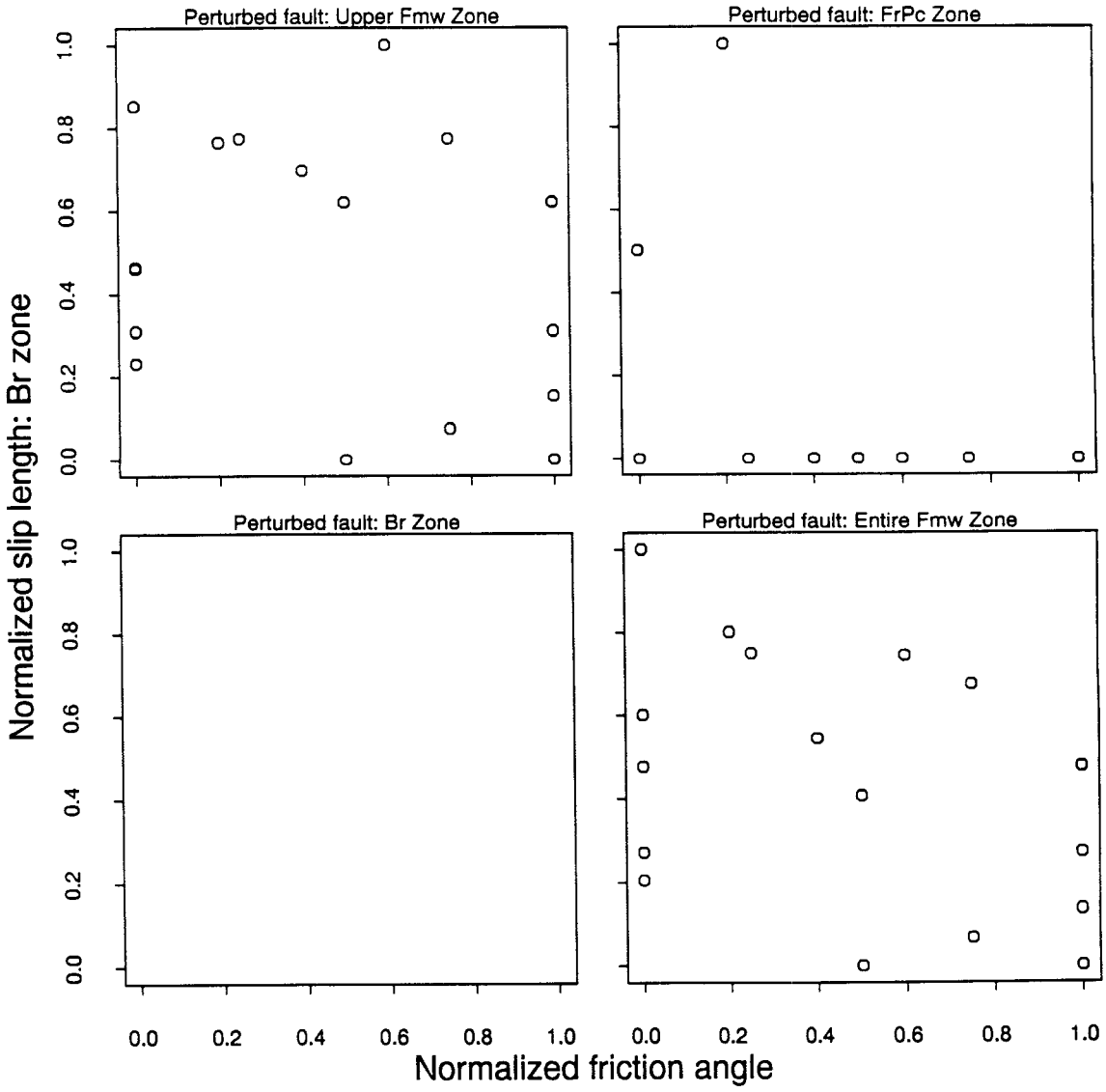

Figure B-18. Sensitivity of Br-zone slip length to changes in the value of the friction angle

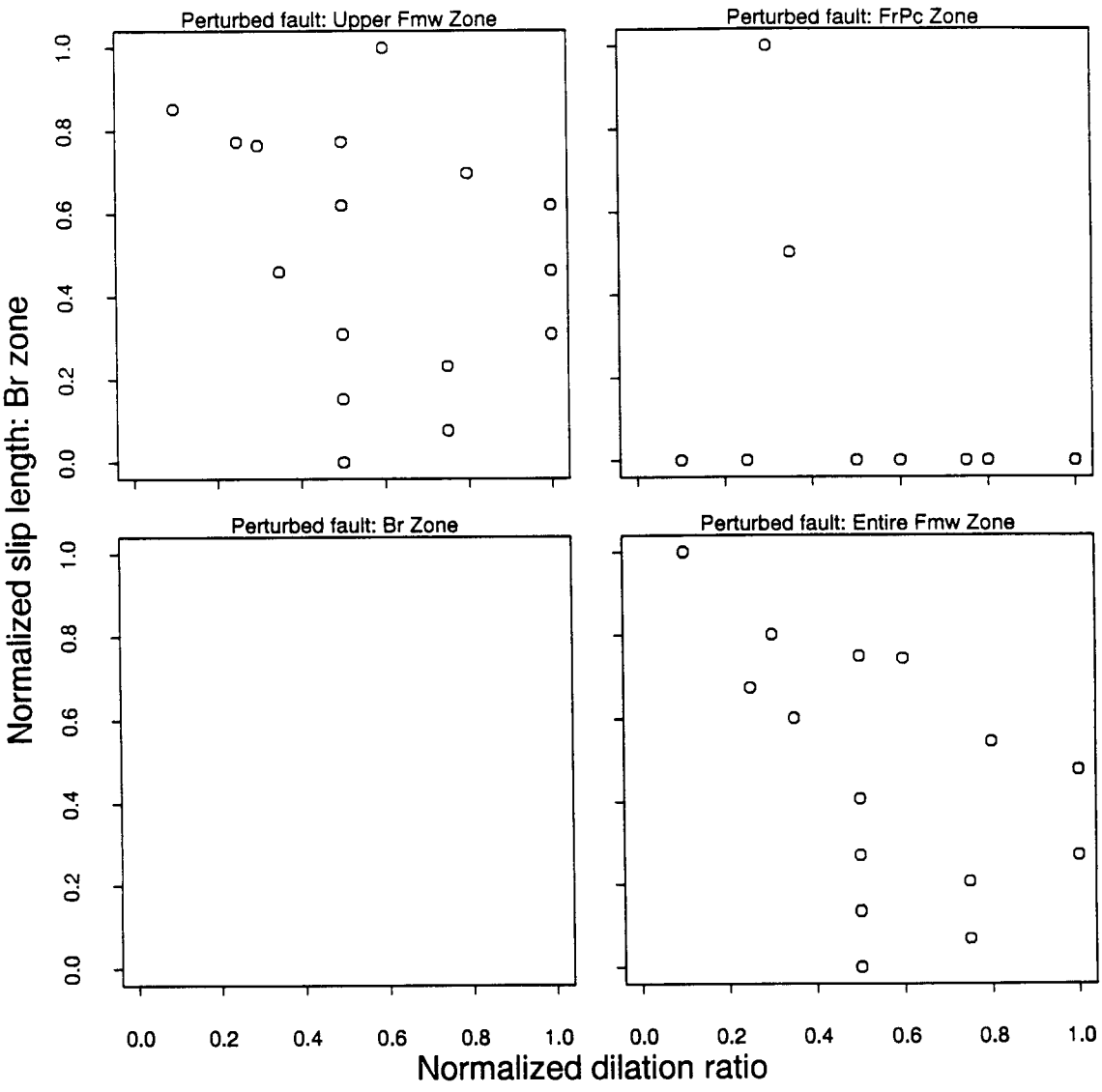

Figure B-19. Sensitivity of Br-zone slip length to changes in the value of the dilation angle

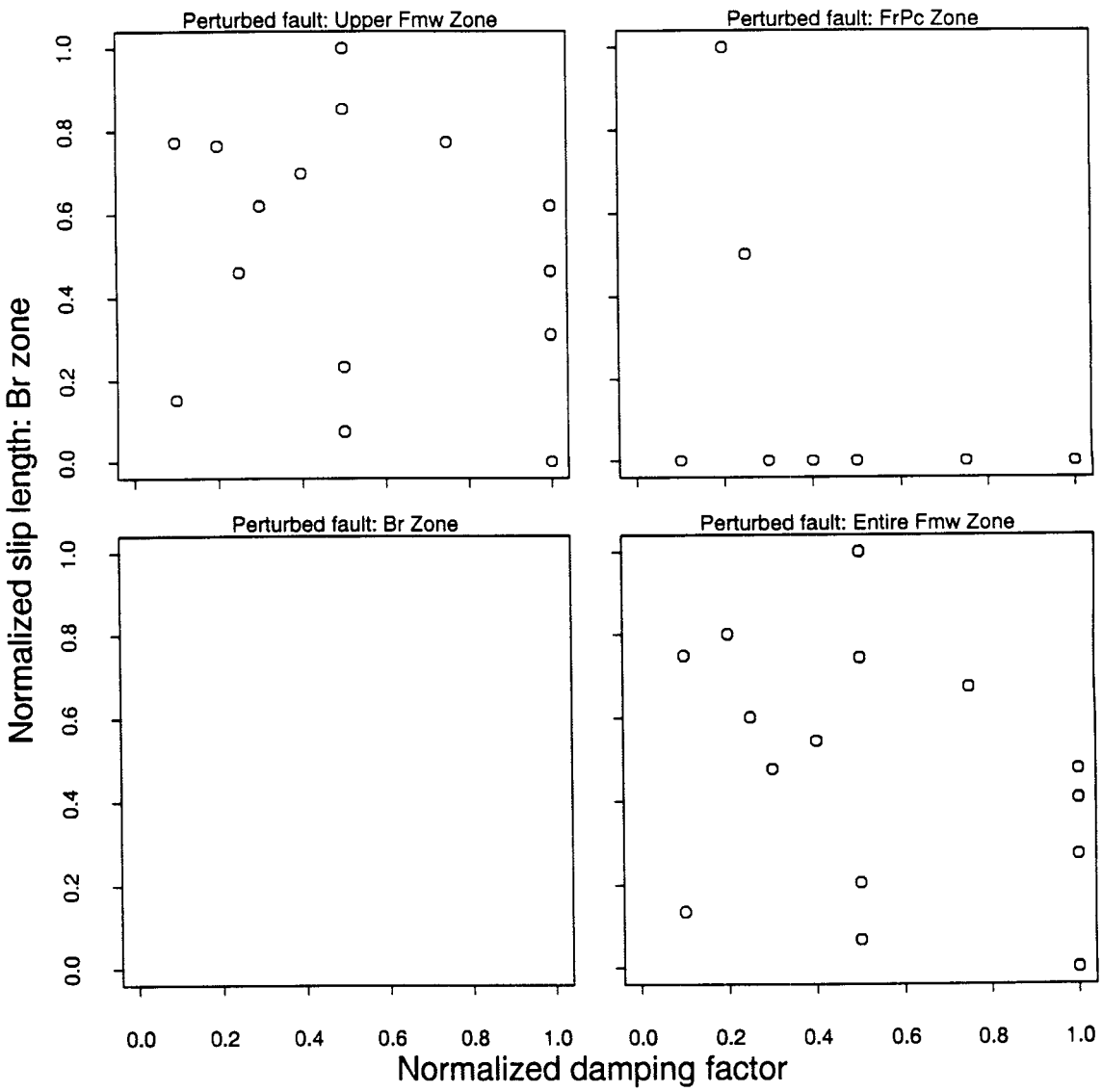

Figure B-20. Sensitivity of Br-zone slip length to changes in the value of the damping factor

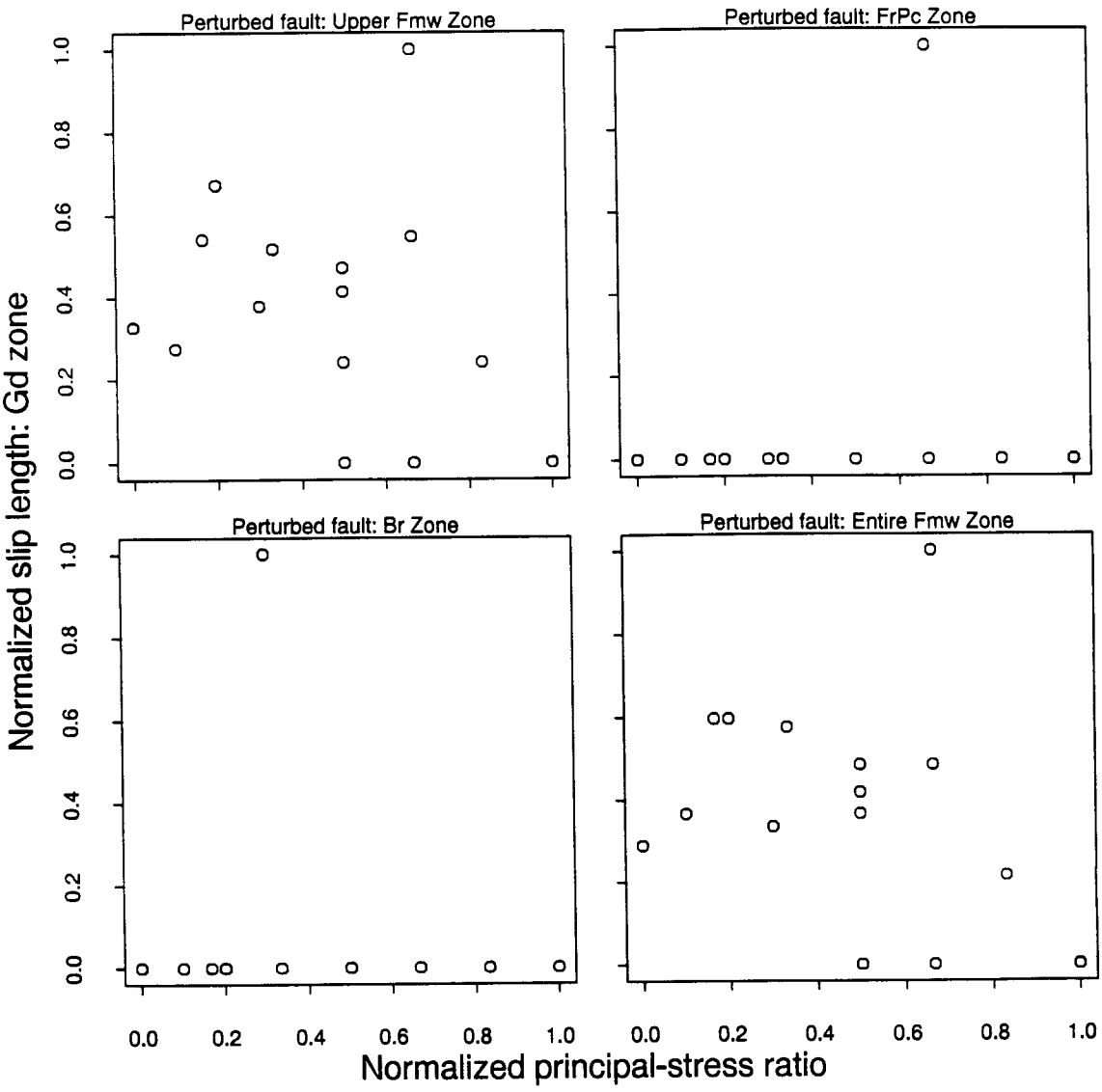

Figure B-21. Sensitivity of Gd-zone slip length to changes in the value of the principal stress ratio k_3

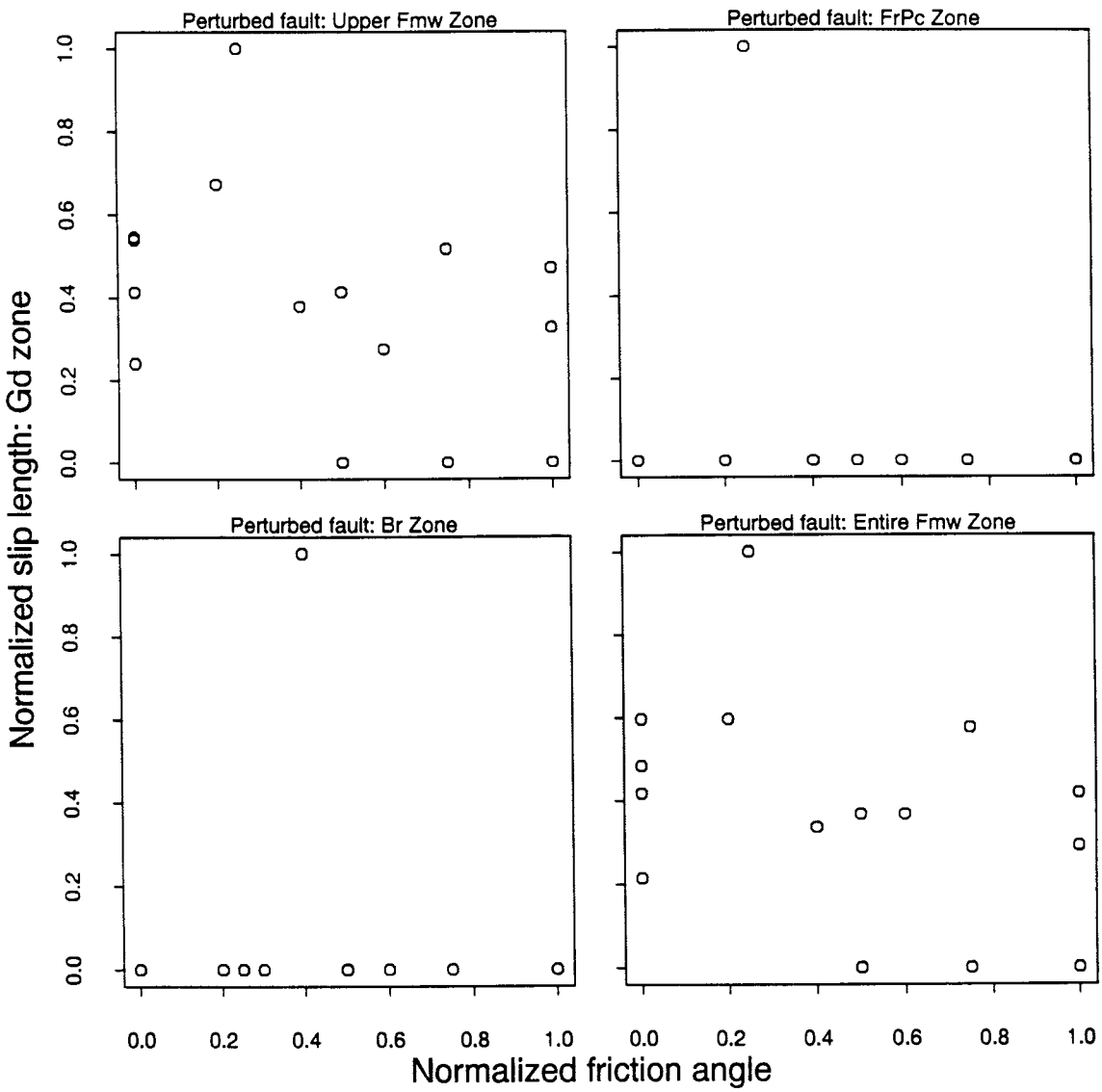

Figure B-22. Sensitivity of Gd-zone slip length to changes in the value of the friction angle

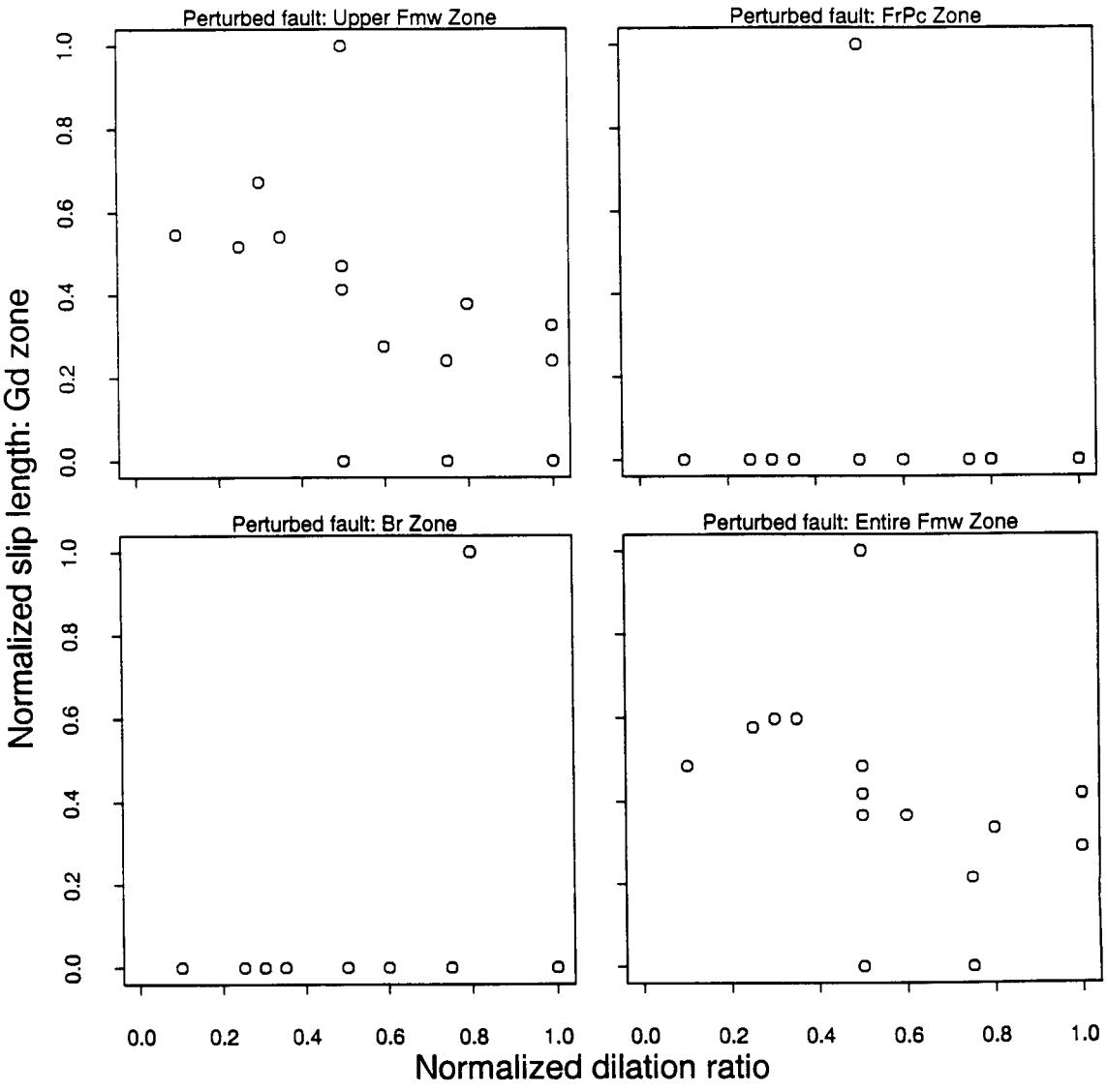

Figure B-23. Sensitivity of Gd-zone slip length to changes in the value of the dilation angle

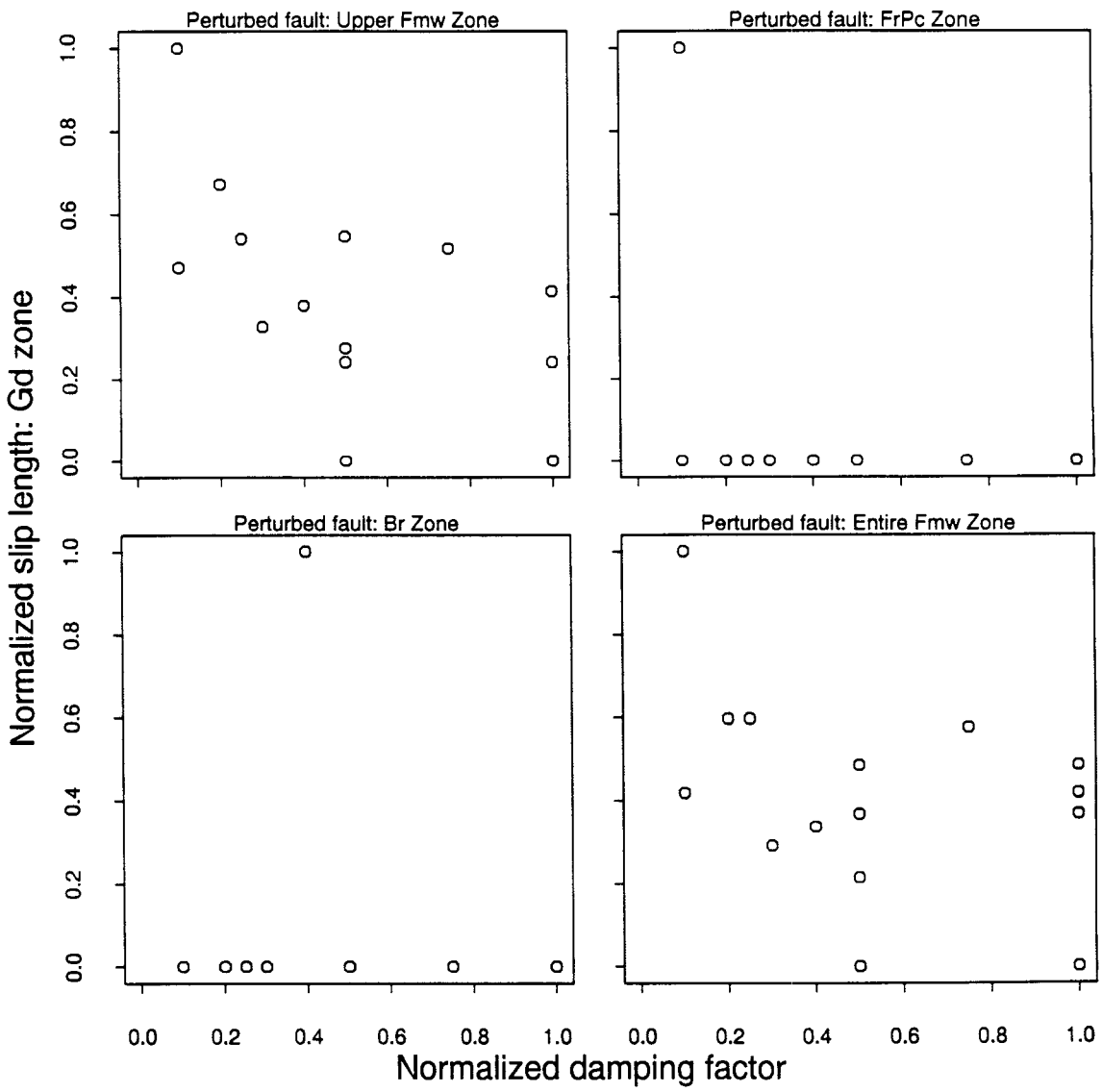

Figure B-24. Sensitivity of Gd-zone slip length to changes in the value of the damping factor

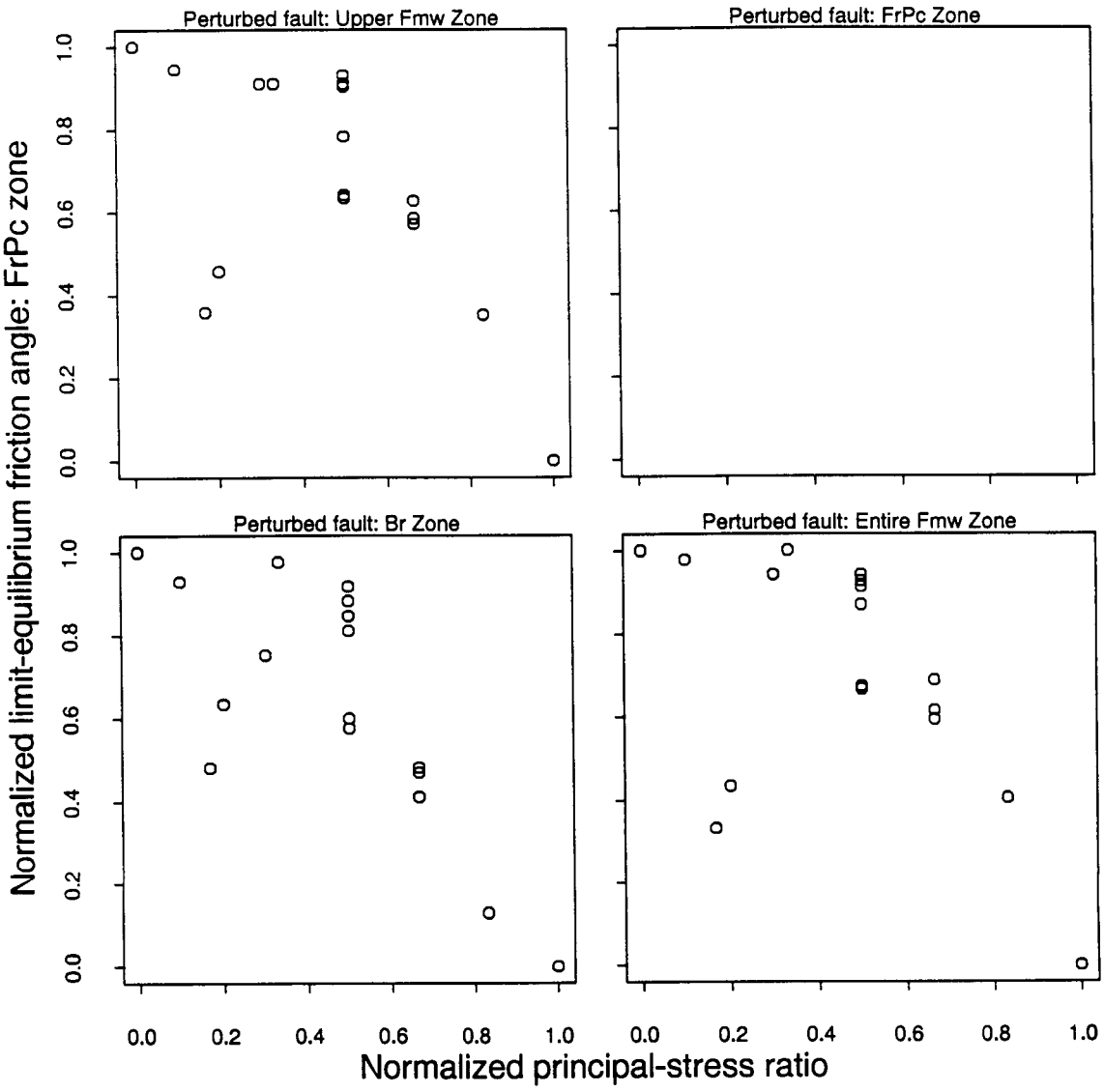

Figure B-25. Sensitivity of the limit-equilibrium friction angle for the FrPc zone to changes in the value of the principal stress ratio k_3

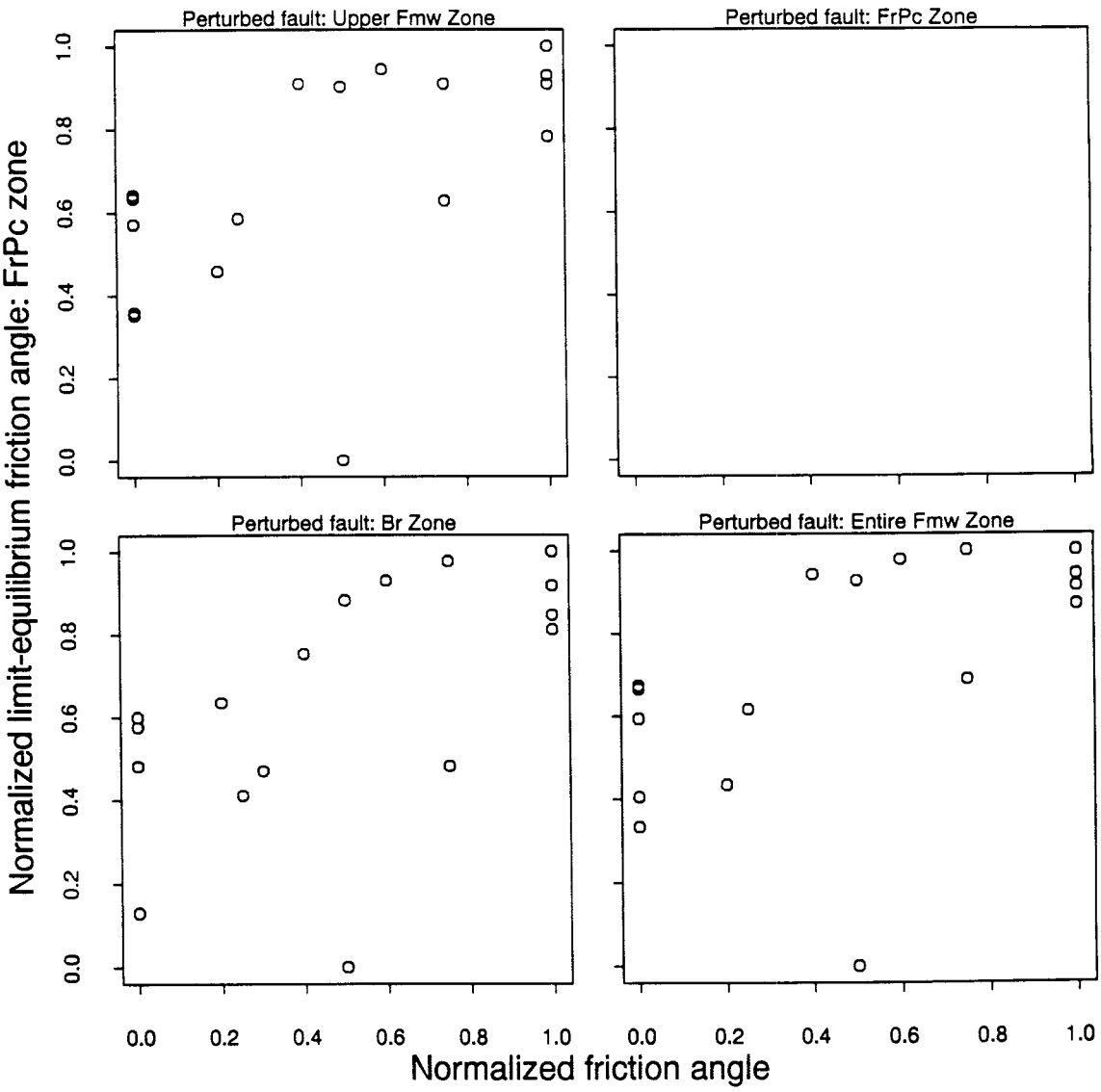

Figure B-26. Sensitivity of the limit-equilibrium friction angle for the FrPc zone to changes in the value of the friction angle

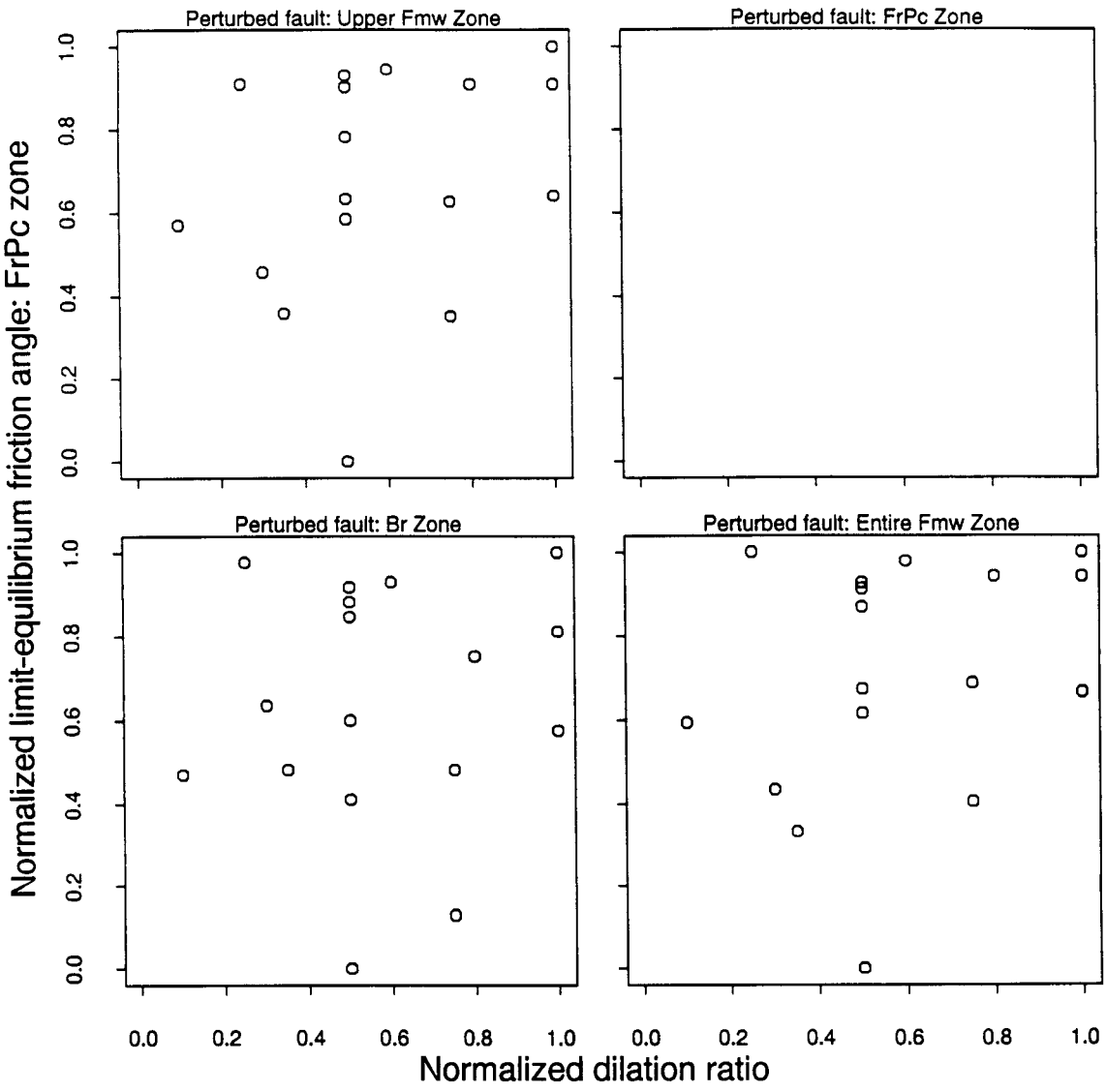

Figure B-27. Sensitivity of the limit-equilibrium friction angle for the FrPc zone to changes in the value of the dilation angle

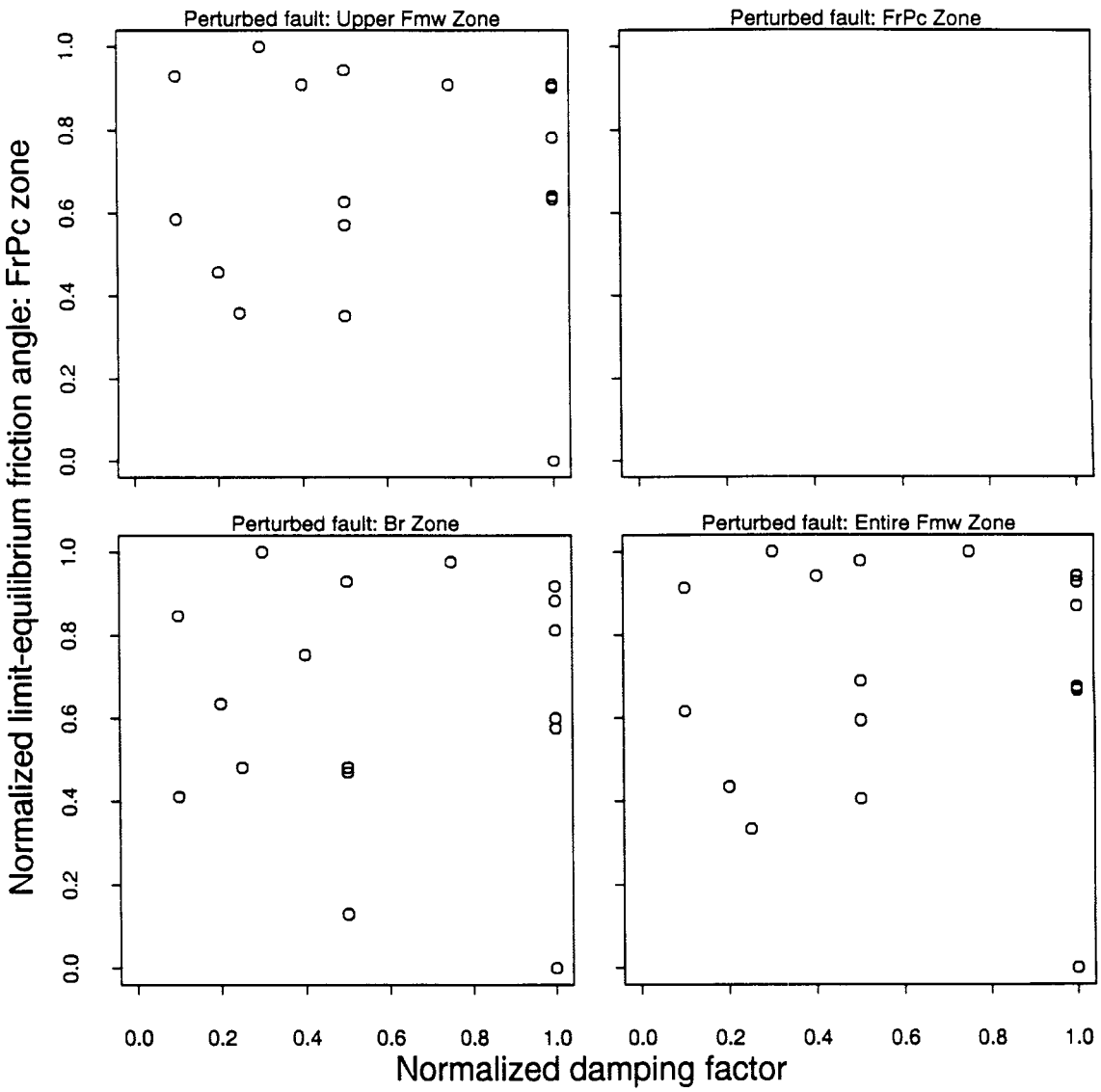

Figure B-28. Sensitivity of the limit-equilibrium friction angle for the FrPc zone to changes in the value of the damping factor

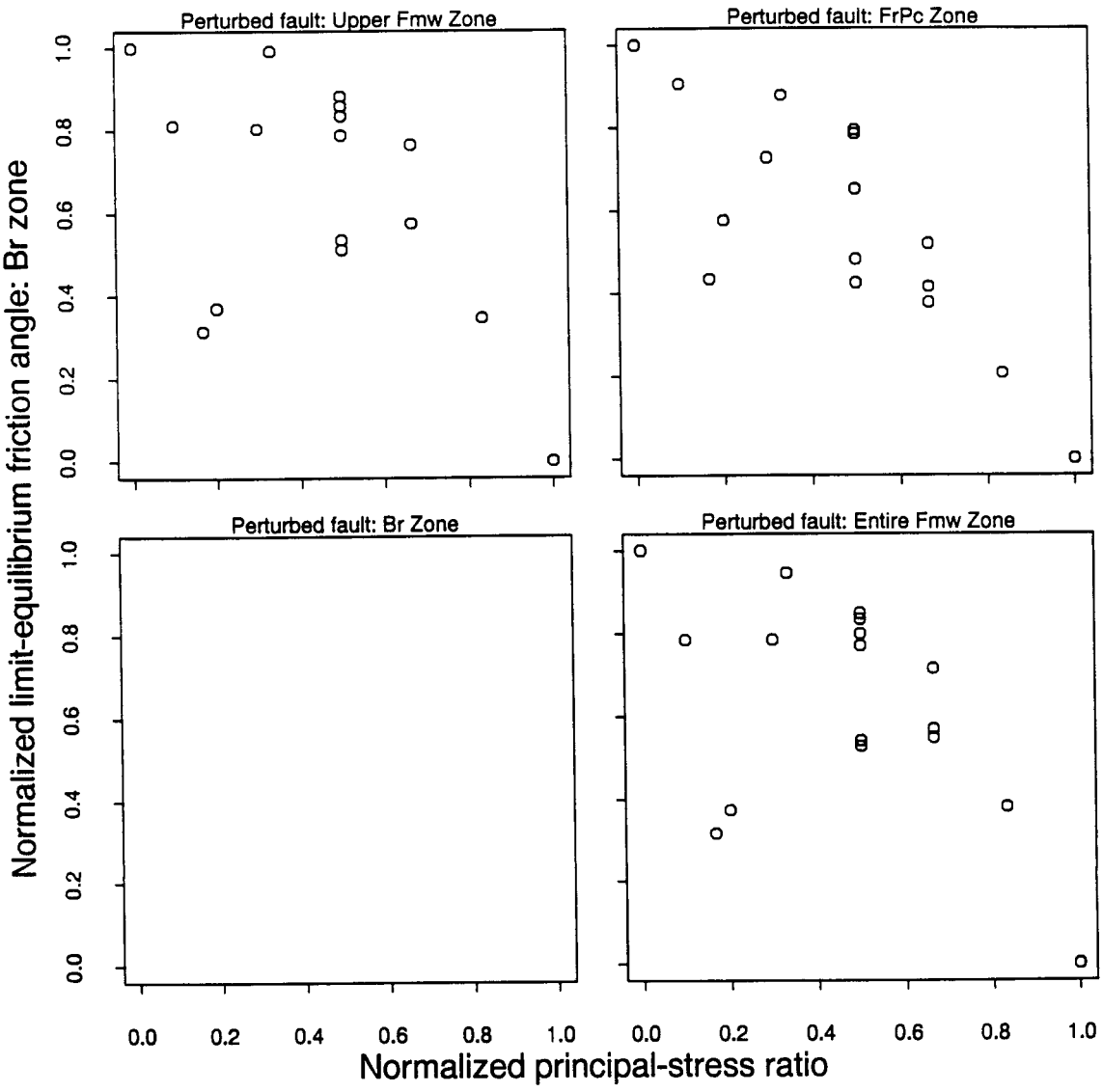

Figure B-29. Sensitivity of the limit-equilibrium friction angle for the Br zone to changes in the value of the principal stress ratio k_3

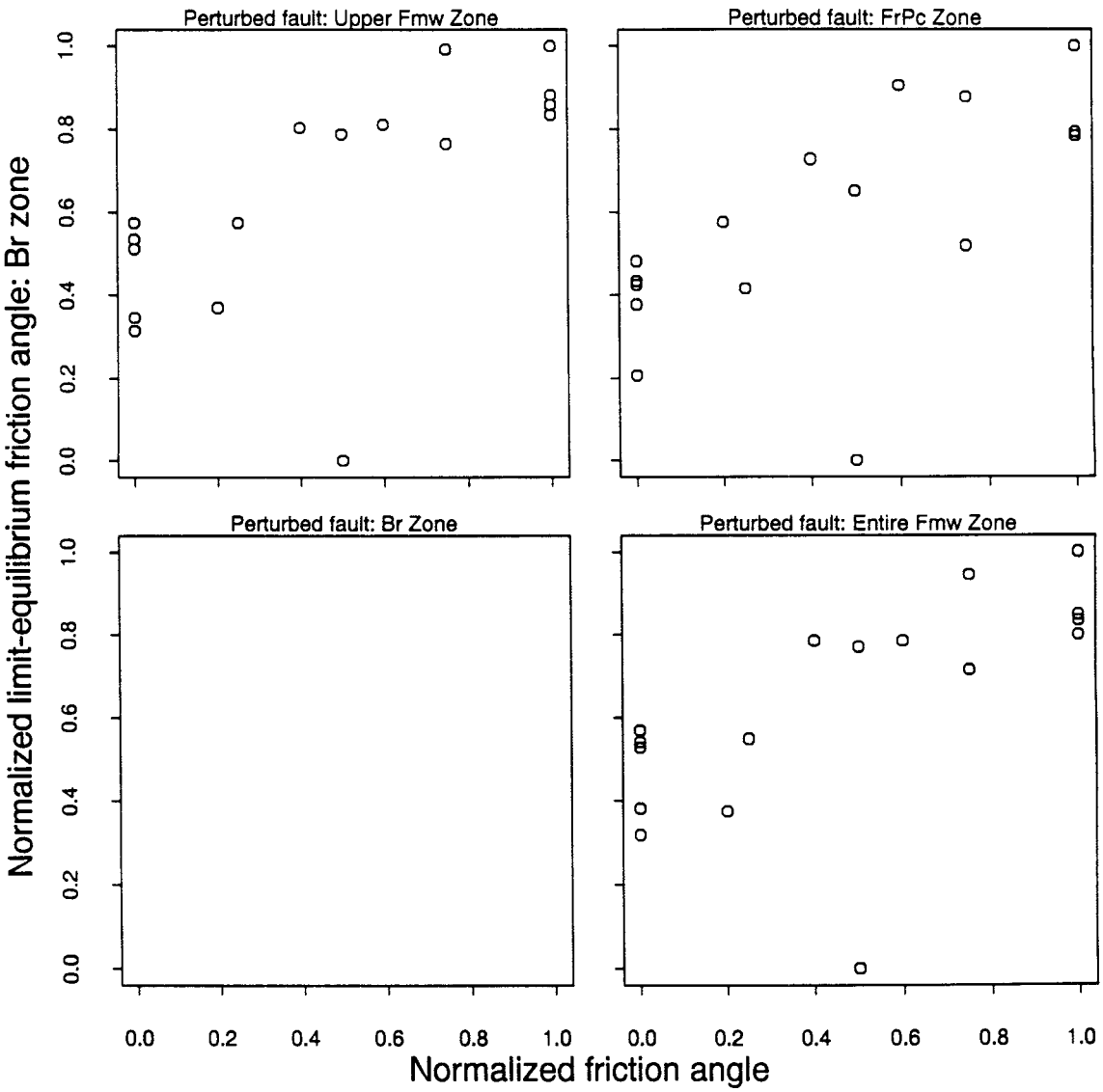

Figure B-30. Sensitivity of the limit-equilibrium friction angle for the Br zone to changes in the value of the friction angle

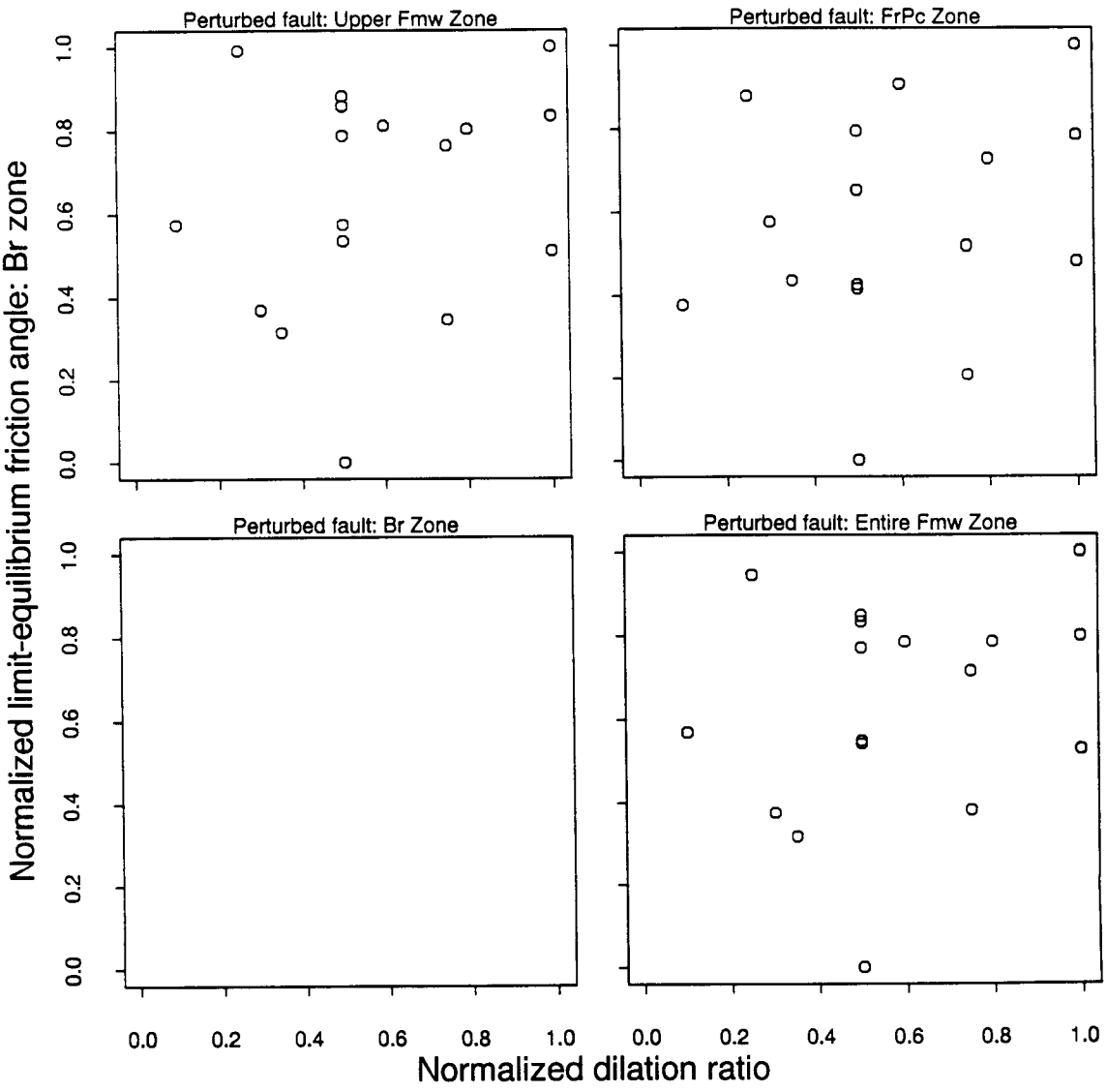

Figure B-31. Sensitivity of the limit-equilibrium friction angle for the Br zone to changes in the value of the dilation angle

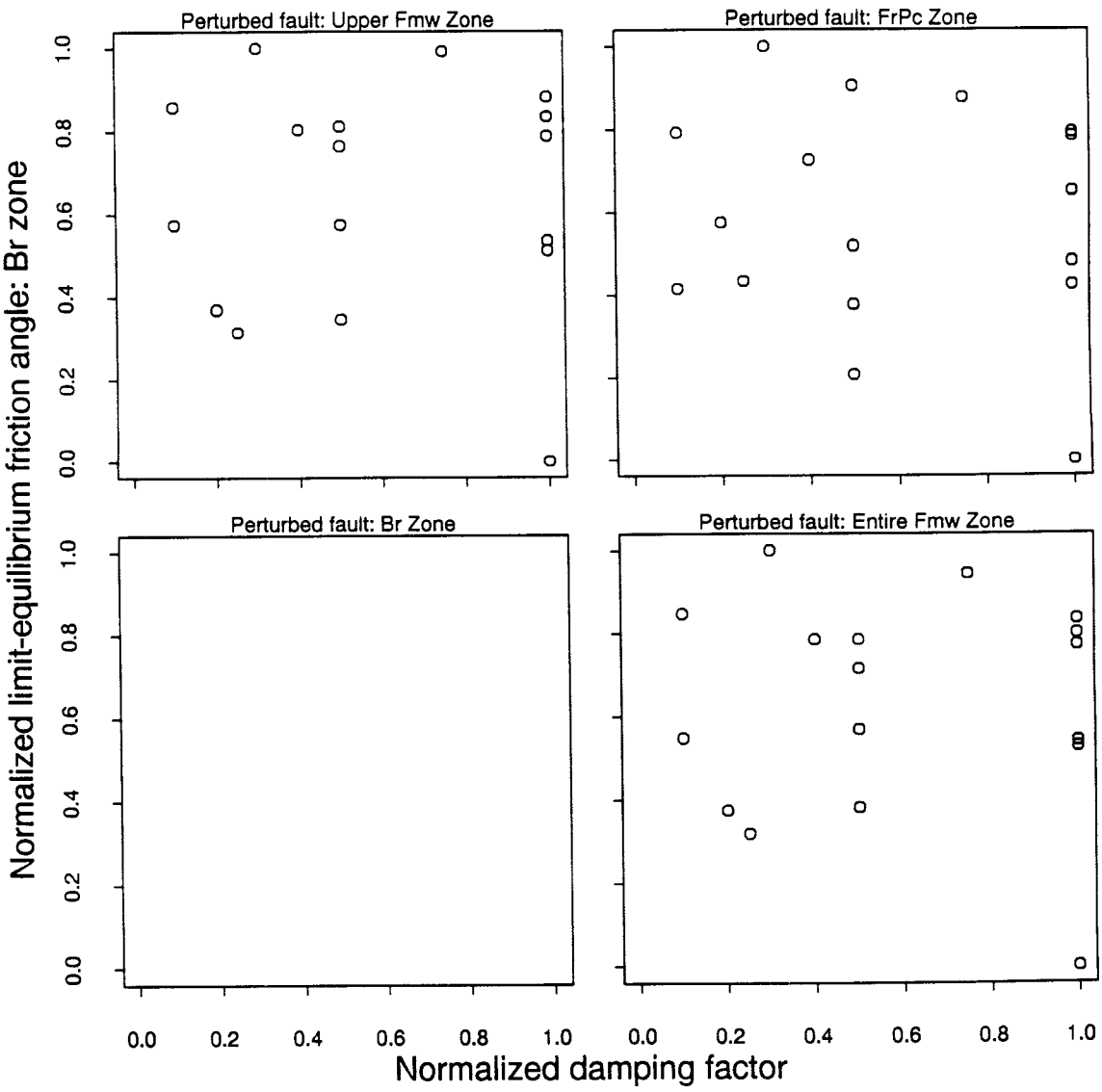

Figure B-32. Sensitivity of the limit-equilibrium friction angle for the Br zone to changes in the value of the damping factor

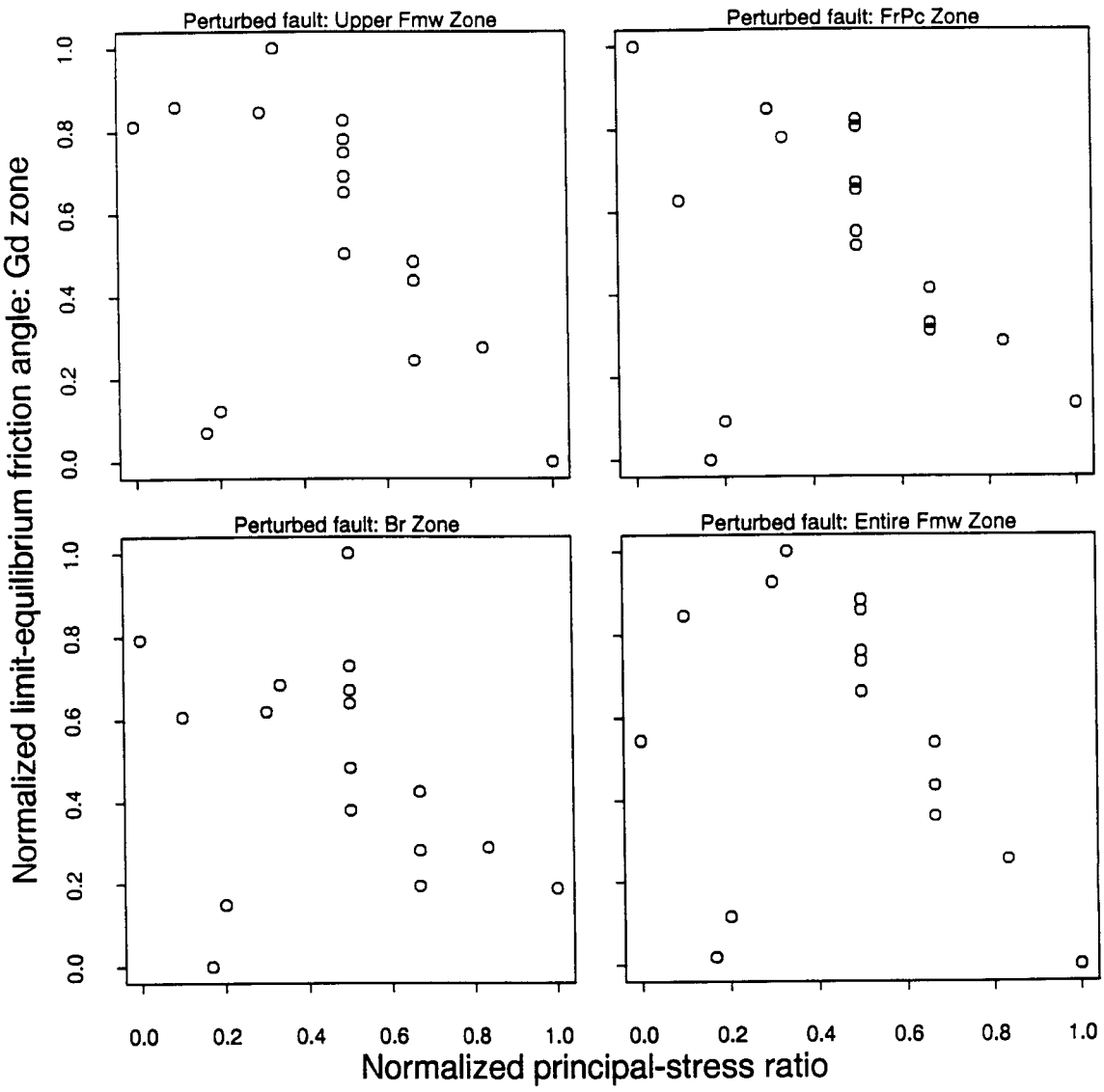

Figure B-33. Sensitivity of the limit-equilibrium friction angle for the Gd zone to changes in the value of the principal stress ratio k_3

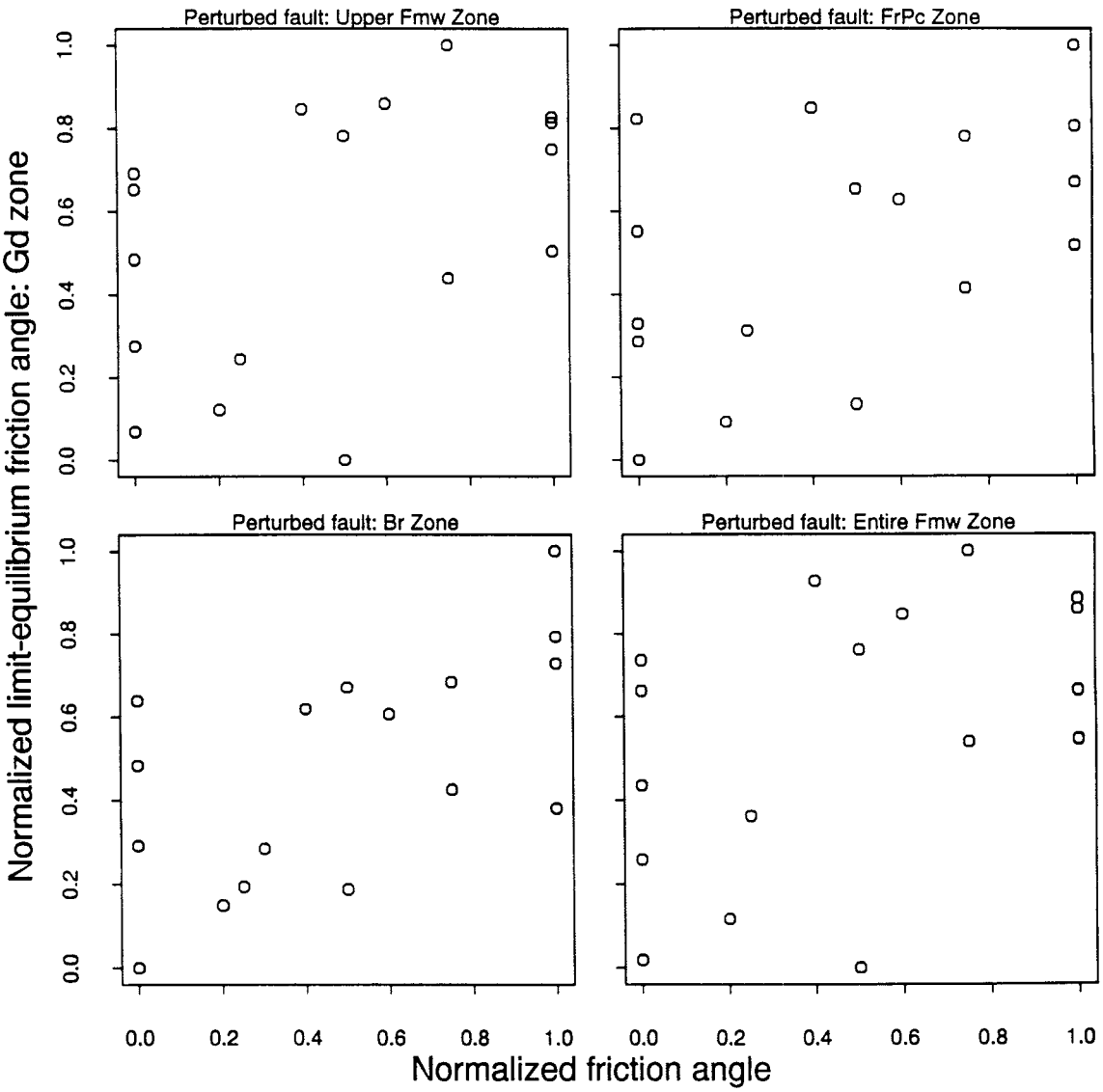

Figure B-34. Sensitivity of the limit-equilibrium friction angle for the Gd zone to changes in the value of the friction angle

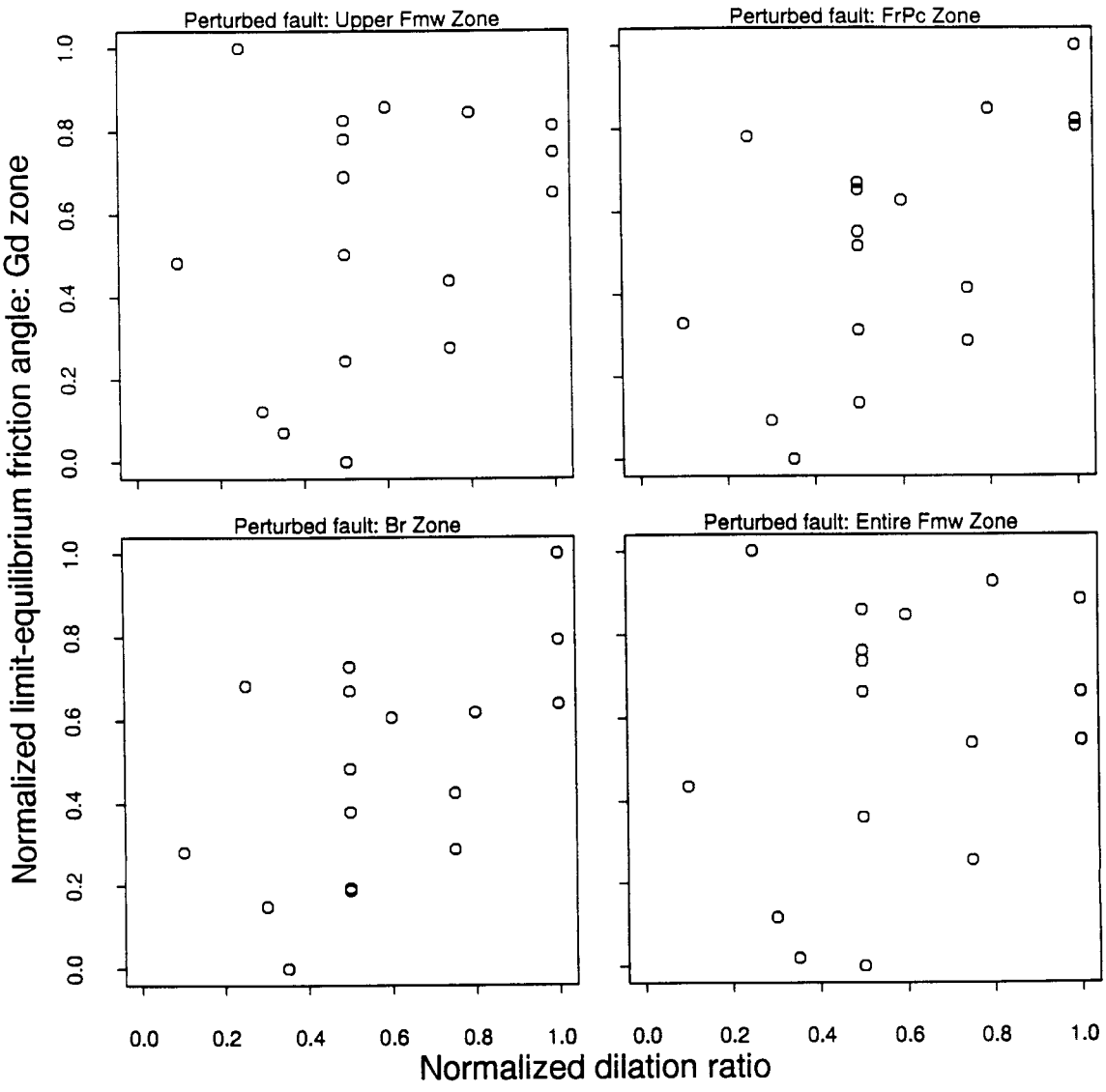

Figure B-35. Sensitivity of the limit-equilibrium friction angle for the Gd zone to changes in the value of the dilation angle

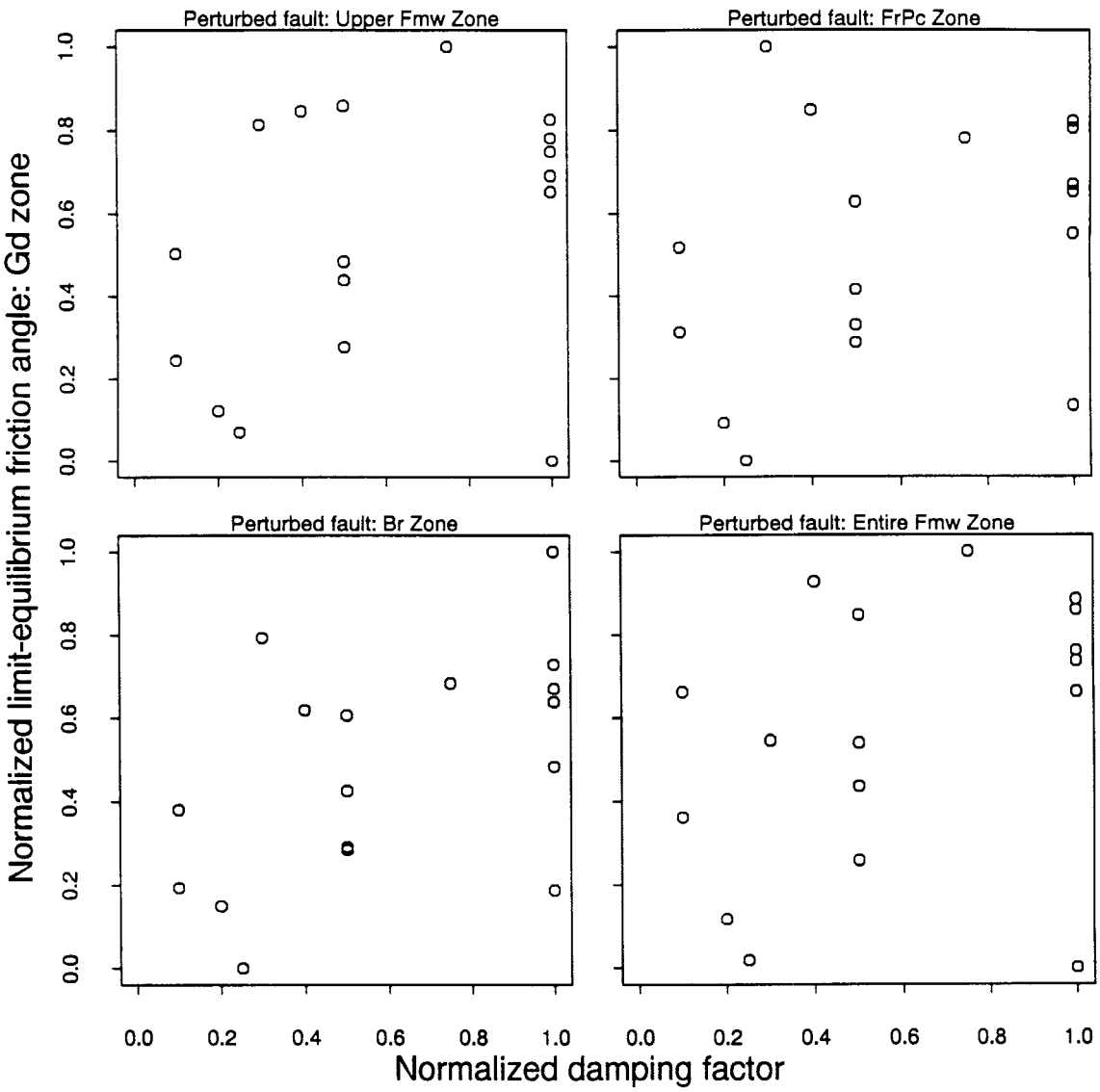

Figure B-36. Sensitivity of the limit-equilibrium friction angle for the Gd zone to changes in the value of the damping factor

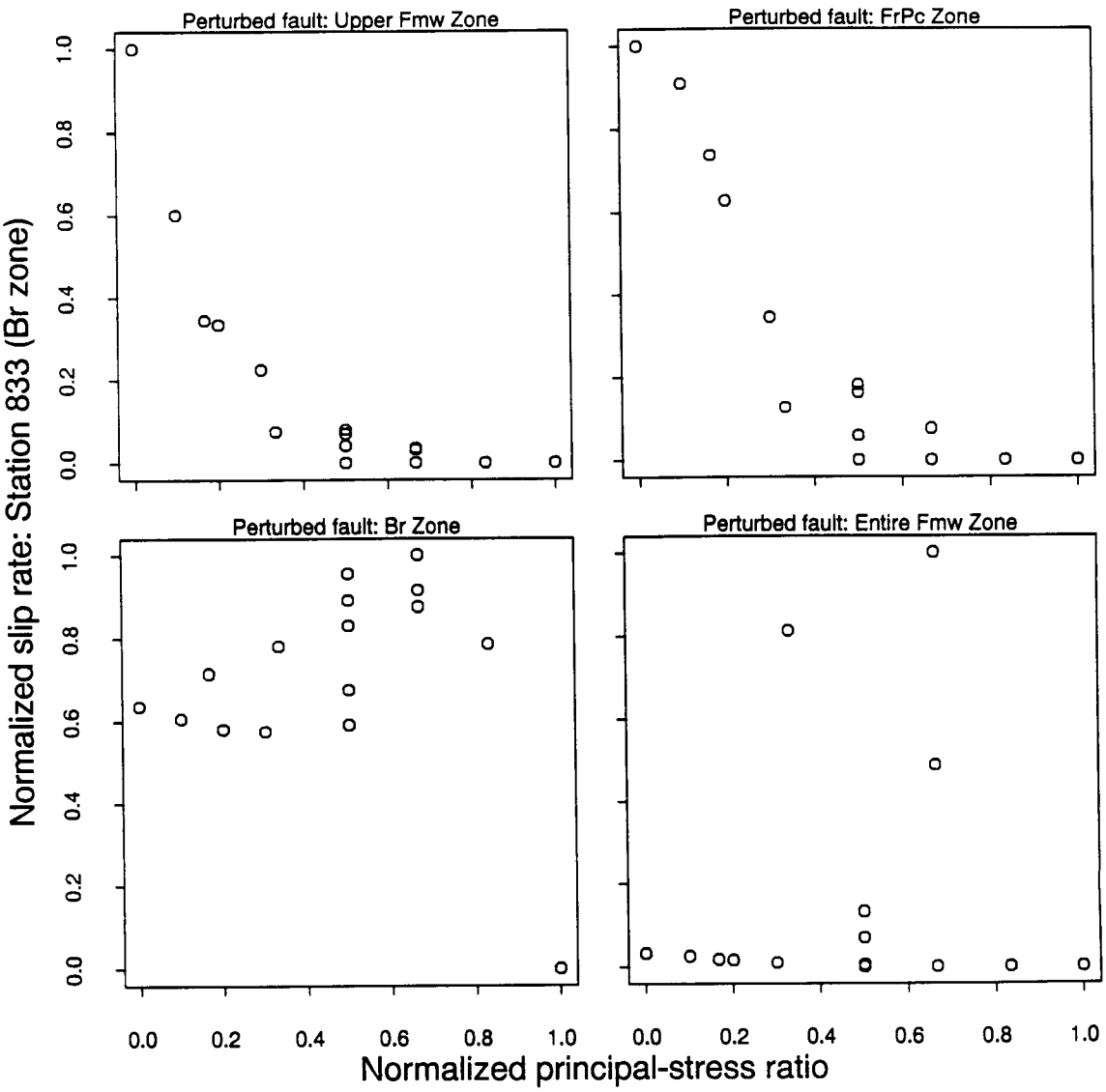

Figure B-37. Sensitivity of the slip rate at Station Br833 to changes in the value of the principal stress ratio k_3

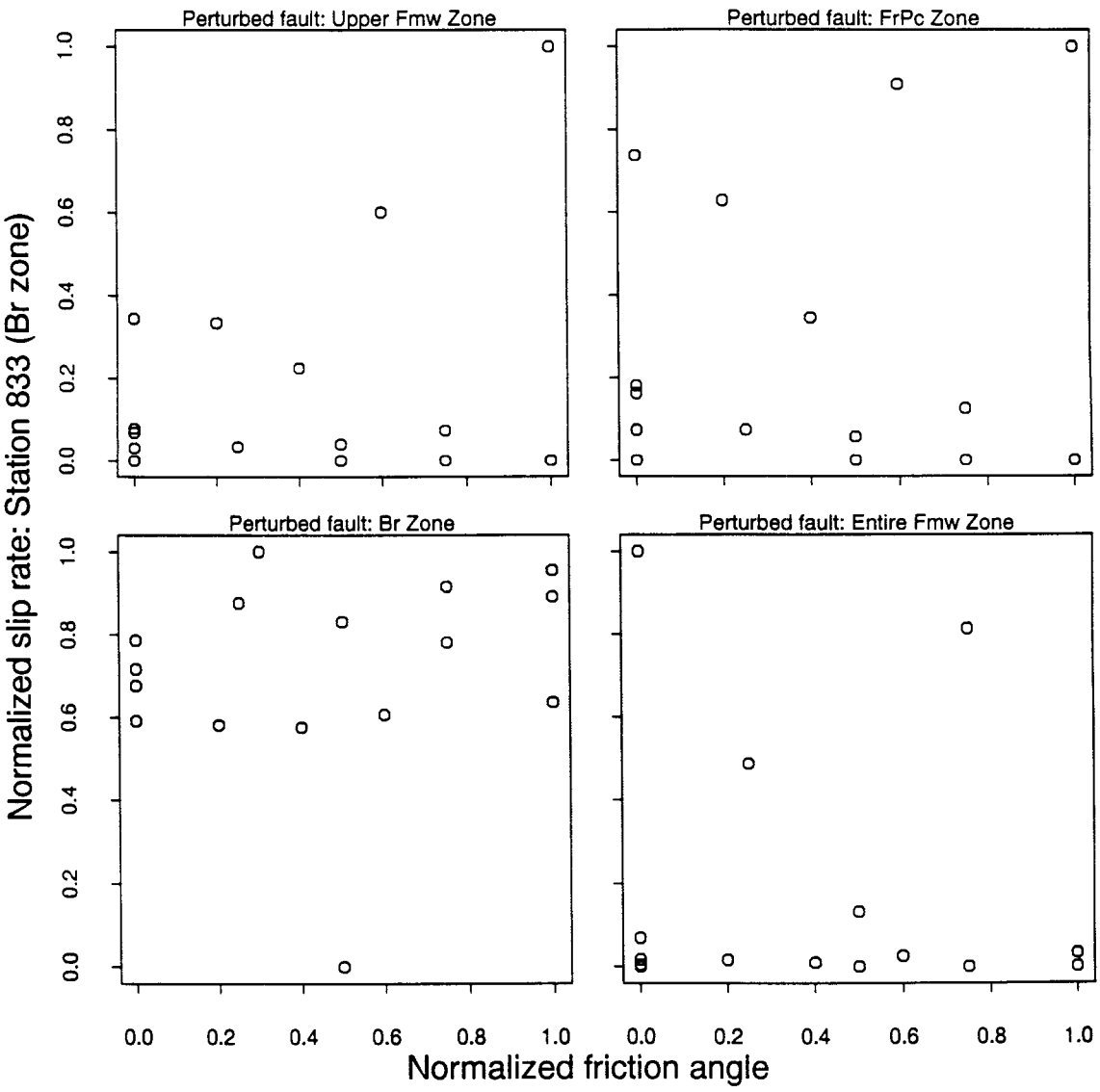

Figure B-38. Sensitivity of the slip rate at Station Br833 to changes in the value of the friction angle

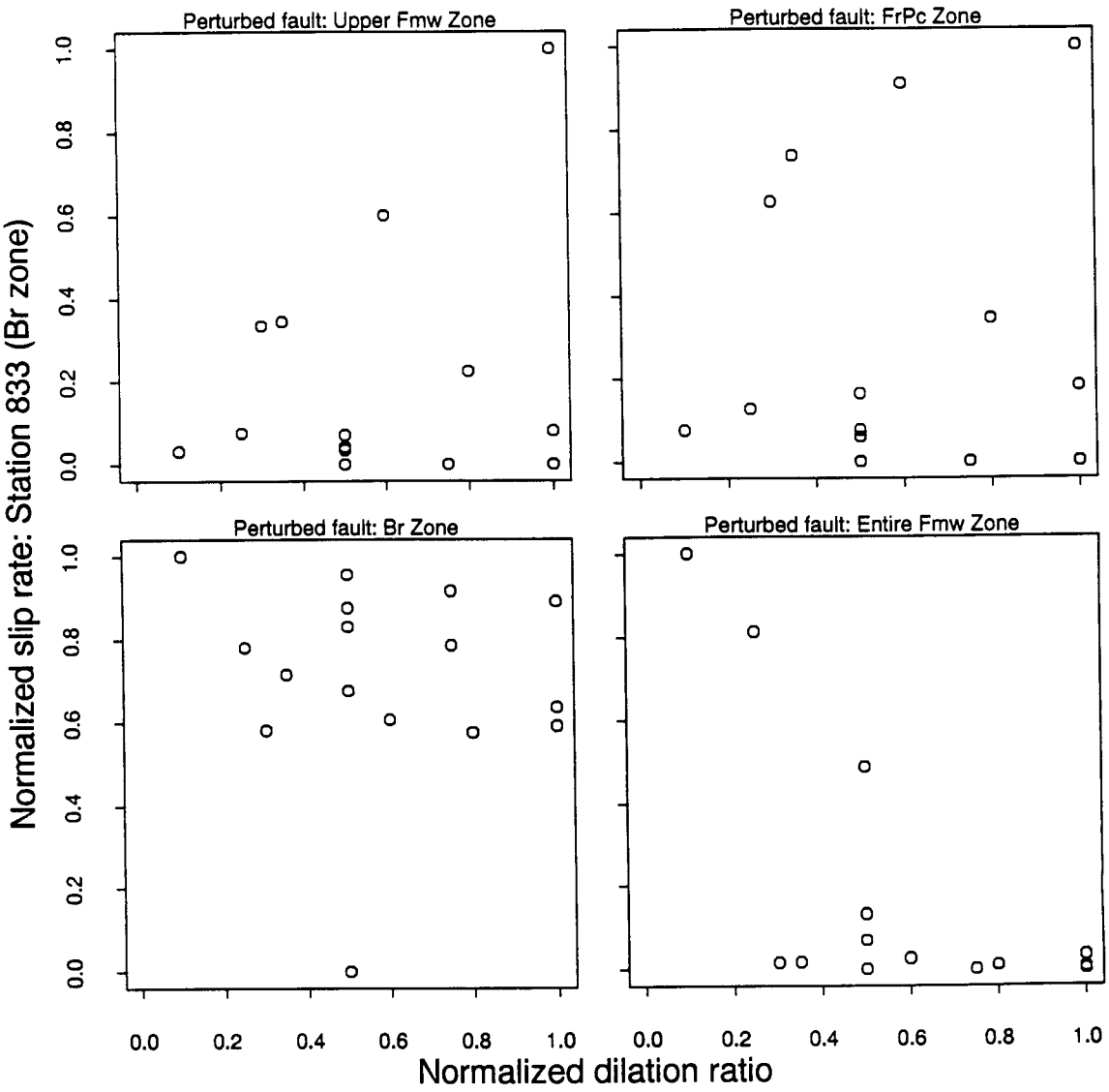

Figure B-39. Sensitivity of the slip rate at Station Br833 to changes in the value of the dilation ratio

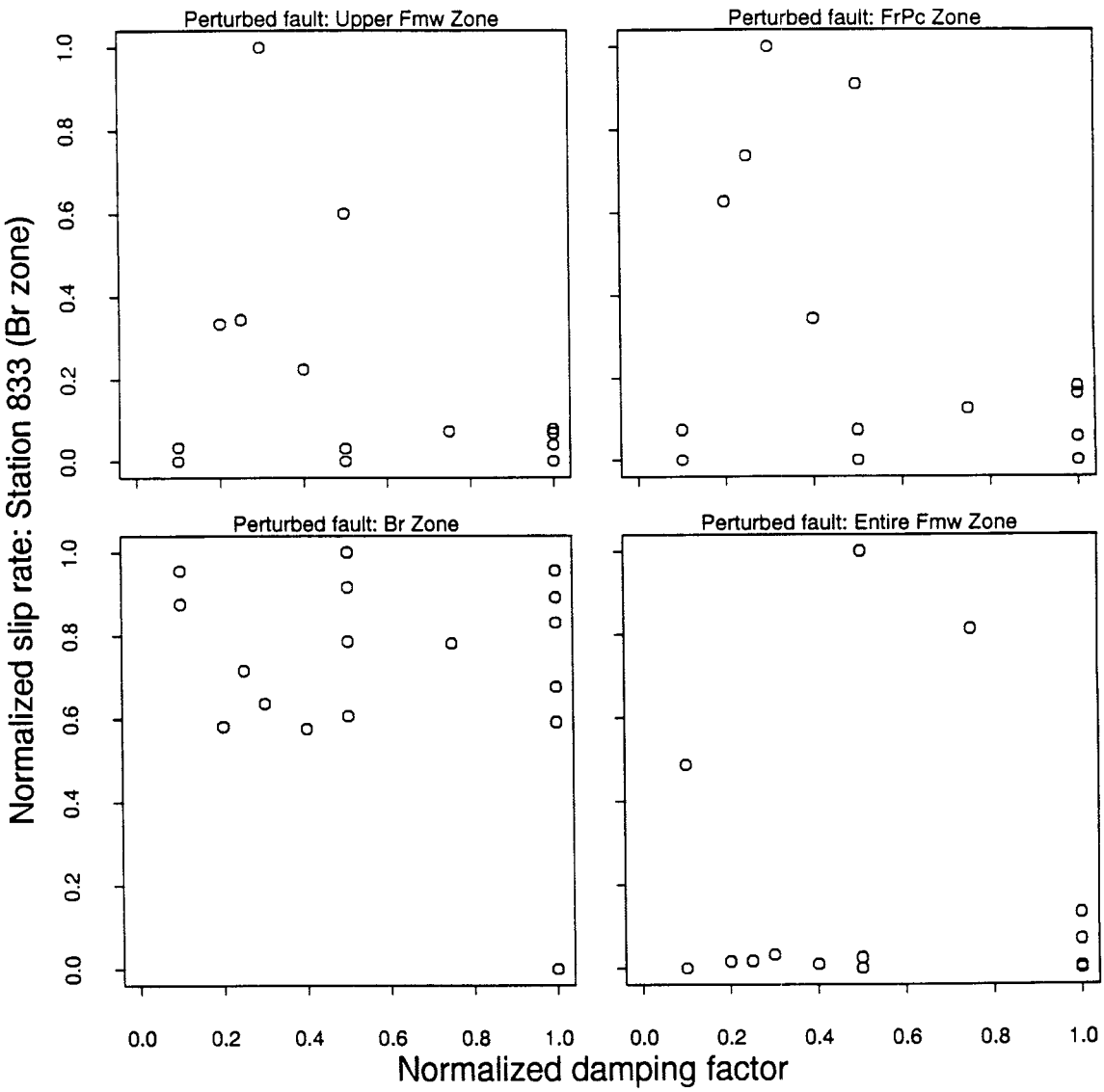

Figure B-40. Sensitivity of the slip rate at Station Br833 to changes in the value of the damping factor

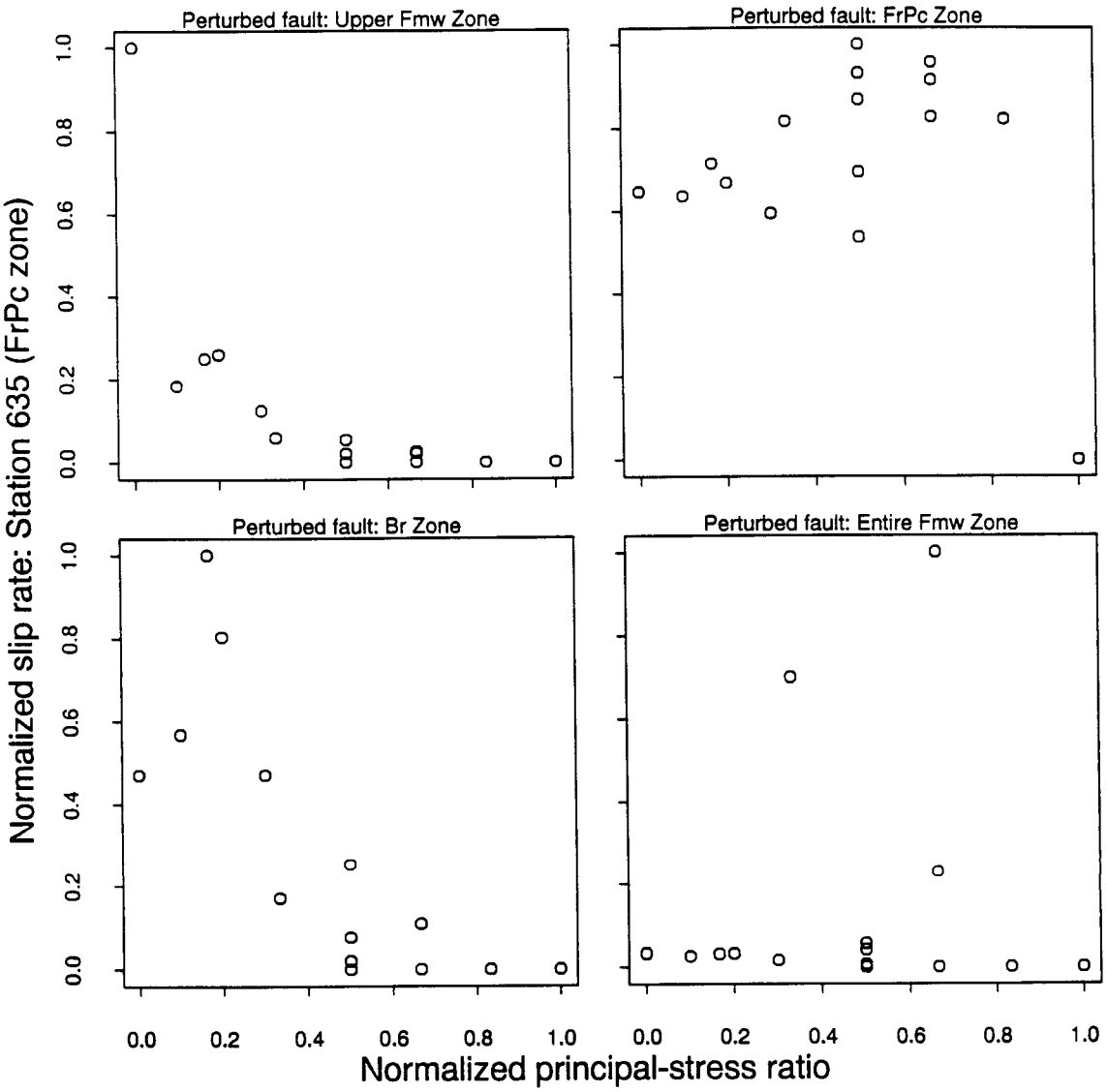

Figure B-41. Sensitivity of the slip rate at Station Fr635 to changes in the value of the principal stress ratio k_3

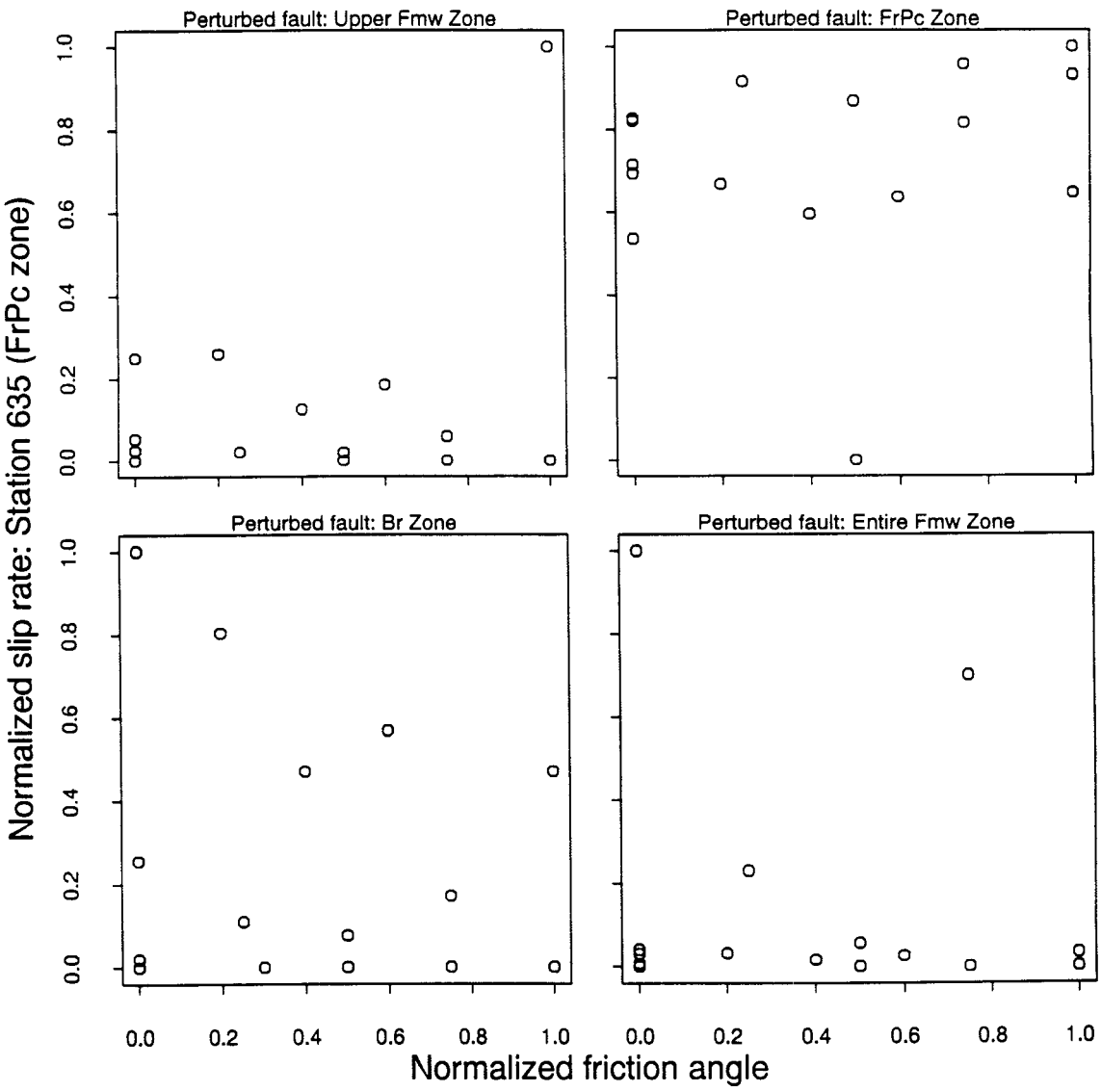

Figure B-42. Sensitivity of the slip rate at Station Fr635 to changes in the value of the friction angle

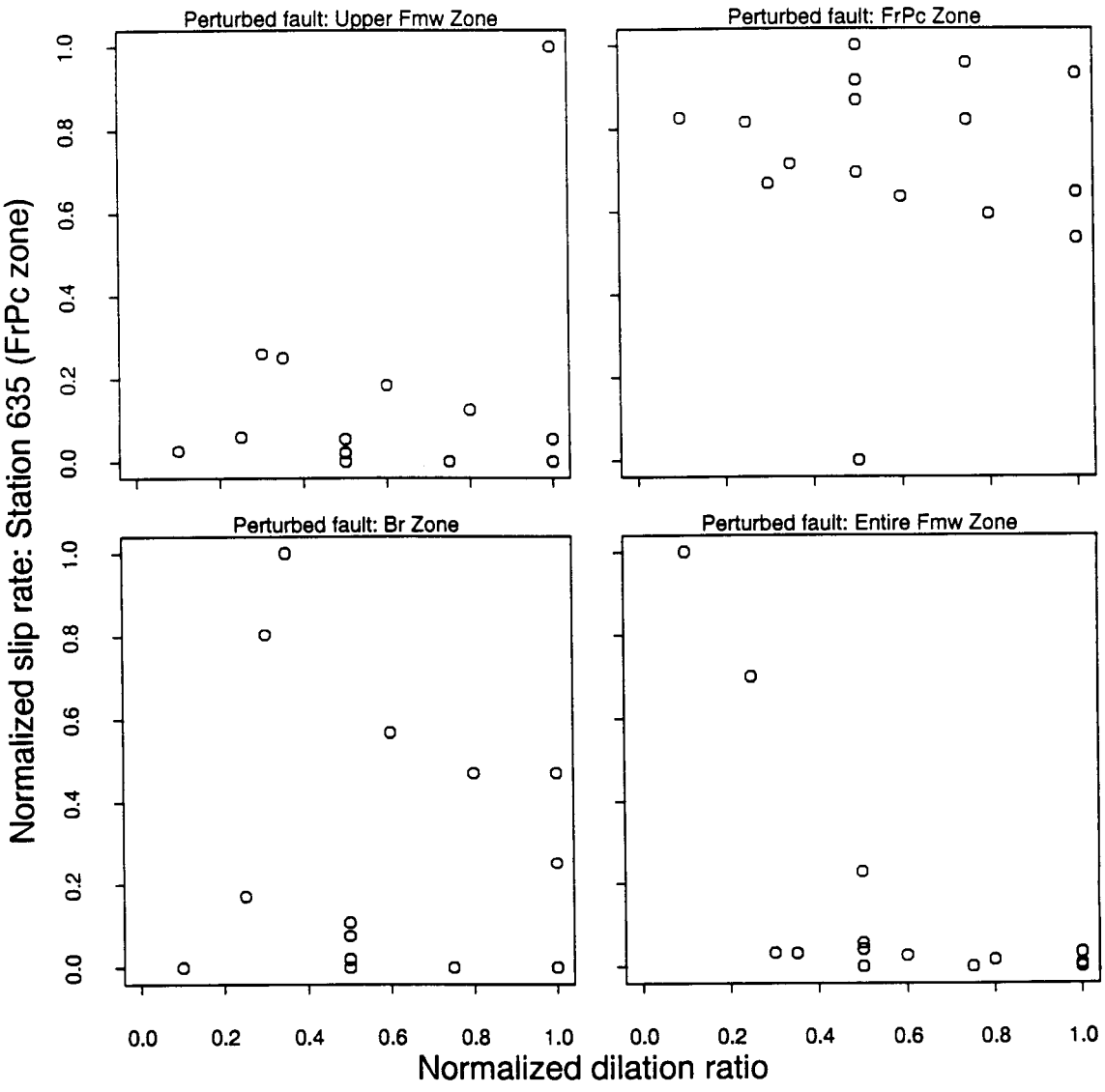

Figure B-43. Sensitivity of the slip rate at Station Fr635 to changes in the value of the dilation angle

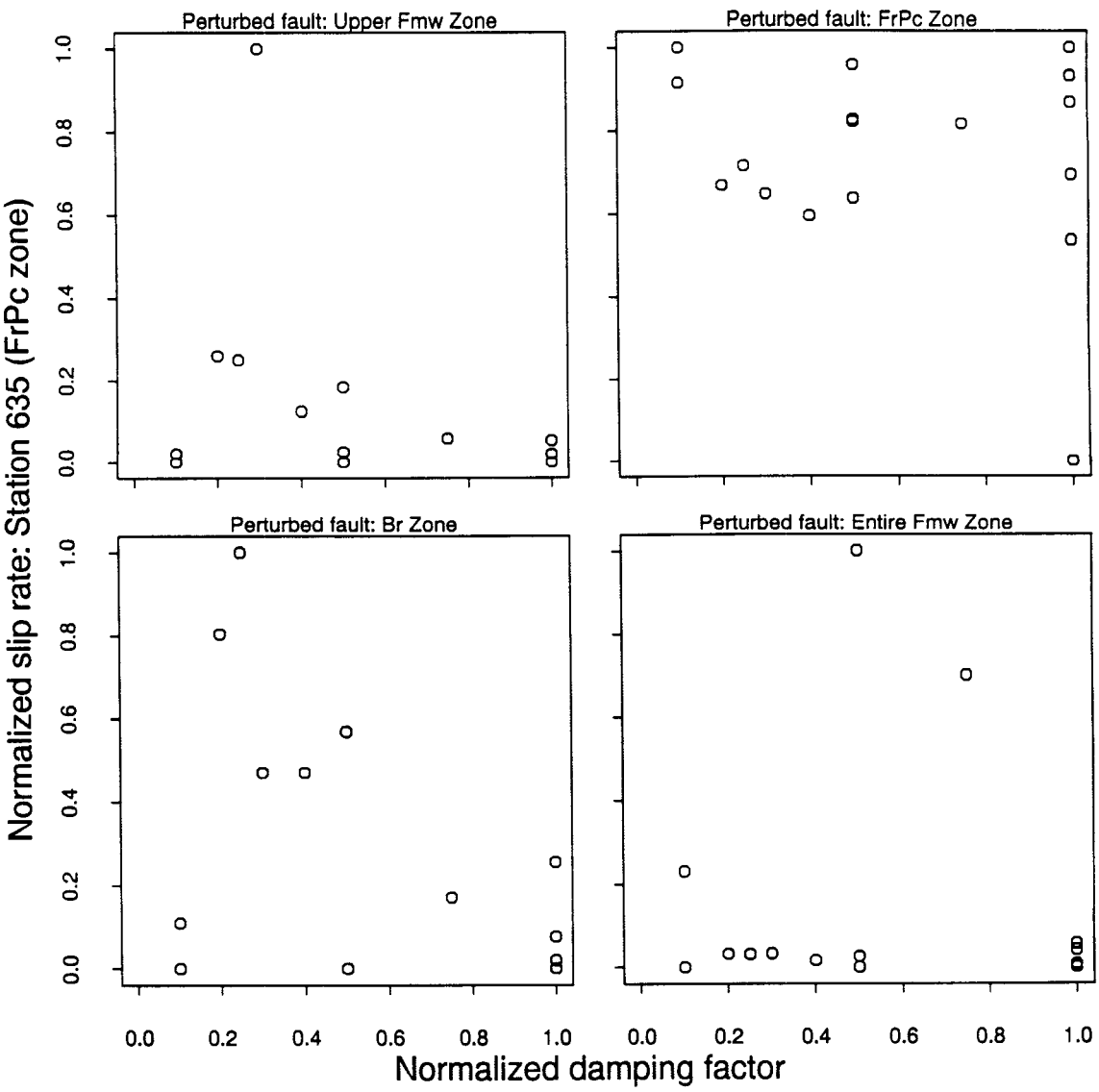

Figure B-44. Sensitivity of the slip rate at Station Fr635 to changes in the value of the damping factor

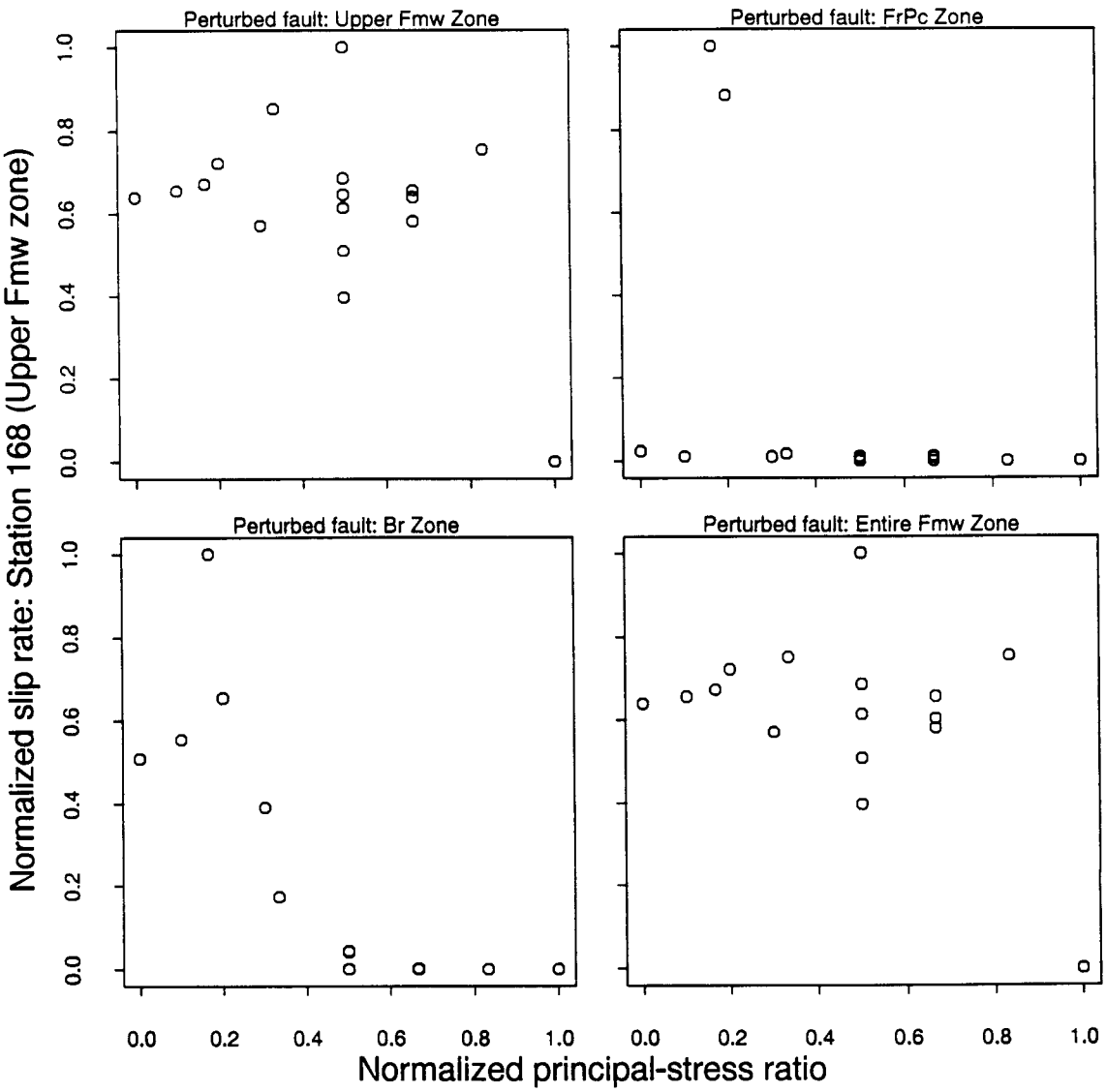

Figure B-45. Sensitivity of the slip rate at Station Fm168 to changes in the value of the principal stress ratio k_3

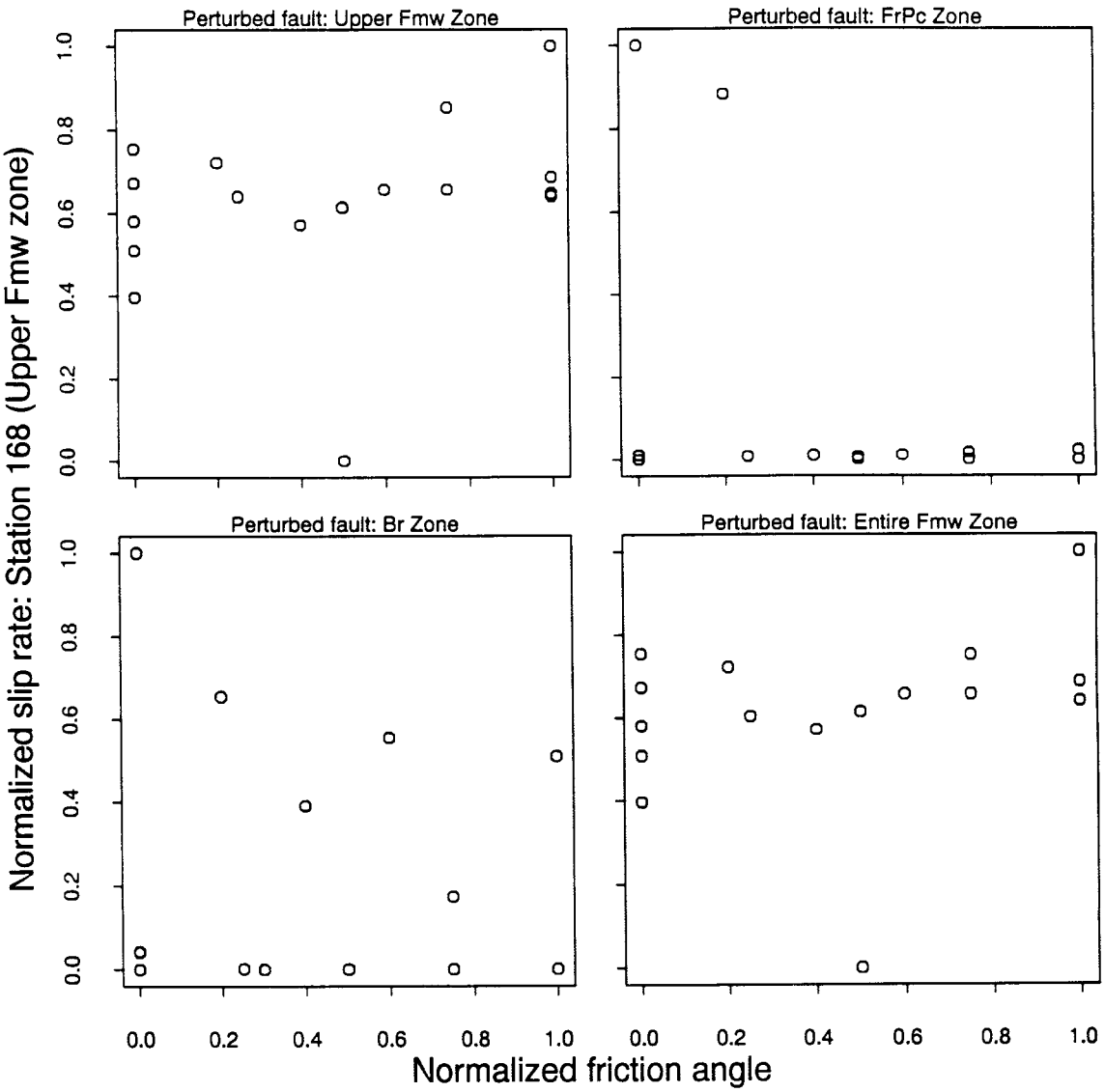

Figure B-46. Sensitivity of the slip rate at Station Fm168 to changes in the value of the friction angle

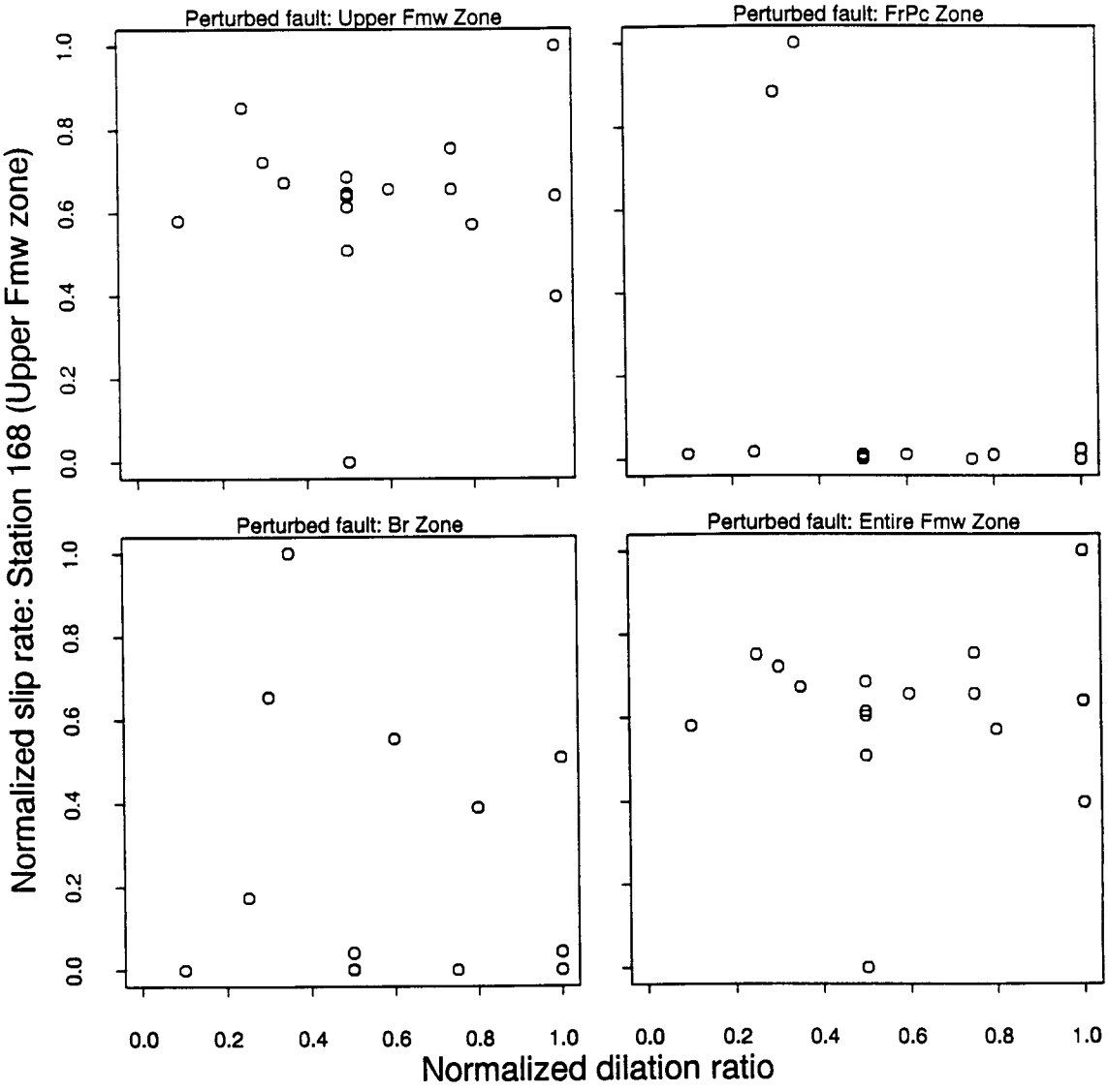

Figure B-47. Sensitivity of the slip rate at Station Fm168 to changes in the value of the dilation angle

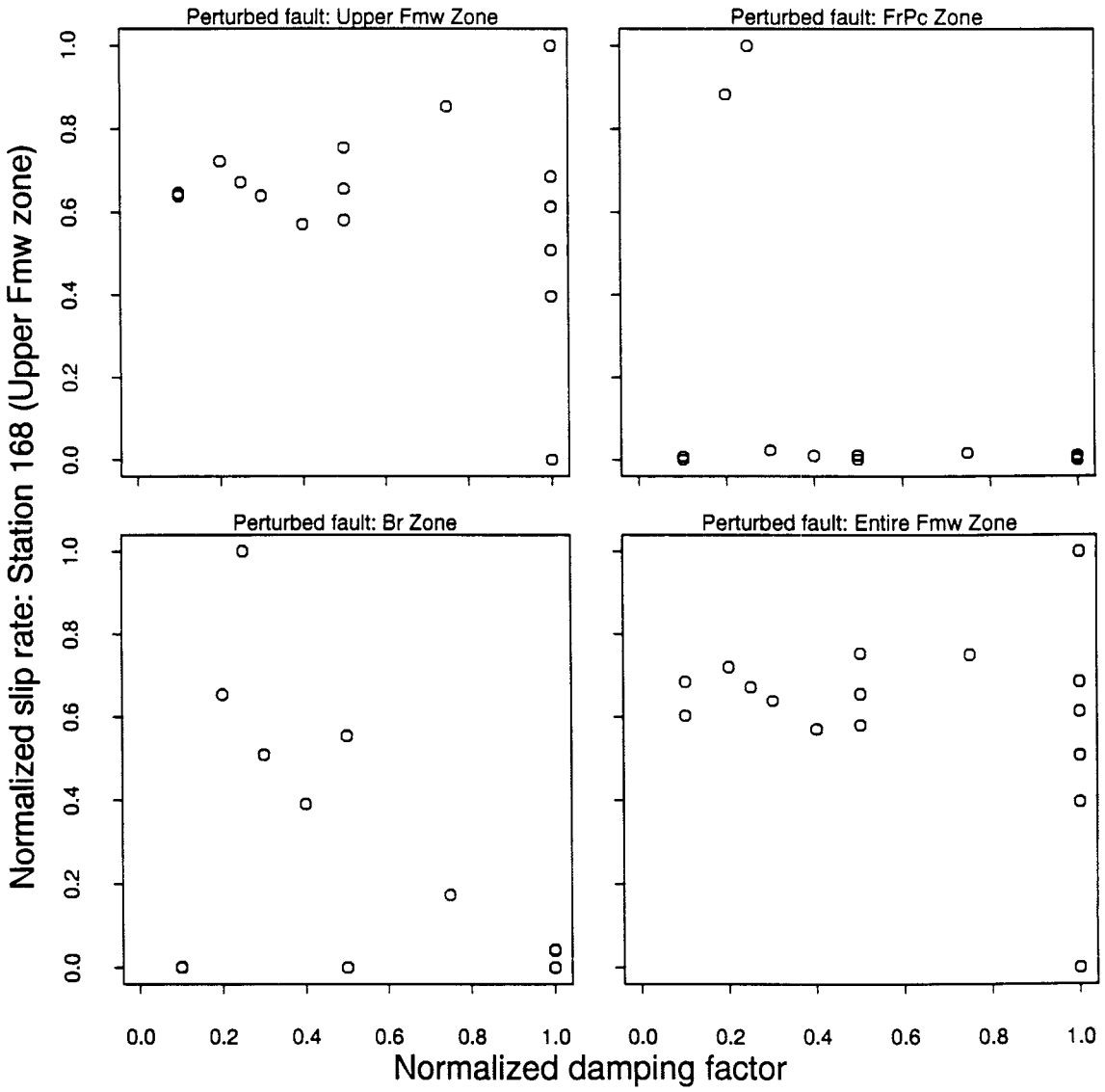

Figure B-48. Sensitivity of the slip rate at Station Fm168 to changes in the value of the damping factor

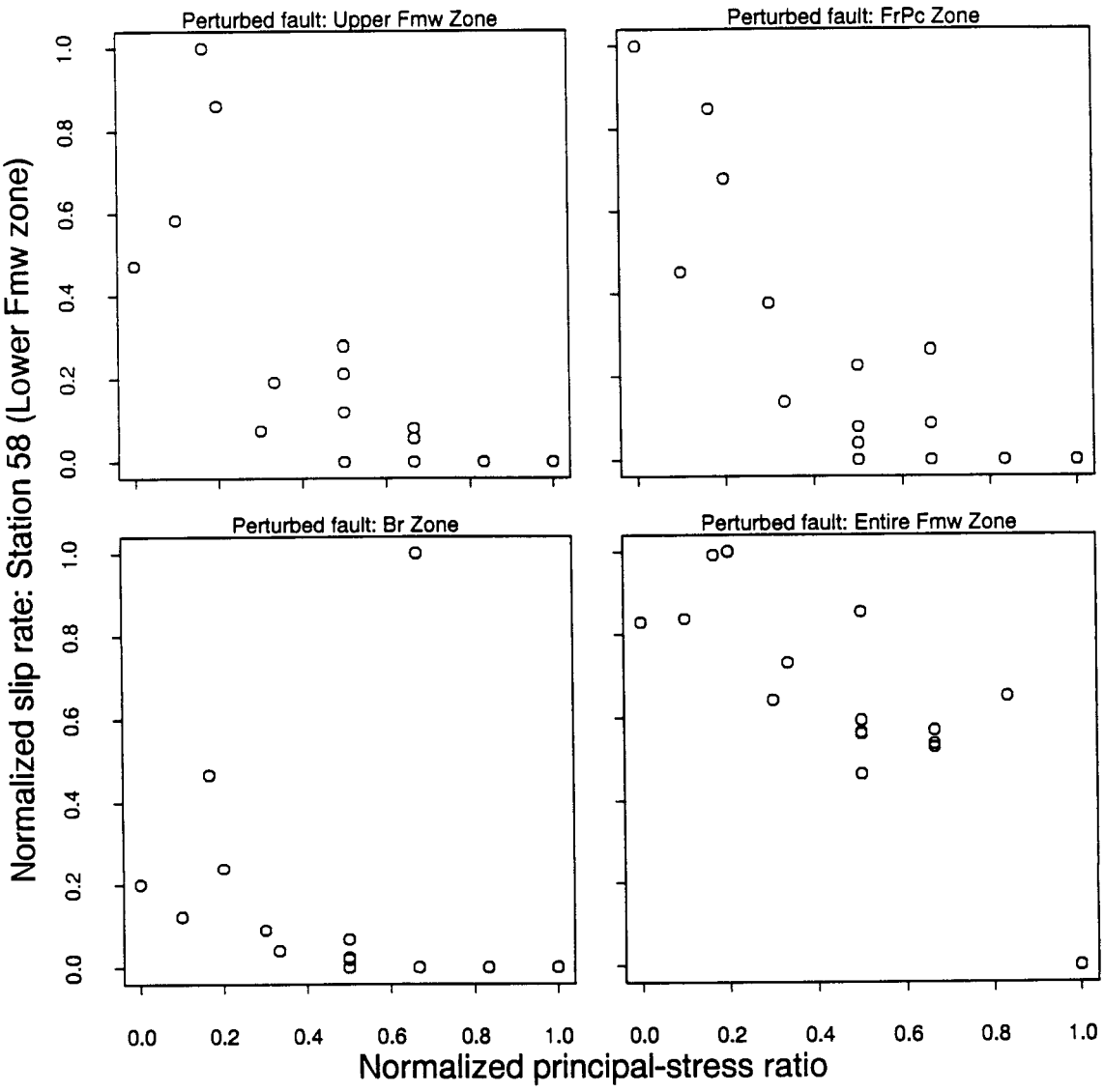

Figure B-49. Sensitivity of the slip rate at Station Fm58 to changes in the value of the principal stress ratio k_3

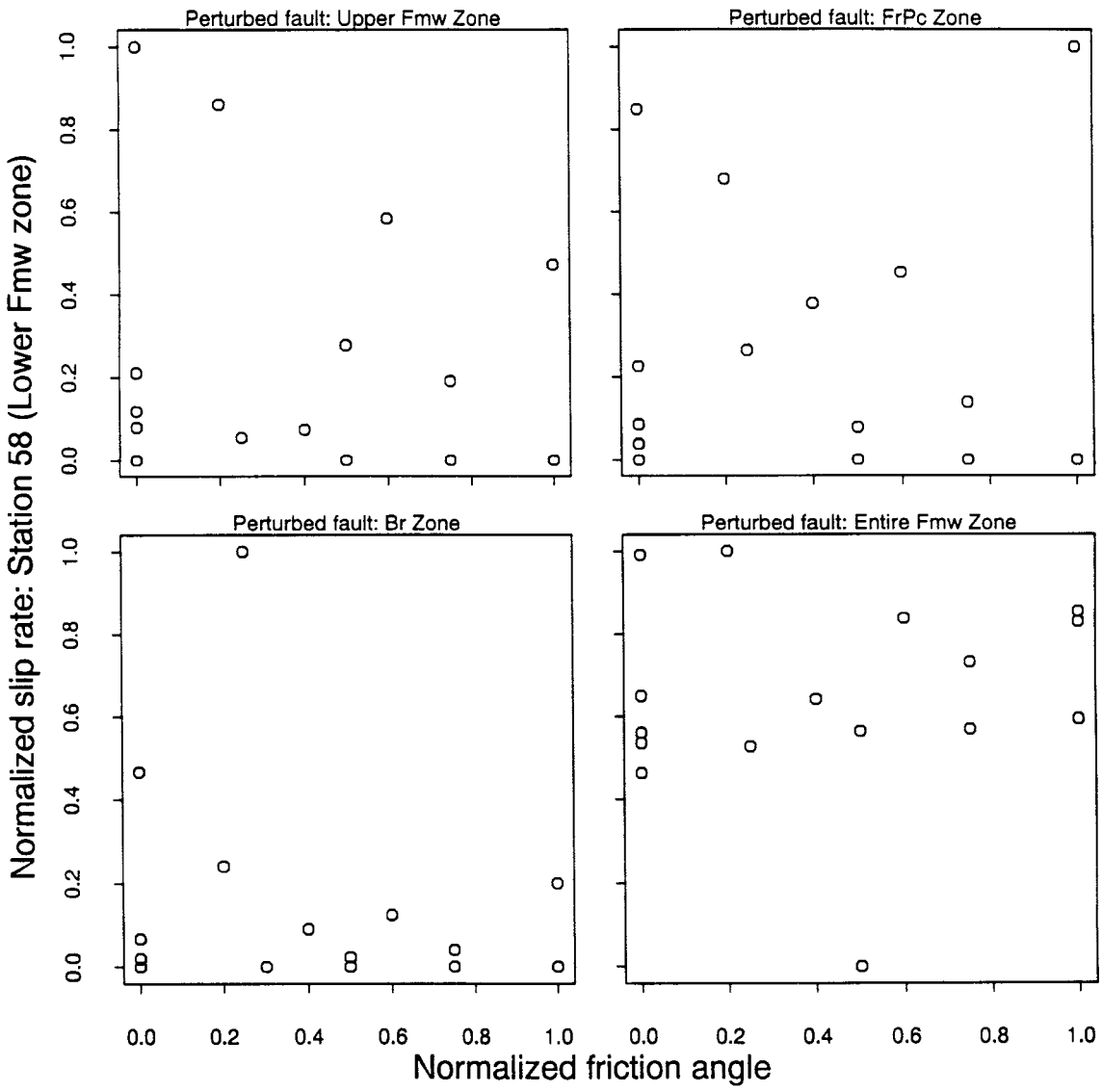

Figure B-50. Sensitivity of the slip rate at Station Fm58 to changes in the value of the friction angle

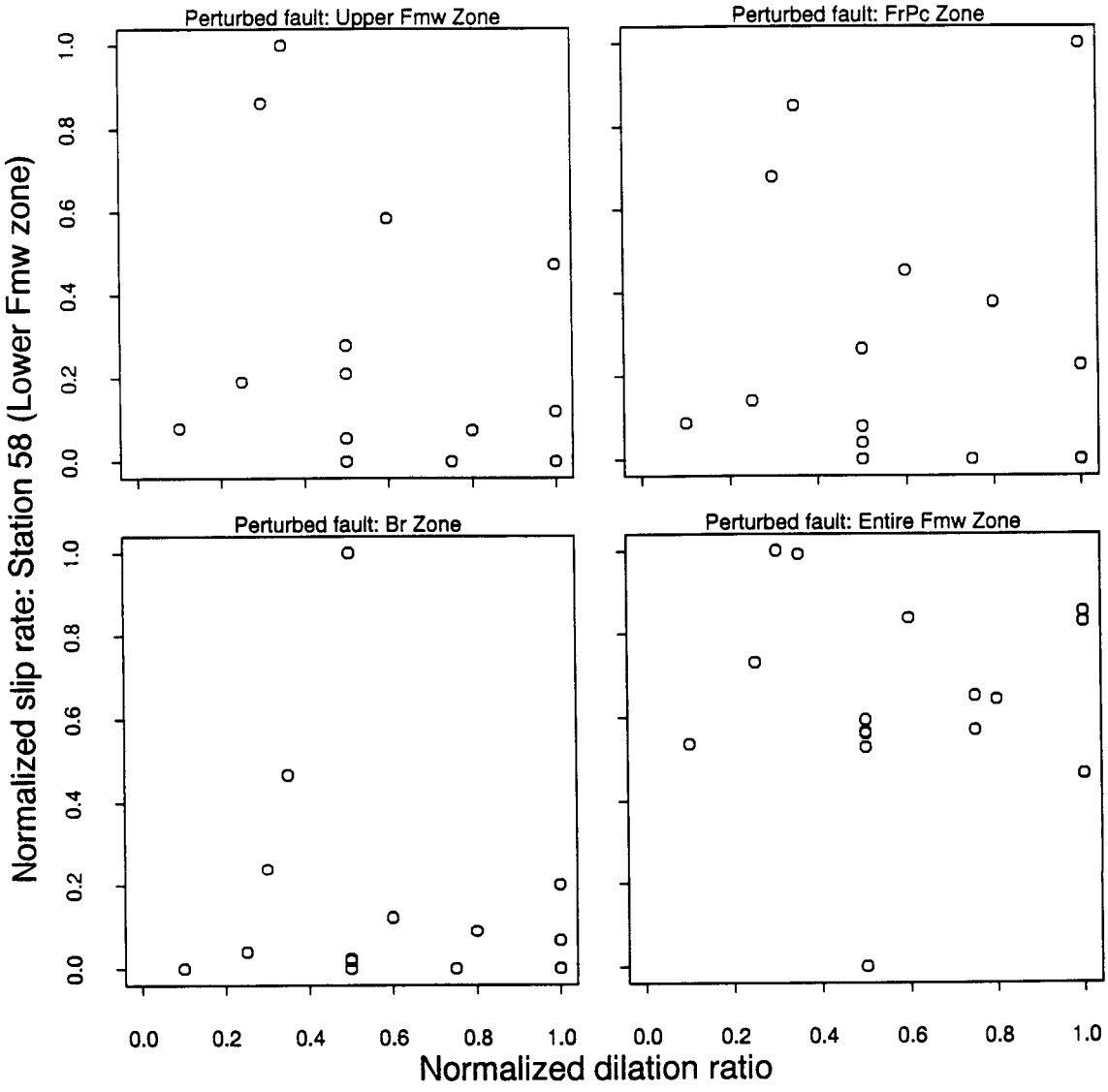

Figure B-51. Sensitivity of the slip rate at Station Fm58 to changes in the value of the dilation angle

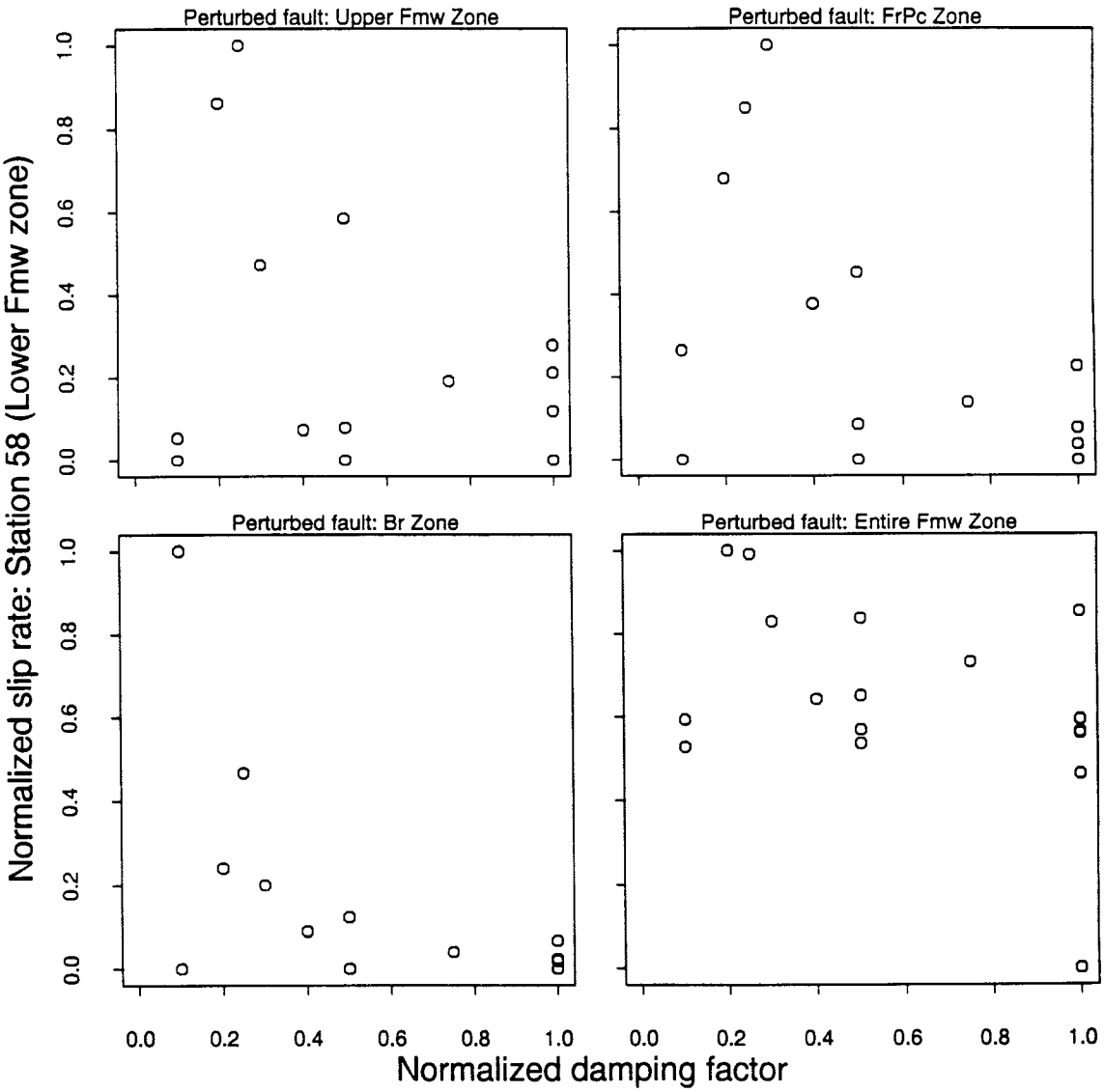

Figure B-52. Sensitivity of the slip rate at Station Fm58 to changes in the value of the damping factor

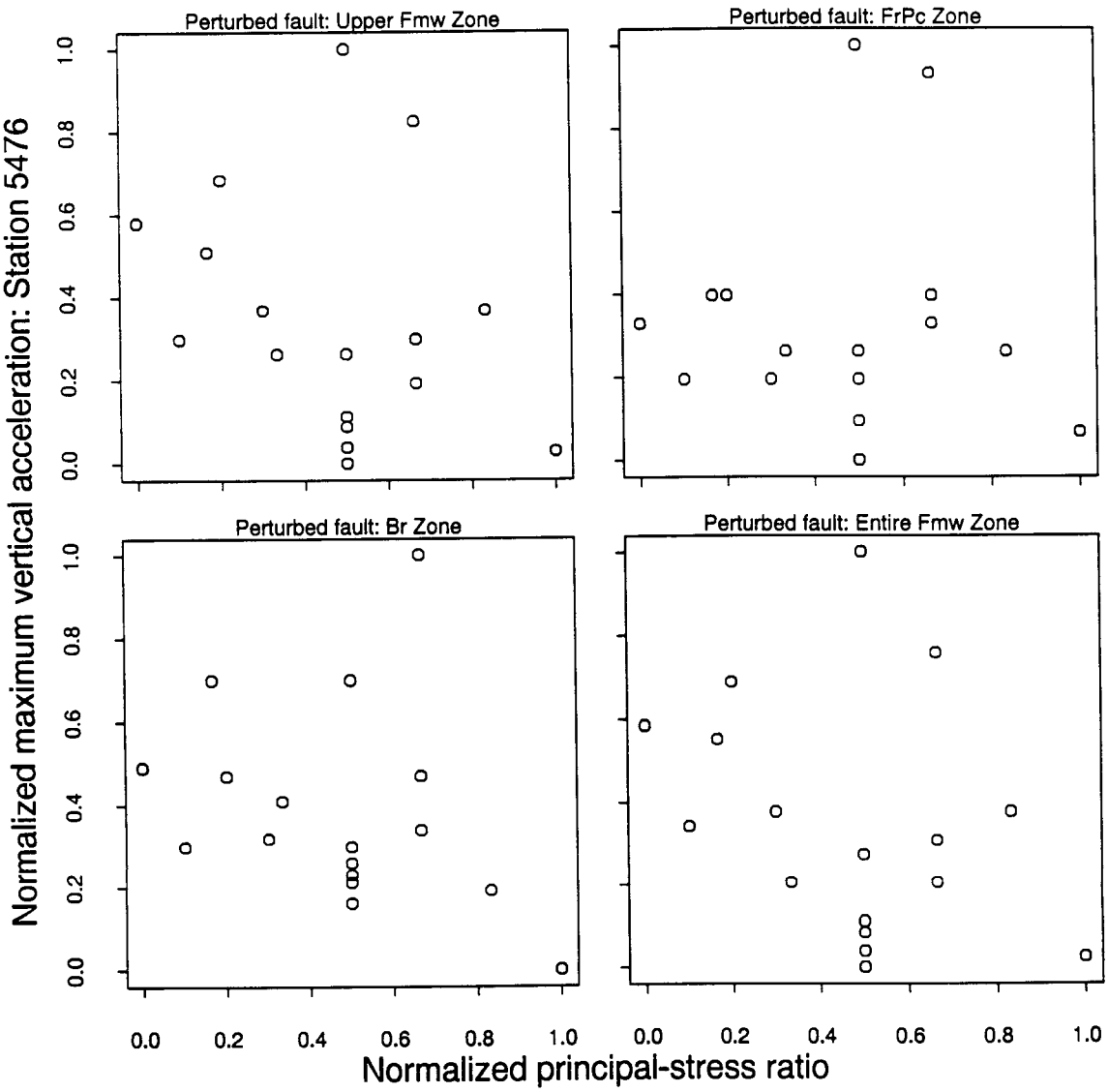

Figure B-53. Sensitivity of the maximum vertical acceleration at Station 5476 to changes in the value of the principal stress ratio k_3

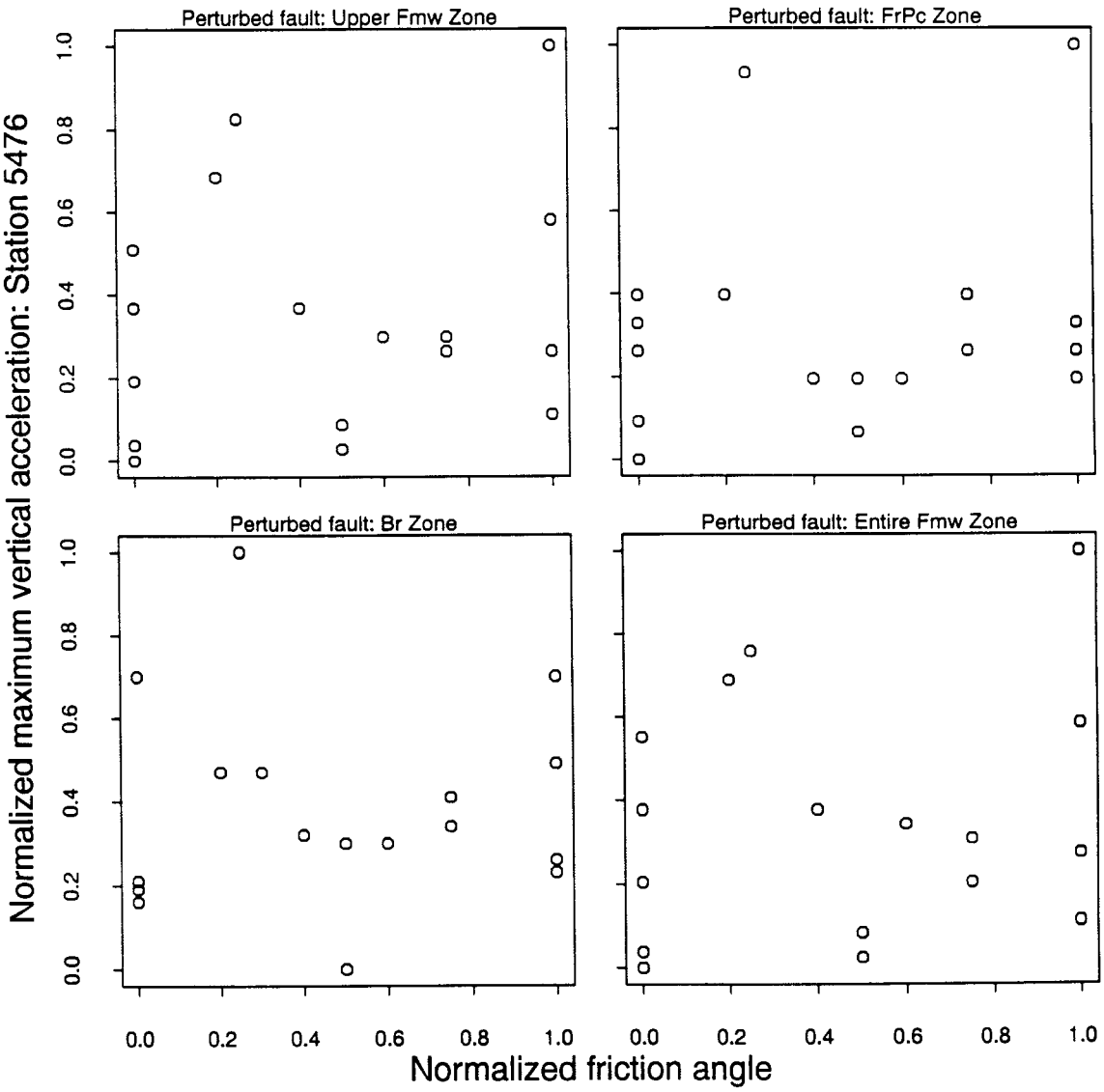

Figure B-54. Sensitivity of the maximum vertical acceleration at Station 5476 to changes in the value of the friction angle

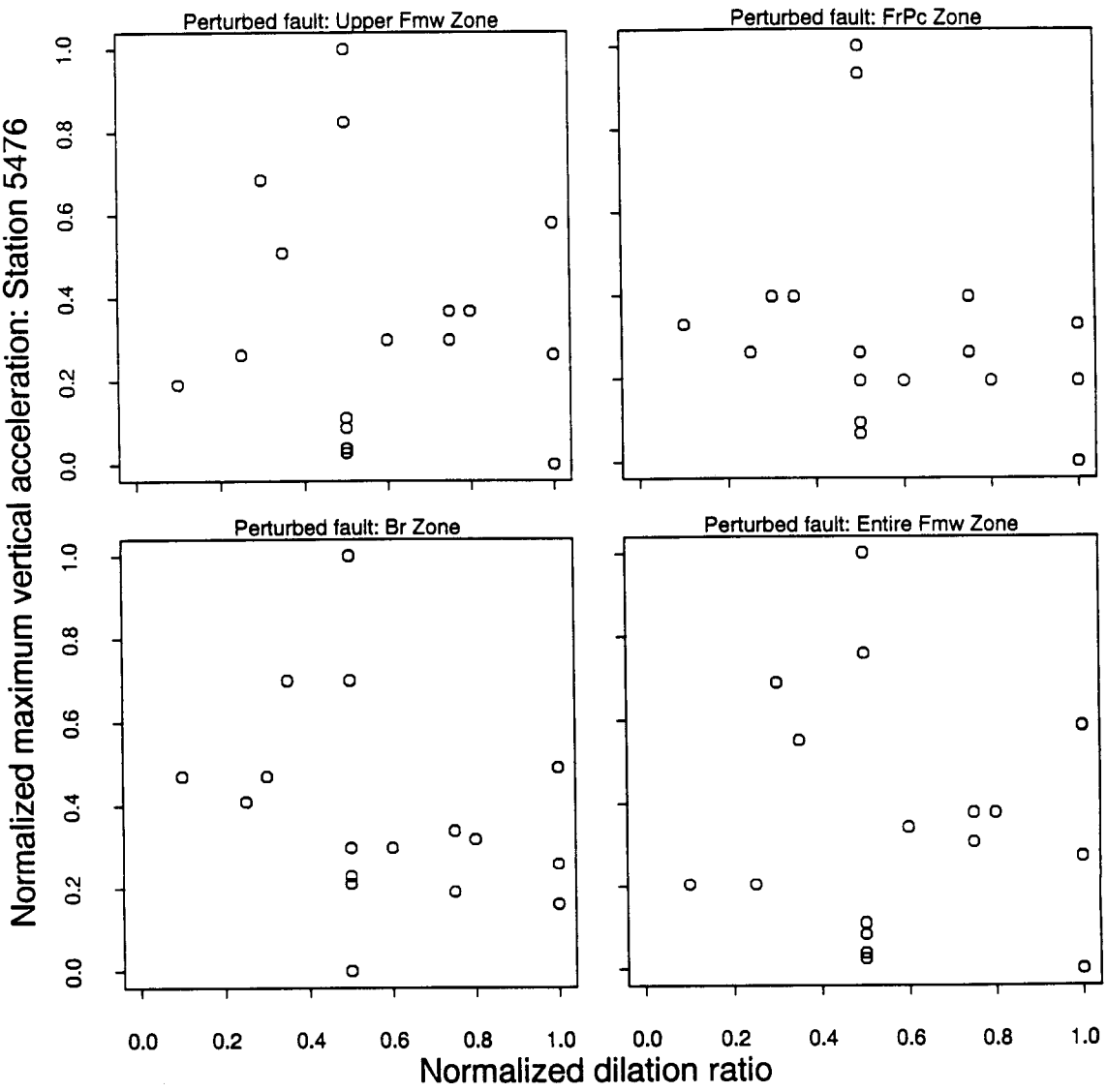

Figure B-55. Sensitivity of the maximum vertical acceleration at Station 5476 to changes in the value of the dilation angle

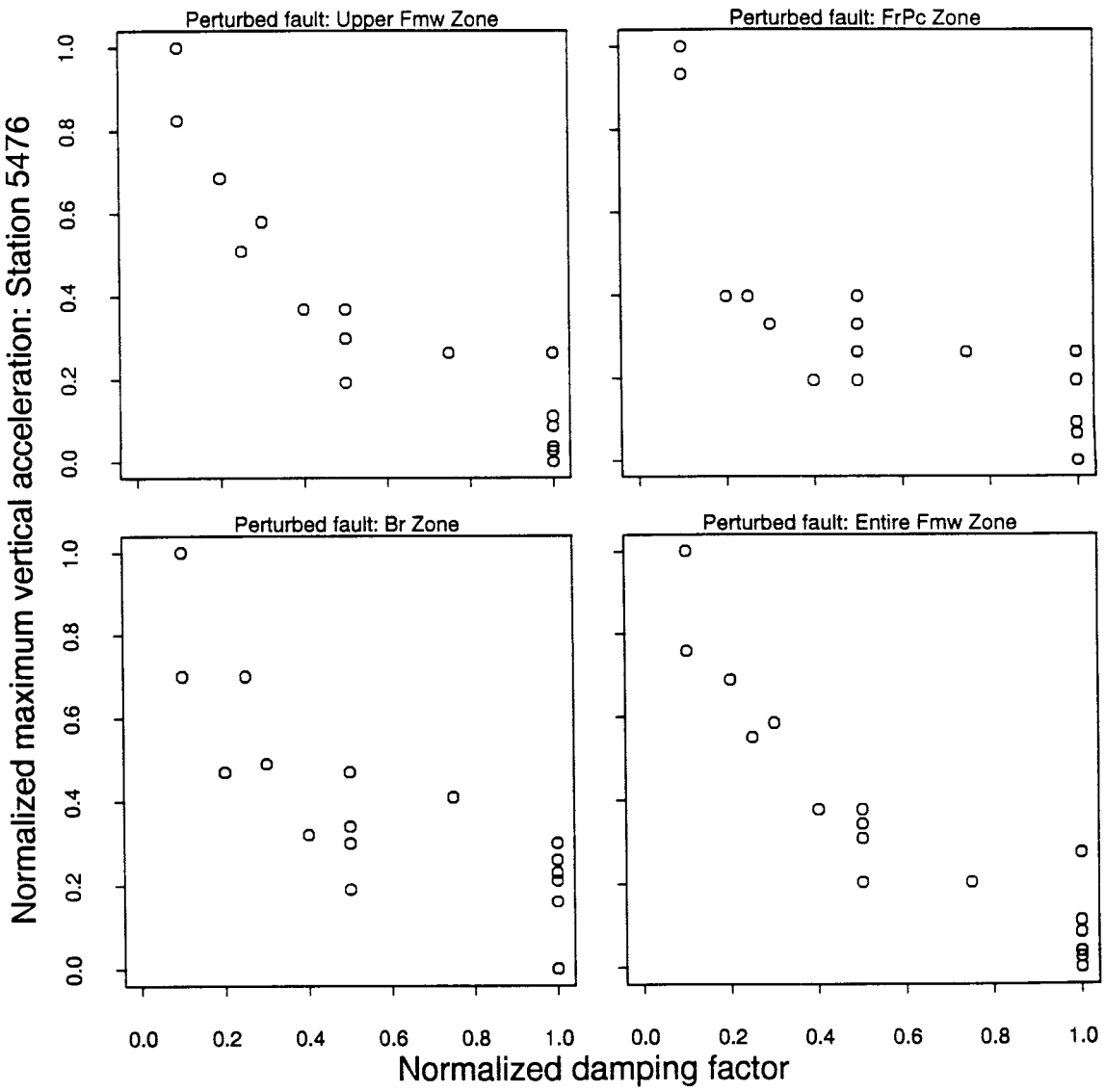

Figure B-56. Sensitivity of the maximum vertical acceleration at Station 5476 to changes in the value of the damping factor

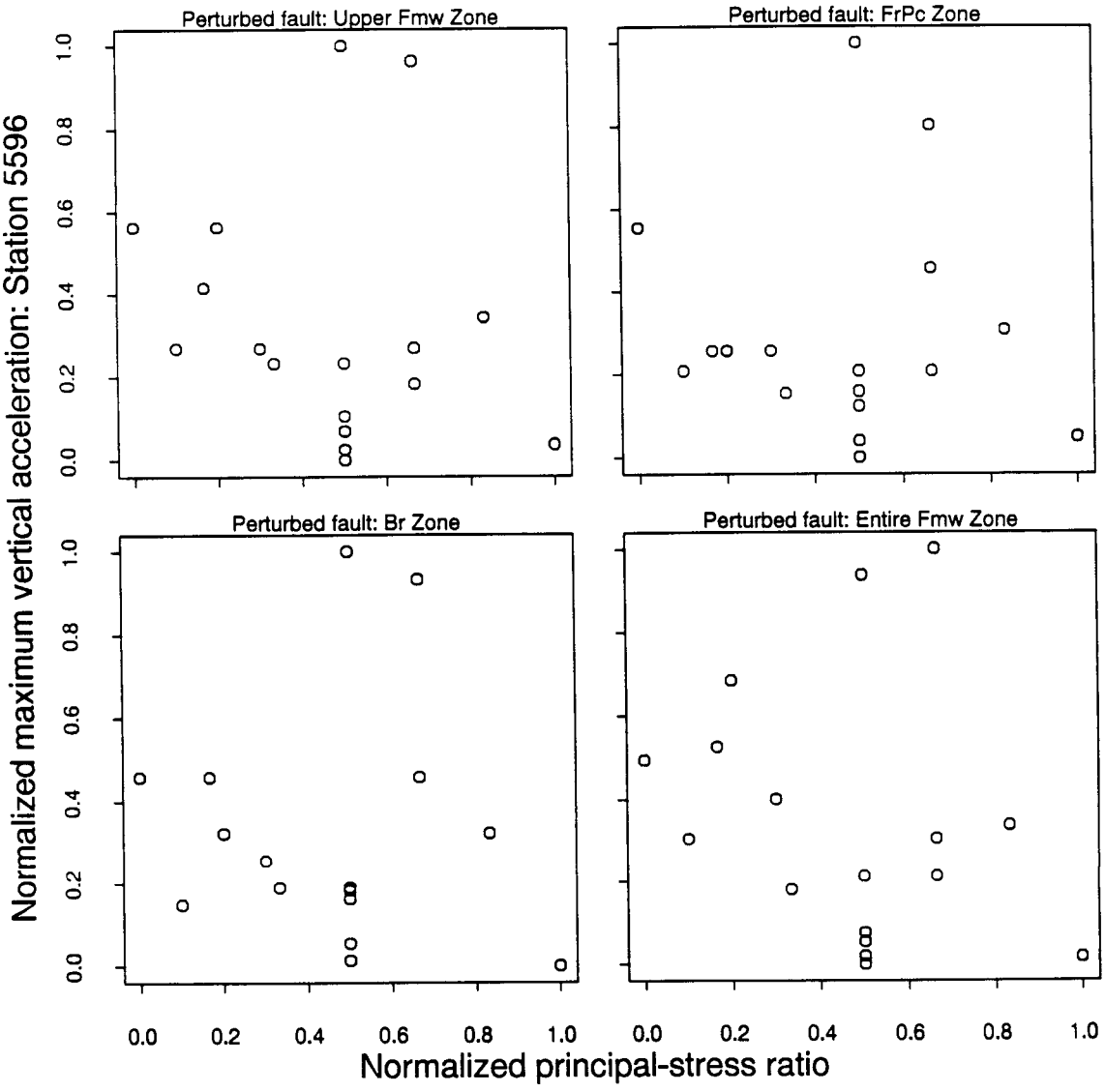

Figure B-57. Sensitivity of the maximum vertical acceleration at Station 5596 to changes in the value of the principal stress ratio k_3

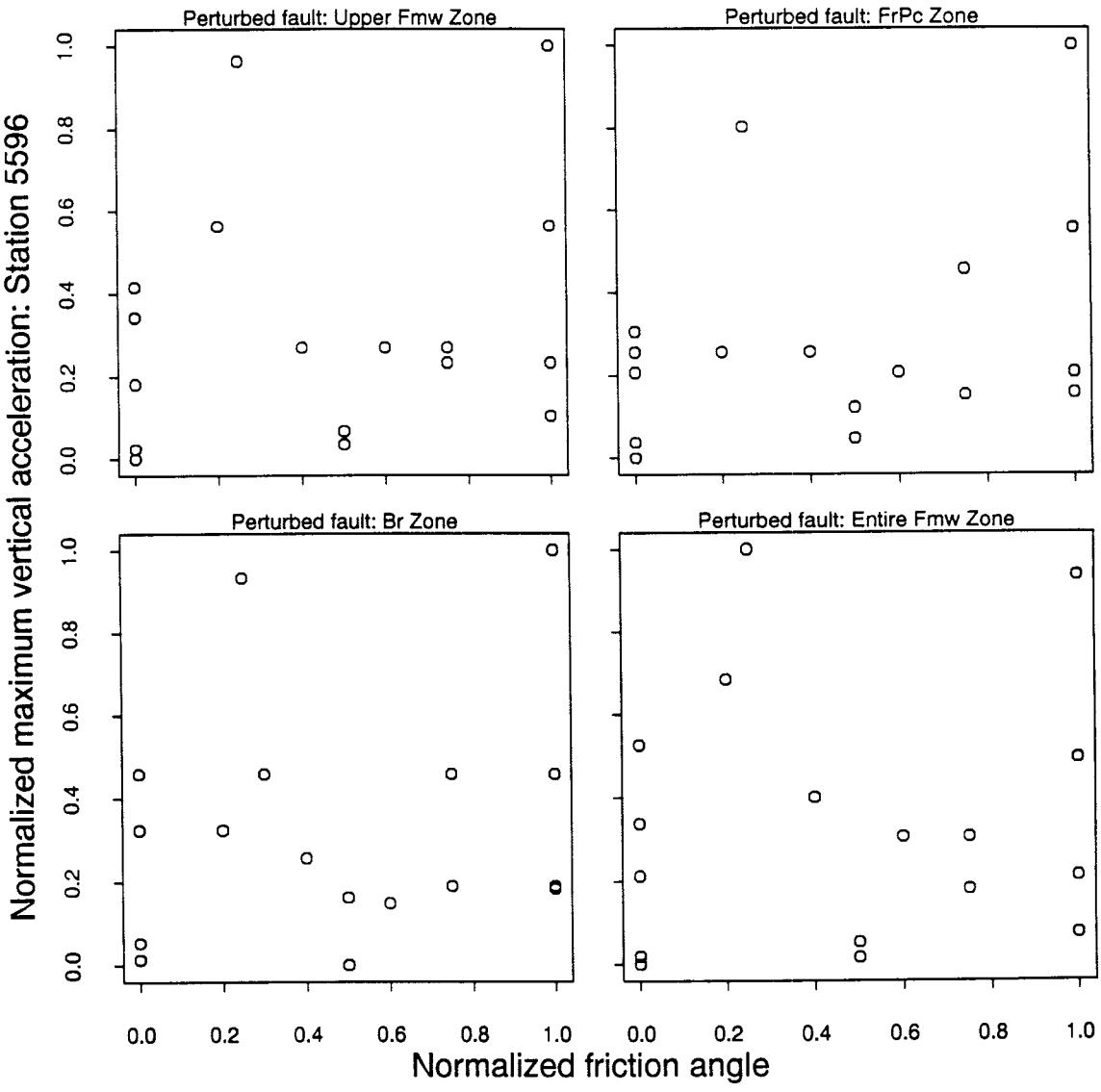

Figure B-58. Sensitivity of the maximum vertical acceleration at Station 5596 to changes in the value of the friction angle

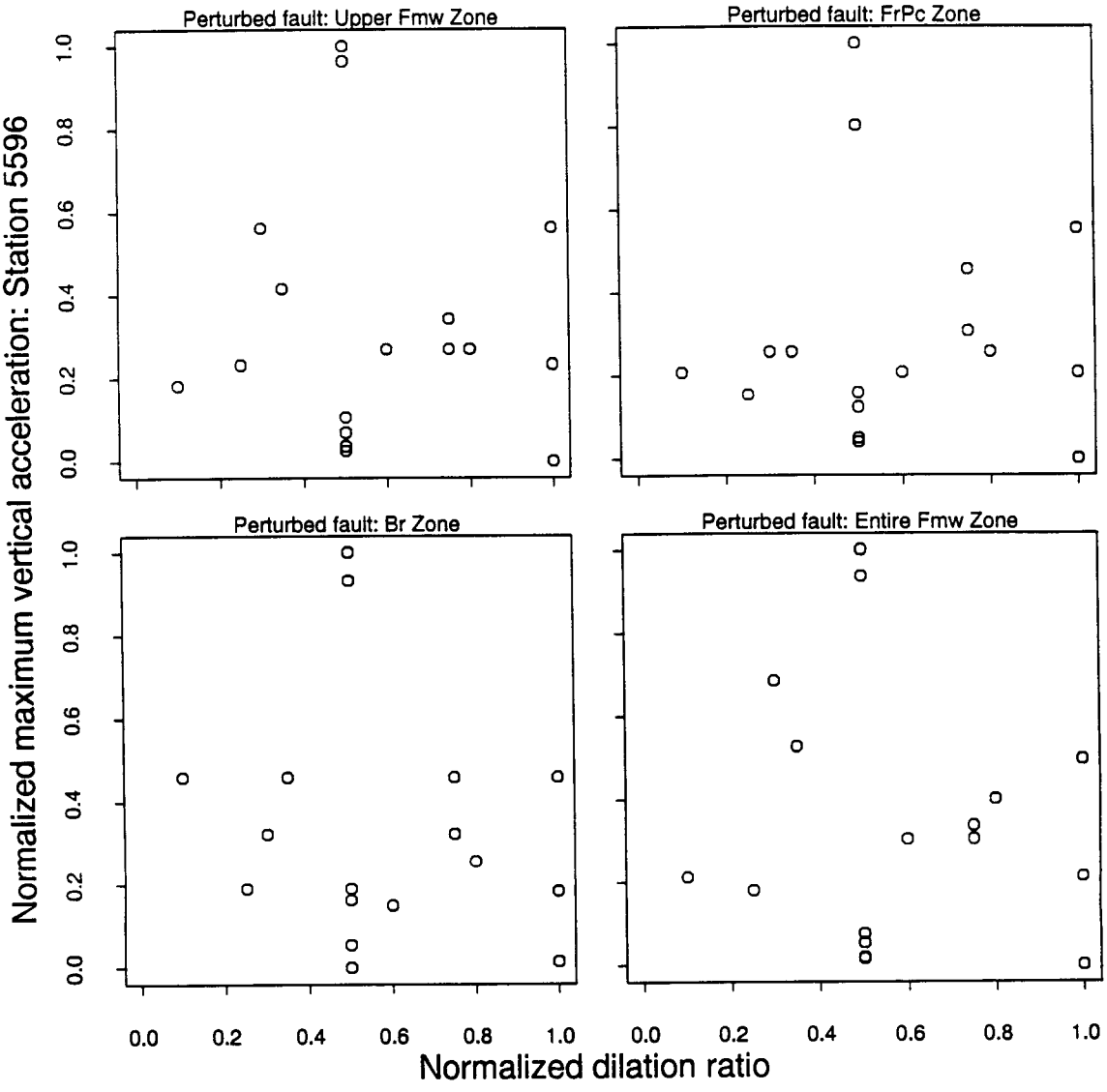

Figure B-59. Sensitivity of the maximum vertical acceleration at Station 5596 to changes in the value of the dilation angle

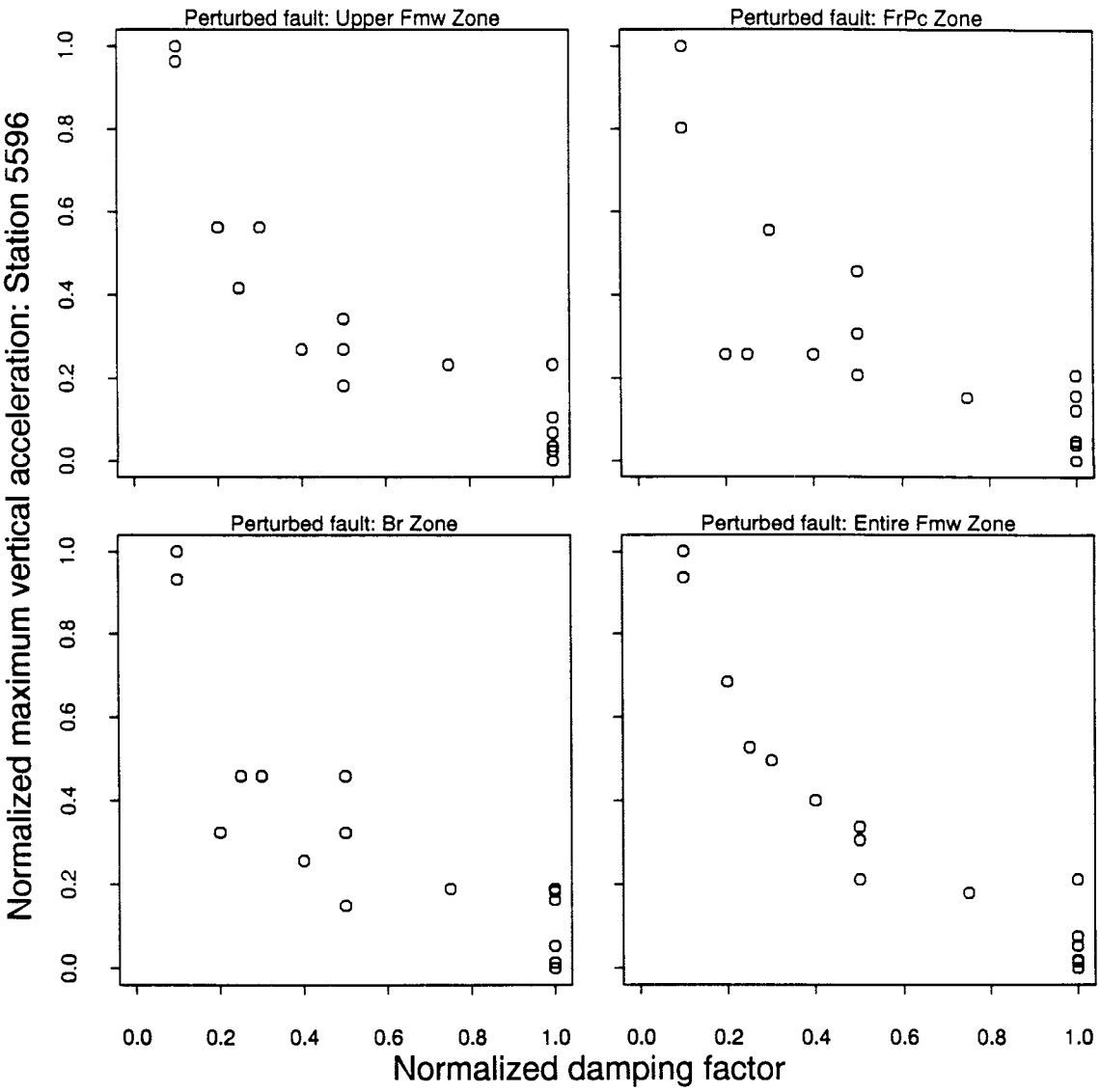

Figure B-60. Sensitivity of the maximum vertical acceleration at Station 5596 to changes in the value of the damping factor

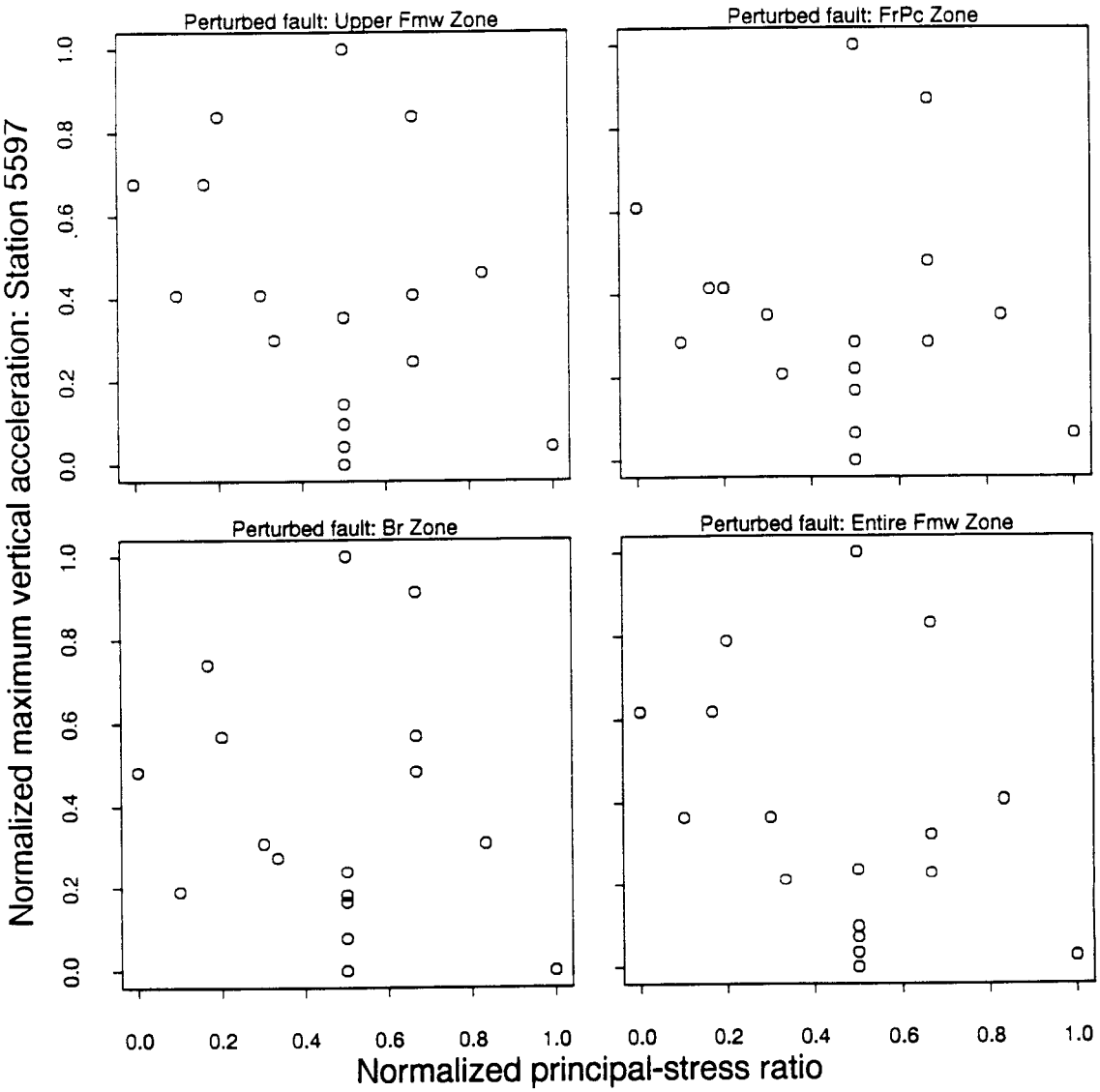

Figure B-61. Sensitivity of the maximum vertical acceleration at Station 5597 to changes in the value of the principal stress ratio k_3

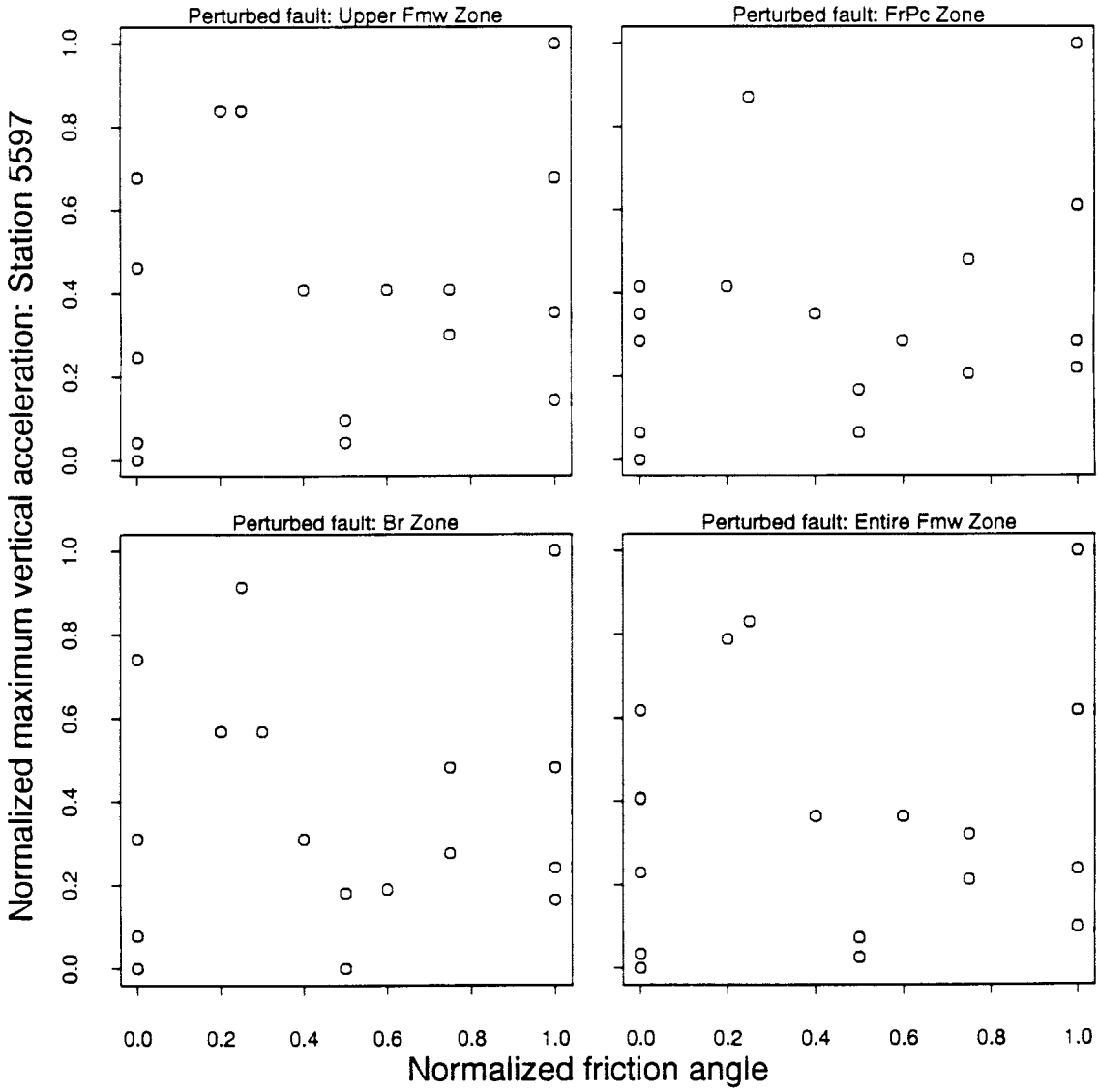

Figure B-62. Sensitivity of the maximum vertical acceleration at Station 5597 to changes in the value of the friction angle

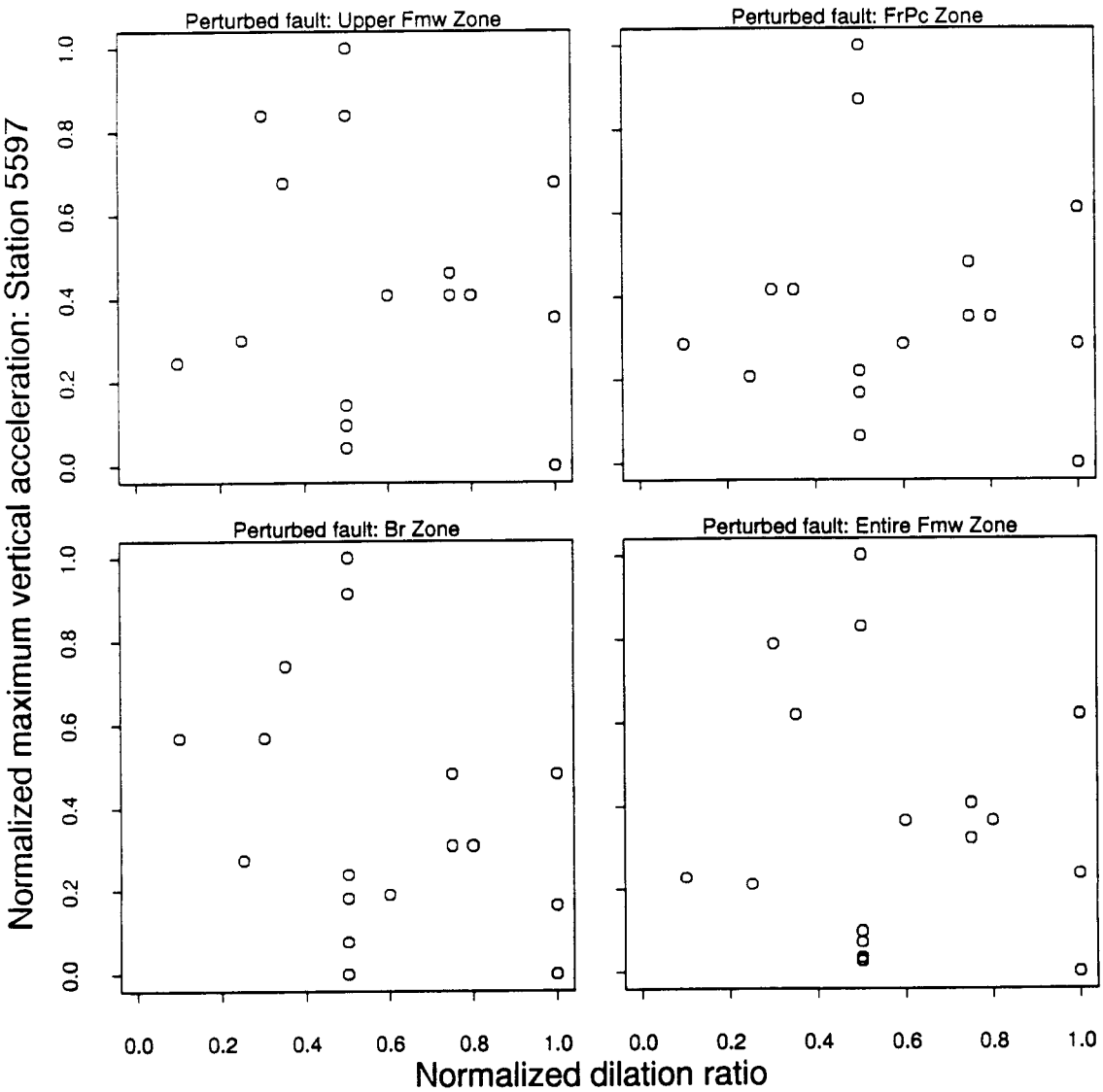

Figure B-63. Sensitivity of the maximum vertical acceleration at Station 5597 to changes in the value of the dilation angle

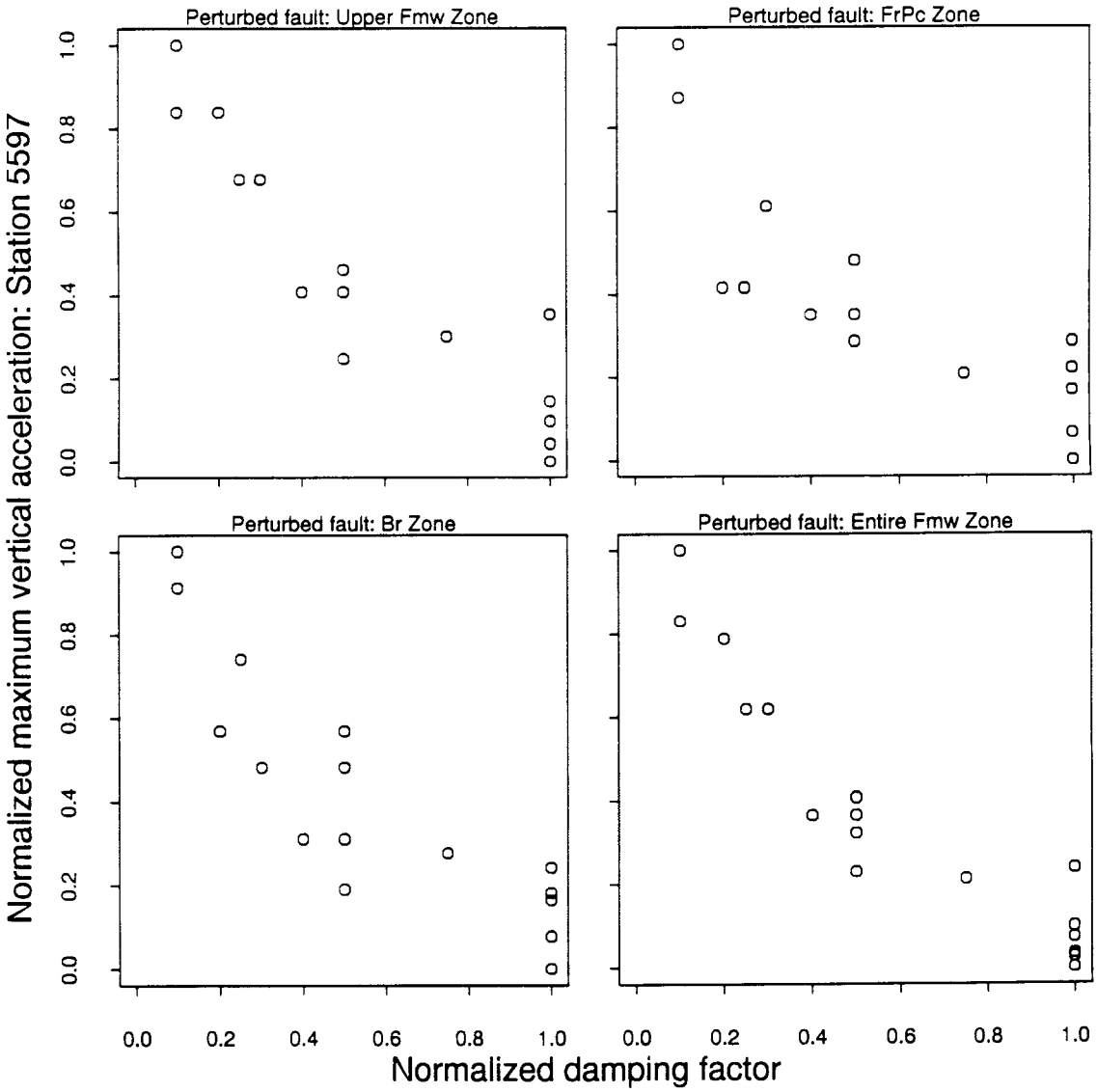

Figure B-64. Sensitivity of the maximum vertical acceleration at Station 5597 to changes in the value of the damping factor

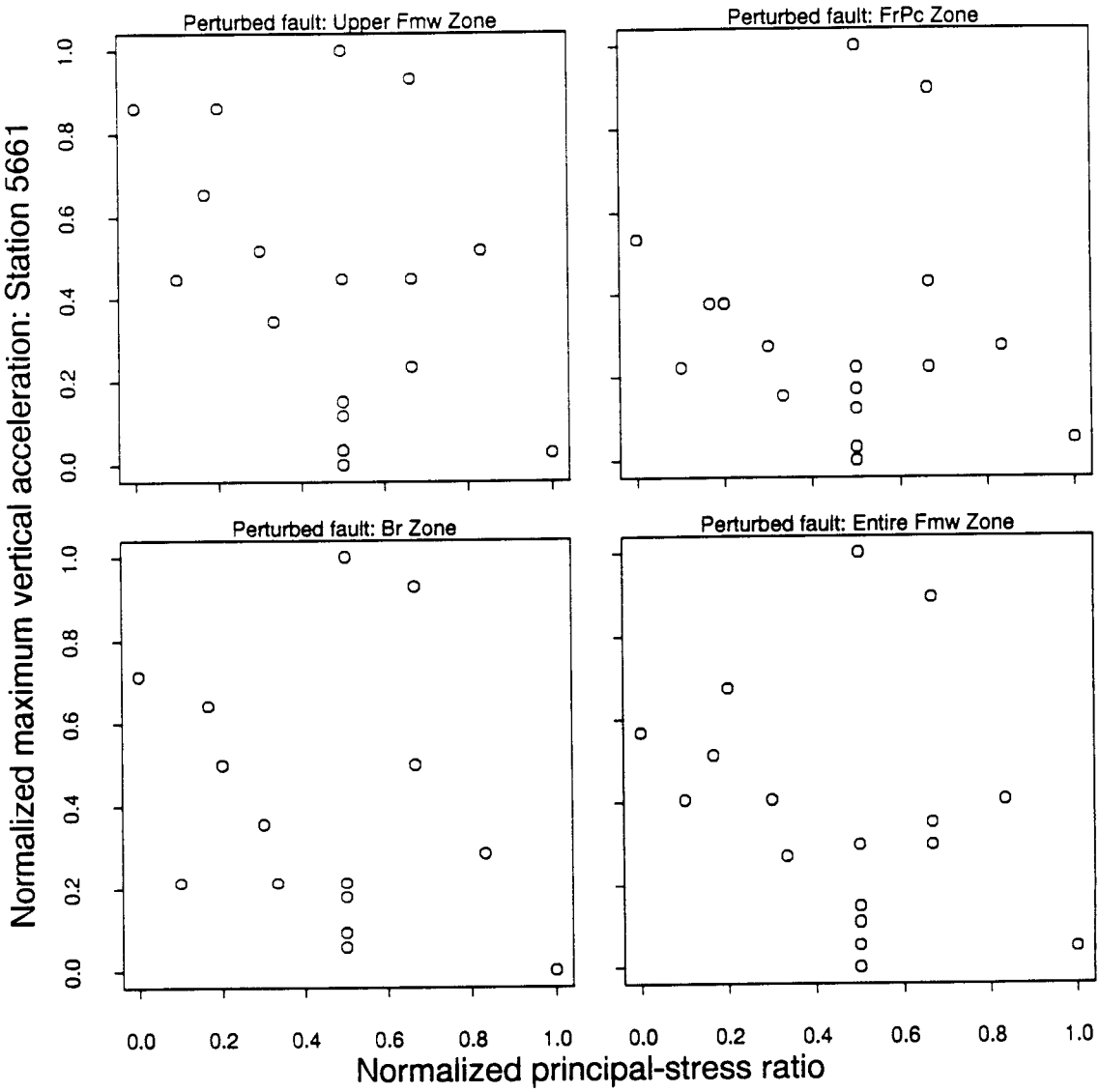

Figure B-65. Sensitivity of the maximum vertical acceleration at Station 5661 to changes in the value of the principal stress ratio k_3

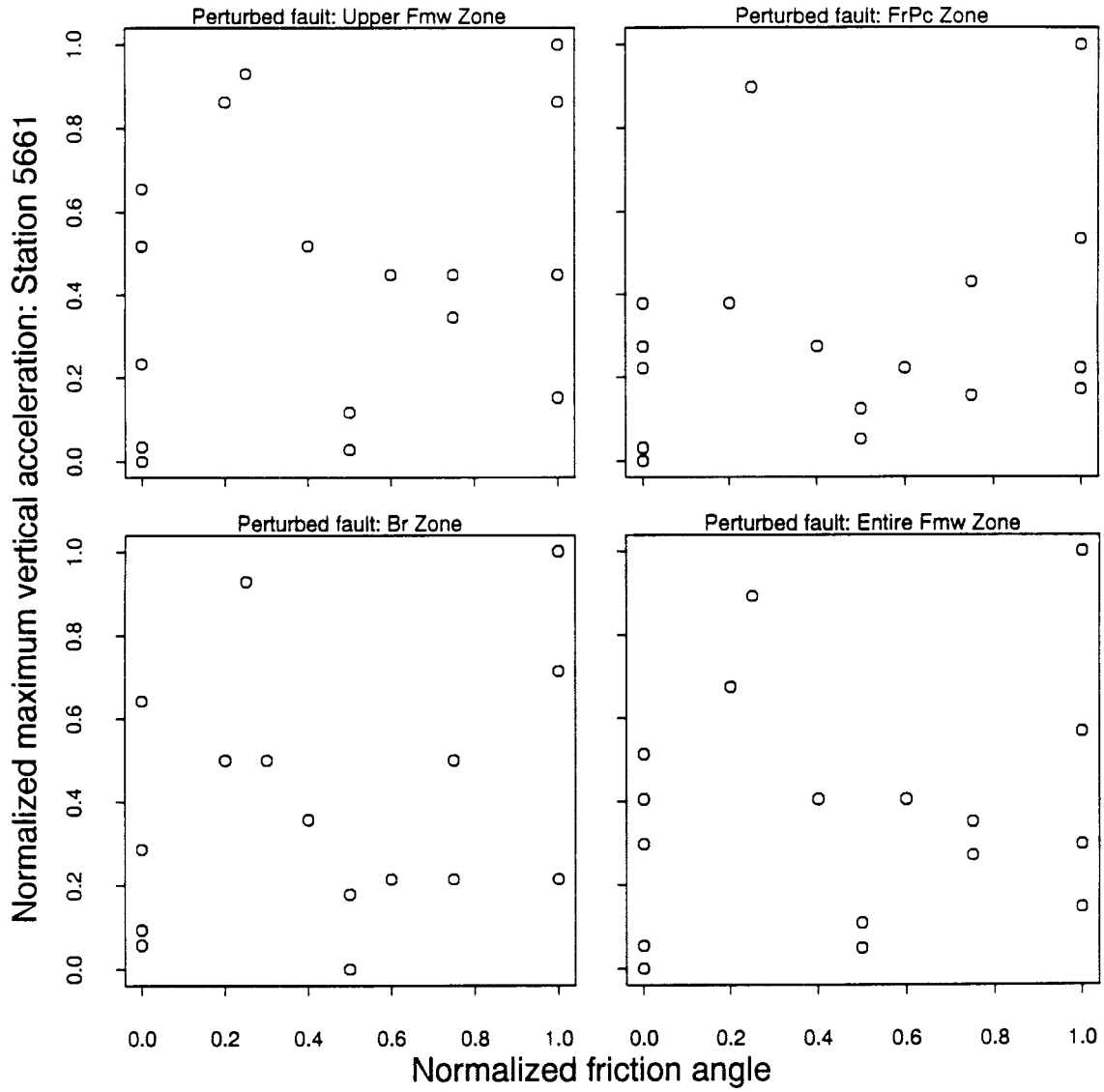

Figure B-66. Sensitivity of the maximum vertical acceleration at Station 5661 to changes in the value of the friction angle

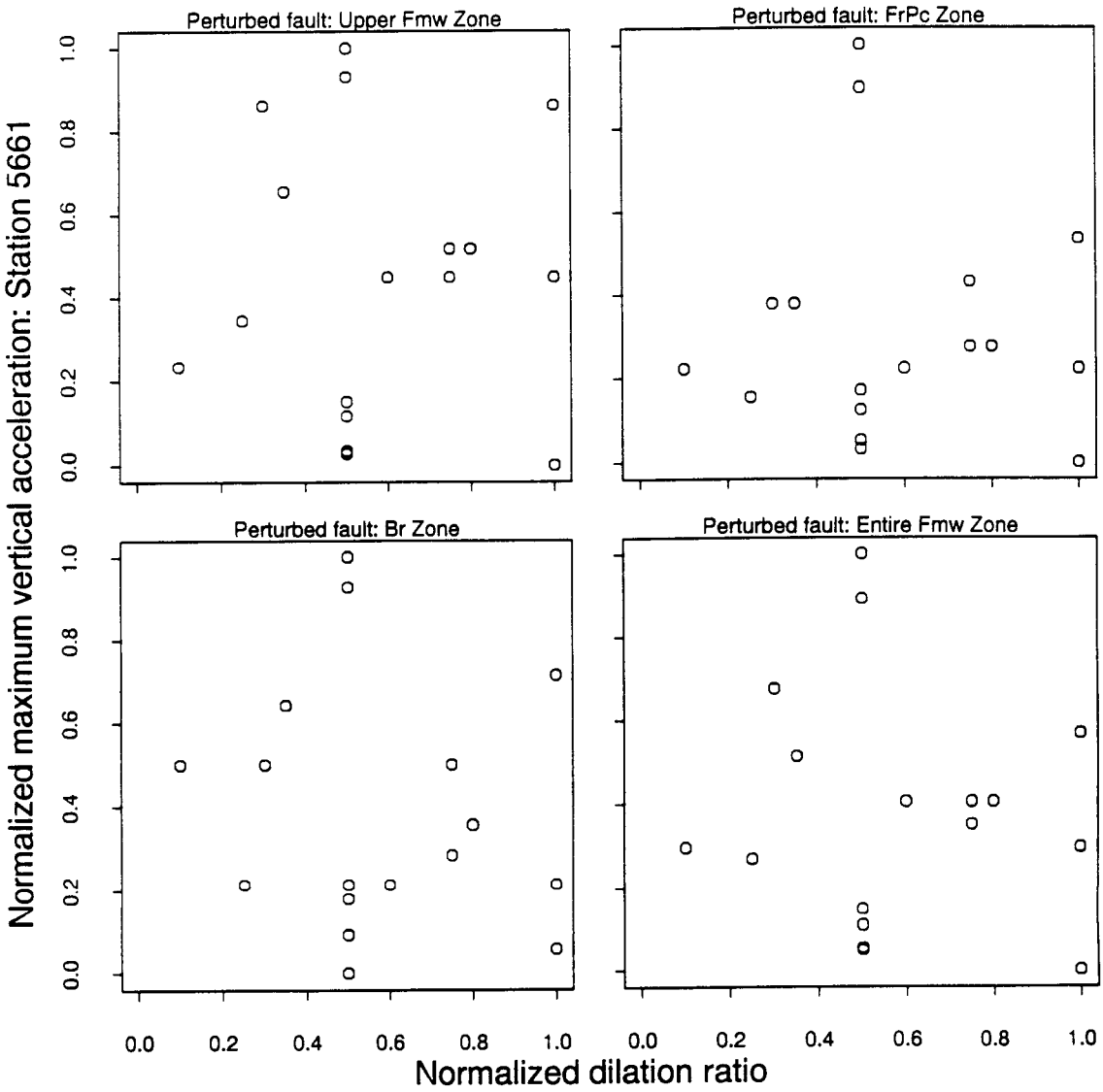

Figure B-67. Sensitivity of the maximum vertical acceleration at Station 5661 to changes in the value of the dilation angle

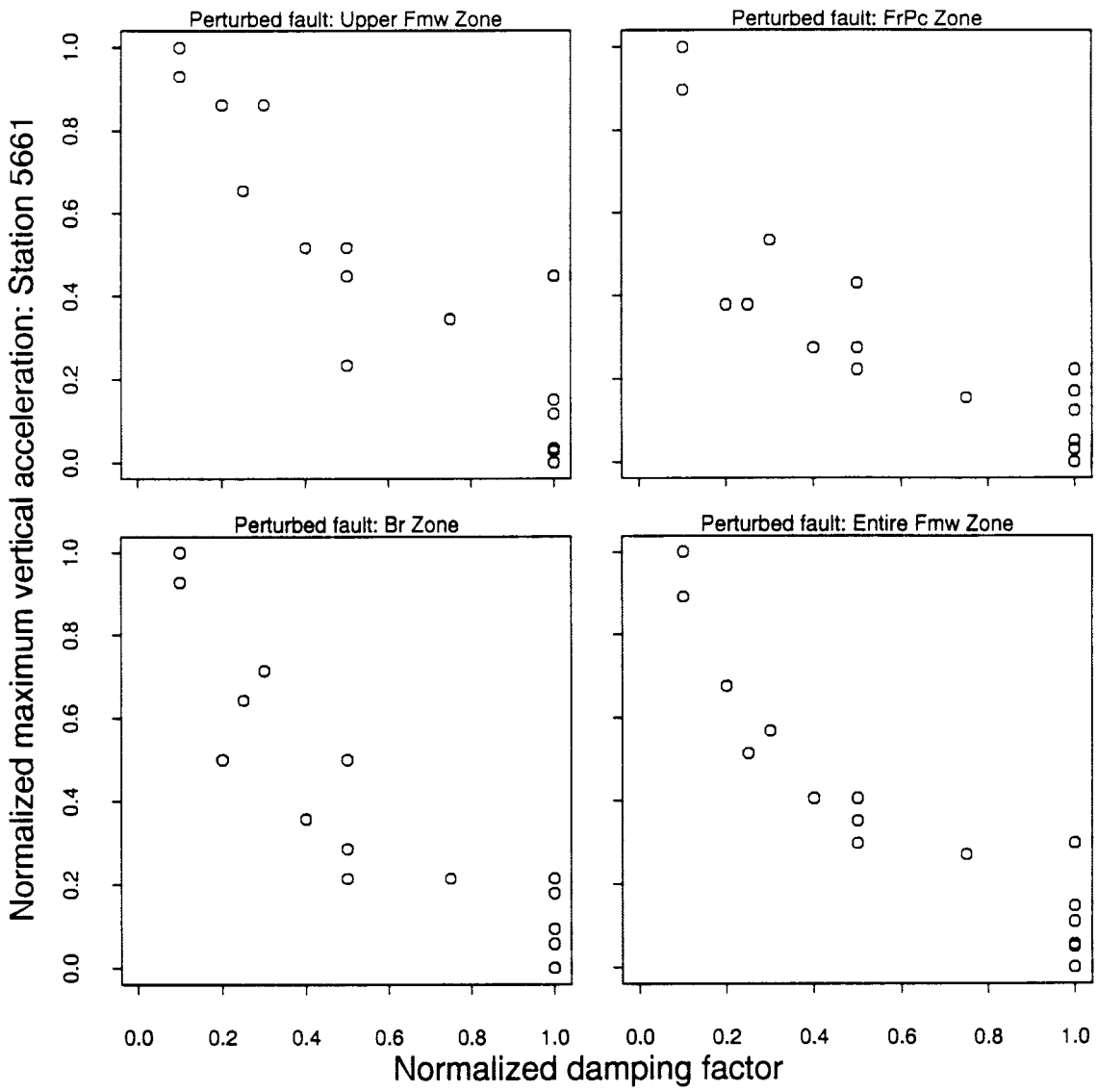

Figure B-68. Sensitivity of the maximum vertical acceleration at Station 5661 to changes in the value of the damping factor

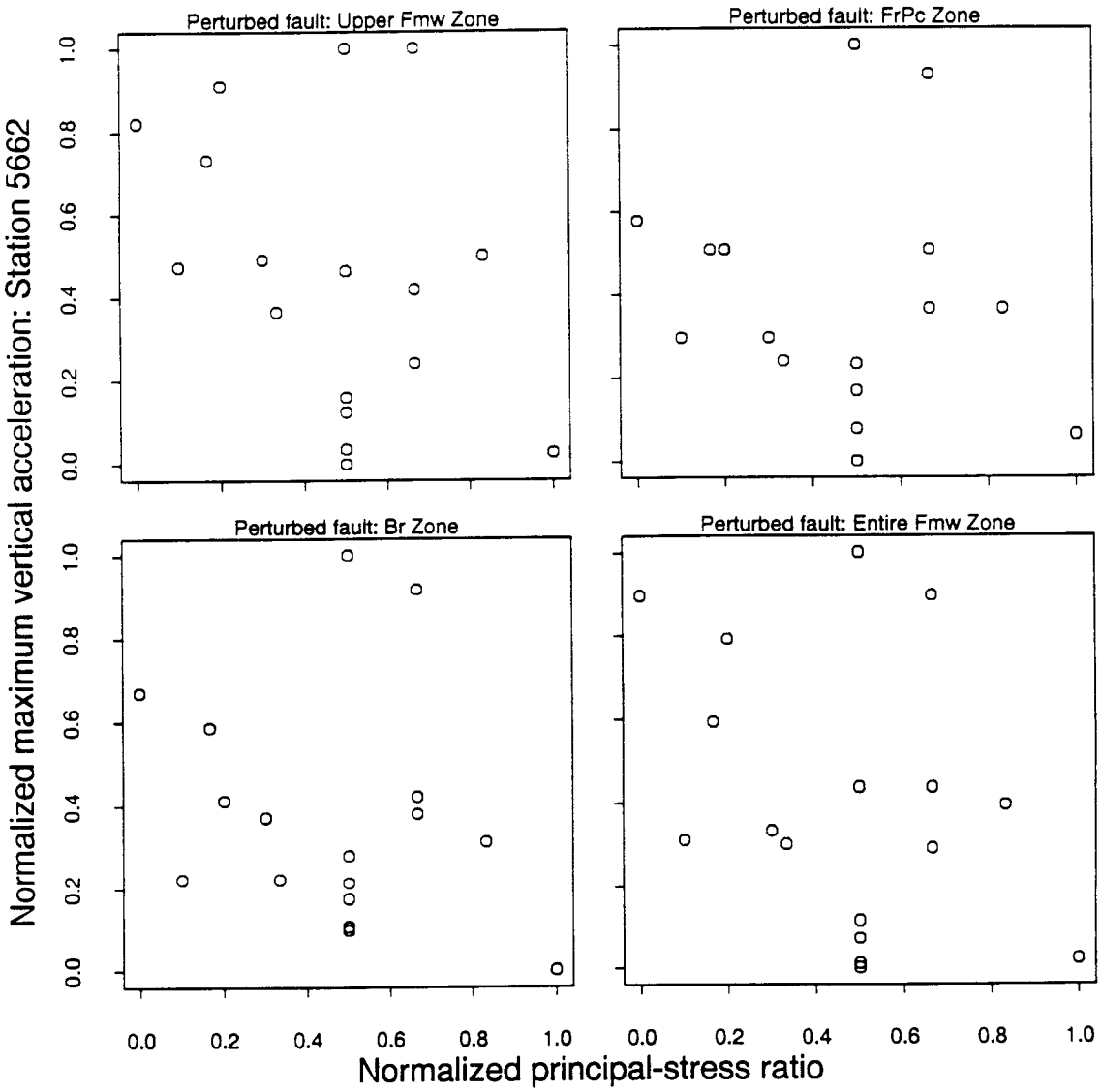

Figure B-69. Sensitivity of the maximum vertical acceleration at Station 5662 to changes in the value of the principal stress ratio k_3

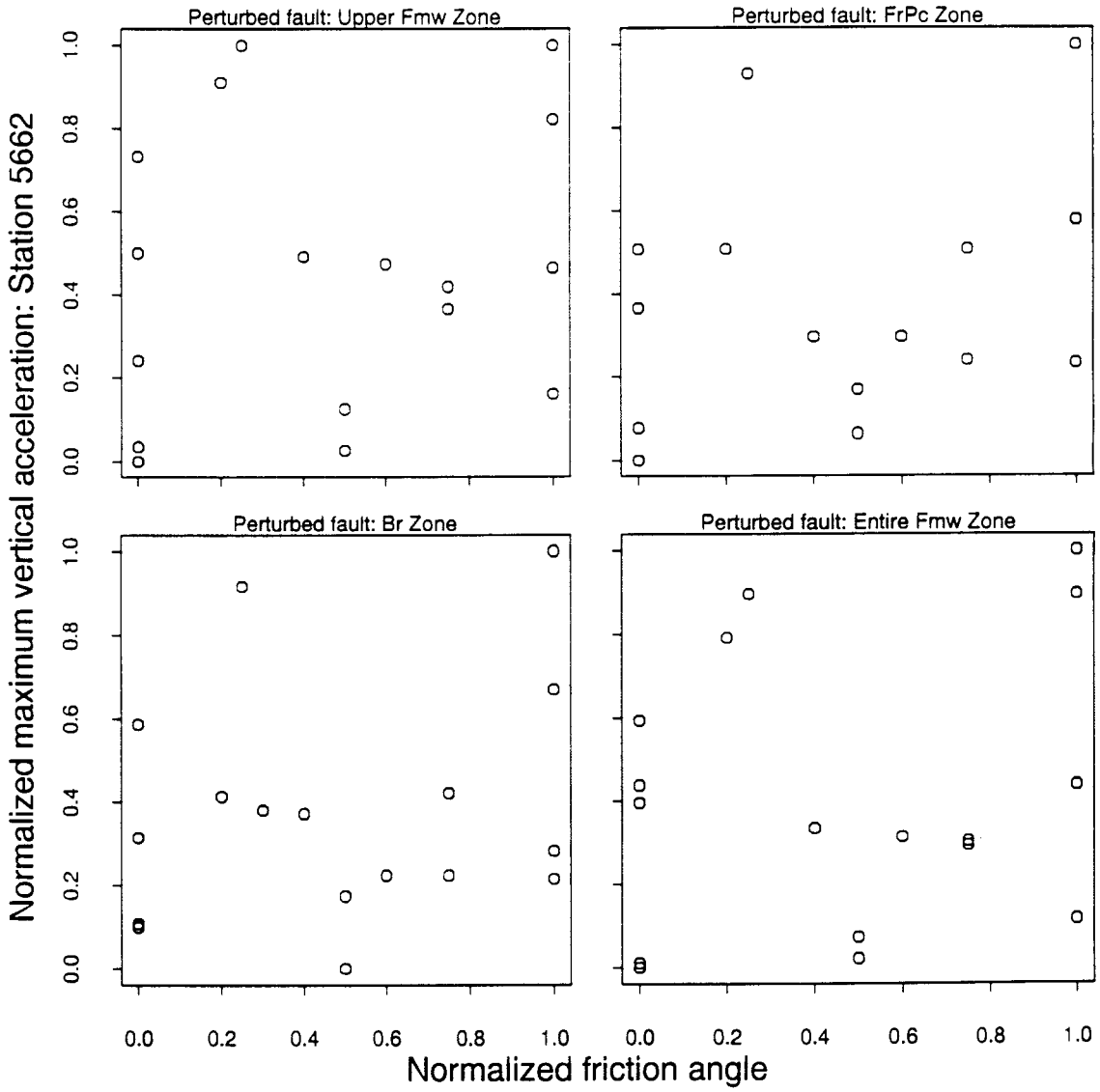

Figure B-70. Sensitivity of the maximum vertical acceleration at Station 5662 to changes in the value of the friction angle

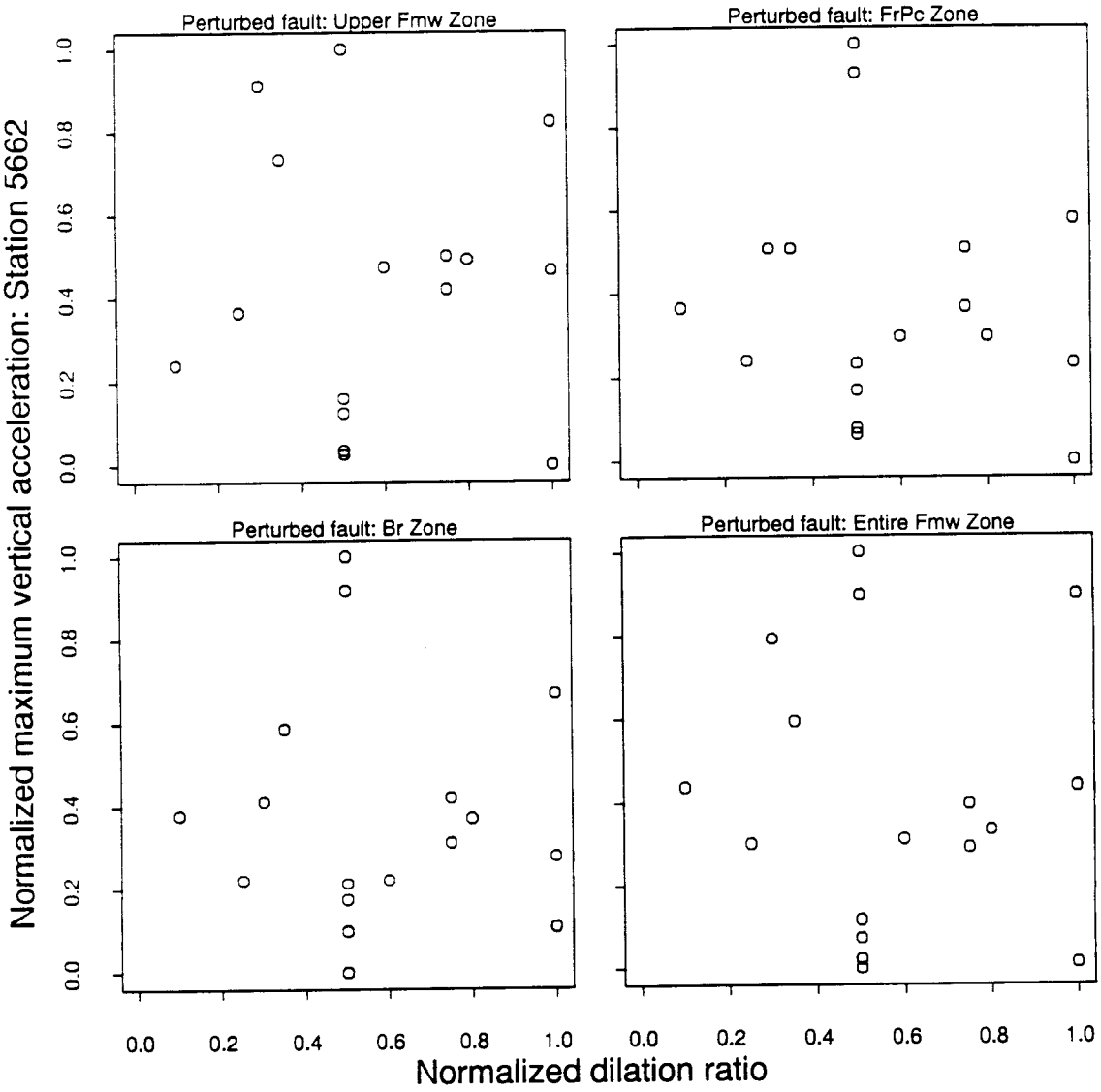

Figure B-71. Sensitivity of the maximum vertical acceleration at Station 5662 to changes in the value of the dilation angle

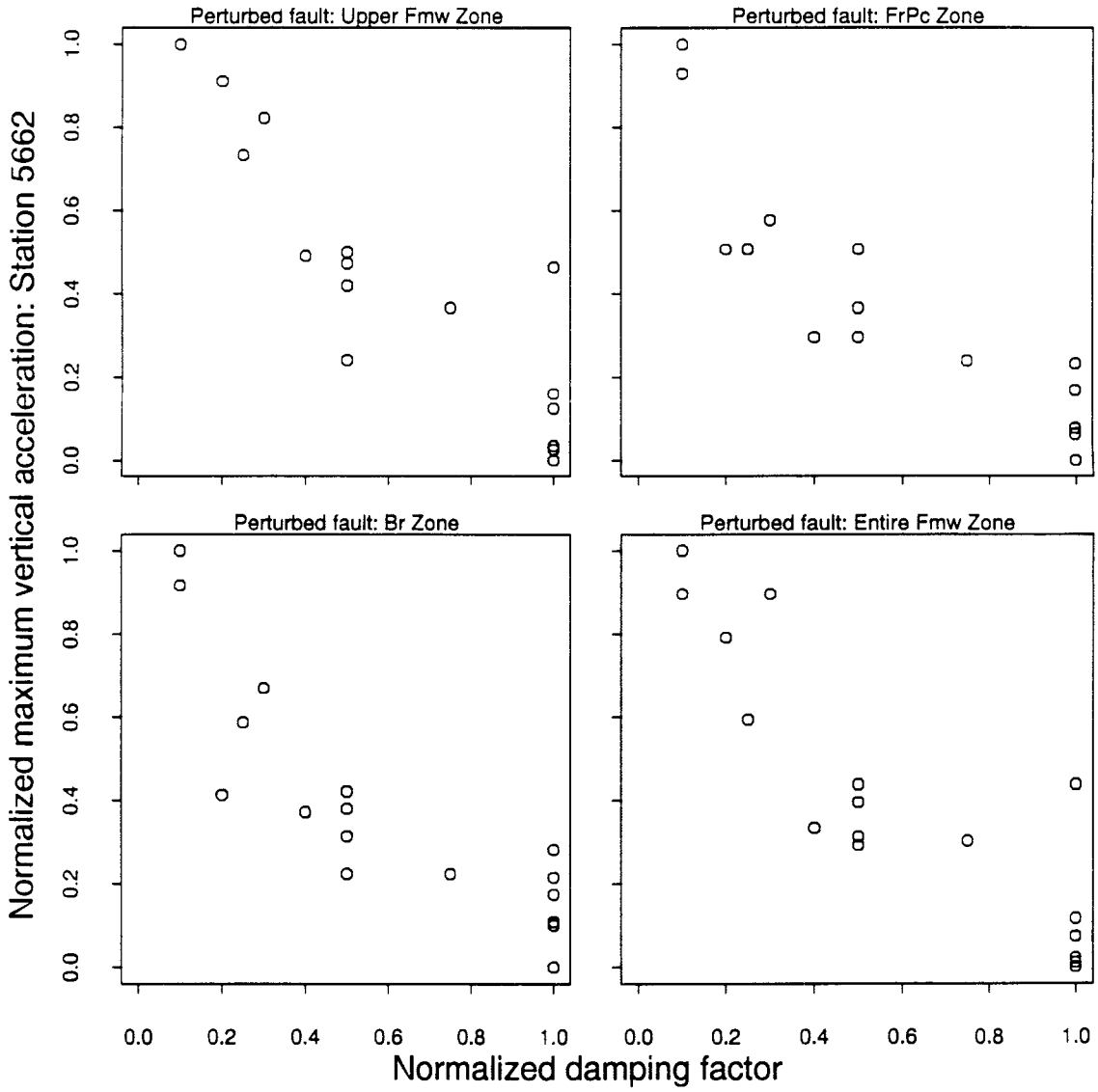

Figure B-72. Sensitivity of the maximum vertical acceleration at Station 5662 to changes in the value of the damping factor

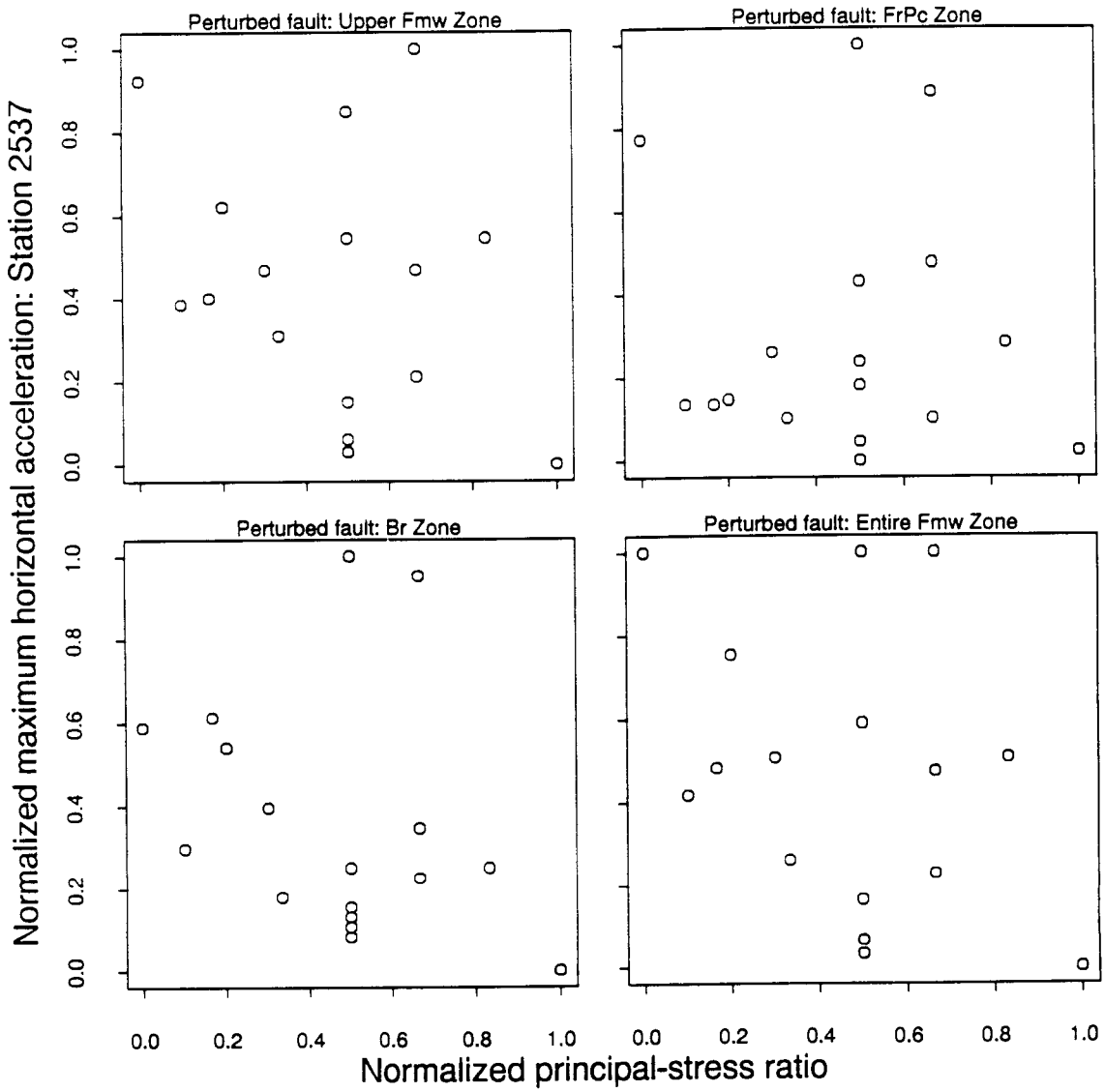

Figure B-73. Sensitivity of the maximum horizontal acceleration at Station 2537 to changes in the value of the principal stress ratio k_3

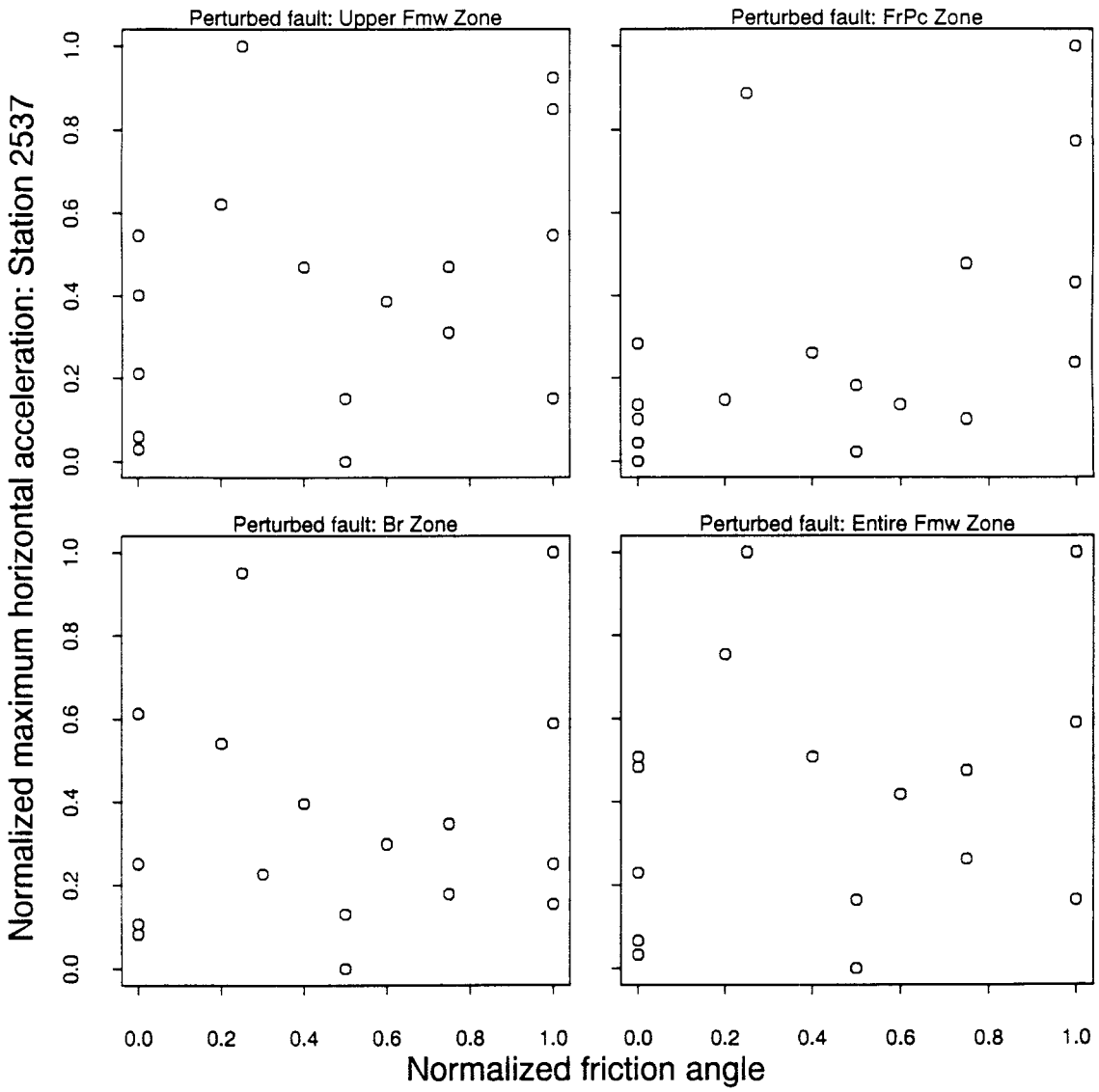

Figure B-74. Sensitivity of the maximum horizontal acceleration at Station 2537 to changes in the value of the friction angle

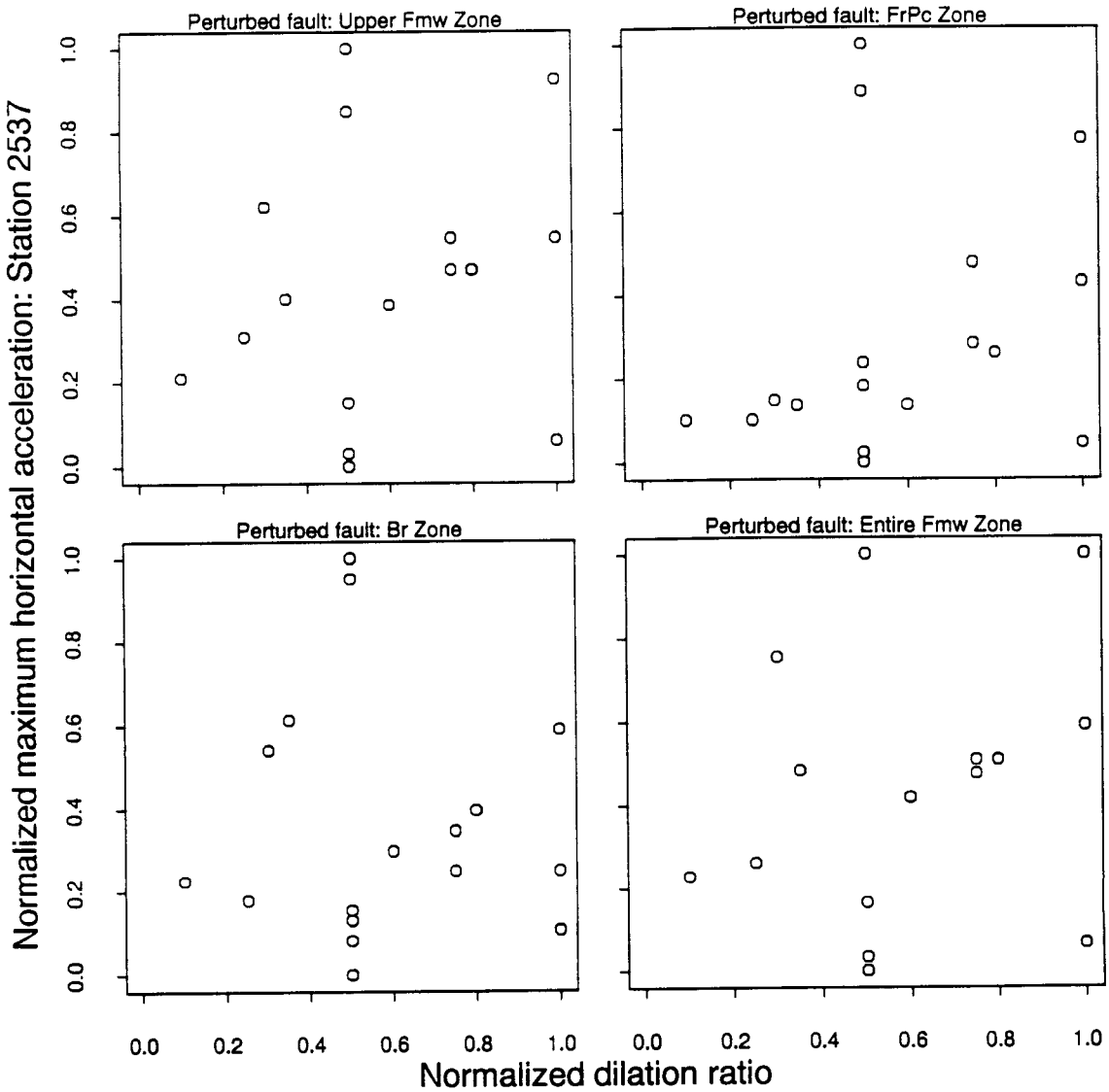

Figure B-75. Sensitivity of the maximum horizontal acceleration at Station 2537 to changes in the value of the dilation angle

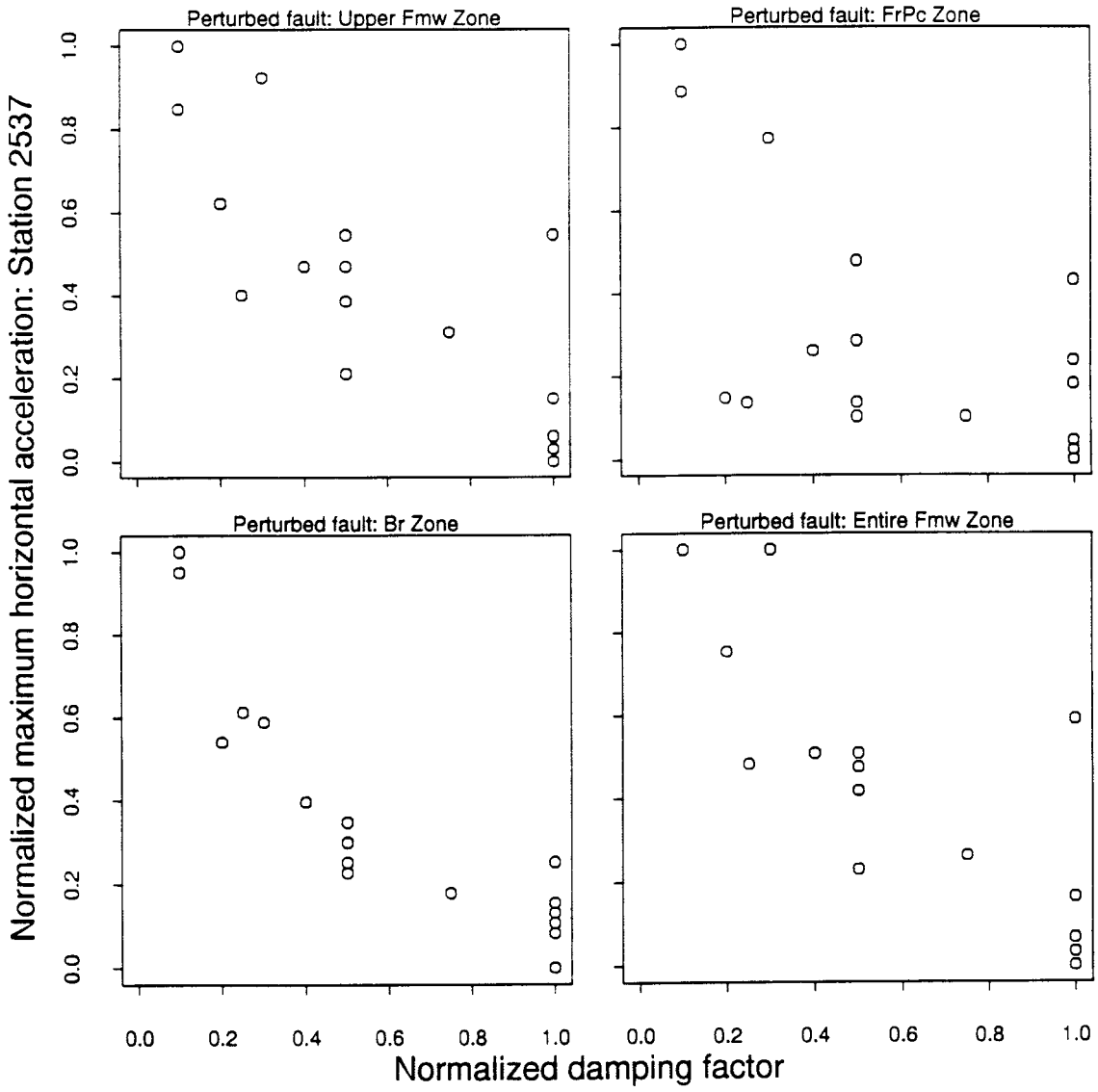

Figure B-76. Sensitivity of the maximum horizontal acceleration at Station 2537 to changes in the value of the damping factor

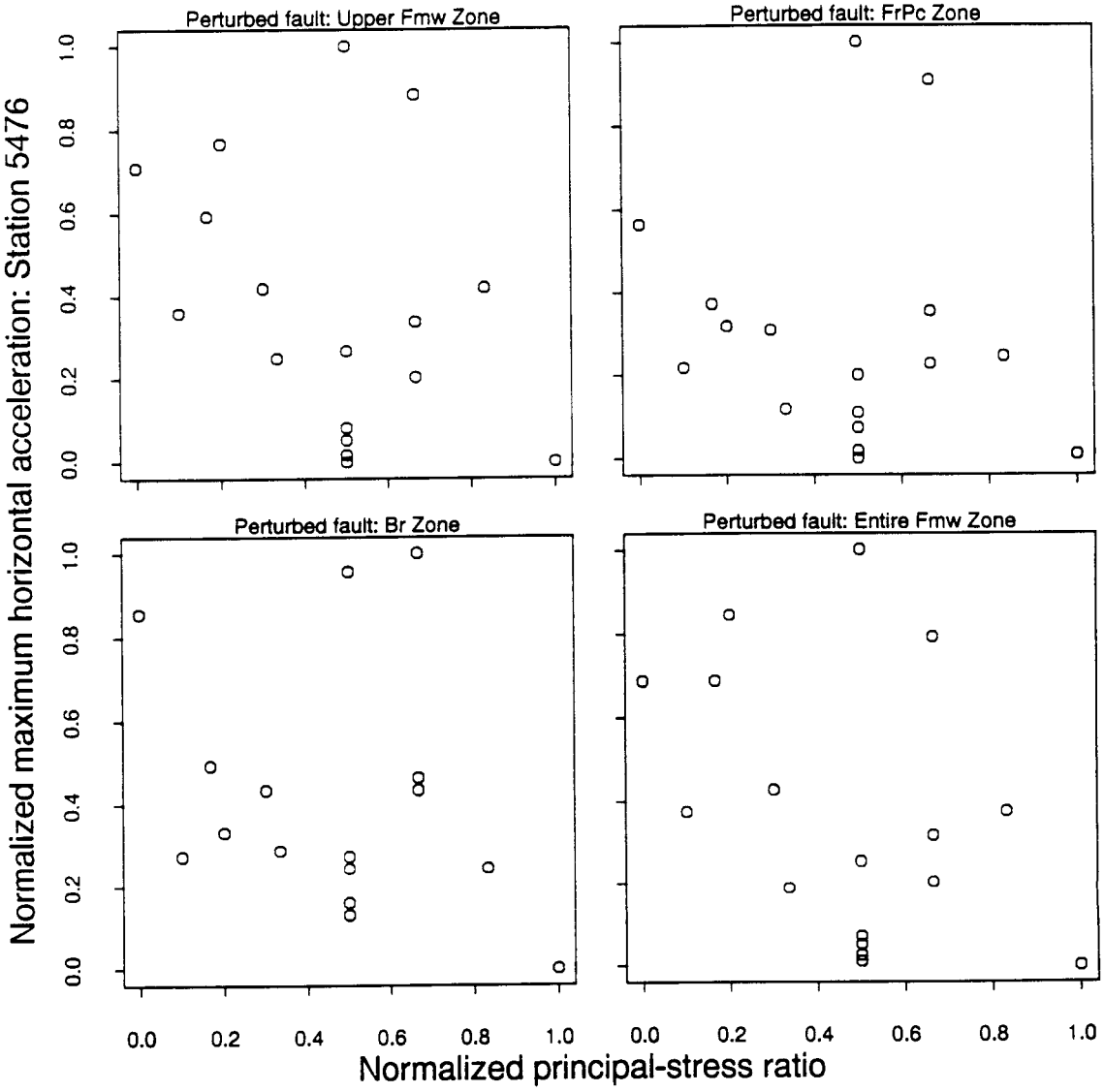

Figure B-77. Sensitivity of the maximum horizontal acceleration at Station 5476 to changes in the value of the principal stress ratio k_3

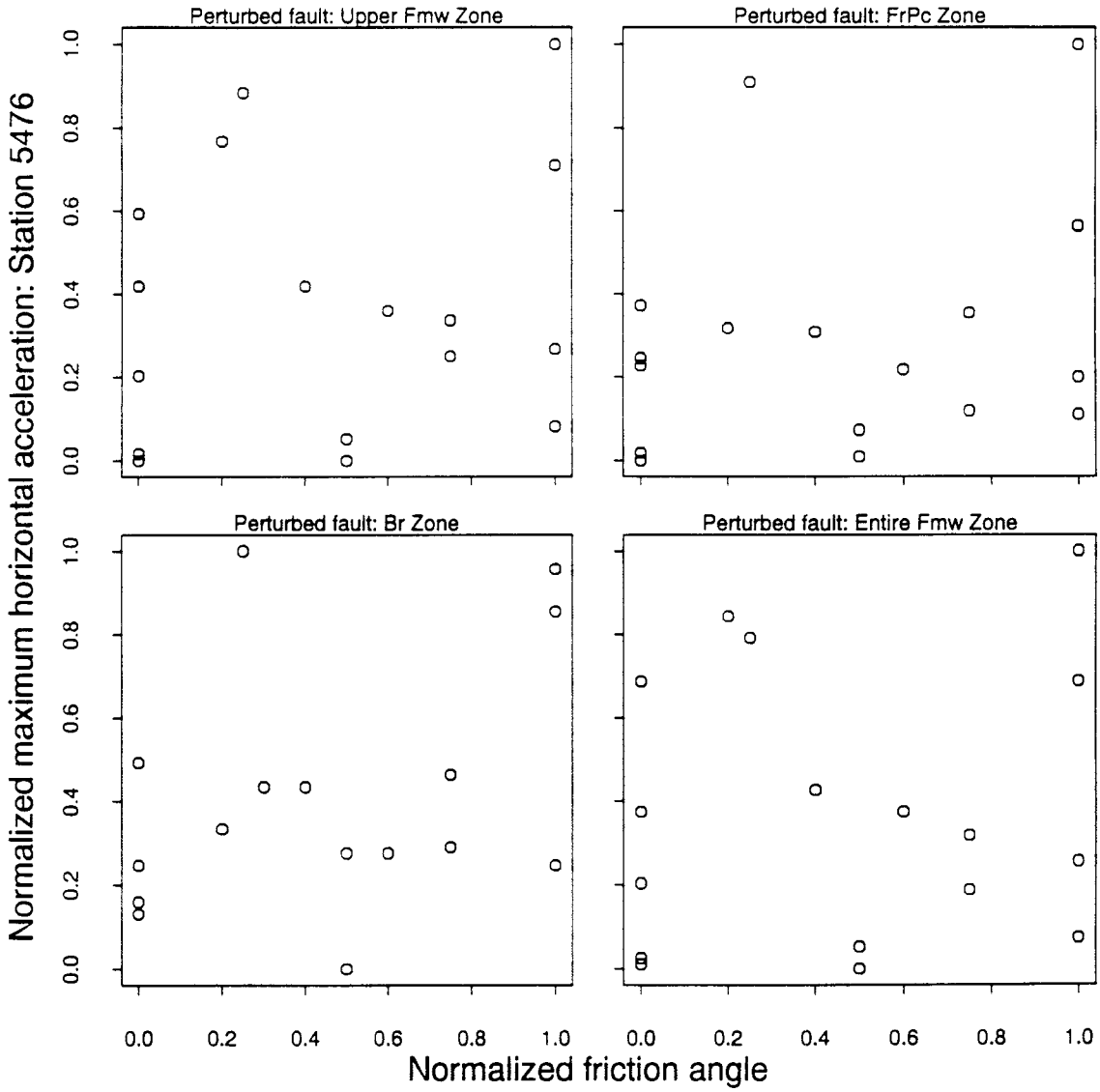

Figure B-78. Sensitivity of the maximum horizontal acceleration at Station 5476 to changes in the value of the friction angle

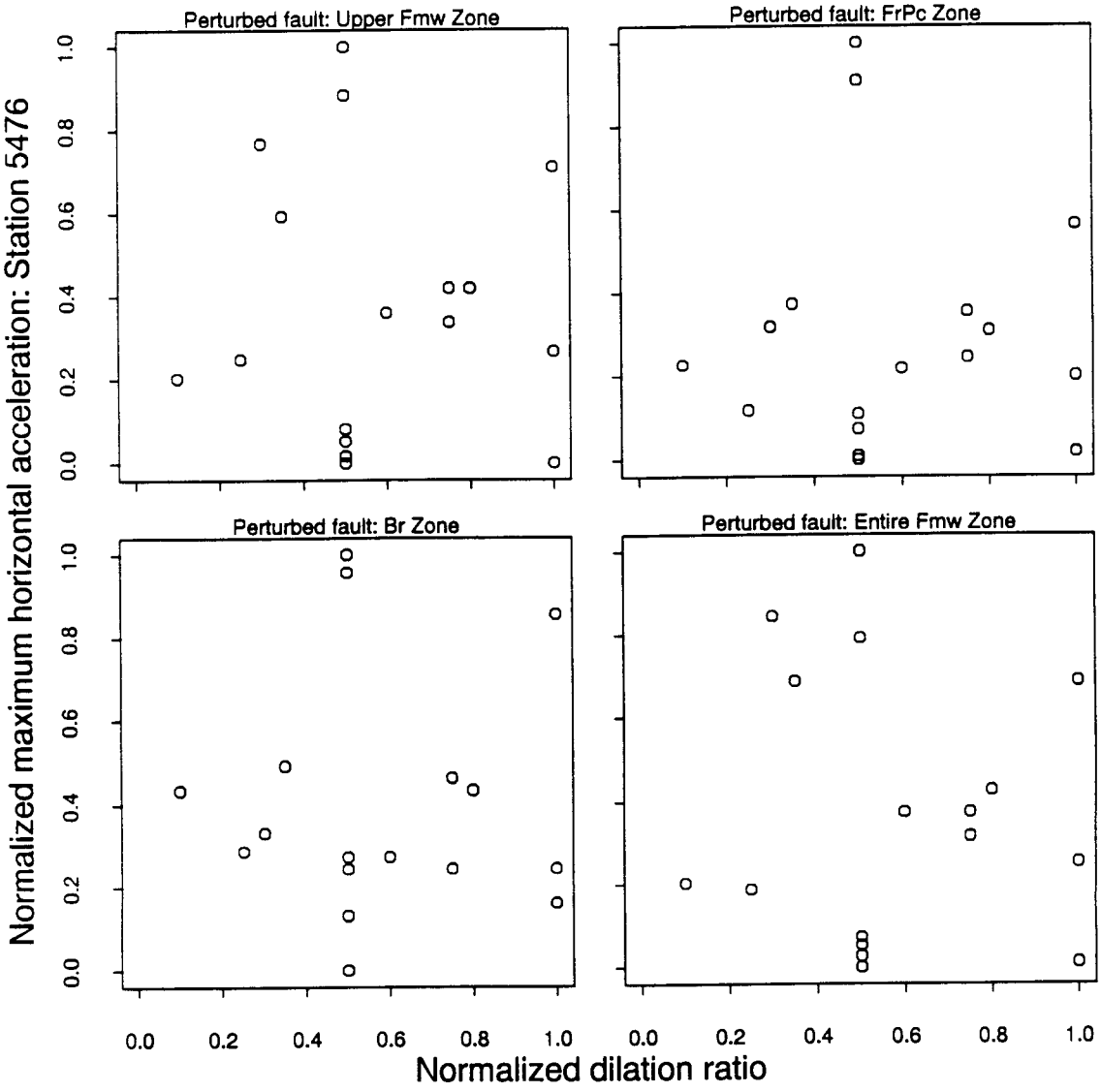

Figure B-79. Sensitivity of the maximum horizontal acceleration at Station 5476 to changes in the value of the dilation angle

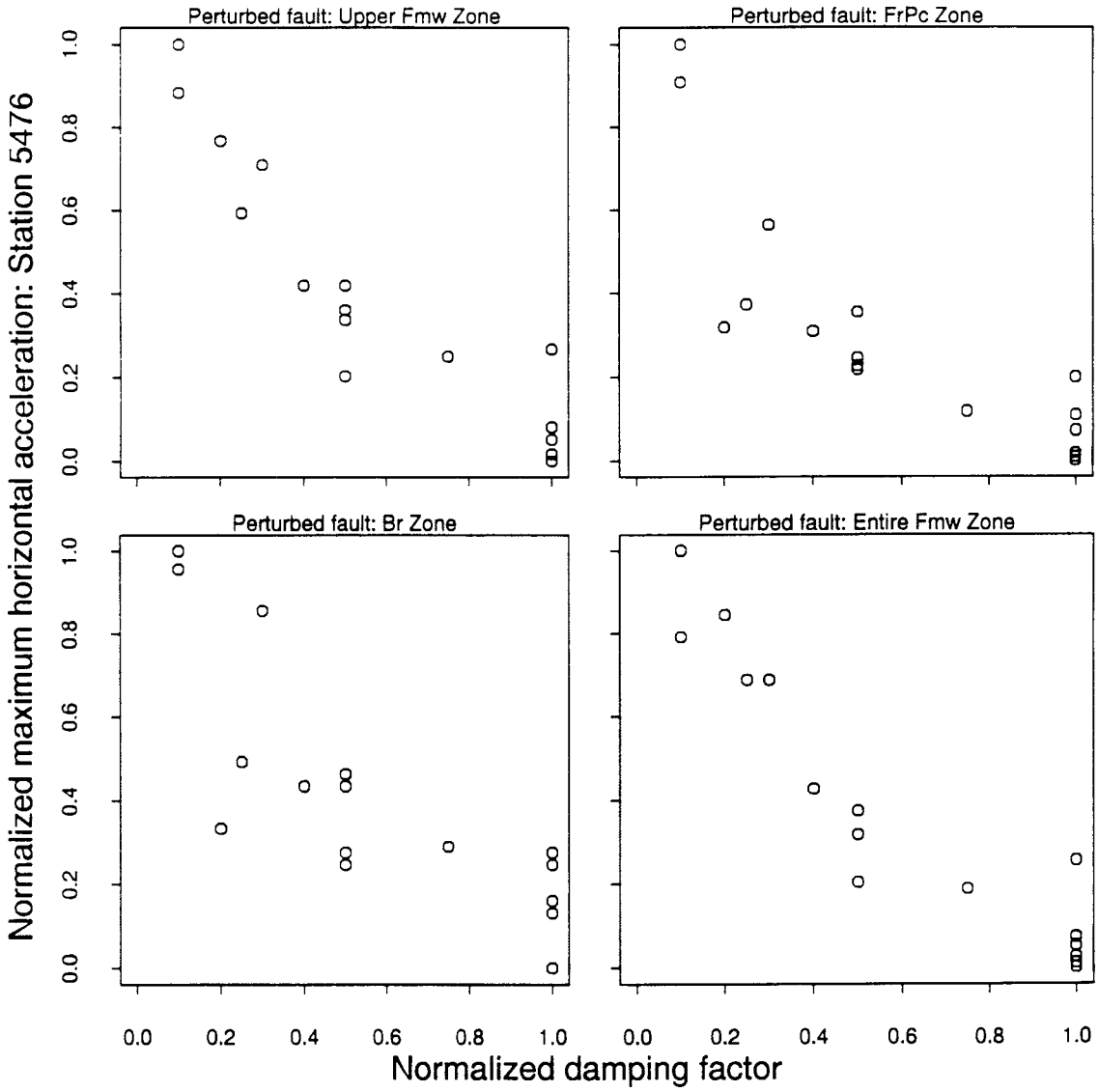

Figure B-80. Sensitivity of the maximum horizontal acceleration at Station 5476 to changes in the value of the damping factor

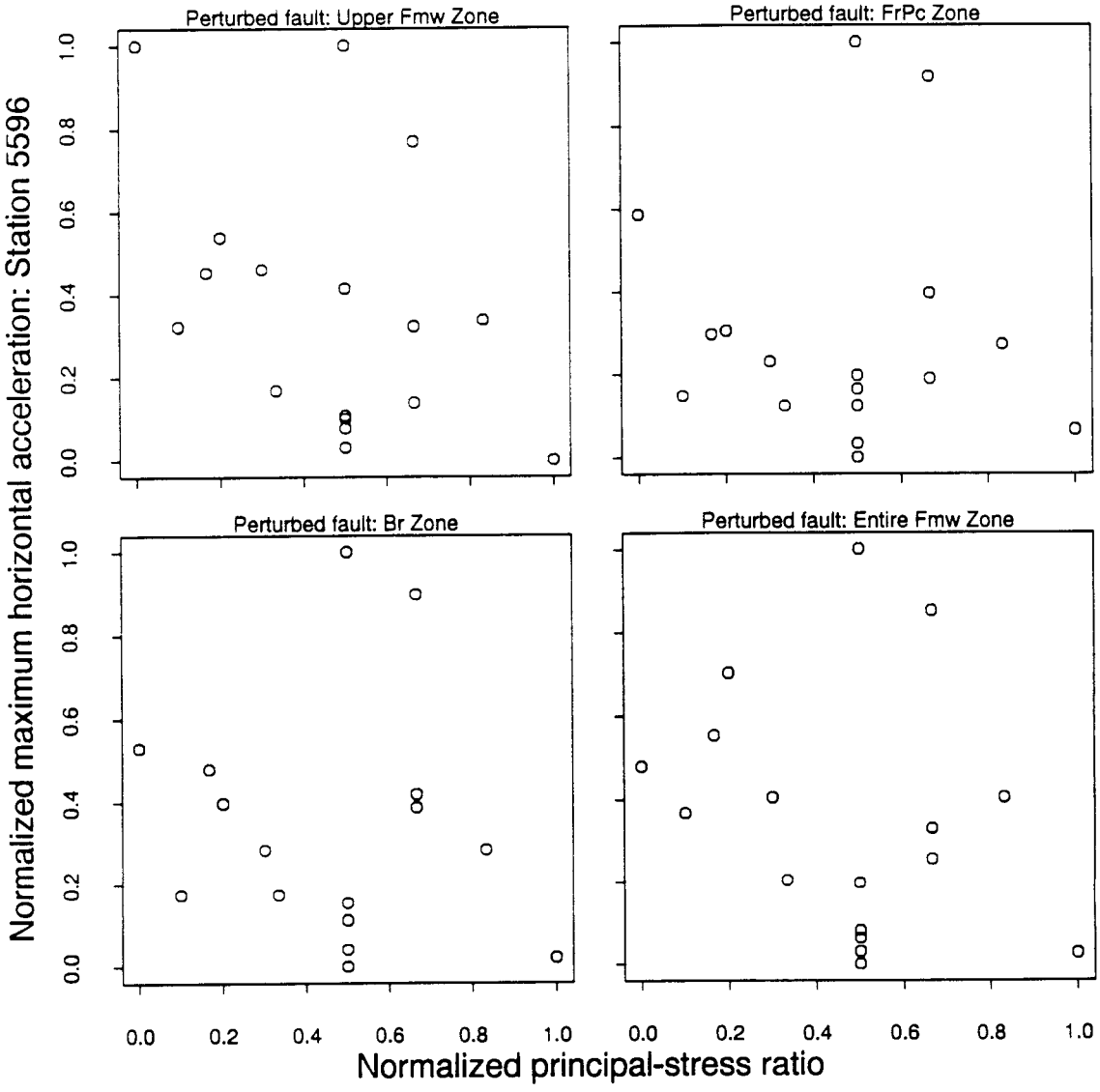

Figure B-81. Sensitivity of the maximum horizontal acceleration at Station 5596 to changes in the value of the principal stress ratio k_3

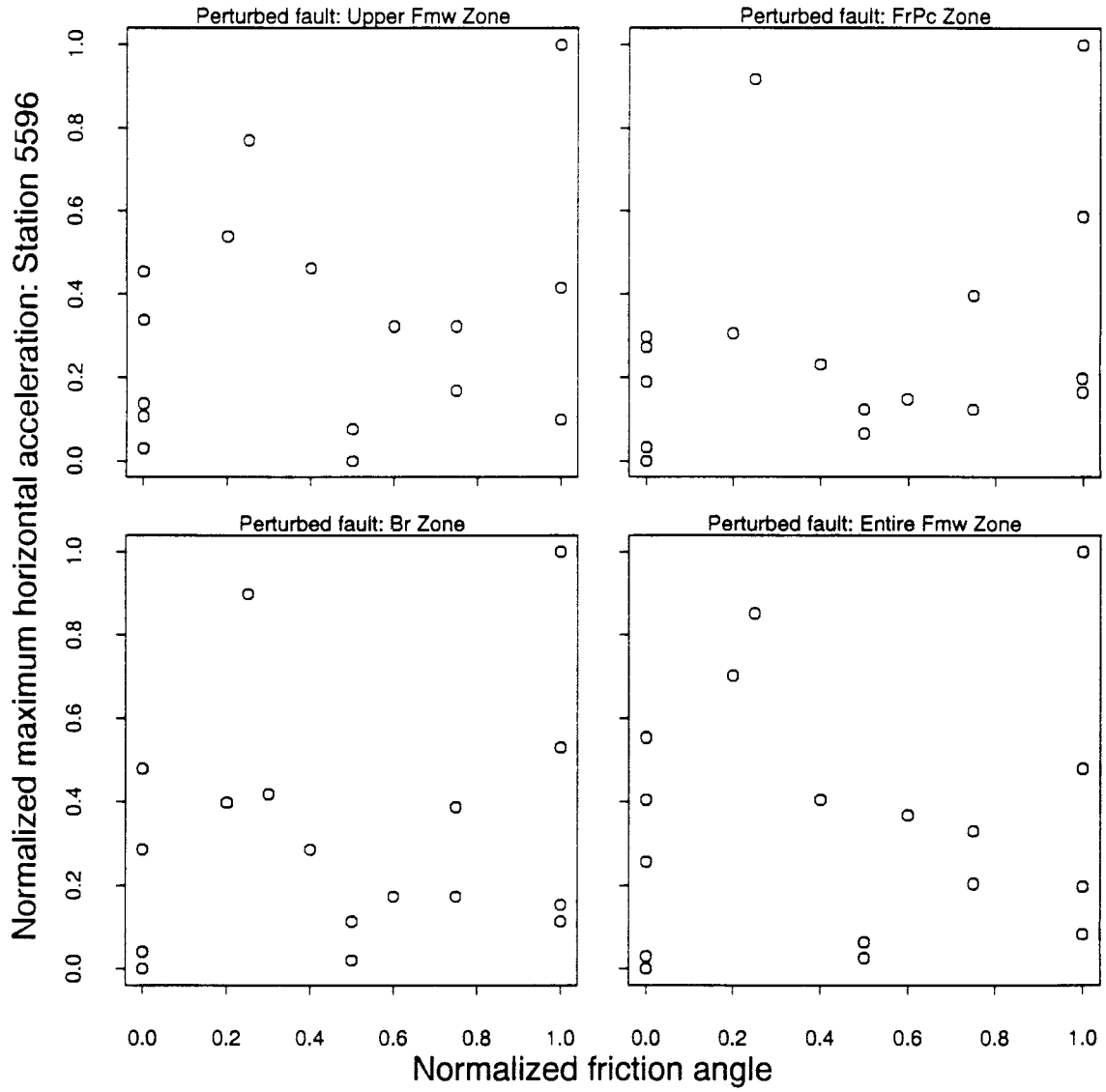

Figure B-82. Sensitivity of the maximum horizontal acceleration at Station 5596 to changes in the value of the friction angle

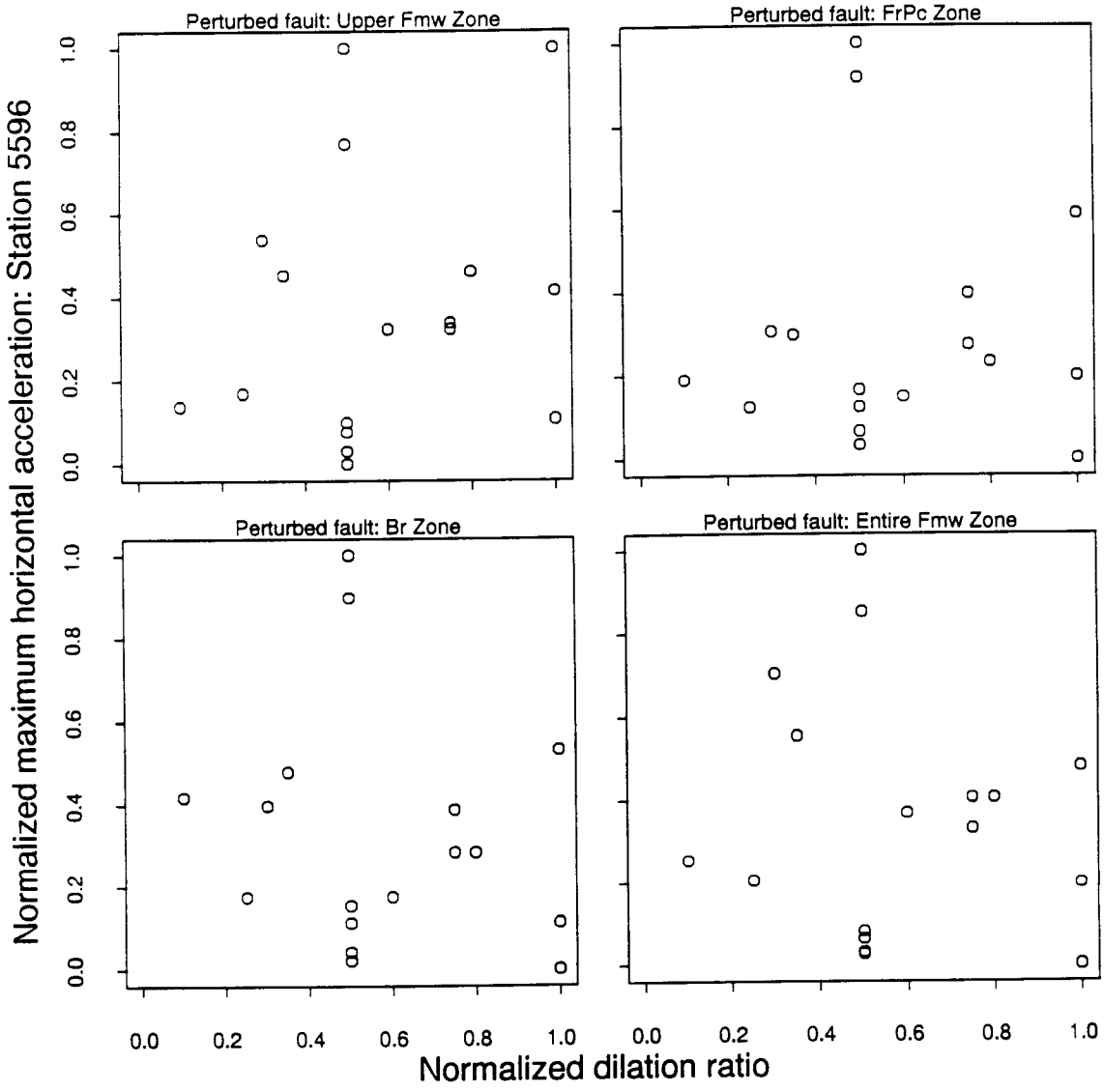

Figure B-83. Sensitivity of the maximum horizontal acceleration at Station 5596 to changes in the value of the dilation angle

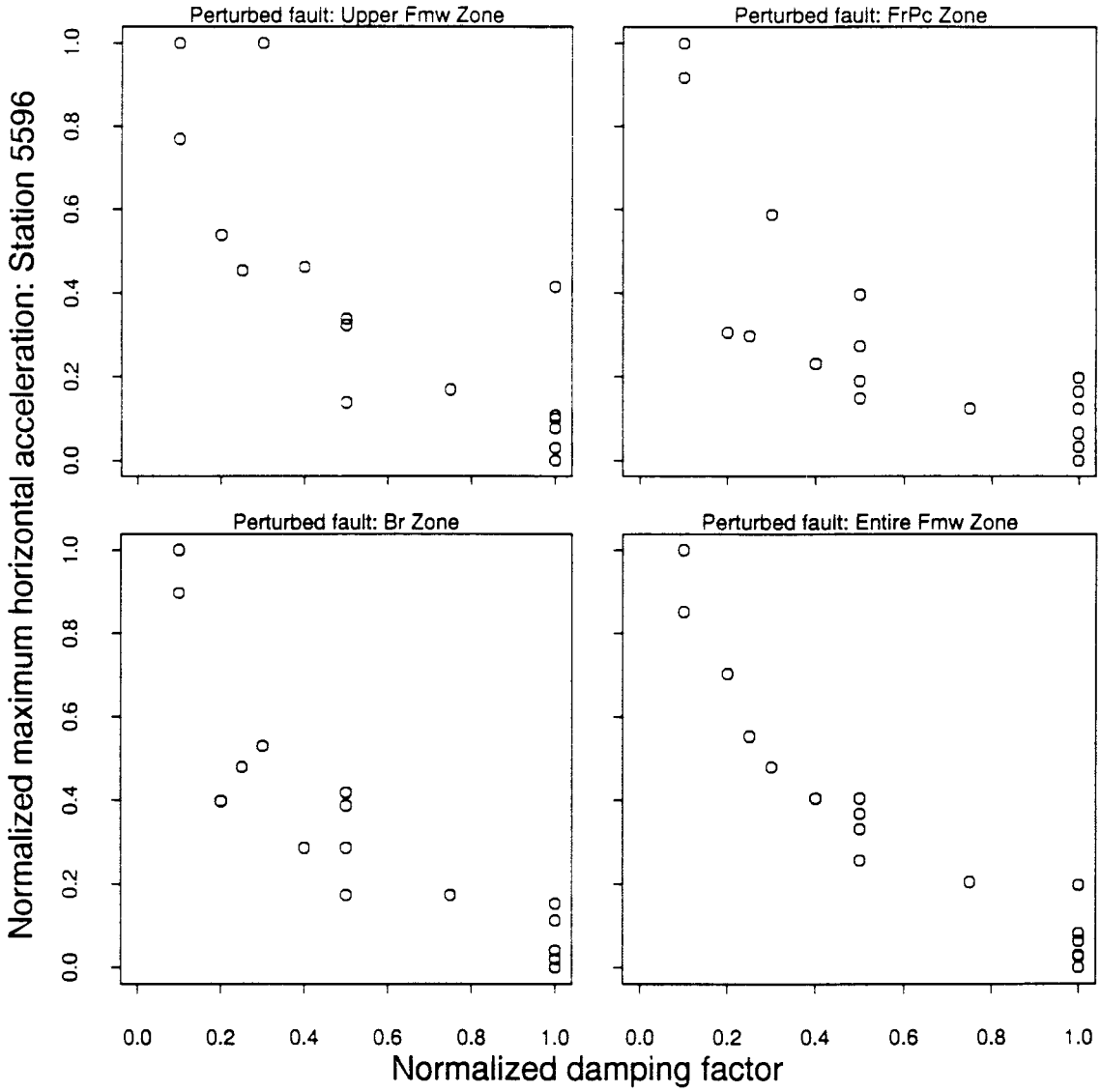

Figure B-84. Sensitivity of the maximum horizontal acceleration at Station 5596 to changes in the value of the damping factor

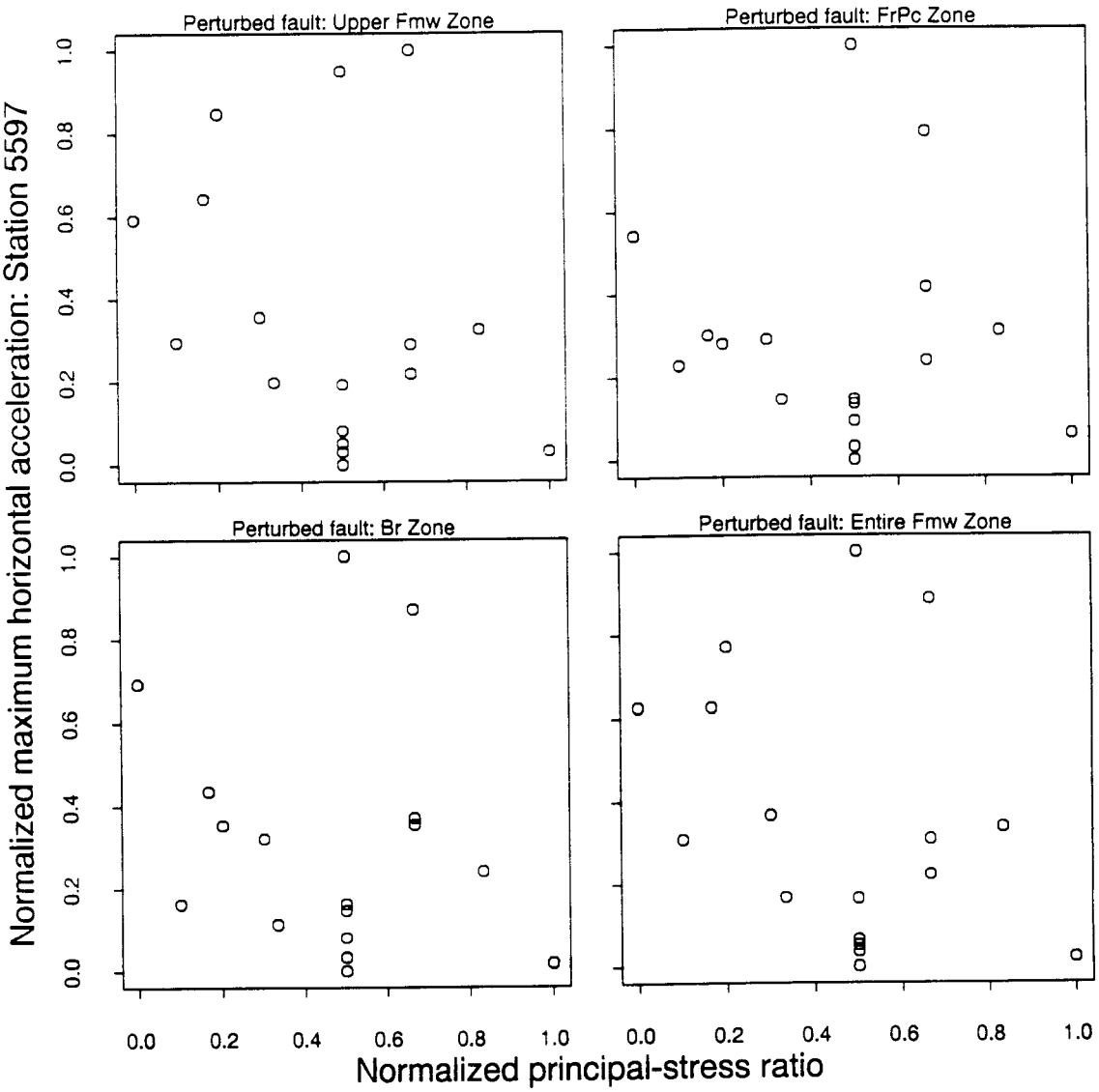

Figure B-85. Sensitivity of the maximum horizontal acceleration at Station 5597 to changes in the value of the principal stress ratio k_3

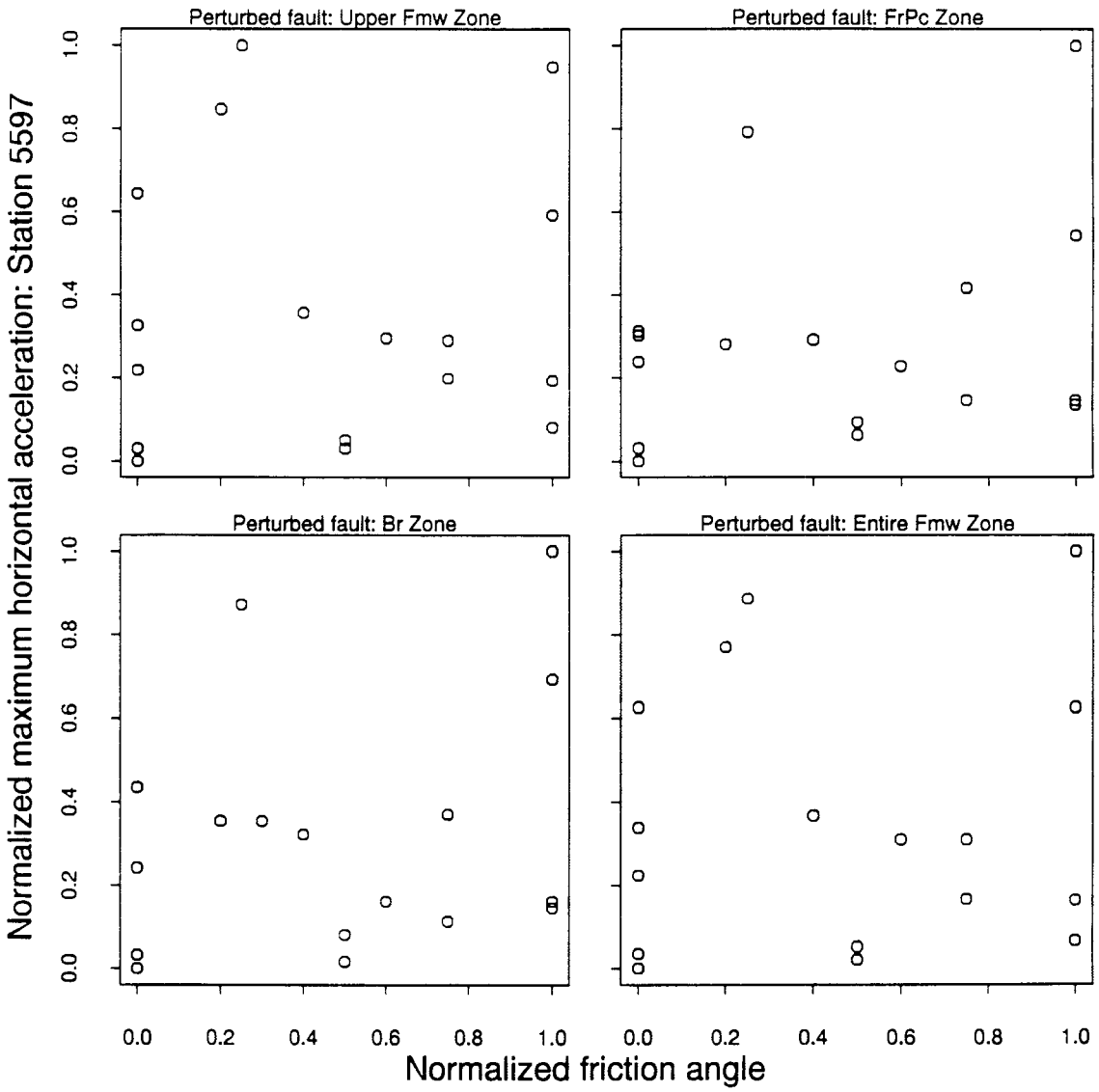

Figure B-86. Sensitivity of the maximum horizontal acceleration at Station 5597 to changes in the value of the friction angle

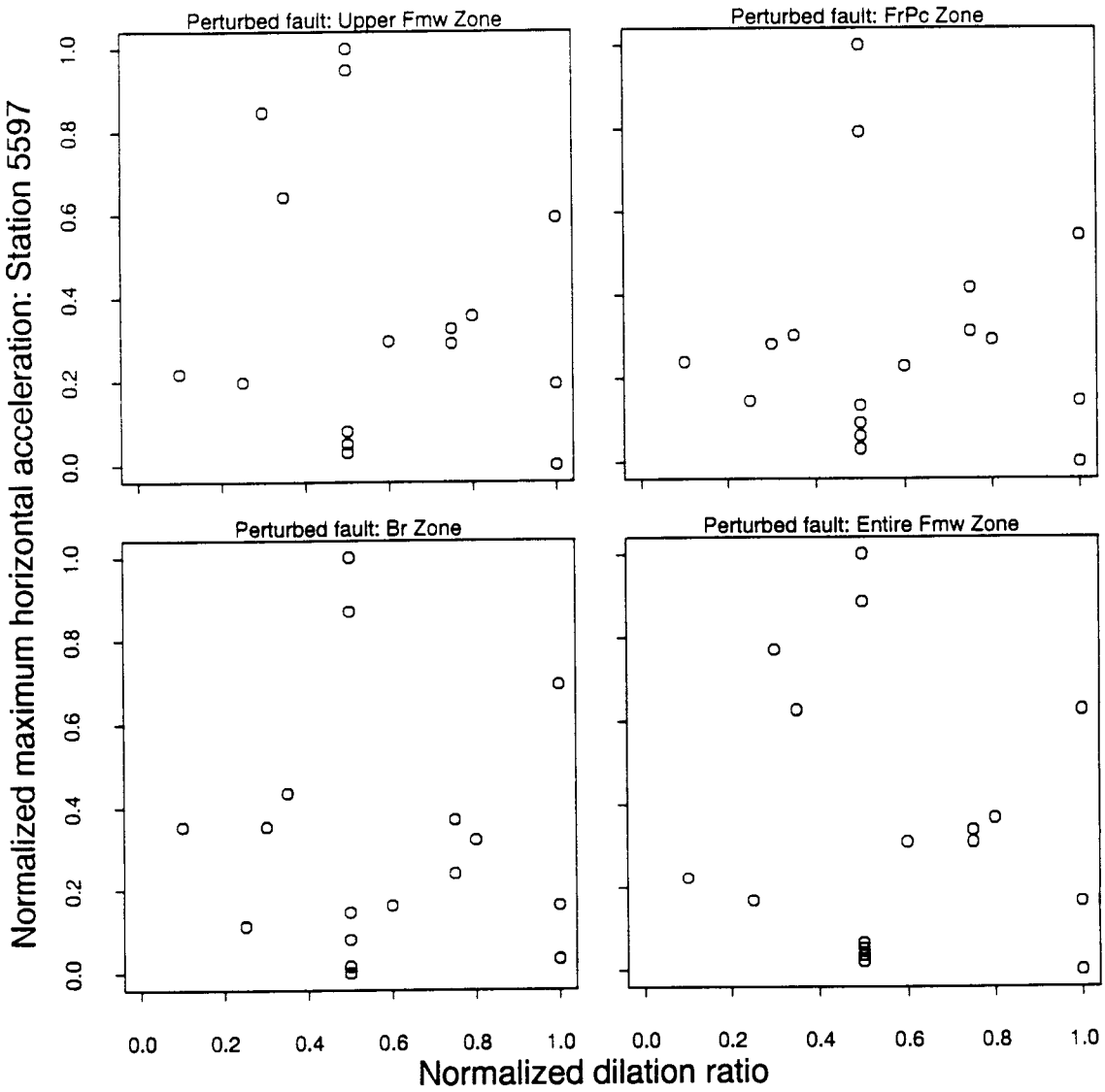

Figure B-87. Sensitivity of the maximum horizontal acceleration at Station 5597 to changes in the value of the dilation angle

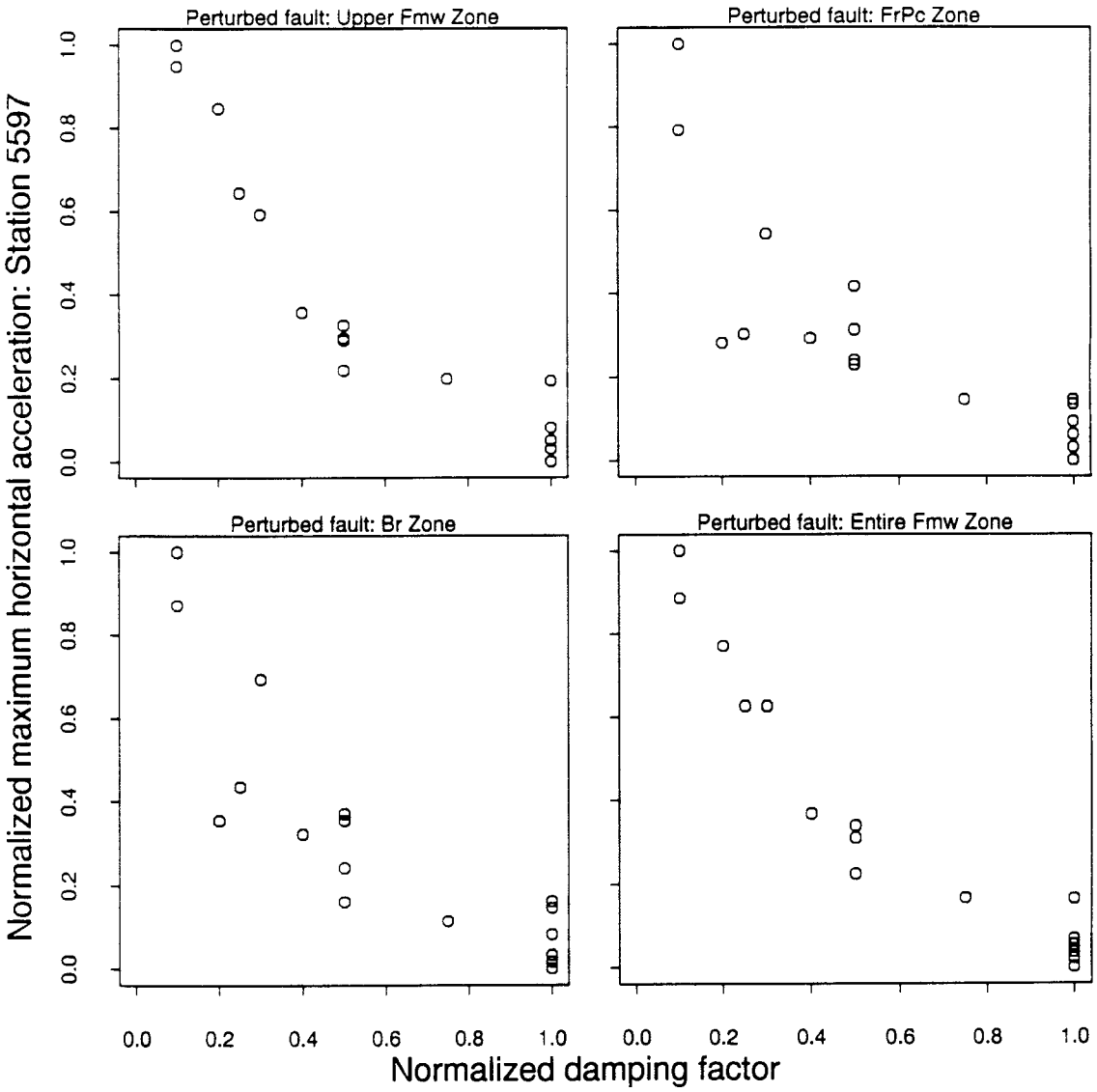

Figure B-88. Sensitivity of the maximum horizontal acceleration at Station 5597 to changes in the value of the damping factor

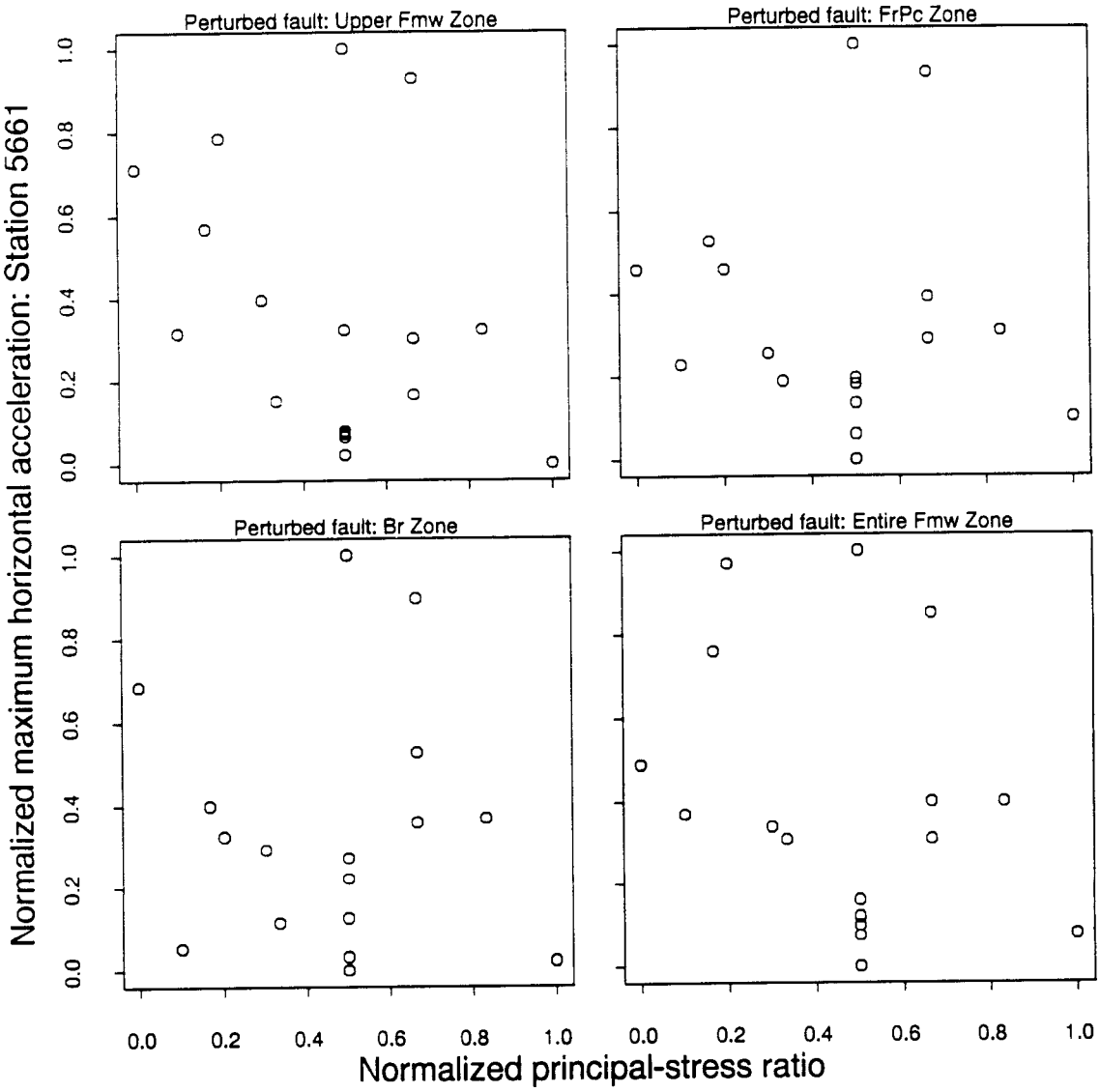

Figure B-89. Sensitivity of the maximum horizontal acceleration at Station 5661 to changes in the value of the principal stress ratio k_3

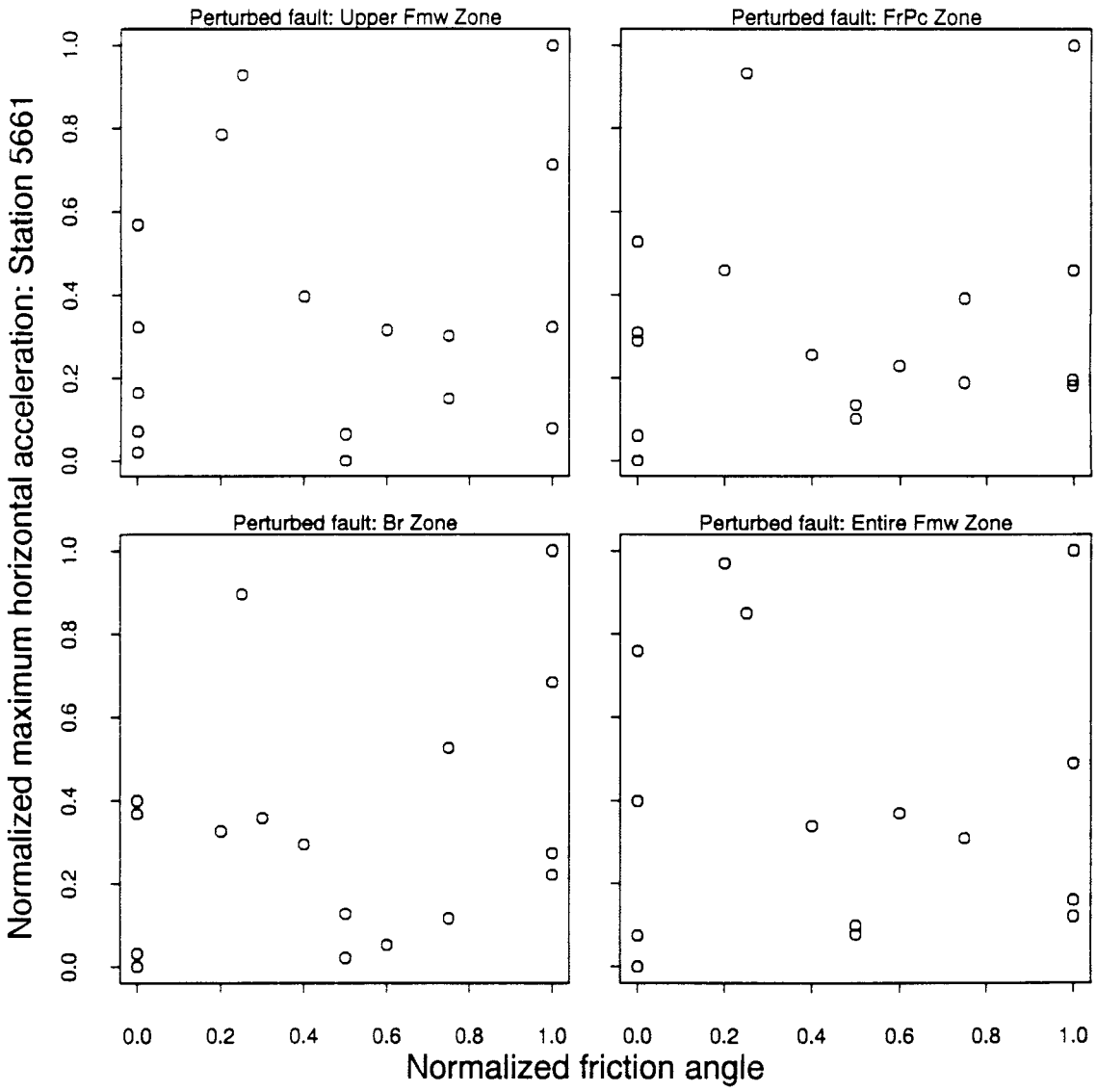

Figure B-90. Sensitivity of the maximum horizontal acceleration at Station 5661 to changes in the value of the friction angle

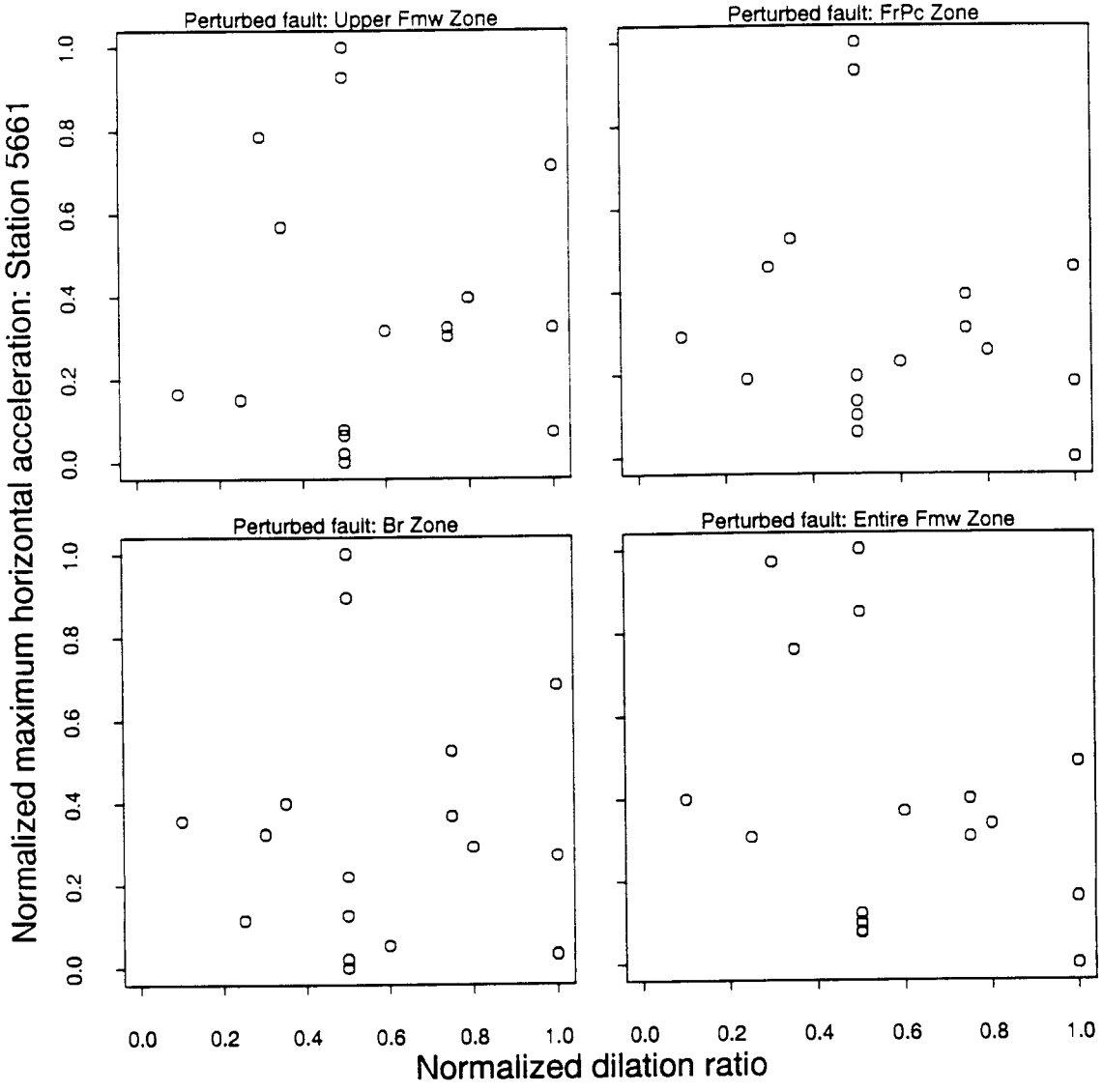

Figure B-91. Sensitivity of the maximum horizontal acceleration at Station 5661 to changes in the value of the dilation angle

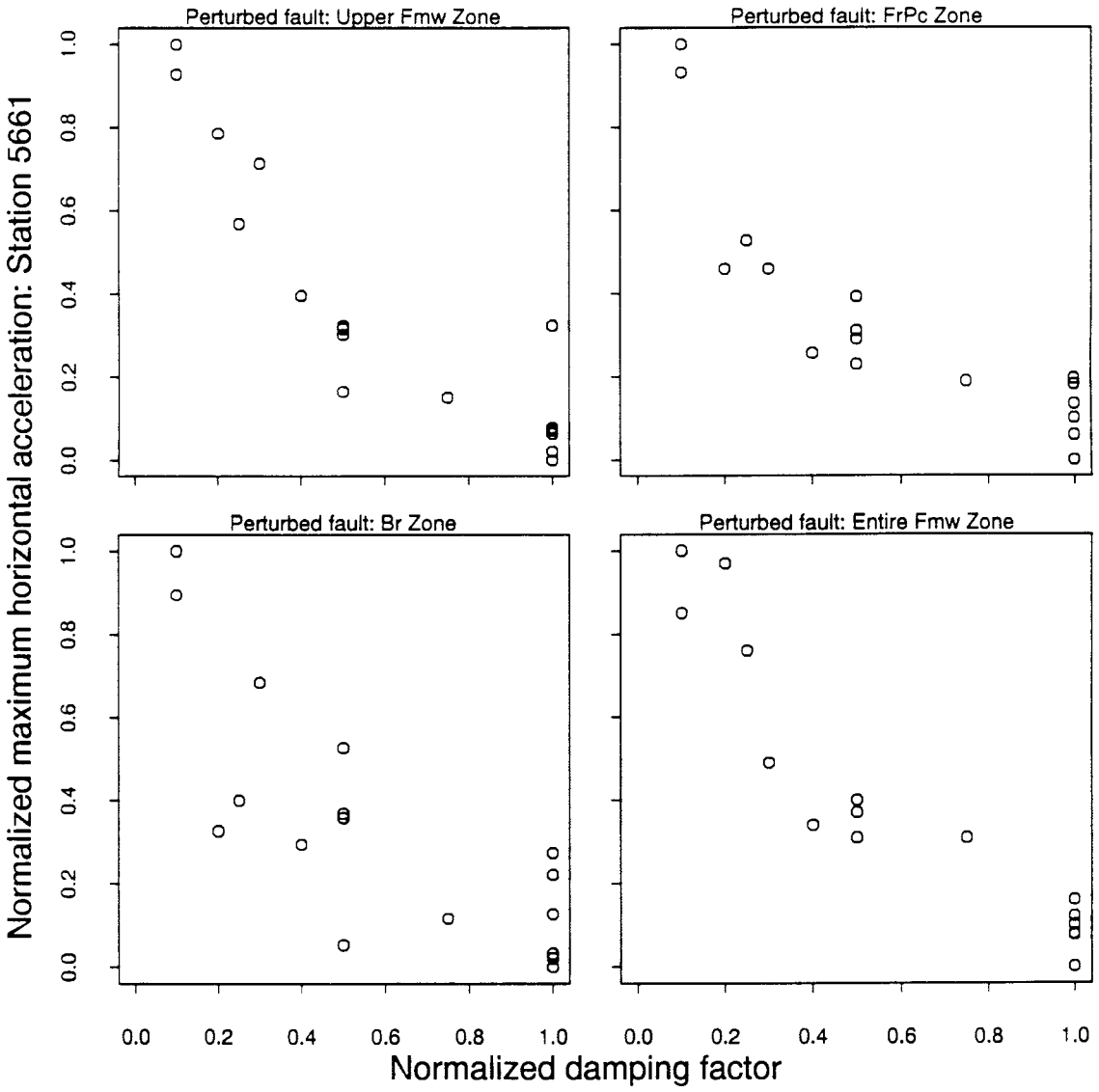

Figure B-92. Sensitivity of the maximum horizontal acceleration at Station 5661 to changes in the value of the damping factor

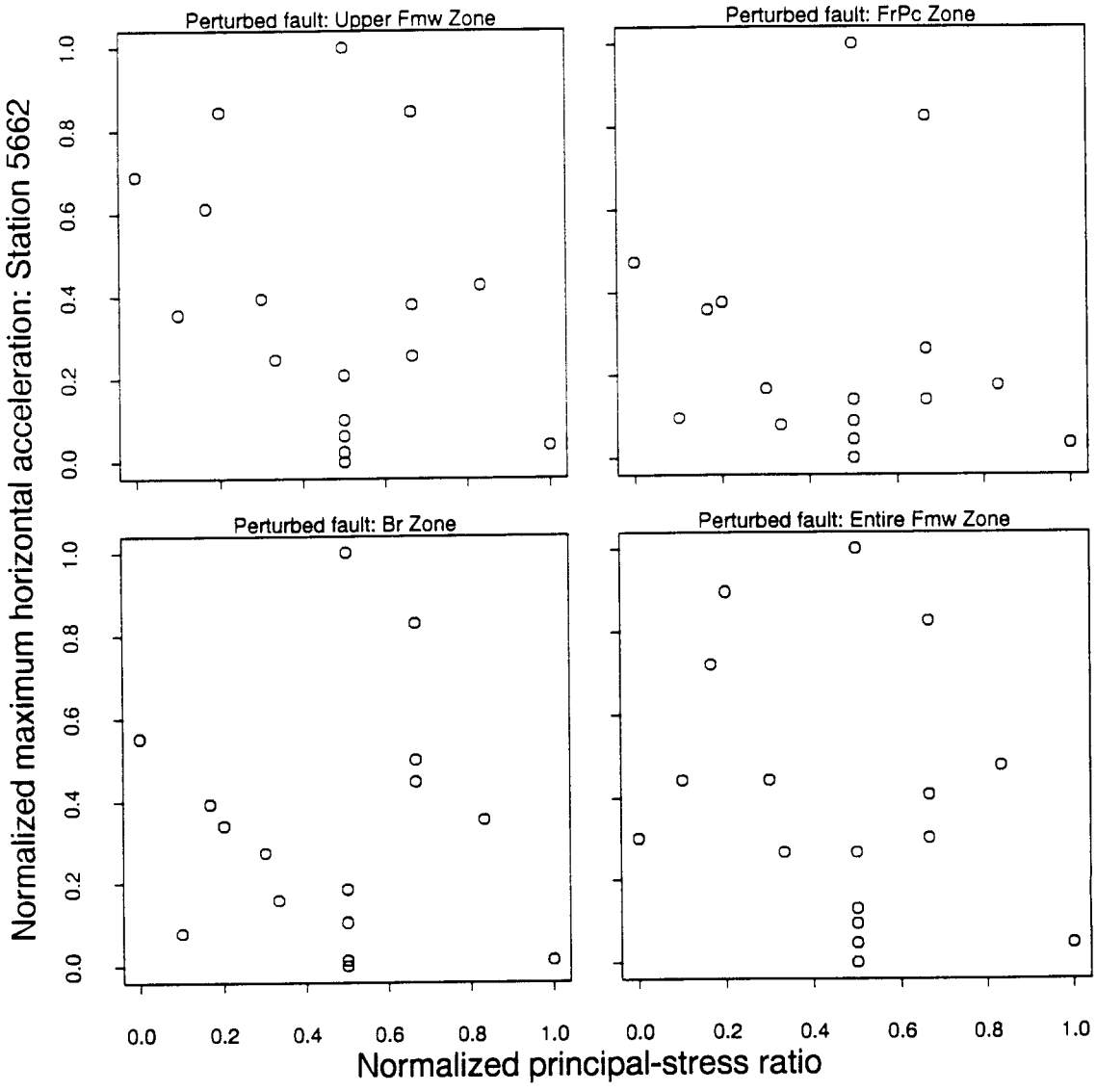

Figure B-93. Sensitivity of the maximum horizontal acceleration at Station 5662 to changes in the value of the principal stress ratio k_3

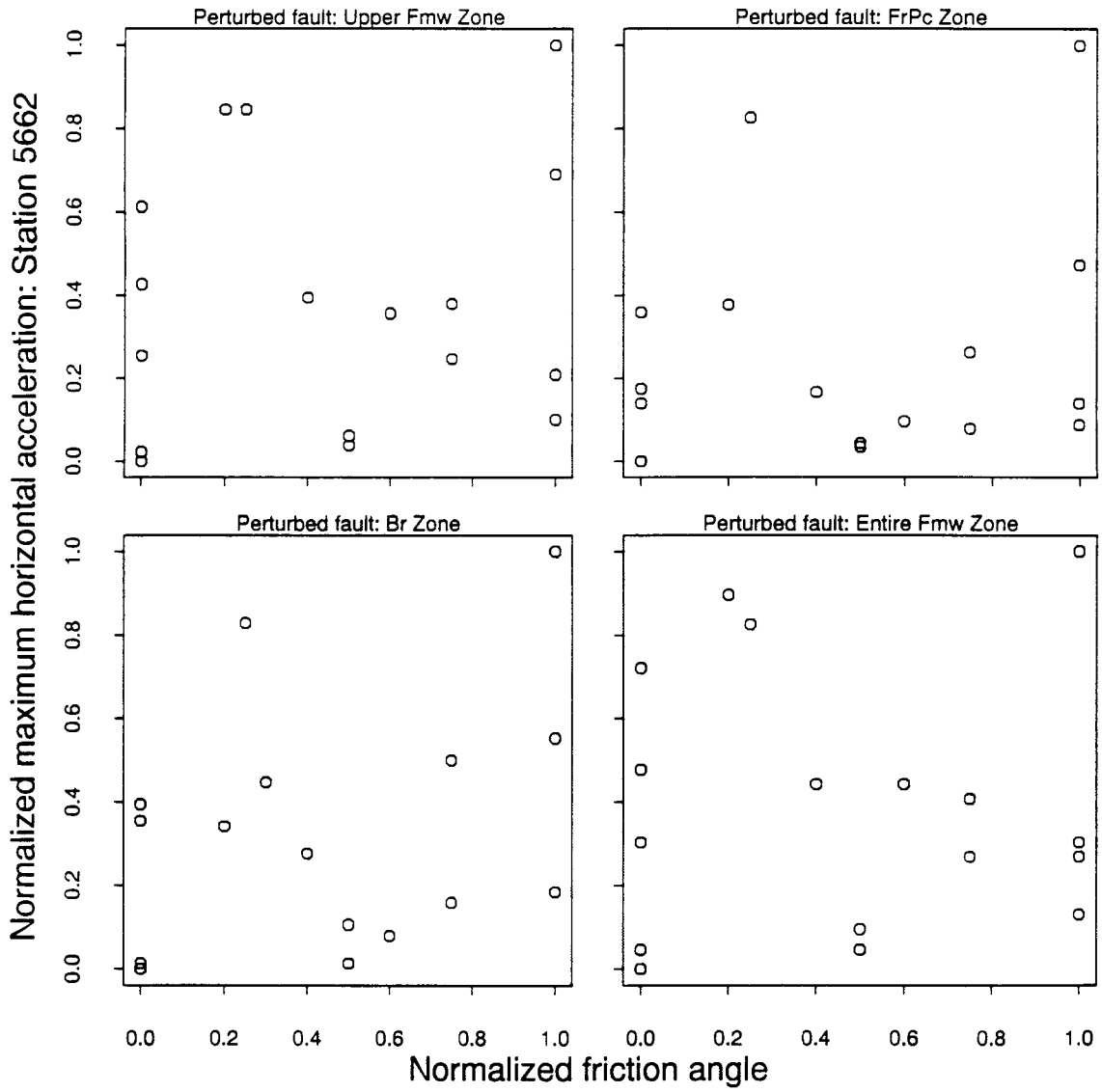

Figure B-94. Sensitivity of the maximum horizontal acceleration at Station 5662 to changes in the value of the friction angle

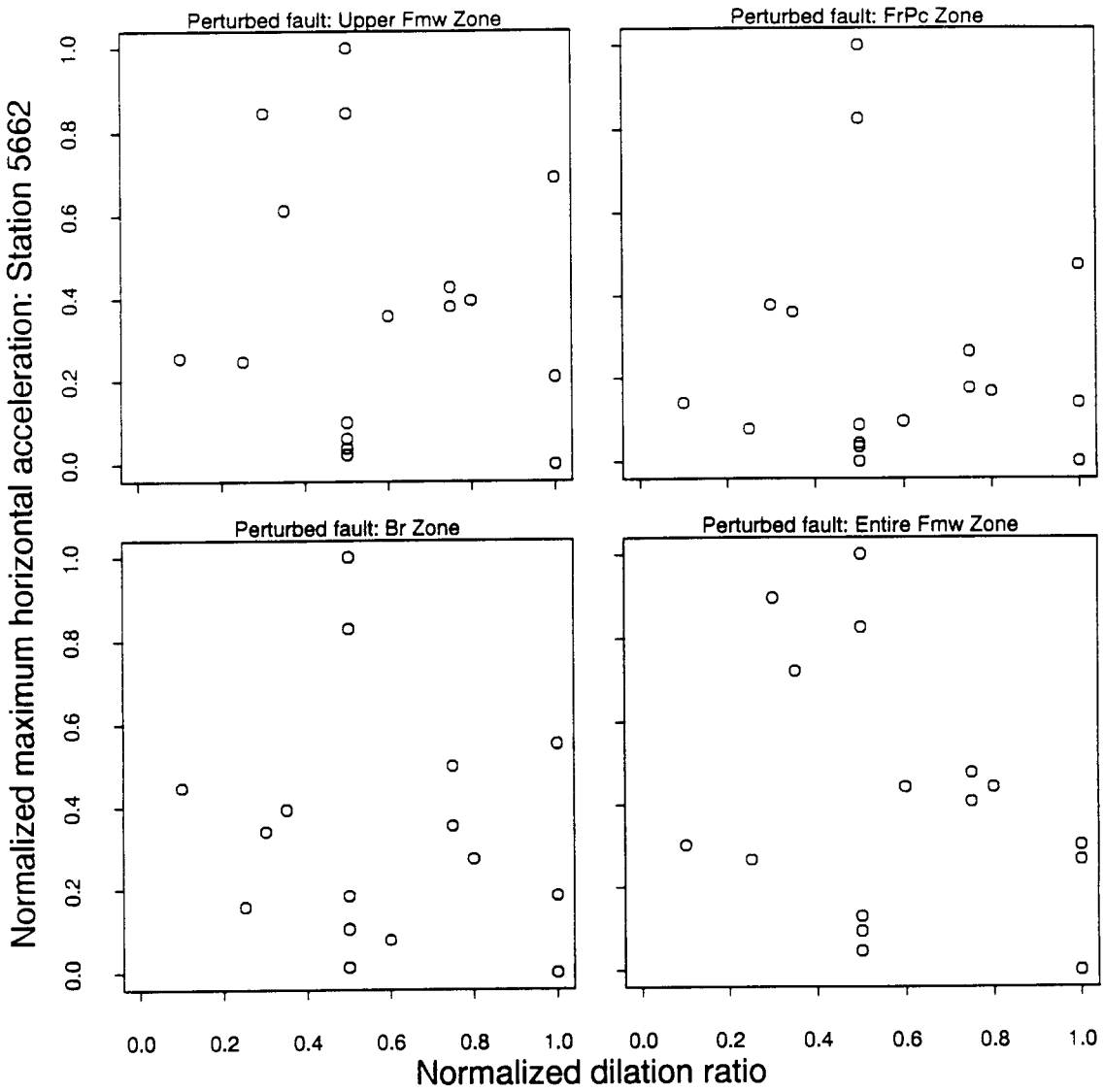

Figure B-95. Sensitivity of the maximum horizontal acceleration at Station 5662 to changes in the value of the dilation angle

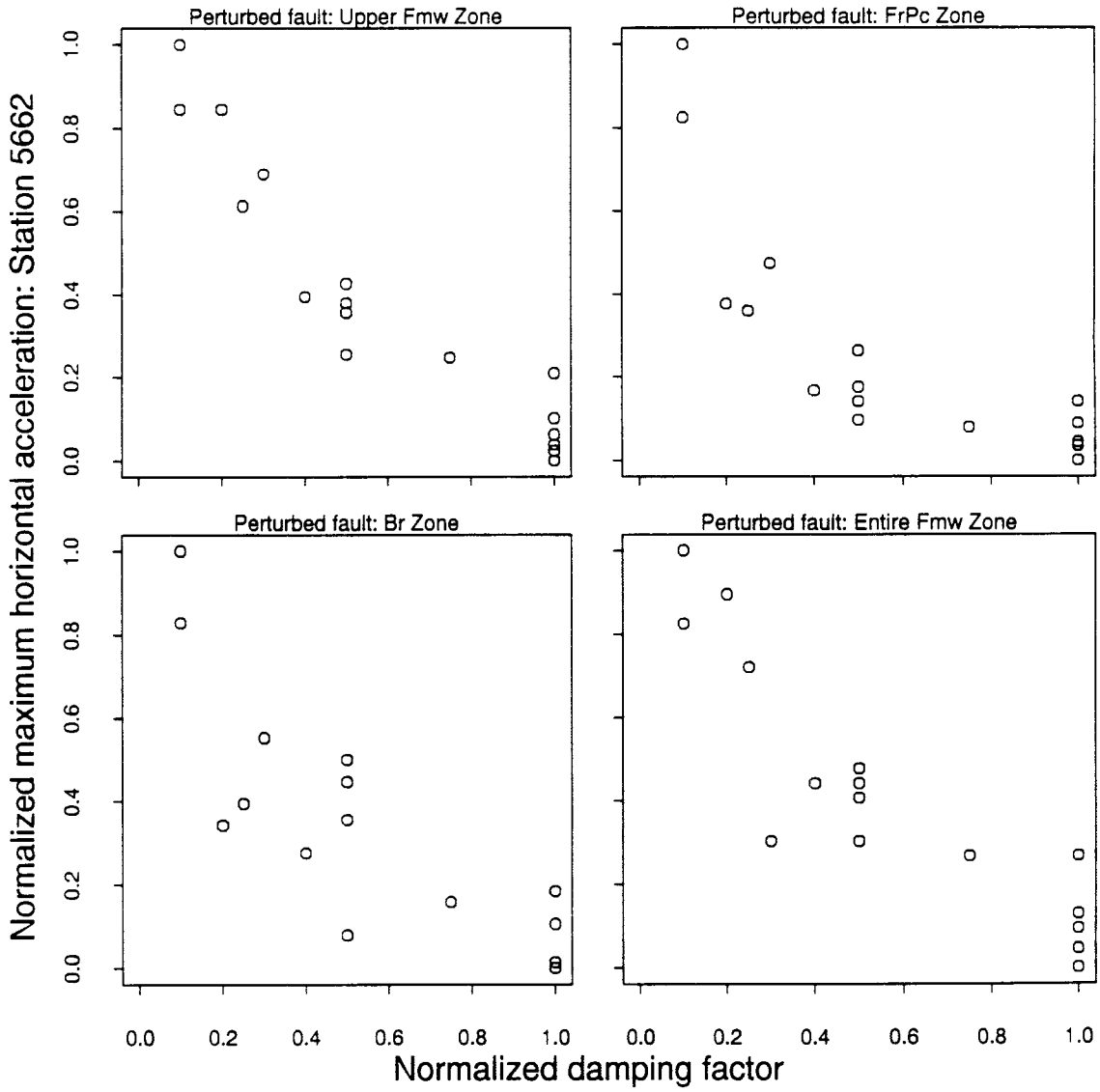

Figure B-96. Sensitivity of the maximum horizontal acceleration at Station 5662 to changes in the value of the damping factor

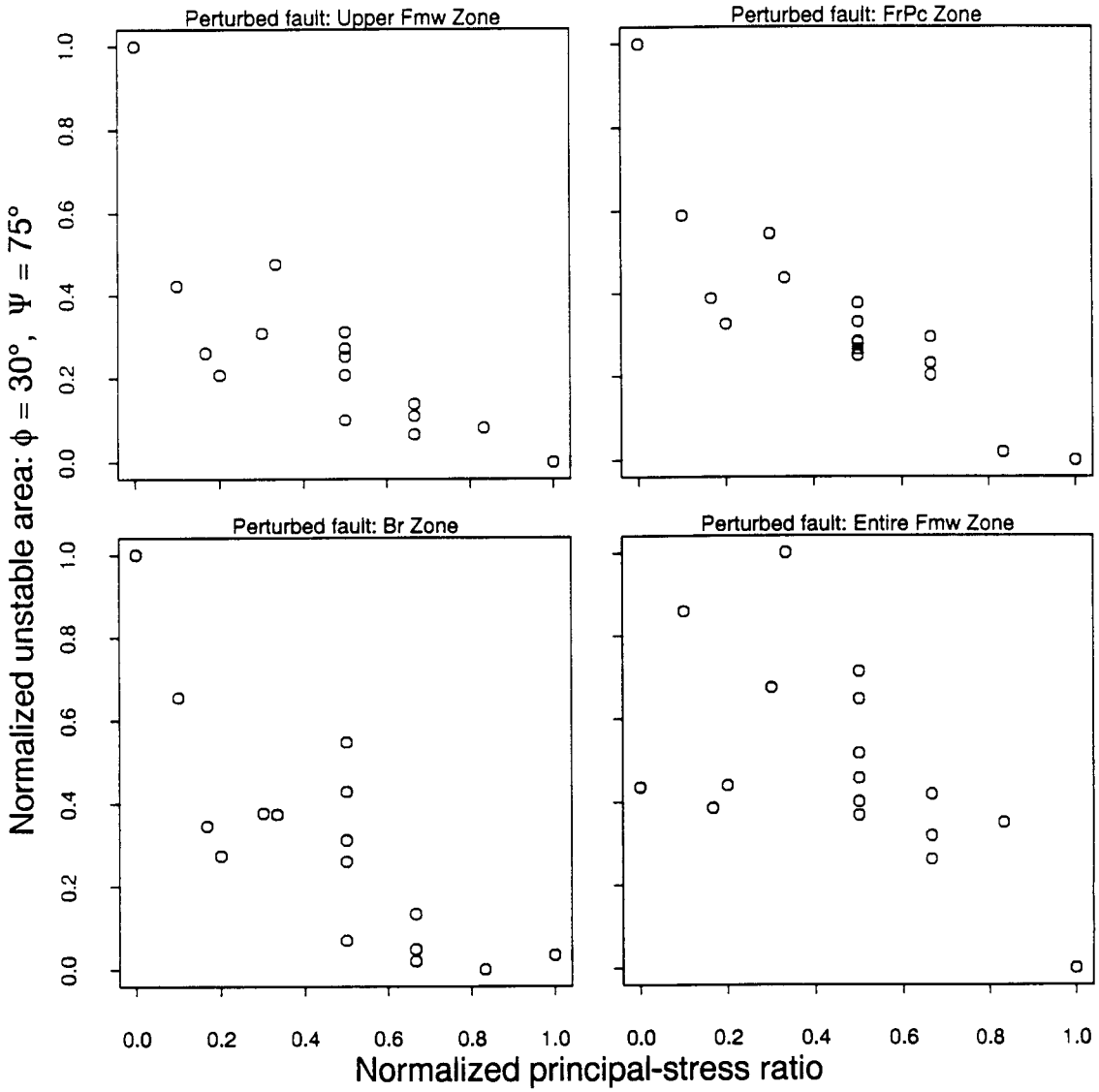

Figure B-97. Sensitivity of the area of potential instability to changes in the value of the principal stress ratio k_3, based on slip on 75° W-dipping planes with 30°-friction angle

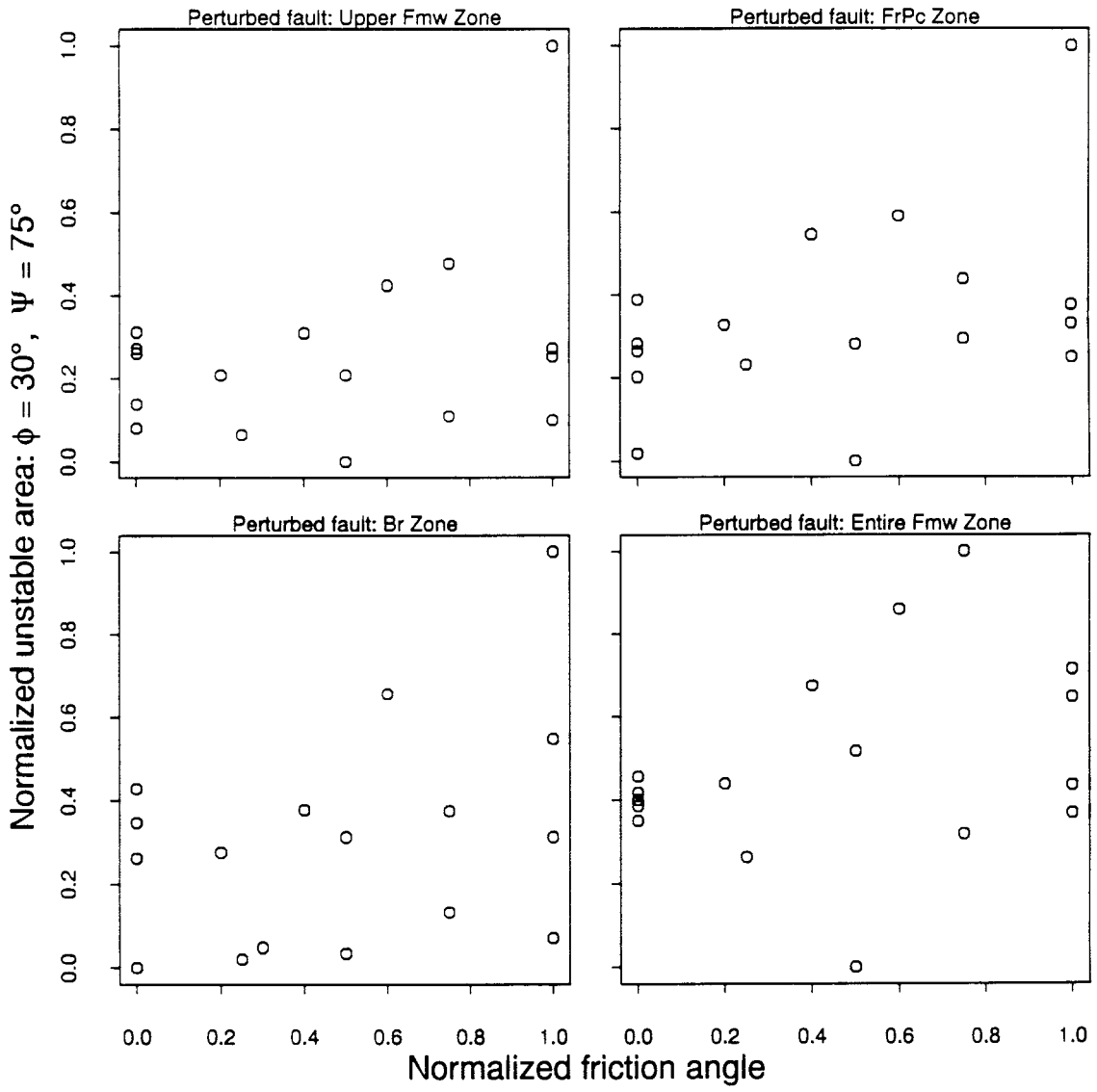

Figure B-98. Sensitivity of the area of potential instability to changes in the value of the rock-mass friction angle, based on slip on 75° W-dipping planes with 30°-friction angle

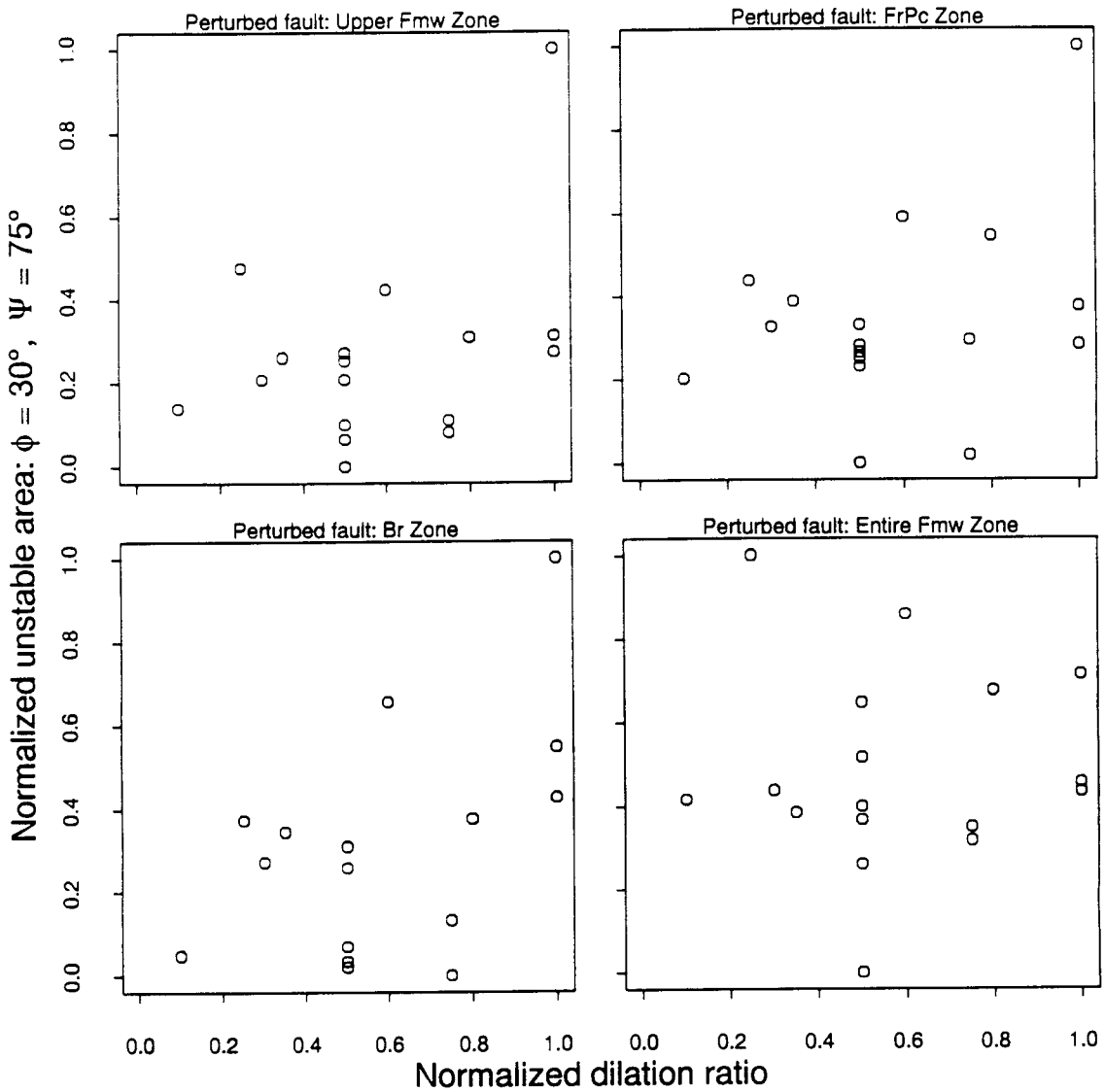

Figure B-99. Sensitivity of the area of potential instability to changes in the value of the dilation angle, based on slip on 75° W-dipping planes with 30°-friction angle

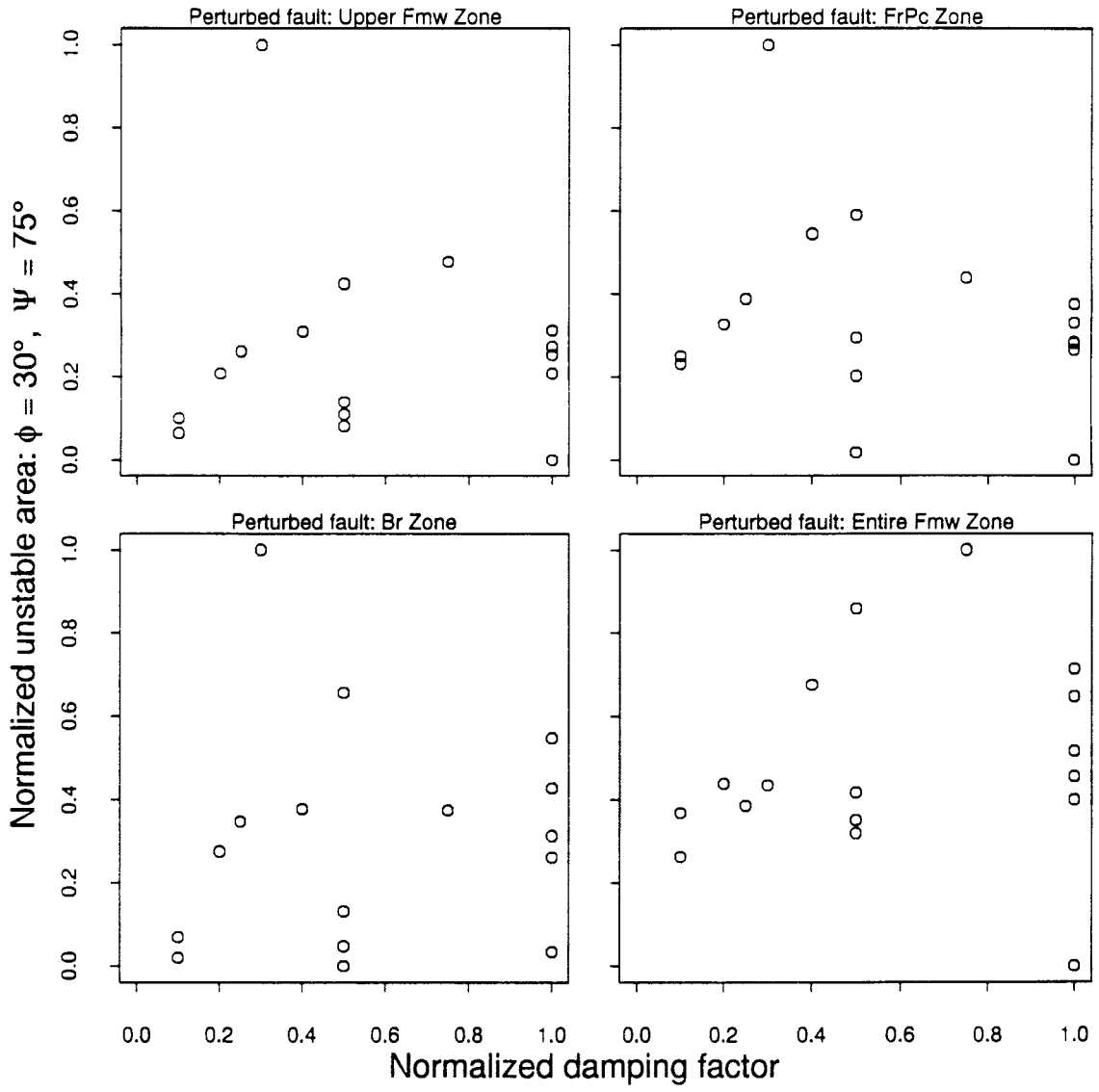

Figure B-100. Sensitivity of the area of potential instability to changes in the value of the damping factor, based on slip on 75° W-dipping planes with 30°-friction angle

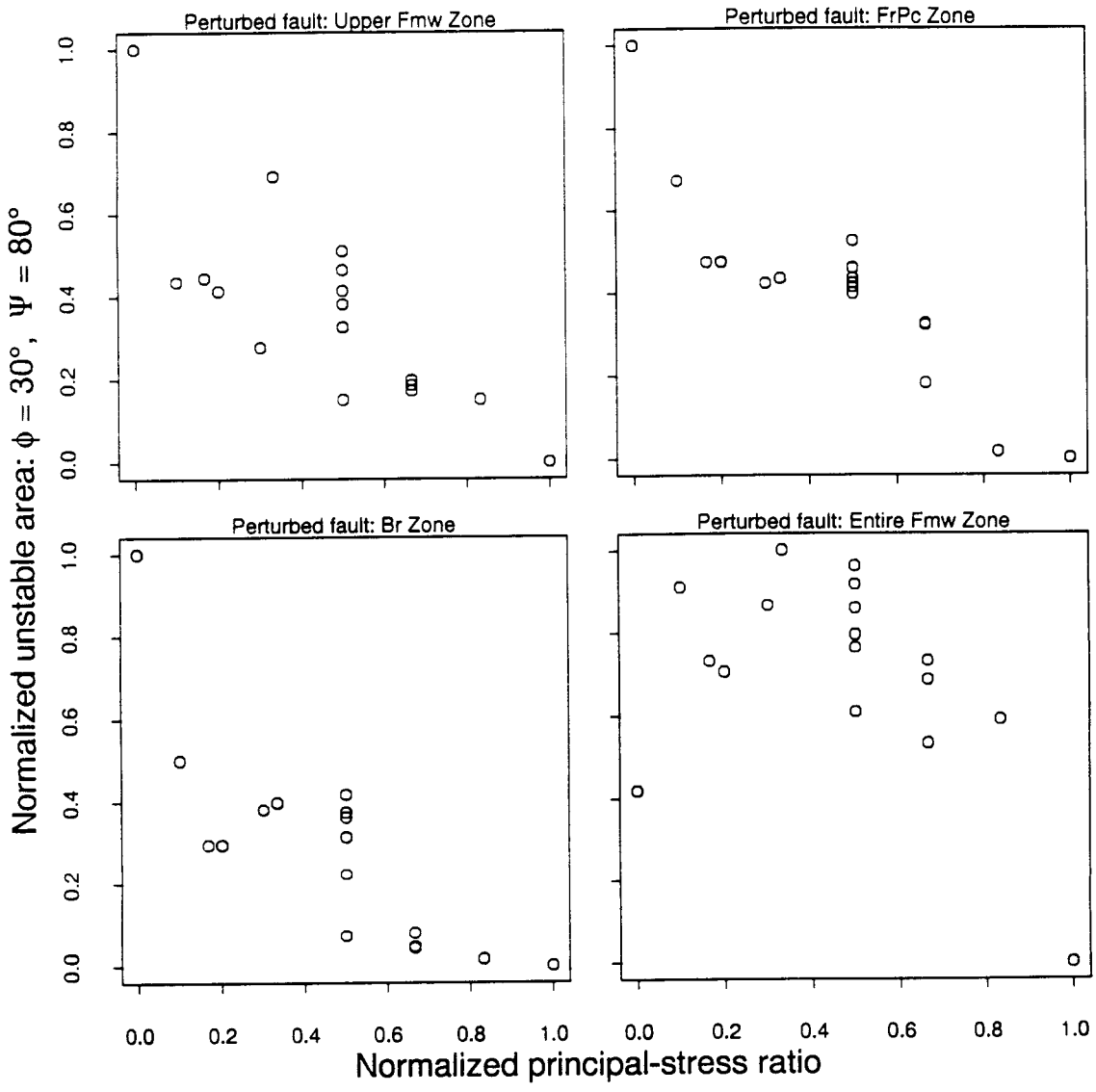

Figure B-101. Sensitivity of the area of potential instability to changes in the value of the principal stress ratio k_3, based on slip on 80° W-dipping planes with 30°-friction angle

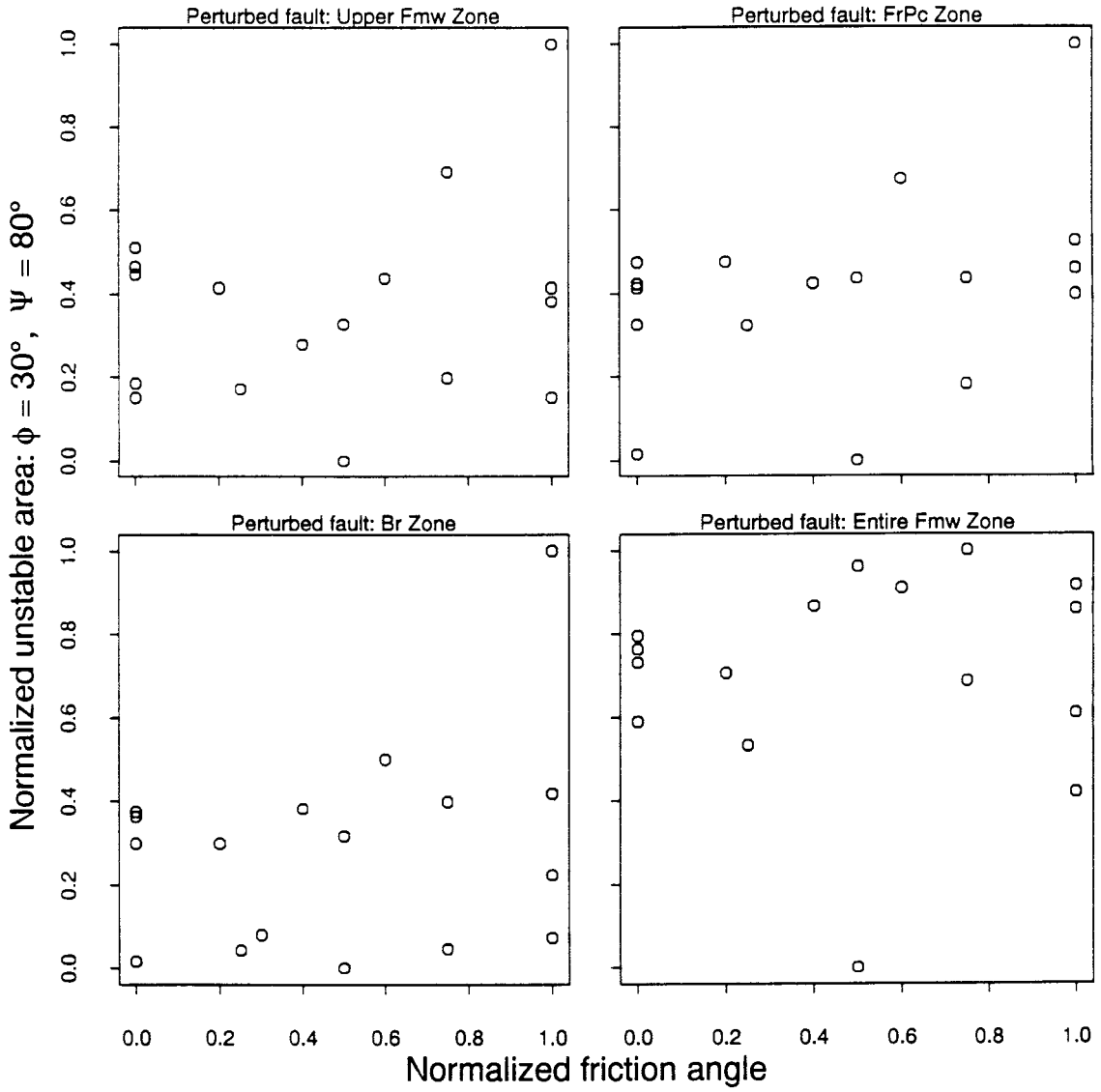

Figure B-102. Sensitivity of the area of potential instability to changes in the value of the rock-mass friction angle, based on slip on 80° W-dipping planes with 30°-friction angle

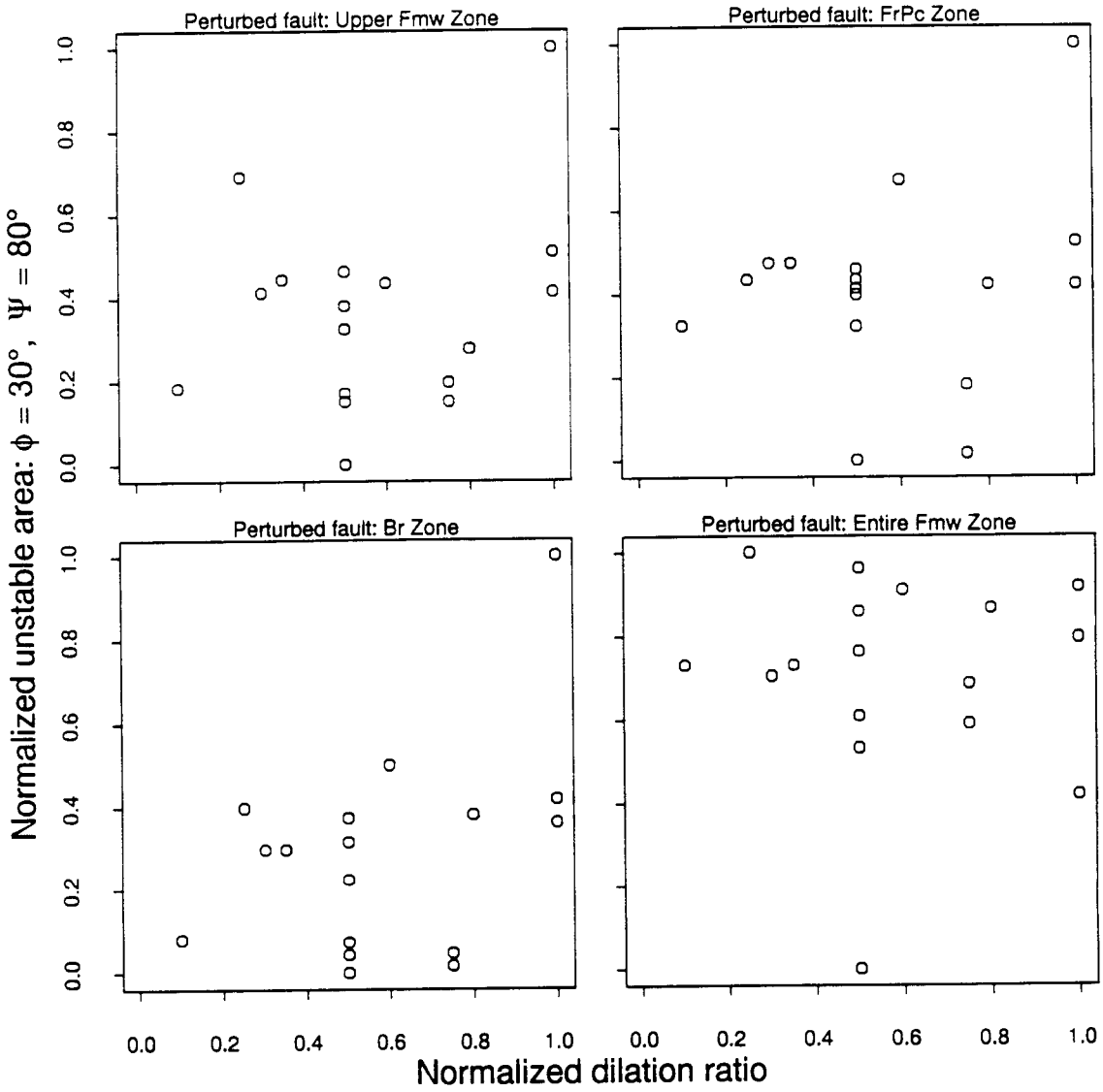

Figure B-103. Sensitivity of the area of potential instability to changes in the value of the dilation angle, based on slip on 80° W-dipping planes with 30°-friction angle

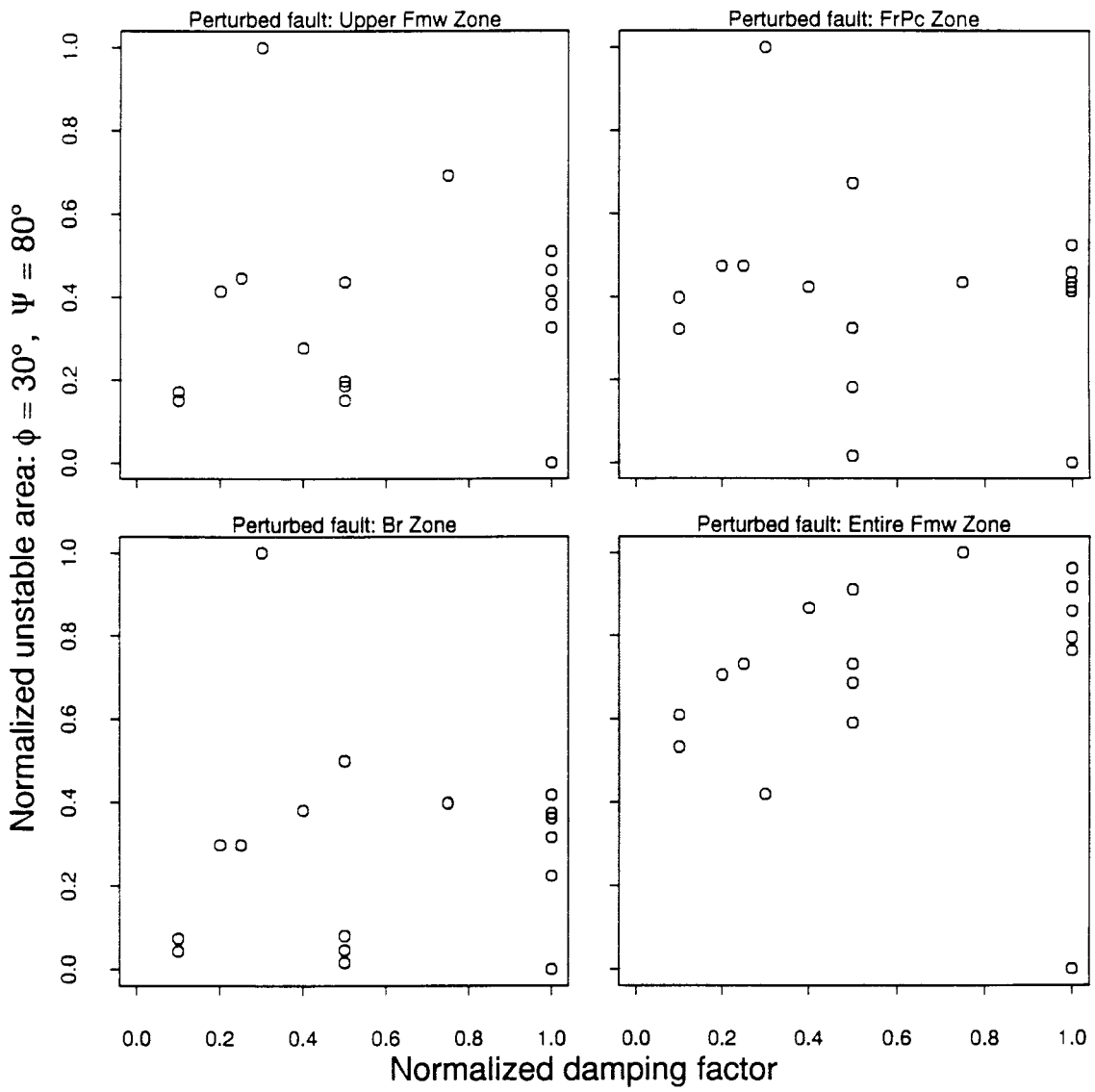

Figure B-104. Sensitivity of the area of potential instability to changes in the value of the damping factor, based on slip on 80° W-dipping planes with 30°-friction angle

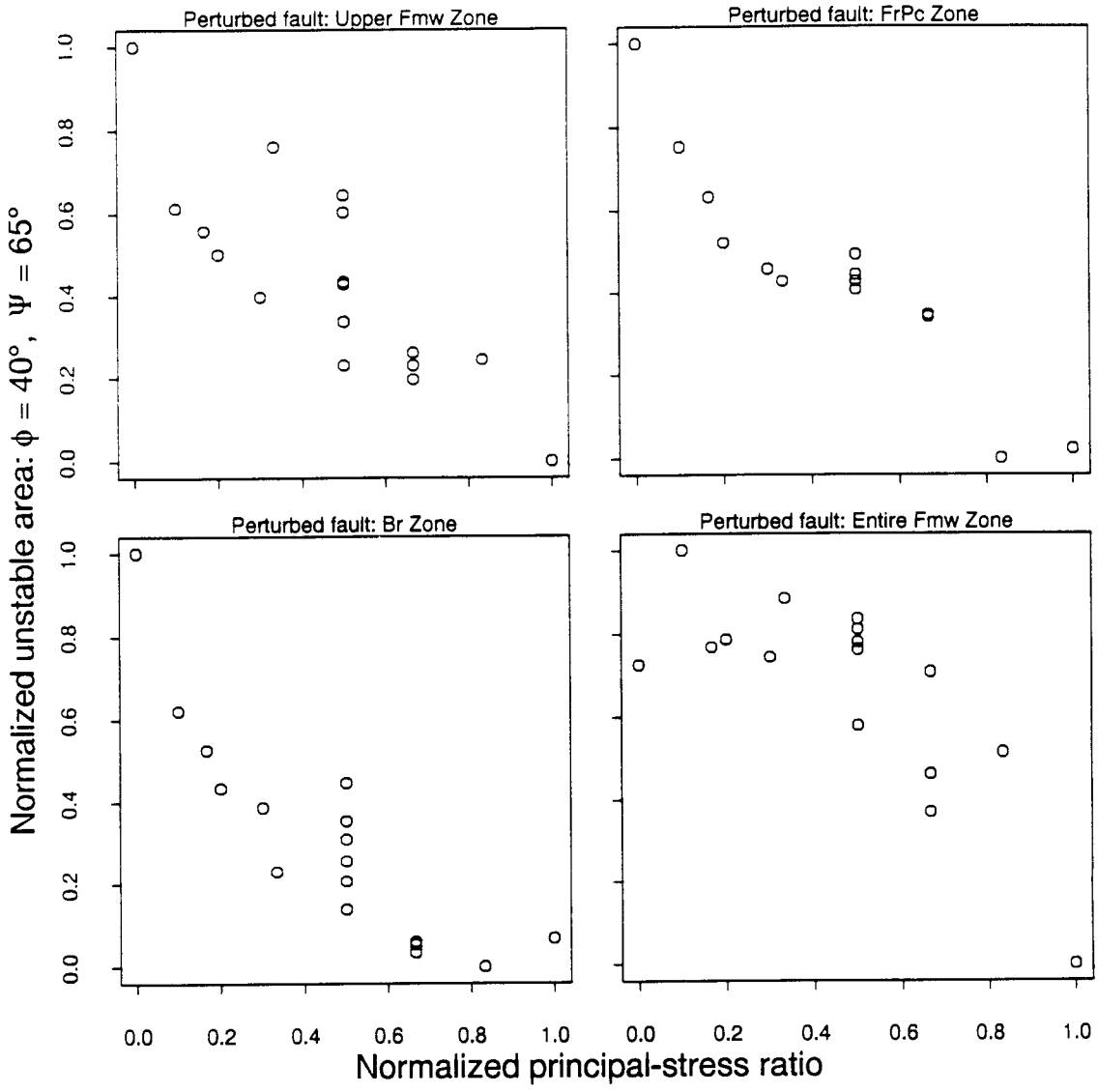

Figure B-105. Sensitivity of the area of potential instability to changes in the value of the principal stress ratio k_3, based on slip on 65° W-dipping planes with 40°-friction angle

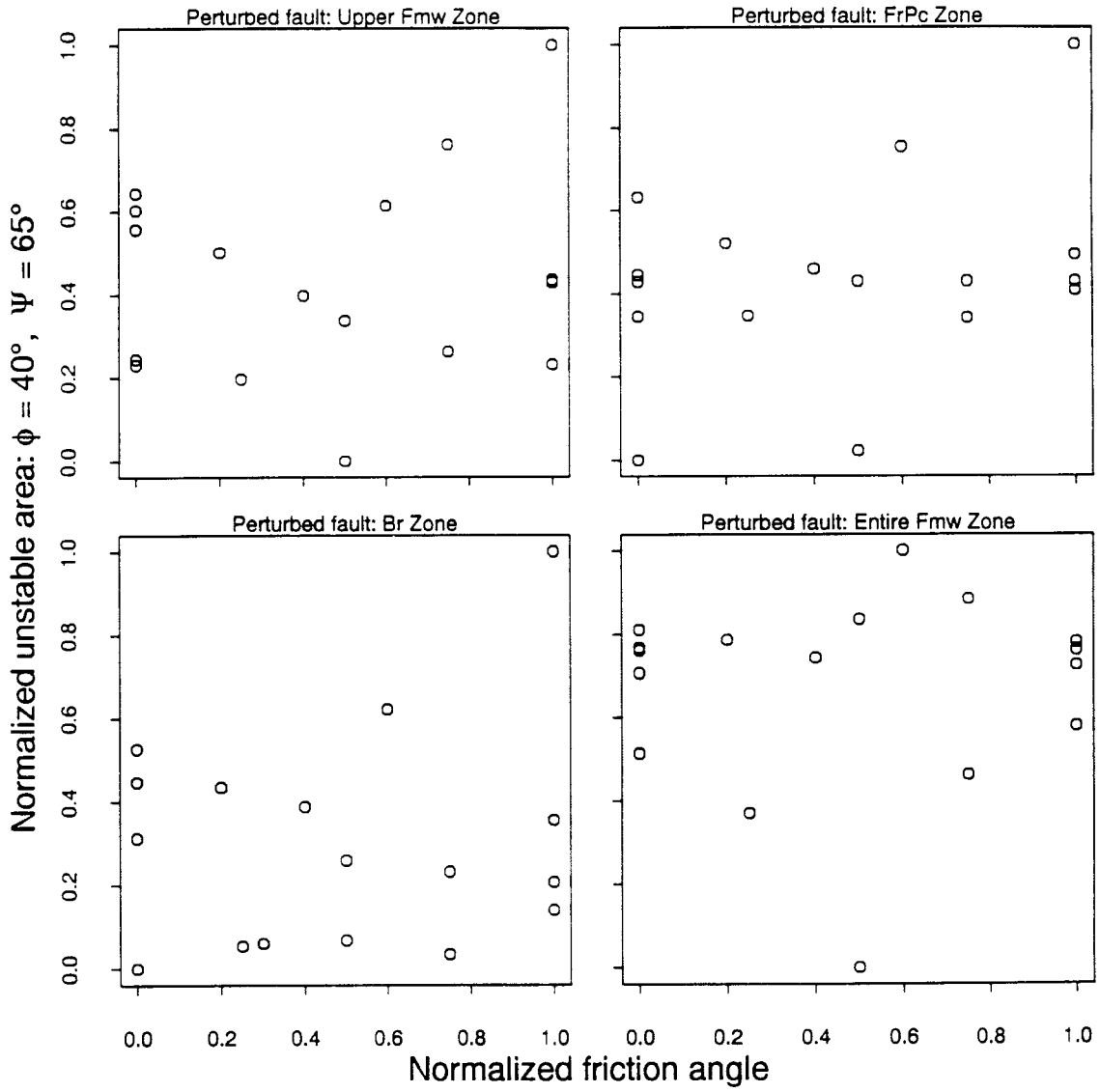

Figure B-106. Sensitivity of the area of potential instability to changes in the value of the rock-mass friction angle, based on slip on 65° W-dipping planes with 40°-friction angle

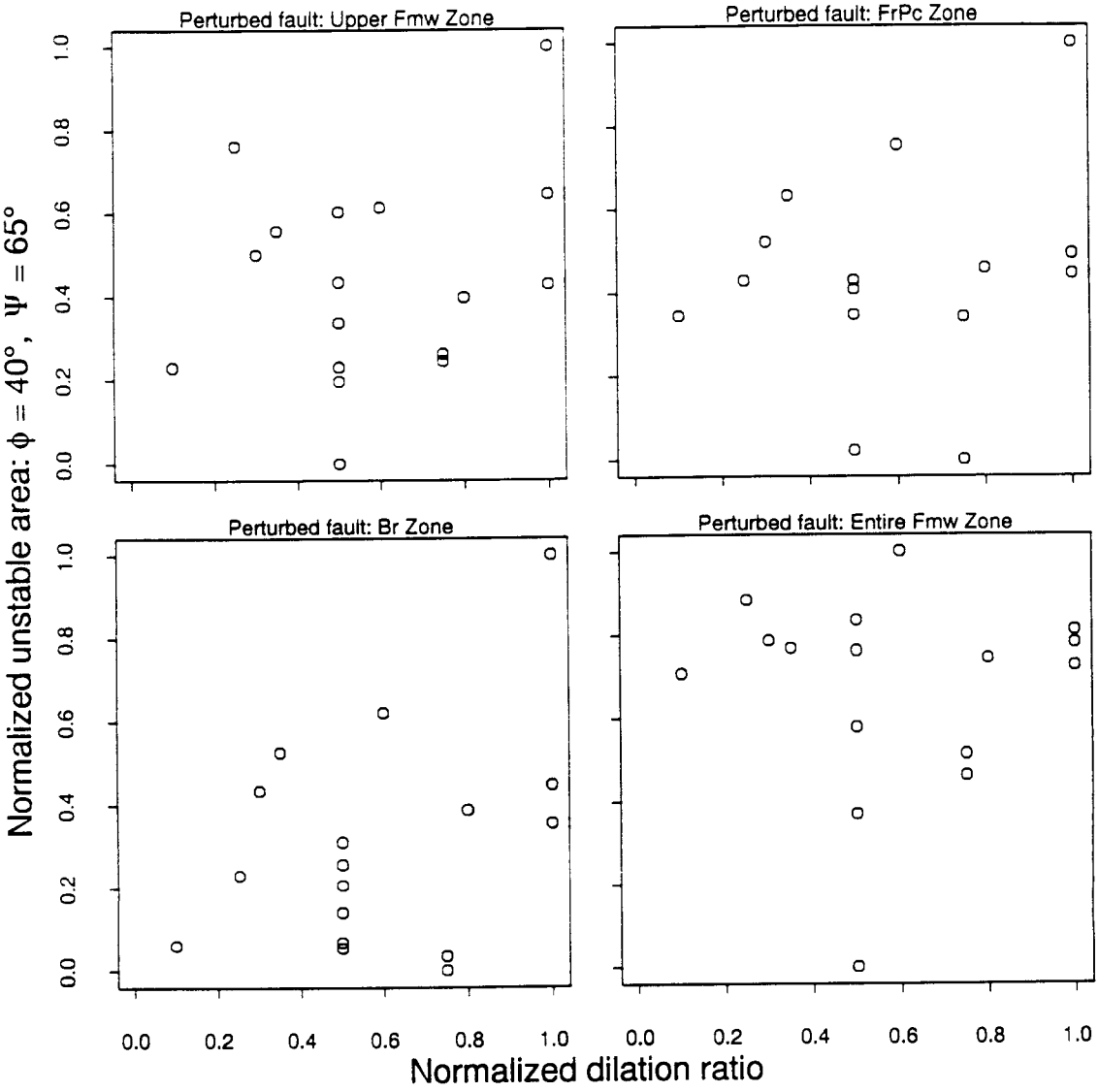

Figure B-107. Sensitivity of the area of potential instability to changes in the value of the dilation angle, based on slip on 65° W-dipping planes with 40°-friction angle

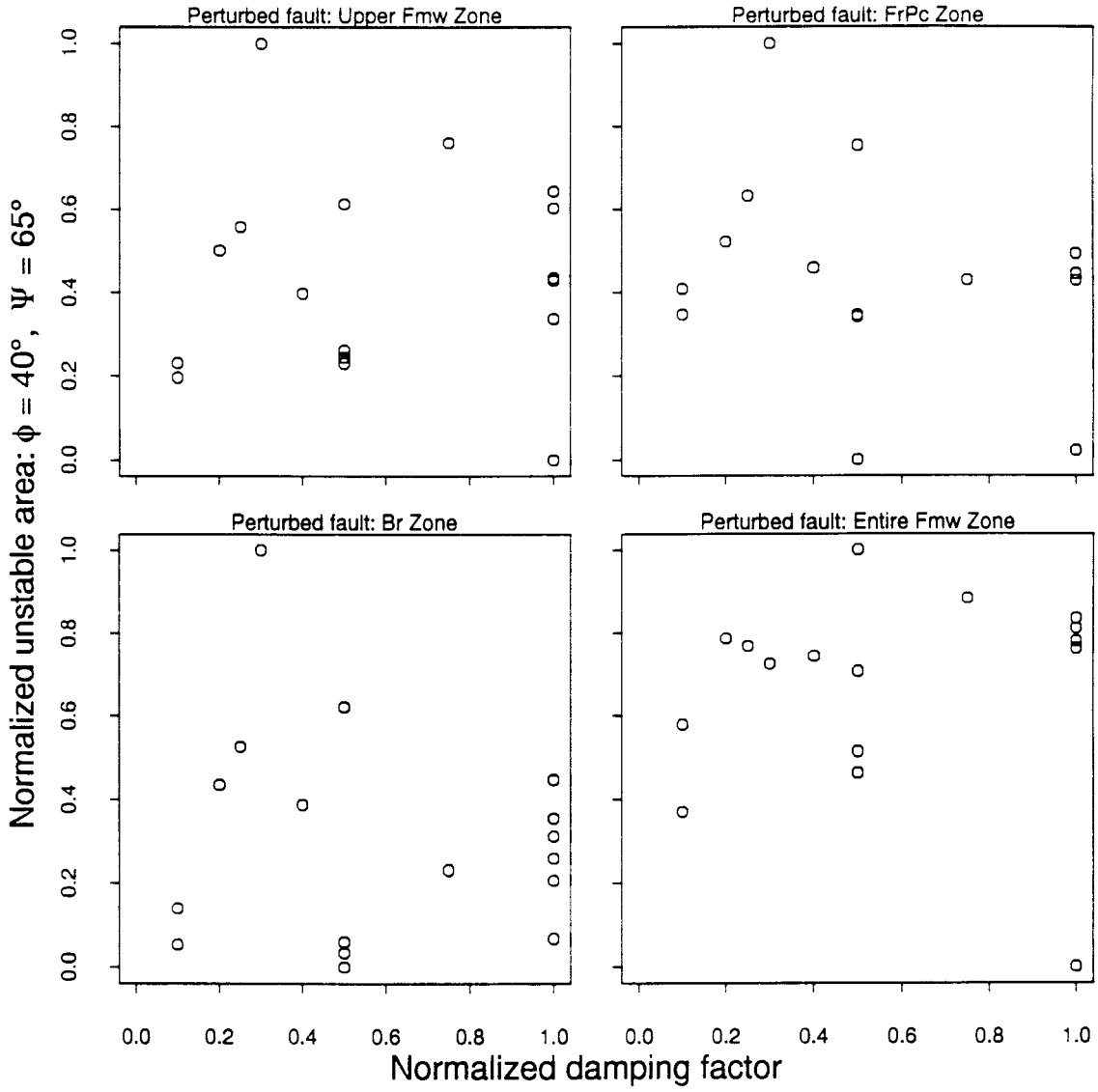

Figure B-108. Sensitivity of the area of potential instability to changes in the value of the damping factor, based on slip on 65° W-dipping planes with 40°-friction angle

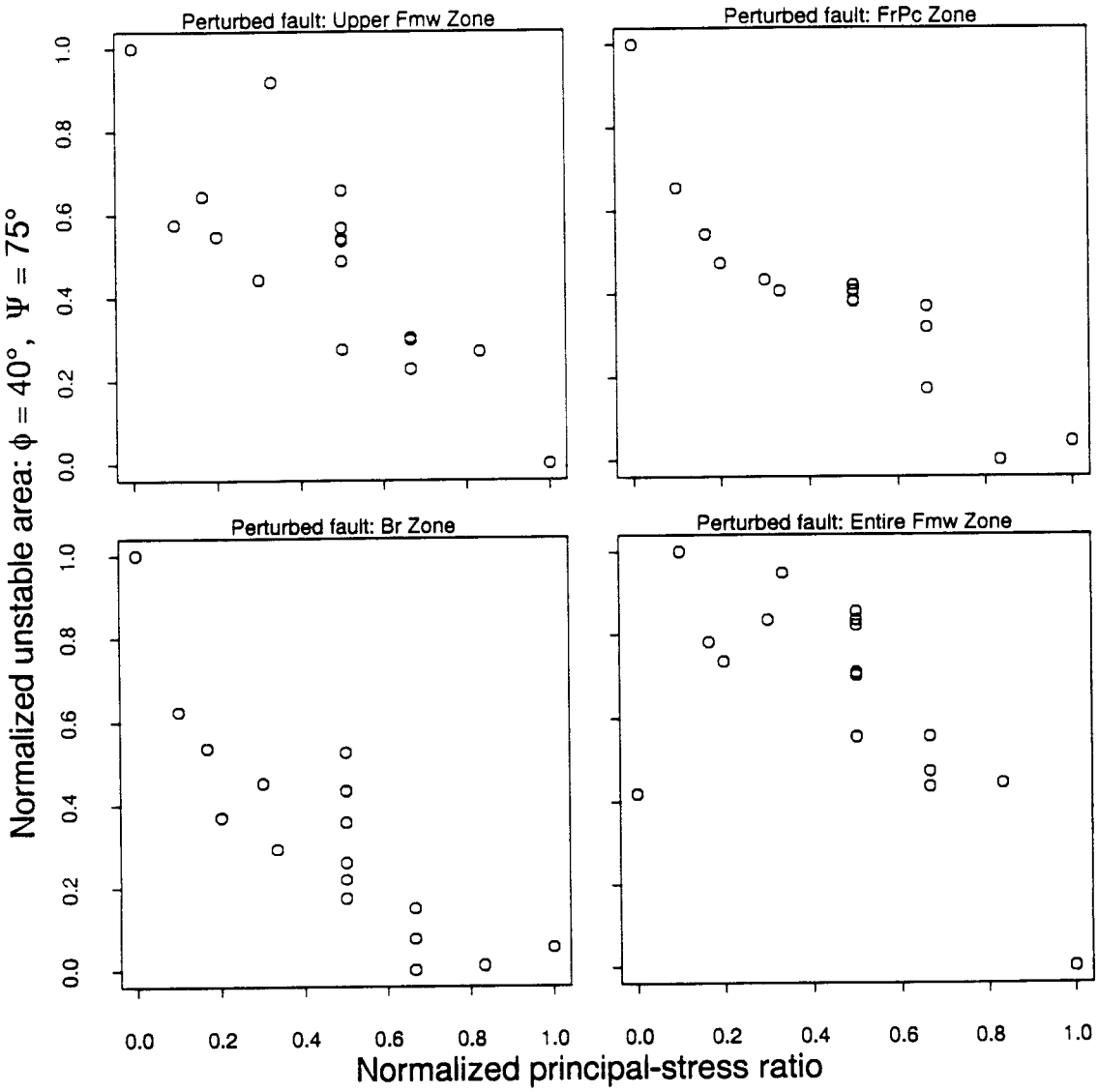

Figure B-109. Sensitivity of the area of potential instability to changes in the value of the principal stress ratio k_3, based on slip on 75° W-dipping planes with 40°-friction angle

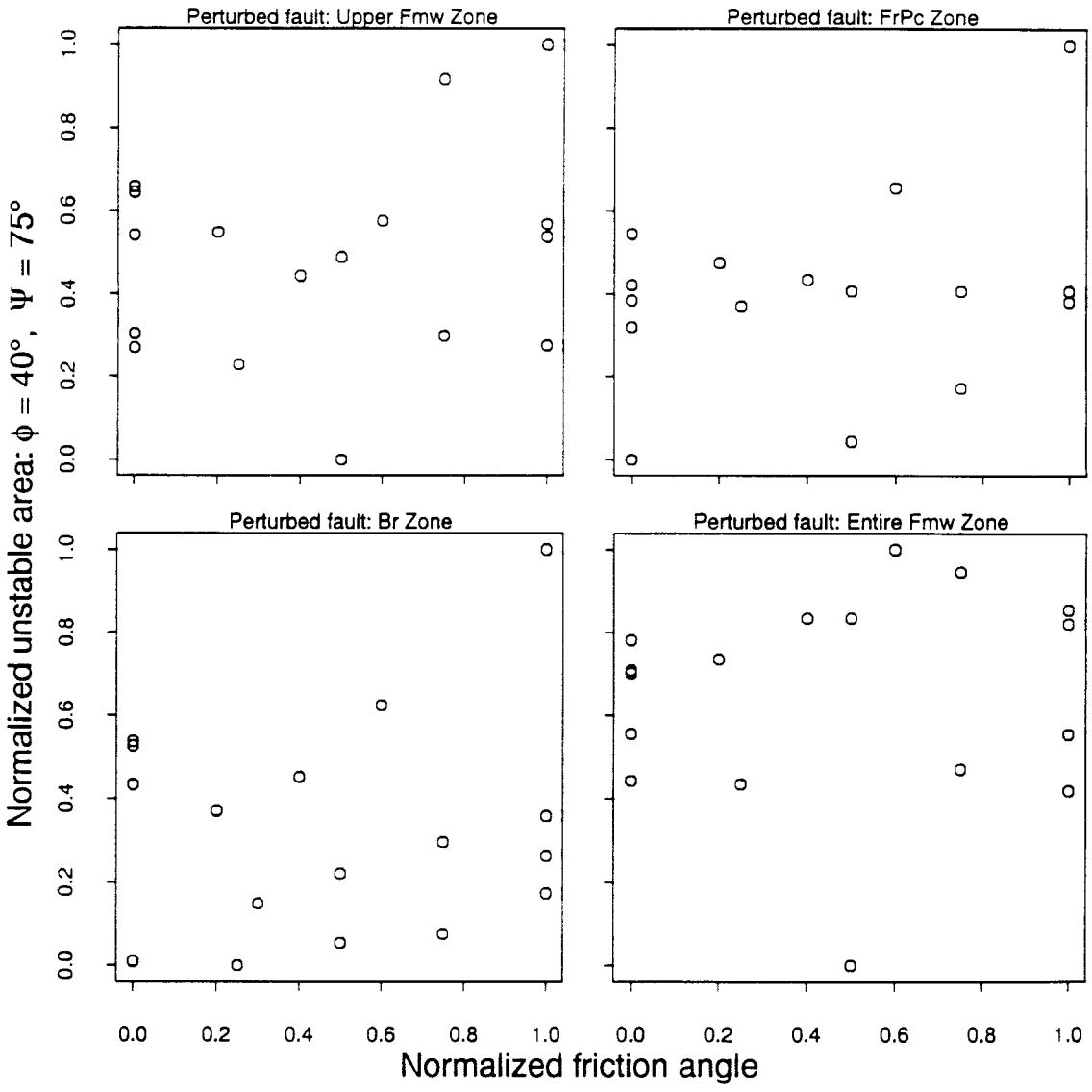

Figure B-110. Sensitivity of the area of potential instability to changes in the value of the rock-mass friction angle, based on slip on 75° W-dipping planes with 40°-friction angle

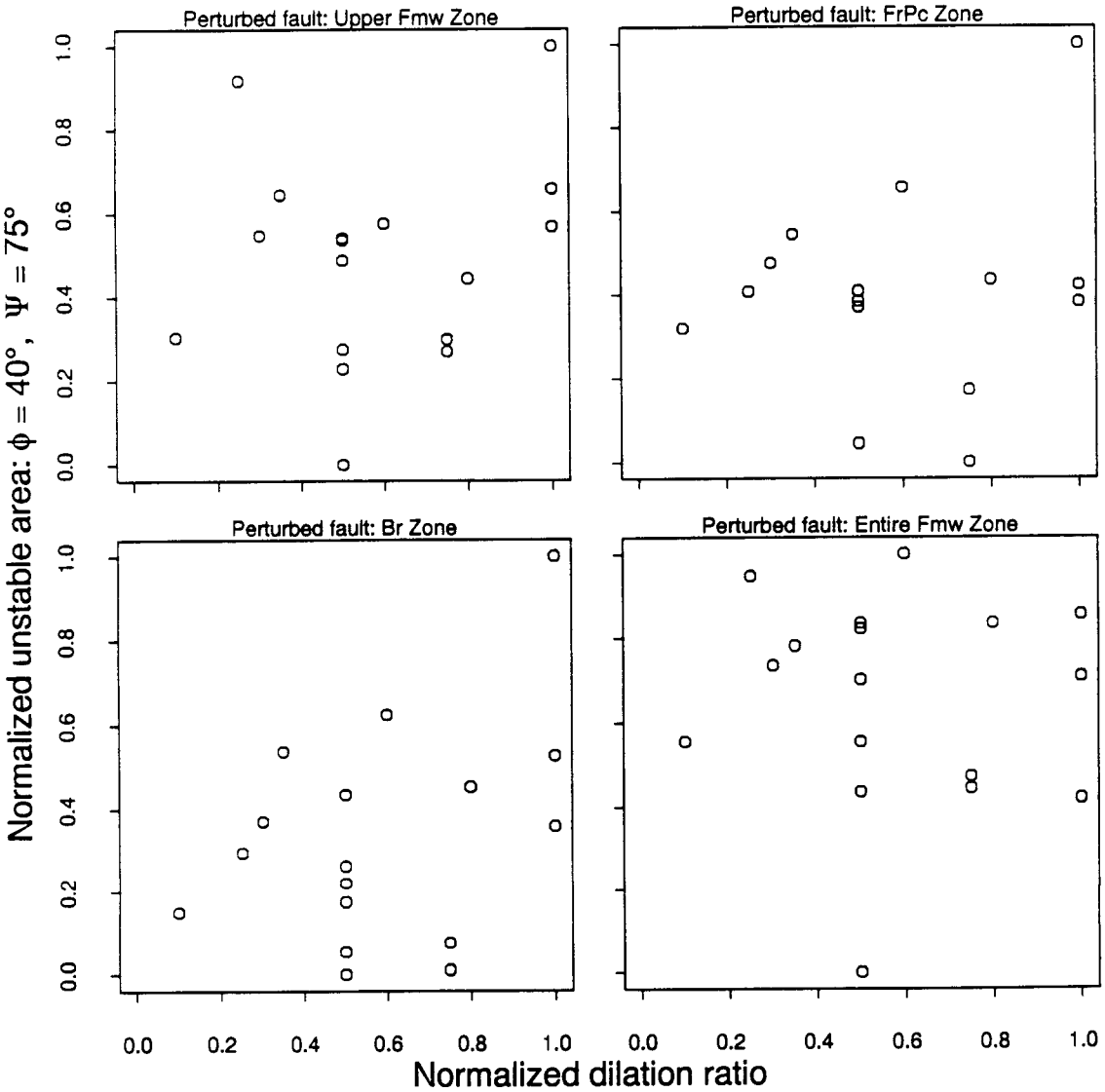

Figure B-111. Sensitivity of the area of potential instability to changes in the value of the dilation angle, based on slip on 75° W-dipping planes with 40°-friction angle

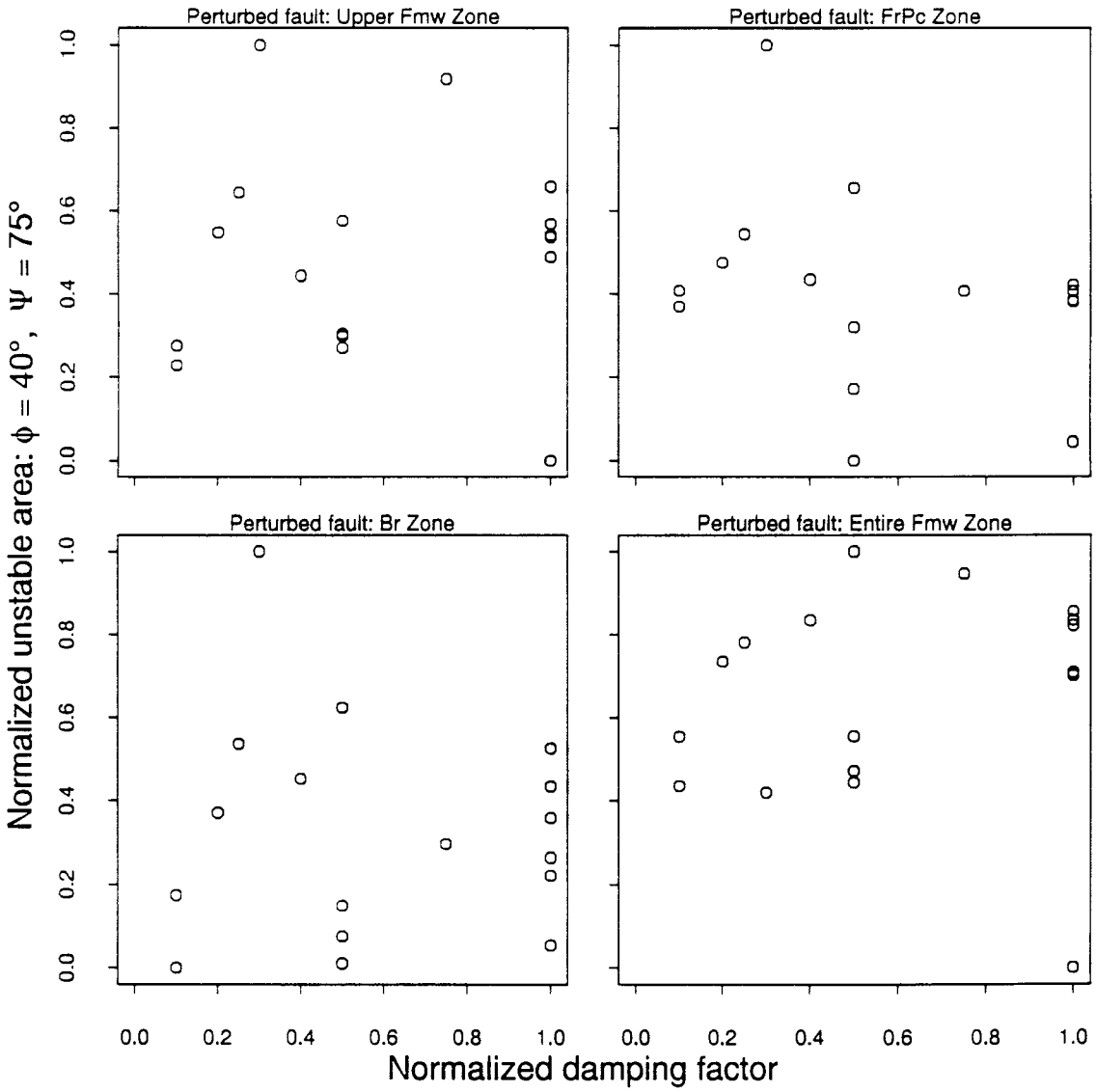

Figure B-112. Sensitivity of the area of potential instability to changes in the value of the damping factor, based on slip on 75° W-dipping planes with 40°-friction angle

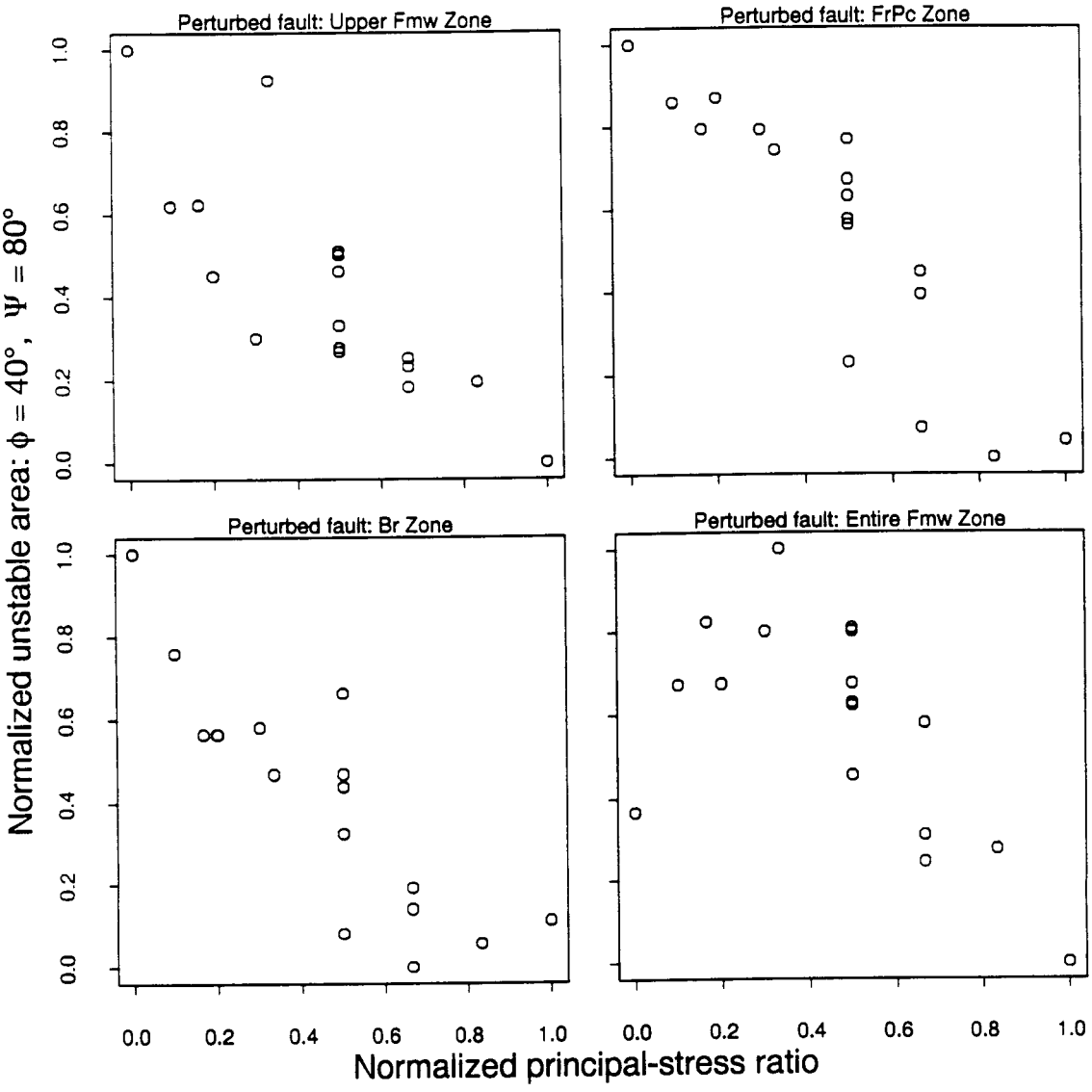

Figure B-113. Sensitivity of the area of potential instability to changes in the value of the principal stress ratio k_3, based on slip on 80° W-dipping planes with 40°-friction angle

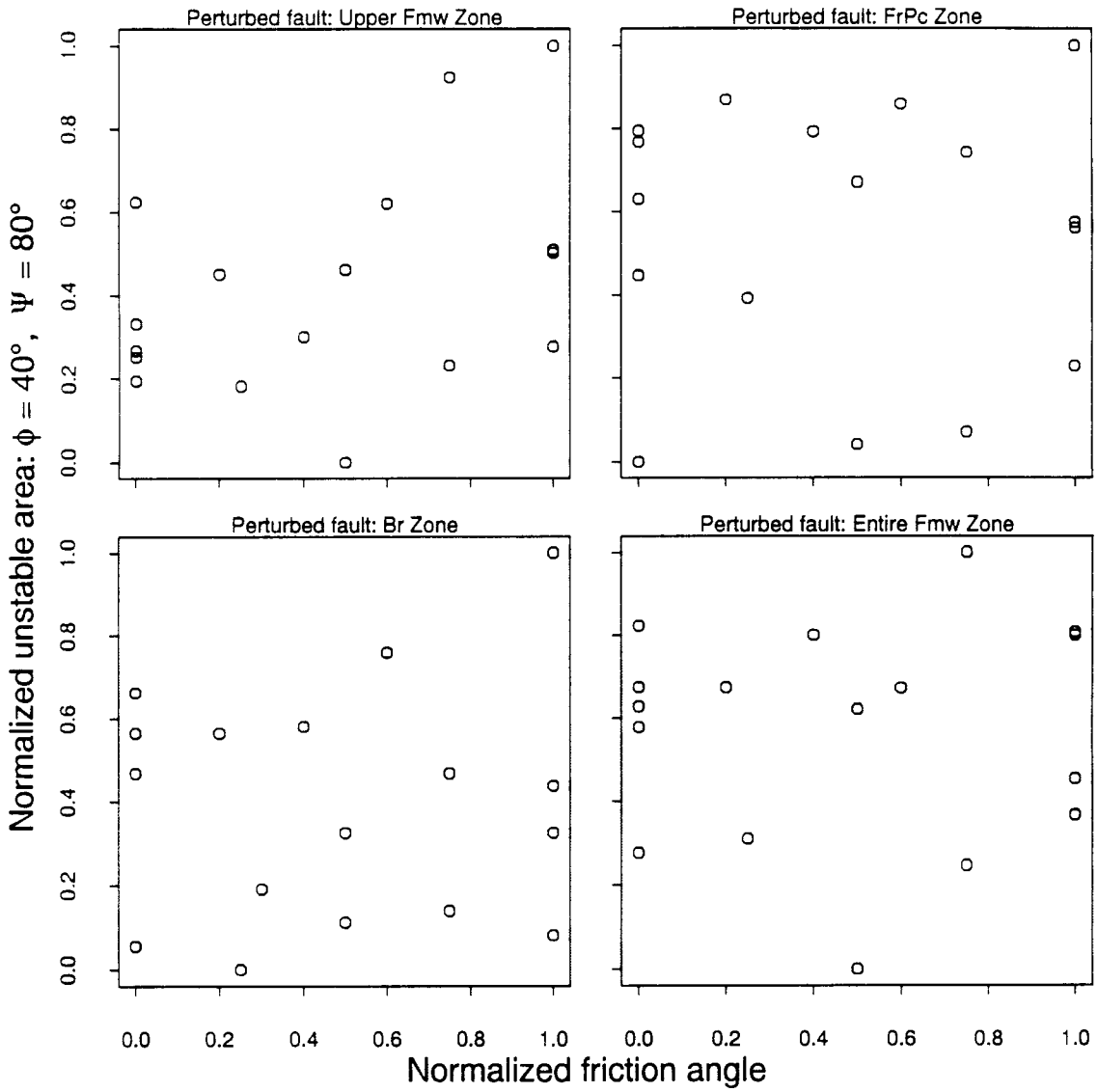

Figure B-114. Sensitivity of the area of potential instability to changes in the value of the rock-mass friction angle, based on slip on 80° W-dipping planes with 40°-friction angle

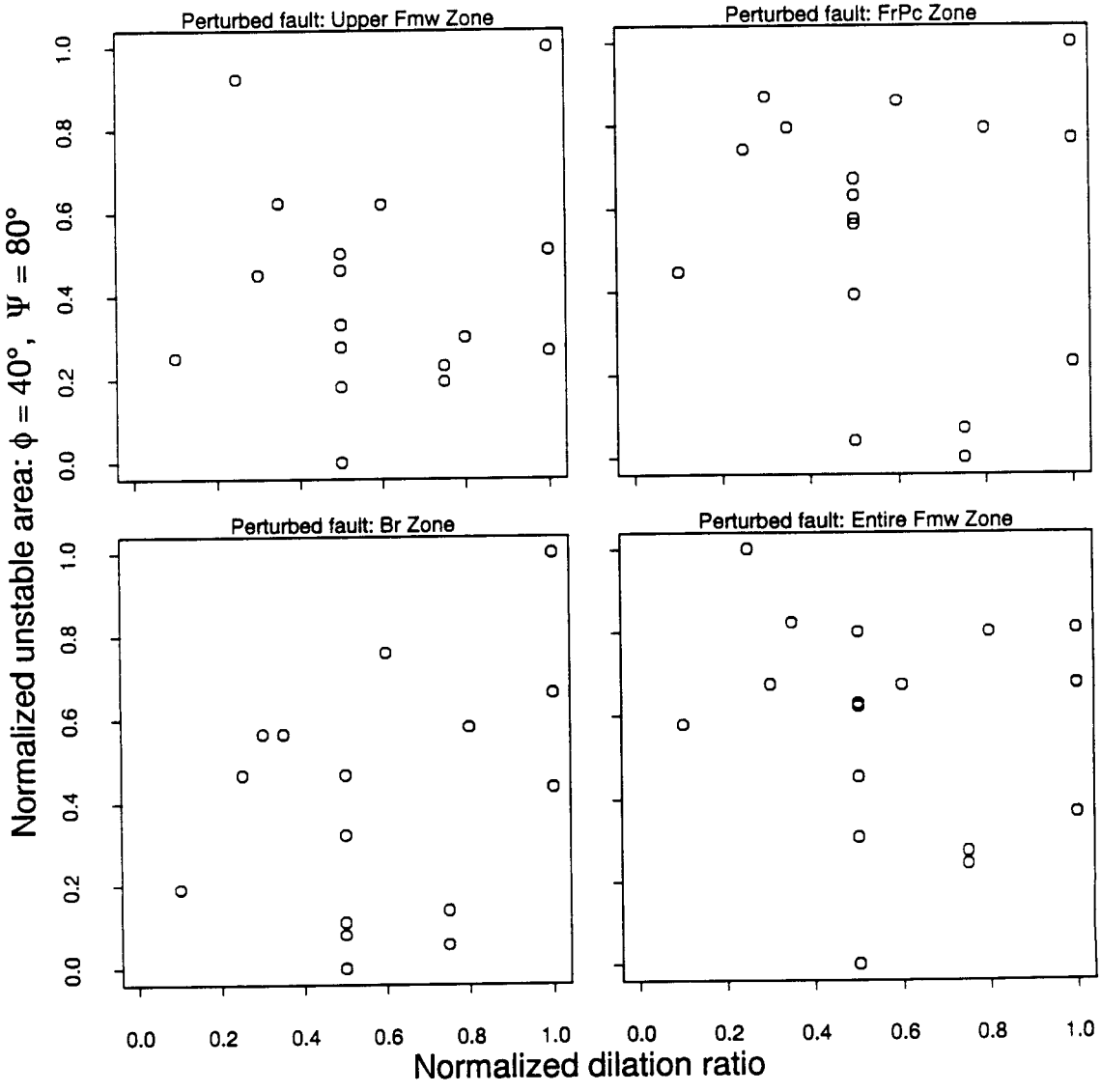

Figure B-115. Sensitivity of the area of potential instability to changes in the value of the dilation angle, based on slip on 80° W-dipping planes with 40°-friction angle

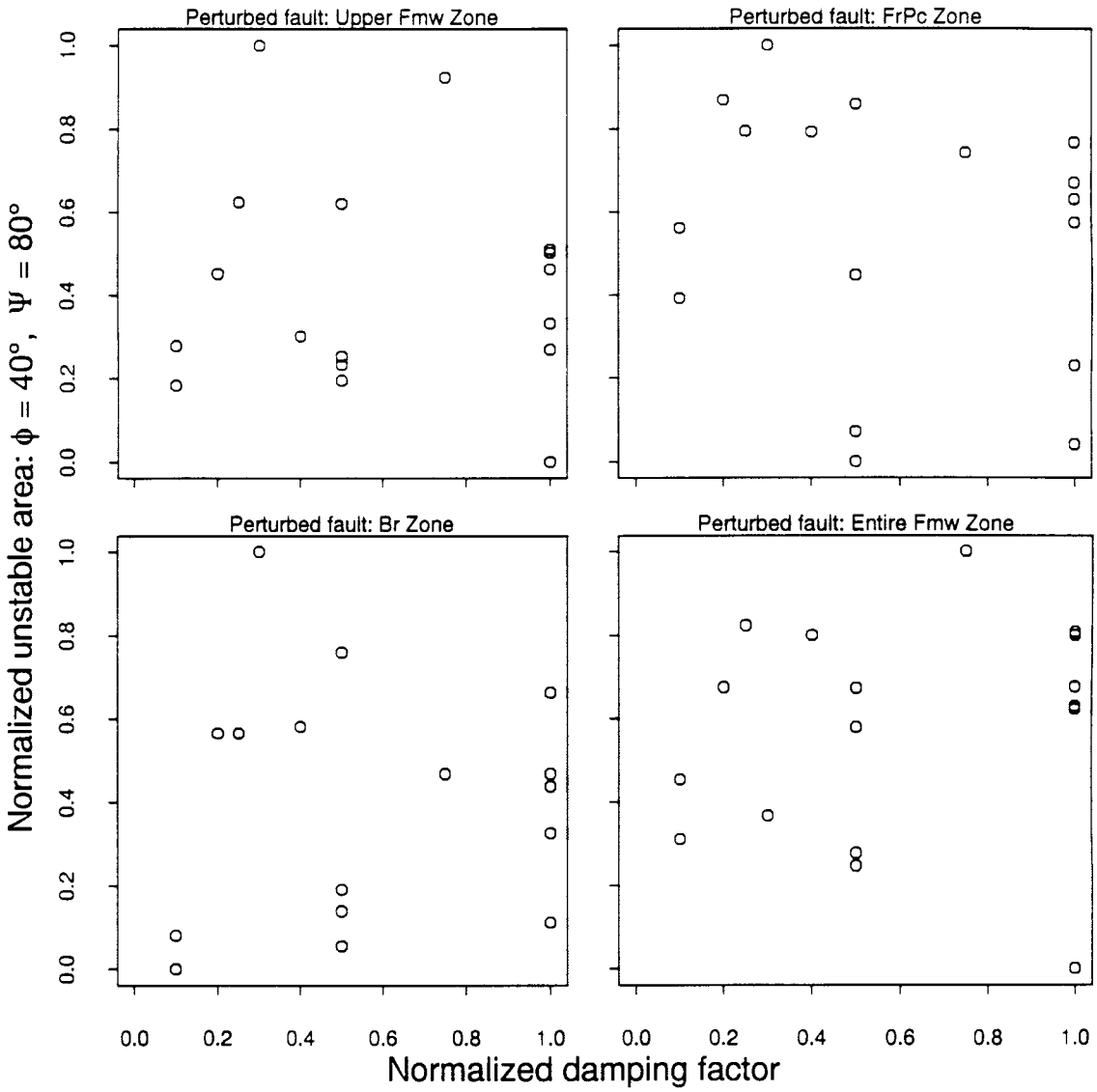

Figure B-116. Sensitivity of the area of potential instability to changes in the value of the damping factor, based on slip on 80° W-dipping planes with 40°-friction angle